Fabrication of Hyperbolic Metamaterials using Atomic Layer Deposition

Shkondin, Evgeniy

Publication date:
2016

Document Version
Publisher's PDF, also known as Version of record

Technical University of Denmark

National Center for Micro- and Nanofabrication (DTU Danchip)

Department of Photonics Engeneering (DTU Fotonik)

PhD thesis by Evgeniy Shkondin

Fabrication of Hyperbolic Metamaterials using Atomic Layer Deposition

Supervisors:
Andrei V. Lavrinenko
Flemming Jensen

December, 2016

Summary

This thesis describes the technological development, design and fabrication of hyperbolic metamaterials (HMMs) - one of the most unusual classes of artificial electromagnetic subwavelength structures. The thesis begins with the review of optical metamaterials. Starting with Maxwell's equations the concept of hyperbolic medium is explained. Metamaterial design, implementation as well as possible applications are reviewed. Electrodynamically, HMMs are described by a dielectric permittivity tensor ε with components of opposite signs (e.g. $\varepsilon_x = \varepsilon_y < 0$, $\varepsilon_z > 0$). HMMs possess unusually high wavevector, optical density of states, and anisotropy, leading to a wide variety of potential applications such as broadband enhancement in the spontaneous emission for a single photon source, subwavelength imaging, sensing, thermal engineering, and steering of optical signals. HMMs have a potential to be a robust and versatile multi-functional platform for nanophotonics in the broad range of operating wavelengths from visible to THz regions and even at microwave region. Despite the proposed architecture of hyperbolic media, which geometry includes simple metal/deielctric multilayers and metallic wires incorporated in dielectric host, the fabrication is still challenging, since ultrathin, continuous, pinhole free nanometer-scale coatings are desired.

The required high-quality thin layers have been fabricated using atomic layer deposition (ALD). It is a relatively new, cyclic, self-limiting thin film deposition technology allowing thickness control on atomic scale. As the deposition relies on a surface reaction, conformal pinhole free films can be deposited on various substrates with advanced topology. This method has been a central theme of the project and a core fabrication technique of plasmonic and dielectric metamaterial components.

The deposition characteristics of the simplest and most studied ALD processes, Al_2O_3 and TiO_2 were studied as a starting point. Later, the growth and characterization of ZnO semiconductor and Cu metal have been explored.

The ability to reproducibly deposit conformal TiO_2 and Al_2O_3 dielectric coatings has been implemented in optical experiment where the effective medium approximation theory (EMA) was tested. Flat dielectric multilayers with strict thicknesses of either 10 or 20 nm of each individual layer, were deposited on Si substrates and characterized using x-ray photoelectron spectroscopy (XPS) and scanning electron microscopy (SEM).

The next milestone was a technology development where the ALD dielectric coatings could be placed as individual, separate units in one or two dimensional lattices (gratings or pillars). This was achieved by combining ALD, deep ultra-violet (UV) stepper lithography and advanced silicon deep reactive ion etching (DRIE) techniques. Three different high aspect ratio, freestanding Al_2O_3 and TiO_2 structures have been successfully manufactured: gratings, pillars and poly-cylindrical

arrays. The challenge of Si template fabrication using DRIE and isolation of the final structures using selective Si etch were addressed.

Fabrication of HMMs requires the implementation of plasmonic components, and traditionally noble metals are used for such purposes due to their abundant free electrons in the conduction band. However, their large real and imaginary parts of the permittivity, especially in the infrared range, result in high loss and weak confinement to the surface. Additionally, the most implemented metals in plasmonics such as Au and Ag are difficult to pattern at nanoscale due to their limited chemistry, adhesion or oxidation issues. Therefore the implementation of alternative plasmonic materials suitable for certain wavelength range has been the focus of this work.

Transparent conductive oxides such as Al-doped ZnO (AZO) have attracted significant attention as alternative plasmonic materials, due to their low loss and metallic behavior in the near/mid infrared range. One more advantage of AZO is the possibility of tuning the permittivity by design, by deciding the dopants or the ratio of different components, thus constituting an advantage over metals having fixed permittivity values. AZO was chosen since the Cu ALD showed up to be far less successful in terms of reproducibility and conformality requirements. AZO has been grown on different substrates in the temperature range $150 - 250\ ^{\circ}C$ and optical, electrical and physical properties have been clarified.

Finally, HMMs with two different geometries has been realized, AZO trenches and AZO pillars standing in a dielectric host (air or Si). Furthermore, it has been proposed that high aspect ratio grating structures with AZO lamellas in a silicon matrix function as a versatile platform supporting both surface and volume infrared waves. By selective etching of Si the performance of the whole structure can be reconfigured. In other words a bi-slab HMM has been suggested, where the effective properties of the structure are controlled by the thickness of the top slab (etching depth).

Resumé

Denne afhandling beskriver den teknologiske udvikling, design og fremstilling af hyperbolske metamaterialer (HMM'er) - en af de mest usædvanlige typer af kunstigt fremstillede elektromagnetiske subwavelength strukturer. Historien begynder med en gennemgang af de optiske metamaterialer. Ved hjælp af Maxwells ligninger forklares begrebet det hyperbolske medium. Der gennemgås design, implementering og mulige anvendelser af metamaterialet. Elektrodynamisk beskrives HMM'er ved brug af den dielektriske permittivitet ε som har komponenter med det modsatte fortegn (f.eks. $\varepsilon_x = \varepsilon_y < 0$, $\varepsilon_z > 0$). HMM'er besidder en usædvanlig høj bølgevektor, optiske tæthedstilstande og anisotropi, hvilken leder til mange forskellige potentielle anvendelser, som for eksempel forbedring af den spontane emission for en enkelt foton-kilde, sub-bølgelængde opløsning, registrering, varmeteknikker og styring af de optiske signaler. HMM'er har et potentiale til at blive en robust og alsidig multifunktionel platform for nanofotonik i et bredt spektrum af operative bølgelængder fra synlig til THz regioner og selv ved mikrobølge region. På trods af den foreslåede arkitektur af det hyperbolske medium, hvis geometri omfatter simple metal/dielektriske multilags strukturer og tynde metalliske søjler indplantet i en dielektrisk matrice, så er fabrikationen stadig udfordrende, da man ønsker at fremstille ultratynde, kontinuerte, pinhole fri film på nanometer-skala.

De tynde film af høj kvalitet er blevet fremstillet ved hjælp af atomarisk lag deponering (ALD). Det er en relativt ny, cyklisk, selvbegrænsende tynd films deponerings teknologi, der tillader tykkelse kontrol på atomar skala. Teknikken er bygget på en kemisk overflade reaktion, så derfor kan konforme, pinhole frie film deponeres på forskellige substrater med avanceret topologi. Denne metode har været et centralt emne i projektet og en kerne fabrikations teknik for plasmoniske og dielektriske komponenter.

Deponerings egenskaberne for de simpleste og mest udforskede ALD processer Al_2O_3 og TiO_2 var udgangspunktet. Senere er væksten og karakteriseringen af ZnO halvleder og Cu metal blevet undersøgt.

Evnen til at deponere reproducerbart konforme TiO_2 og Al_2O_3 dielektriske tynde film er blevet implementeret i en optisk eksperiment, hvor den effektive medium teori (EMA) blev testet. Flade dielektriske multilag med tykkelser på enten 10 eller 20 nm for hvert enkelt lag blev deponeret på Si substrater og karakteriseret ved hjælp af røntgen fotoelektron spektroskopi (XPS) og scanning elektron mikroskopi (SEM).

Den næste milepæl var at udvikle en teknik, der kunne tillade en placering af de individuelle, separate ALD dielektriske strukturer i én eller to dimensionelle gitre (linier eller søjler). Dette blev opnået ved at kombinere ALD, dyb ultraviolet (UV) stepper litografi og avanceret silicium dyb reaktiv ion ætsning (DRIE) teknikker. Tre forskellige høj aspekt ratio, fritstående Al_2O_3 og TiO_2 strukturer er blevet

fremstillet: linjer, søjler og multicylindre. Udfordringen ved fremstilling af Si-skabelon med DRIE og isolering af de færdiggjorde strukturer ved hjælp af en selektiv Si æts er blevet beskrevet.

Fremstilling af HMM kræver realisering af plasmoniske komponenter, og traditionelt anvendes ædle metaller til sådanne formål på grund af mængden af frie elektroner i deres ledningsbånd. Men deres store reelle og imaginære dele af permittivitet, især i det infrarøde område, resulterer i store optiske tab og svag confinement til overfladen. Derudover er de mest anvendte metaller i plasmonic som Au og Ag vanskelige at mønstre på nanoskala på grund af deres begrænsede kemi, vedhæftning eller oxidering. Derfor har implementering af alternative plasmoniske materialer som er egnet til bestemte bølgelængdeområder været en vigtig del af dette arbejde.

Transparente og ledende oxider, som Al-doperet ZnO (AZO), har tiltrukket en betydelig opmærksomhed som et alternativt plasmonisk materiel, på grund af deres lave optiske tab og metallisk adfærd i det nær/mid infrarøde spektrum. En yderligere fordel ved AZO er muligheden for at tune permittiviten ved at vælge det rette dopings koncentration og/eller ved at optimere deponerings opskriften. Således udgør det en fordel i forhold til metaller med deres faste permittivitets værdier. AZO blev valgt, da Cu ALD viste sig at være langt mindre succesrig med hensyn til reproducerbarhed og konformalitets krav. AZO er blevet deponeret på forskellige substrater i temperaturområdet $150-250\ ^{\circ}C$, og dets optiske, elektriske og fysiske egenskaber er blevet undersøgt.

Endelig er HMM med to forskellige geometrier blevet fremstilt, AZO rister og AZO linjer stående i en dielektrisk matrice (luft eller Si). Endvidere er det blevet vist, at højt aspekt ratio AZO lameller i et silicium medium fungerer som en alsidig platform, der understøtter både overflade og volume infrarøde bølger. Ved selektiv ætsning af Si kan der sker en præstation omdannelse af hele strukturen. Med andre ord er en bi-plade HMM blevet fremstillet, hvor de effektive egenskaber af strukturen som helhed styres af tykkelsen af den øverste plade (ætse dybden).

Preface

This PhD thesis has been submitted to the Department of Photonics Engineering at the Technical University of Denmark in partial fulfillment of the requirements for acquiring the PhD degree. The research providing the foundation for the thesis has been conducted over a period of three years from November 15th, 2013, to November 15th, 2016. It has been carried out partially at the Danish National Center for Micro- and Nanofabrication (DTU Danchip) and partially at the Department of Photonics Engineering (DTU Fotonik), both located at the Technical University of Denmark (DTU). It has been supervised by Prof. Andrei V. Lavrinenko and co-supervised by Prof. Flemming Jensen. The thesis work was publicly funded by a DTU internal institute stipend.

Evgeniy Shkondin

Kgs. Lyngby
Denmark

December, 2016

Acknowledgements

Above all, I would like to thank my supervisors Andrei V. Lavrinenko (DTU Fotonik) and Flemming Jensen (DTU Danchip).
Andrei V. Lavrinenko for introducing me to the field of plasmonics and metamaterials and for teaching me the important topics of this thesis during the course of "*Nanophotonics*". Flemming Jensen for his support during technology development, and his practical guidance of this work. I would like to thank them both for for the opportunity to work in a exciting and learning environment, their time and efforts, discussions of my ideas and proof reading of the manuscripts and presentations.

I would like to express my special thanks to Osamu Takayama who not being my official supervisor, has been an "*Éminence grise*" of the project. His decisions and ideas helped not only the realization of several types of hyperbolic metamaterials, but also the observation of Dyakonov plasmons supported on their boundaries. I'm thankful to Mohammad Esmail Aryaee Panah for all FTIR measurements, which proved the hyperbolic nature of my structures.

I would like to express my sincere gratitude to Pernille Voss Larsen who helped me to get on well with the machines in the cleanroom at a the very first days of work. I would also like to thank Mikkel Dysseholm Mar for coming along with my project and for useful advices on fabrication. Additionally, I would like to thank Berit Herstrøm and Jonas Michael Lindhard for their help with dry etch techniques.

I acknowledge the support of all of the technical staff of DTU Danchip and I am especially, endlessly grateful to Peter Windmann for keeping my workhorse ALD tool up and running, while providing invaluable technical details.

I would like to thank Elena Khomtchenko and Matthias Keil who did all work related to Deep-UV stepper lithography.

Furthermore, I would like to express my thanks to Pei Liu and Hossein Alimadadi from DTU CEN for TEM characterization of produced pillar structures.

I also want to thank Flemming Bjerg Grumsen from DTU Mechanical Engineering for assisting in XRD measurements and providing access to the equipment.

Moreover, I am thankful to our collaborators outside DTU, especially the Birck Nanotechnology Center of Purdue University in US and the Nanooptics Group of CIC nanoGUNE research center in Spain for bringing the optical characterization of produced hyperbolic metamaterials to the whole new level.

I would like to thank the whole Metamaterials group at DTU Photonics, the current as well as former members - Radu Malureanu, Sergei Zhukovsky, Andrei Andryieuski and Maksim Zalkovskij for their help, advices and discussions of the ideas at the group meetings.

In addition, I wish to thank the whole DTU Danchip research unit for a warm, stimulating and friendly atmosphere.

Finally, I owe my thanks to my family and friends for their patience, love and support.

LIST OF ABBREVIATIONS AND ACRONYMS

ALD Atomic Layer Deposition.

ASE Advanced Silicon Etching.

AZO Aluminium Doped Zinc Oxide.

BARC Bottom Anti-Reflective Coating.

BEOL Back End of the Line.

Cu(dmap)2 Copper dimethylamino-2-propoxide.

CVD Chemical Vapor Deposition.

DEZ Diethylzinc.

DRIE Deep Reactive Ion Etching.

EBL Electron Beam Lithography.

EDX Energy Dispersive X-Ray Spectroscopy.

EMA Effective Medium Approximation.

EMT Effective Medium Theory.

ENZ Epsilon Near Zero.

FIB Focus Ion Beam.

FTIR Fourier Transform Infrared Spectroscopy.

GPC Growth Per Cycle.

HAADF High Angle Annular Dark-Field Imaging.

HMM Hyperbolic Metamaterial.

IBE Ion Beam Etching.

IC Integrated Circuit.

ICP Inductively Coupled Plasma.

LG modes Laguerre-Gauss Modes.

LPCVD Low Pressure Chemical Vapor Deposition.

OAM Orbital Angular Momentum.

PC Photonic Crystal.

PEALD Plasma Enhanced Atomic Layer Deposition.

PVD Physical Vapor Deposition.

RCA Wafer cleaning procedure, historically called for *"Radio Corporation of America"*.

RIE Reactive Ion Etching.

SAED Selected Area Electron Diffraction.

sccm Standard Cubic Centimeters per Minute.

SE Spectroscopic Ellipsometry.

SEM Scanning Electron Microscope.

SOI Silicon on Insulator.

SP Surface Plasmons.

SPP Surface Plasmons Polaritons.

TCO Transparent Conducting Oxide.

TEM Transmission Electron Microscopy.

TIR Total Internal Reflection.

TMA Trimethylaluminium.

TTIP Titaniumtetraisopropoxide.

UV Ultraviolet.

XPS X-ray Photoelectron Spectroscopy.

XRD X-Ray Diffraction.

CONTENTS

Page

CHAPTER 1

HYPERBOLIC METAMATERIALS: THEORY AND DESIGN

Metamaterials are artificial, nano-engineered composites with designed properties beyond those available in nature with applications in all aspect of materials science. Optical metamaterials with hyperbolic dispersion have shown promises for next generation optical materials with electromagnetic responses that cannot be obtained from conventional media. This chapter reviews the fundamental concepts of hyperbolic media, and illustrate a practical approach of the metamaterial realization based on thin films and nanowires. Additionally, a unified view of practical applications based on hyperbolic dispersion is revealed.

1.1 Introduction

In the 1960's, Veselago suggested that negative refraction of light can be found in a material with simultaneous negative permittivity ε and permeability μ [1]. It took more than three decades before researchers were able to design metamaterials to achieve such an intriguing effect.

Among many optical metamaterials proposed and fabricated since then, the hyperbolic metamaterials (HMMs) have become an active research area, due to their ability to access and manage the near-field which is defined by distances shorter than the wavelength of light in vacuum [2]-[5]. This feature comes from the excitation of coupled surface plasmons (SPs) [6] inside of HMMs. SPs are collective electron oscillations that exist at the interface between two materials where the real part of the dielectric function changes sign across the interface (e.g. a metal-dielectric interface). The charge motion creates electromagnetic field outside (as

well as evanescent field inside) the metal. The combined excitation, including both the charge motion and the associated electromagnetic field, is called either a surface plasmon polariton (SPP) (also called *propagating* surface plasmons) at a planar interfaces, or a *localized* surface plasmon for the closed surface of a small particles or wire medium. The electromagnetic field generated by plasmons decays rapidly inside the structures, and thereby interacts principally with the near-field of the interfaces. Dealing with metal-dielectric multilayers or metallic nanowires, the electromagnetic field bounded to confined free electrons of plasmonic structures lead to a collective oscillation response. This behavior can be interpreted in terms of effective media, with unusual hyperbolic dispersion, unlike common isotropic dispersion of dielectrics, or zero-propagation (evanescent decay of pure metals). In order to mathematically describe such effective media one should start with Maxwell's equations.

1.2 Hyperbolic Media

For any material, the nature of its electromagnetic response is defined by the sign of the dielectric permittivity and magnetic permeability. The classical field theory of light-matter interactions is governed by Maxwell's equations:

$$\nabla \times \mathbf{E} = -\frac{\partial \mathbf{B}}{\partial t} \tag{1.1}$$

$$\nabla \times \mathbf{H} = \mathbf{J} + \frac{\partial \mathbf{D}}{\partial t} \tag{1.2}$$

$$\nabla \cdot \mathbf{D} = \rho \tag{1.3}$$

$$\nabla \cdot \mathbf{B} = 0 \tag{1.4}$$

Electric displacement $\mathbf{D}$ and magnetic induction $\mathbf{B}$ is given by:

$$\mathbf{D} = \varepsilon_0 \mathbf{E} + \mathbf{P} = \varepsilon_0 (1 + \chi_e)\mathbf{E} = \varepsilon_0 \bar{\bar{\boldsymbol{\varepsilon}}} \mathbf{E}$$
$$\mathbf{B} = \mu_0 (\mathbf{H} + \mathbf{M}) = \mu_0 (1 + \chi_m)\mathbf{H} = \mu_0 \bar{\bar{\boldsymbol{\mu}}} \mathbf{H}$$

The vacuum permittivity and permeability in SI units are $\varepsilon_0 = 8.85 \times 10^{-12} \frac{\mathrm{F}}{\mathrm{m}}$ and $\mu_0 = 4\pi \times 10^{-7} \frac{\mathrm{H}}{\mathrm{m}}$. Only nonmagnetic media are under the investigation. The relative permeability $\bar{\bar{\boldsymbol{\mu}}}$ and permittivity $\bar{\bar{\boldsymbol{\varepsilon}}}$ tensors can be written as:

$$\bar{\bar{\boldsymbol{\varepsilon}}} = \begin{pmatrix} \varepsilon_{xx} & 0 & 0 \\ 0 & \varepsilon_{yy} & 0 \\ 0 & 0 & \varepsilon_{zz} \end{pmatrix} \qquad \bar{\bar{\boldsymbol{\mu}}} = \begin{pmatrix} 1 & 0 & 0 \\ 0 & 1 & 0 \\ 0 & 0 & 1 \end{pmatrix} \tag{1.5}$$

Electric and magnetic fields can be described by implementing plane wave approximation expressions:

$$\mathbf{E} = \boldsymbol{E_0} e^{i(\omega t - \mathbf{k}\cdot\mathbf{r})} \qquad \mathbf{H} = \boldsymbol{H_0} e^{i(\omega t - \mathbf{k}\cdot\mathbf{r})} \tag{1.6}$$

Taking Maxwell's equation 1.1 and using the definition of magnetic induction and plane-wave expressions of the fields:

$$\nabla \times \{\boldsymbol{E_0} e^{i(\omega t - \mathbf{k}\cdot\mathbf{r})}\} = -\frac{\partial}{\partial t}\mu_0 \bar{\bar{\boldsymbol{\mu}}} \{\boldsymbol{H_0} e^{i(\omega t - \mathbf{k}\cdot\mathbf{r})}\} \tag{1.7}$$

It leads to following expression:

$$\begin{pmatrix} \frac{\partial}{\partial x} \\ \frac{\partial}{\partial y} \\ \frac{\partial}{\partial z} \end{pmatrix} \times \begin{pmatrix} \boldsymbol{E_x} e^{i(\omega t - \mathbf{k}\cdot\mathbf{r})} \\ \boldsymbol{E_y} e^{i(\omega t - \mathbf{k}\cdot\mathbf{r})} \\ \boldsymbol{E_z} e^{i(\omega t - \mathbf{k}\cdot\mathbf{r})} \end{pmatrix} = -\frac{\partial}{\partial t}\mu_0 \begin{pmatrix} 1 & 0 & 0 \\ 0 & 1 & 0 \\ 0 & 0 & 1 \end{pmatrix} \begin{pmatrix} \boldsymbol{H_x} e^{i(\omega t - \mathbf{k}\cdot\mathbf{r})} \\ \boldsymbol{H_y} e^{i(\omega t - \mathbf{k}\cdot\mathbf{r})} \\ \boldsymbol{H_z} e^{i(\omega t - \mathbf{k}\cdot\mathbf{r})} \end{pmatrix} \tag{1.8}$$

After calculations the relation becomes:

$$\mathbf{k} \times \mathbf{E} = \mu_0 \omega \mathbf{H} \tag{1.9}$$

Now, the same procedure repeats with Maxwell equation 1.2:

$$\nabla \times \{\boldsymbol{H_0} e^{i(\omega t - \mathbf{k}\cdot\mathbf{r})}\} = \mathbf{J} + \frac{\partial}{\partial t}\varepsilon_0 \bar{\bar{\boldsymbol{\varepsilon}}} \{\boldsymbol{E_0} e^{i(\omega t - \mathbf{k}\cdot\mathbf{r})}\} \tag{1.10}$$

In the absence of sources, the equation above can be written as:

$$\begin{pmatrix} \frac{\partial}{\partial x} \\ \frac{\partial}{\partial y} \\ \frac{\partial}{\partial z} \end{pmatrix} \times \begin{pmatrix} \boldsymbol{H_x} e^{i(\omega t - \mathbf{k}\cdot\mathbf{r})} \\ \boldsymbol{H_y} e^{i(\omega t - \mathbf{k}\cdot\mathbf{r})} \\ \boldsymbol{H_z} e^{i(\omega t - \mathbf{k}\cdot\mathbf{r})} \end{pmatrix} = \frac{\partial}{\partial t}\varepsilon_0 \begin{pmatrix} \varepsilon_{xx} & 0 & 0 \\ 0 & \varepsilon_{yy} & 0 \\ 0 & 0 & \varepsilon_{zz} \end{pmatrix} \begin{pmatrix} \boldsymbol{E_x} e^{i(\omega t - \mathbf{k}\cdot\mathbf{r})} \\ \boldsymbol{E_y} e^{i(\omega t - \mathbf{k}\cdot\mathbf{r})} \\ \boldsymbol{E_z} e^{i(\omega t - \mathbf{k}\cdot\mathbf{r})} \end{pmatrix} \tag{1.11}$$

After calculations it appears as:

$$\mathbf{k} \times \mathbf{H} = -\varepsilon_0 \bar{\bar{\boldsymbol{\varepsilon}}} \omega \mathbf{E} \tag{1.12}$$

Combining equations 1.9 and 1.12 yields the eigenvalue problem for the electrical field:

$$\mathbf{k} \times (\mathbf{k} \times \mathbf{E}) = -\omega^2 \mu_0 \varepsilon_0 \bar{\bar{\boldsymbol{\varepsilon}}} \mathbf{E} \tag{1.13}$$

or written in matrix form:

$$\begin{pmatrix} k_0^2\varepsilon_{xx} - k_y^2 - k_z^2 & k_x k_y & k_x k_z \\ k_x k_y & k_0^2\varepsilon_{yy} - k_x^2 - k_z^2 & k_z k_y \\ k_x k_z & k_z k_y & k_0^2\varepsilon_{zz} - k_x^2 - k_y^2 \end{pmatrix} \begin{pmatrix} \boldsymbol{E_x} \\ \boldsymbol{E_y} \\ \boldsymbol{E_z} \end{pmatrix} = 0 \tag{1.14}$$

where $k_0 = \frac{\omega}{c} = \omega\sqrt{\varepsilon_0 \mu_0}$.

To find the nontrivial solutions to equation 1.13 it is necessary to calculate the determinant of the matrix and solve this equation:

$$\mathrm{Det}\left|\begin{pmatrix} k_0^2\varepsilon_{xx}-k_y^2-k_z^2 & k_xk_y & k_xk_z \\ k_xk_y & k_0^2\varepsilon_{yy}-k_x^2-k_z^2 & k_zk_y \\ k_xk_z & k_zk_y & k_0^2\varepsilon_{zz}-k_x^2-k_y^2 \end{pmatrix}\right| = 0 \qquad (1.15)$$

which leads to:

$$\underbrace{\Big[\Big(k_0^2(\varepsilon_{zz}k_0^2-k_x^2-k_y^2)\varepsilon_{yy}-k_0^2(k_x^2+k_z^2)\varepsilon_{zz}+k_x^2(k_x^2+k_y^2+k_z^2)\Big)\varepsilon_{xx}+ \quad \dots \quad \dots \quad + \Big(-k_0^2(k_y^2+k_z^2)\varepsilon_{zz}+k_y^2(k_x^2+k_y^2+k_z^2)\Big)\varepsilon_{yy}+k_z^2\varepsilon_{zz}(k_x^2+k_y^2+k_z^2)\Big]k_0^2=0}_{\text{Dispersion relations}}$$

In case of a *uniaxial* crystal $\varepsilon_{xx}=\varepsilon_{yy}=\varepsilon_\square$, the relation is:

$$\underbrace{\Big(\varepsilon_\square k_0^2-k_x^2-k_y^2-k_z^2\Big)}_{\text{Spherical dispersion}}k_0^2\underbrace{\Big((\varepsilon_{zz}k_0^2-k_x^2-k_y^2)\varepsilon_\square-k_z^2\varepsilon_{zz}\Big)}_{\text{Elliptical dispersion}}=0$$

The imposition of non-trivial solutions to the eigenvalue problem equation leads to the following dispersion relations:
A spherical iso-frequency surface in the k-space describes *ordinary* or TE waves polarized in the $\{xy\}$ plane:

$$k_x^2+k_y^2+k_z^2=\varepsilon_\square k_0^2 \qquad (1.16)$$

The ellipsoidal iso-frequency surface in the k-space describes *extraordinary* or TM waves polarized in the plane of optical axis:

$$\boxed{\frac{k_x^2}{\varepsilon_{zz}}+\frac{k_y^2}{\varepsilon_{zz}}+\frac{k_z^2}{\varepsilon_\square}=k_0^2} \qquad (1.17)$$

The iso-frequencies in k-space for four possible cases, given by equation 1.17 are depicted in Figure 1.1. If both permittivities ε_{zz} and $\varepsilon_\square$ are negative, the media can be described by a free electron gas (pure metal) with evanescently decayed field and as a result no iso-frequency surfaces (Figure 1.1 a). For all positive values of ε_{zz} and $\varepsilon_\square$ the material is normal isotropic dielectric with elliptic or spherical dispersion (Figure 1.1 b).

If one of the permittivities is negative, the situation changes substantially and the extreme anisotropy takes place. Permittivity components with an opposing sign result in hyperbolic iso-frequency surfaces - hence *hyperbolic* media.

The choice $\varepsilon_{zz} < 0$ and $\varepsilon_{\square} > 0$ corresponds to a two-fold hyperboloid, and the hyperbolic media is called *dielectric* or Type I. The choice $\varepsilon_{zz} > 0$ and $\varepsilon_{\square} < 0$ represents one-fold hyperboloid, and the hyperbolic media is called *metallic* or Type II. (Figure 1.1 c) and d)

In contrast to isotropic dielectric, the hyperbolic media can support arbitrary large k vectors, they remain propagating in both HMM types, while in the isotropic medium becomes evanescent due to the bounded nature of iso frequency contours (ellipsoid).

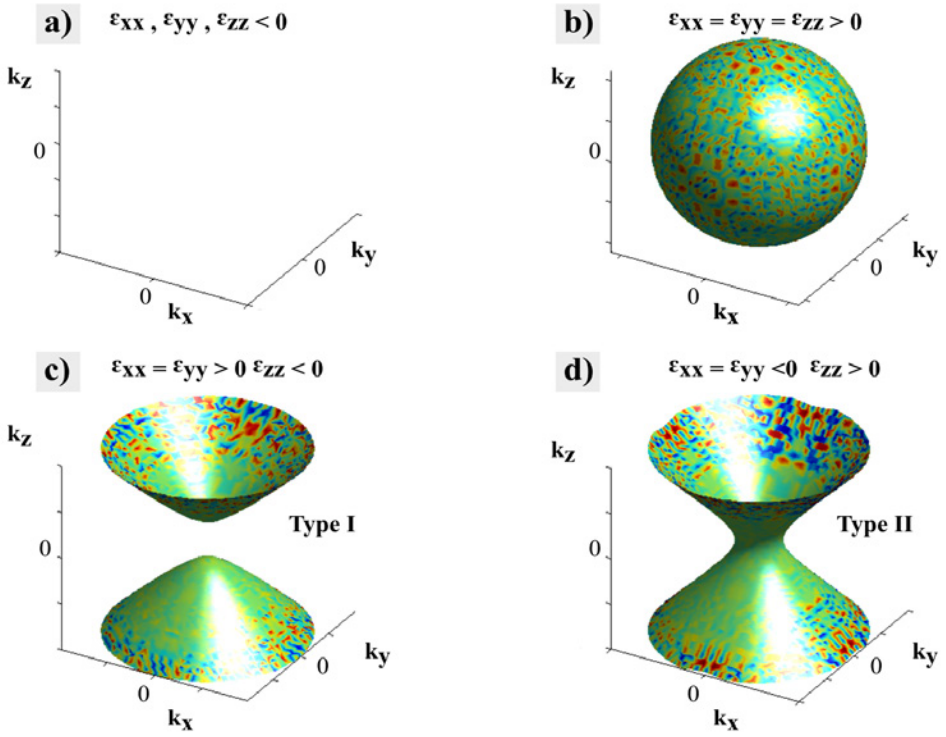

Figure 1.1: Isofrequency surfaces in momentum space for different media. a) Metal or any other material with a negative permittivity b) Isotropic dielectric c) Hyperboloid of Type I ($\varepsilon_{xx} = \varepsilon_{yy} > 0$ $\varepsilon_{zz} < 0$) d) Hyperboloid of Type II ($\varepsilon_{xx} = \varepsilon_{yy} < 0$ $\varepsilon_{zz} > 0$)

Another unique feature of a hyperbolic medium is a directional light emission. Figure 1.2 a) represents both types of hyperbolic materials with $\varepsilon_{zz,\square} = \pm 5$. The values are chosen for illustrative purposes. Considering Type II HMM shown as orange contours in the $\{xz\}$ plane, one can se a direction of group velocity $\boldsymbol{v_g}(\omega) = \frac{\partial}{\partial \boldsymbol{k}}\omega(\boldsymbol{k})$. Both types of hyperbolic media are placed in k-space, within a proximity given by their permittivity and located within the asymptotes shown as blue dotted lines. The expressions of these asymptotes can be found straightforwardly:

$$k_z = \pm k_{x,y}\sqrt{-\frac{\varepsilon_\square}{\varepsilon_{zz}}} \tag{1.18}$$

The expressions of asymptotes show the directional nature of light propagation. This future is forbidden in a conventional dielectric environment, since in ellipsoidal iso-frequency the group velocity $\boldsymbol{v_g}$ is pointed in all directions, resulting in an isotropic emission pattern. Directionality of electromagnetic radiation can also be expressed using half-angle notation:

$$\theta = \arctan\left(\sqrt{-\frac{\varepsilon_\square}{\varepsilon_{zz}}}\right) \tag{1.19}$$

One of the consequences of this directionality is the negative refraction of energy. Let us consider an interface between an isotropic medium with $\varepsilon = 2$ (green circle in Figure 1.2 a) and a hyperbolic environment of Type I. A light wave coming from an isotropic medium contains a $\boldsymbol{k}$ vector and the energy flow, that can be represented by the time averaged Poynting vector $\boldsymbol{S} = \frac{1}{2}\Re\{\boldsymbol{E} \times \boldsymbol{H}^*\}$. In an isotropic medium both the $\boldsymbol{k}$ vector and the Poynting vector are parallel. In a hyperbolic environment k_x and k_z components of the refracted wavevector $\boldsymbol{k_r}$ should be connected by the dispersion relation given by equation 1.17. Since there are no discontinuities in the $\{xy\}$ plane, the k_x component should be the same in both media. It leads to two possible solutions of the refracted wavevector, one represented by a solid blue arrow (Figure 1.2 a) and another represented by a dotted blue arrow, both satisfying equation 1.17. However, only one is physically correct (solid arrows), since the refracted Poynting vector should have a positive z-component, due to the causality principle. Evaluation of the x-components of the S vector gives the negative value, which means that energy is negatively refracted when passing from an isotropic to a hyperbolic medium and vice versa. The finite-element simulation illustrated in Figure 1.2 b), reproduced from reference [7], shows the energy flow propagating through the HMM slab of Type I. The inset depicts the wavevectors and Poynting vectors at the interface of an isotropic and hyperbolic media.

The negative refraction of TM waves was probably the first phenomenon of hyperbolic metamaterials to be studied [8]-[9]. This effect rises the possibility of realizing a lens based on a hyperbolic metamaterial slab. The possible HMMs applications will be discussed in the next sessions.

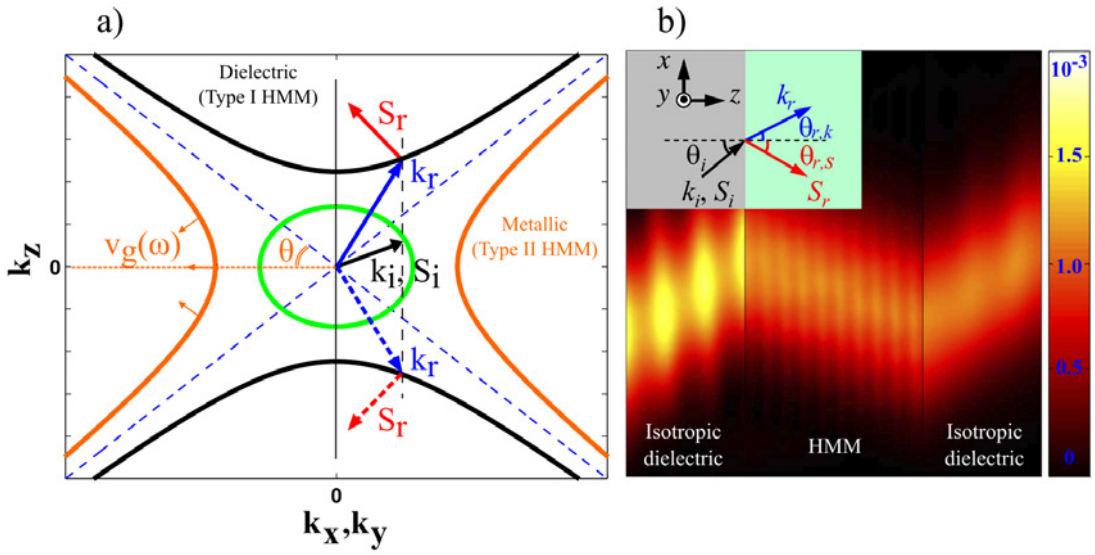

Figure 1.2: a) Isofrequency contours in the $[k_{x,y},\ k_z]$ plane for a dielectric isotropic material with $\varepsilon = 2$ (green circle); hyperbolic media Type I with $\varepsilon_\square = 5$, $\varepsilon_{zz} = -5$ (black hyperbola); hyperbolic media Type II with $\varepsilon_\square = -5$, $\varepsilon_{zz} = 5$ (orange hyperbola). The group velocity is directed as the orange arrows perpendicular to the counter of the HMM Type II. Light is incident from an isotropic medium, where the wavevector k_i and Poynting vector S_i are parallel (black arrow). The refracted wave can be represented by two possible sets of wavevector k_r and S_r (solid and dotted arrows) both sets satisfies equation 1.17. Only the case of solid arrows satisfies the causality principle. b) Finite-element simulations are showing negative refraction of a TM Gaussian beam at $\lambda_0 = 632.8$ nm through the slab of the hyperbolic metamaterial Type I. (The color represents the time-averaged Poynting vector). the inset shows a schematic diagram of negative refraction for a TM wave incident from an isotropic medium to a hyperbolic medium Type I ($\varepsilon_\square = 5$, $\varepsilon_{zz} = -5$). The figure partially reproduced from ref. [7],[10],[11].

1.3 Implementations

The obvious question is what sort of materials that possess the highly anisotropic permittivities which obeys the hyperbolic dispersion relation. Permittivity from the physics point of view presents the macroscopic response of a system of charged particles to an external applied electrical field. A positive permittivity characterizes dielectrics with the polarization parallel to the field. A negative permittivity, indicating an antiparallel polarization, characterizes free electron gasses (metals) and some dielectric and semiconductors at infrared frequencies. Many natural materials possess directional dependent permittivities with opposite sign, even if such behavior may seem to be somewhat exotic. Highly ordered pyrolytic graphite displays hyperbolic behavior in the ultraviolet region [12]. Bismuth, SiC and

sapphire possess hyperbolic frequency bands in the mid/far infrared range. [13]. Recently, tetradymites, Bi_2Se_3 and Bi_2Te_3 studied by Esslinger *et. al.* [14] have shown to be hyperbolic in visible light. These alternatives normally possess high optical loses or are too scarce to be implemented in any practical applications.

Progress in nanofabrication techniques allow the confinement of free electrons in less than three dimensions. The materials with desired permittivity tensor $\bar{\bar{\varepsilon}}$ can now be designed and called *hyperbolic metamaterials*. Currently, two structures have been proposed and studied: deep subwavelength alternating metal-dielectric multilayers and lattice of metallic nanowires incorporated in dielectric host. The optical response of these structures can be homogenized via an effective medium theory (EMT), resulting in a hyperbolic effective permittivity tensor. Both structures are presented in Figure 1.3. These structures are similar to common photonic crystals (PCs) in topographic point of view, but PCs should not be confused with HMMs, although they both exhibit periodicity, PCs are not metamaterials since they cannot be represented by effective bulk parameters. Also, the pitch (lattice constant or periodicity) of PCs are typically on the order of operating wavelength, while those of metamaterials are sufficiently smaller than the wavelength. The physical mechanism of light-matter interaction in such structures is the coupling of surface plasmons [6],[15] in metal-dielectric multilayers or localized surface plasmons in the case of metallic nanowires [16].

1.3.1 Multilayers

The effective permittivity tensor $\bar{\bar{\varepsilon}}$ for a multilayer stack (Figure 1.3 a) can be derived quite easily. The external electric field is directed either parallel or perpendicular to the surface. The goal is to find two effective permittivities $\varepsilon_{\square}$ and ε_{zz} as shown in Figure 1.3 a. Let us assume that the bulk permittivities of metal and dielectric components are ε_m and ε_d with volume filling fractions p_m and p_d. respectively. The dielectric constituent of the filling factor is $p_d = 1 - p_m$. Regardless the direction of the impinging wave, the following relation holds for each layer as well as for the whole structure:

$$\boldsymbol{D_i} = \varepsilon_0 \varepsilon_i \boldsymbol{E_i} \tag{1.20}$$

When the incident wave is polarized parallel to the layers, the electric field $\mathbf{E}$ must be continues across the boundary between the layers [17]:

$$\boldsymbol{E_m} = \boldsymbol{E_d} = \boldsymbol{E_e} \tag{1.21}$$

The effective electrical displacement is given by:

$$\boldsymbol{D_e} = p_m \boldsymbol{D_m} + p_d \boldsymbol{D_d} \tag{1.22}$$

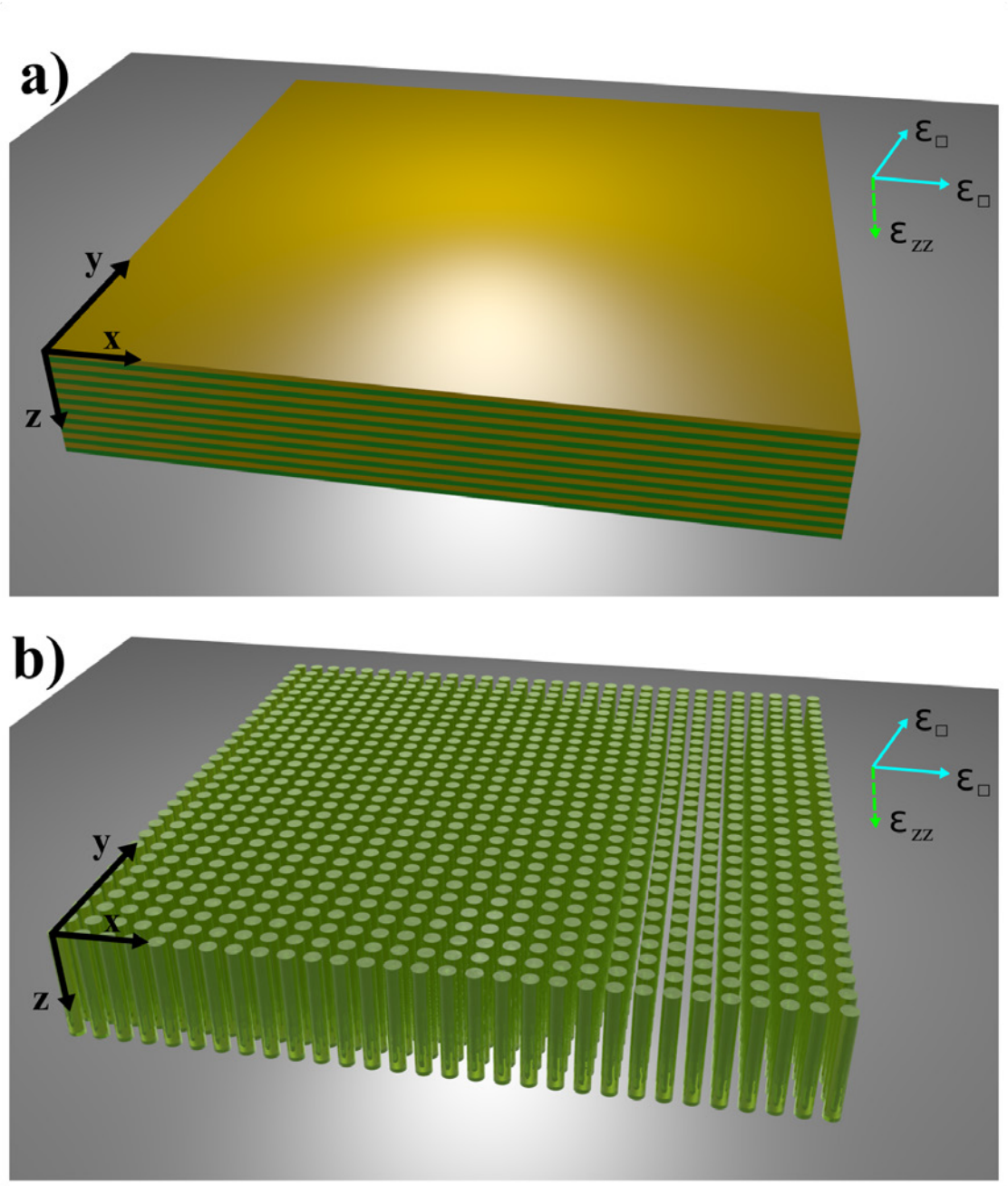

Figure 1.3: Schematics of a) a layered metal-dielectric structure and b) a two-dimensional wire array.

Combining the three previous equations 1.20-1.22:

$$\varepsilon_{xx} = \varepsilon_{yy} = \varepsilon_{\square} = p_m\varepsilon_m + p_d\varepsilon_d \tag{1.23}$$

In the case of polarization perpendicular to the surface, the situation is slightly different. In this case the electric displacement must be continuous at the boundary between the layers, and electric field is evaluated as a weighted average sum:

$$\boldsymbol{D_m} = \boldsymbol{D_d} = \boldsymbol{D_e} \tag{1.24}$$

$$\boldsymbol{E_e} = p_m\boldsymbol{E_m} + p_d\boldsymbol{E_d} \tag{1.25}$$

Combining equations 1.20, 1.24 and 1.25:

$$\varepsilon_{zz} = \frac{\varepsilon_m\varepsilon_d}{p_d\varepsilon_m + p_m\varepsilon_d} \tag{1.26}$$

This approach allows to generalize the $\varepsilon_{\square}$ and εzz components of the effective permittivity tensor to the systems consisting of an arbitrary number of materials:

$$\varepsilon_{xx} = \varepsilon_{yy} = \varepsilon_{\square} = \sum_i p_i\varepsilon_i \qquad \varepsilon_{zz}^{-1} = \sum_i p_i\varepsilon_i^{-1} \qquad \text{with } \sum_i p_i = 1 \tag{1.27}$$

In general the material permittivities ε_i of individual metal and dielectric components are complex quantities which depend on the angular frequency (exhibiting temporal dispersion), and so are $\varepsilon_{\square}$ and ε_{zz}. The real parts accounts for the polarization response, while the imaginary describes the dissipative losses in the materials [11]. The real and imaginary parts of the effective parameters of Ag/SiO_2 multilayer stacks are plotted in Figure 1.4 for two different filling ratios.

The figure outlines that the real multilayer stack behaves differently as p and ω are varied. There are regions in ω where the dispersion is no longer Type I or Type II hyperbolic, but where the dispersion is elliptic ($\varepsilon_x, \varepsilon_z > 0$), or act as metal ($\varepsilon_x, \varepsilon_z < 0$). Additionally, the proper tuning of p_m and ω allows to enter the ENZ regime [18]-[20].

The choice of materials depends on the target spectral range, losses and impedance match. The later requires that the real parts of metallic and dielectric permittivities do not differ by more than an order of magnitude, otherwise the radiation will simply be reflected [11]. The plasma frequency of commonly used Ag and Au lies in the ultraviolet region [21]. In the visible spectrum the negative real part of Ag and Au permittivities can be impedance matched with common dielectrics such as Al_2O_3 and TiO_2, and as such a perfect choice for HMMs in the visible range. At lower frequencies, approaching the infrared, real part of Ag and Au permittivities $\varepsilon_{Au,Ag}$ becomes so negative that it causes an impedance mismatch and needs to be replaced with other plasmonic materials that are better suited for infrared region, such as doped semiconductors and transparent conducting oxides (TCO's).

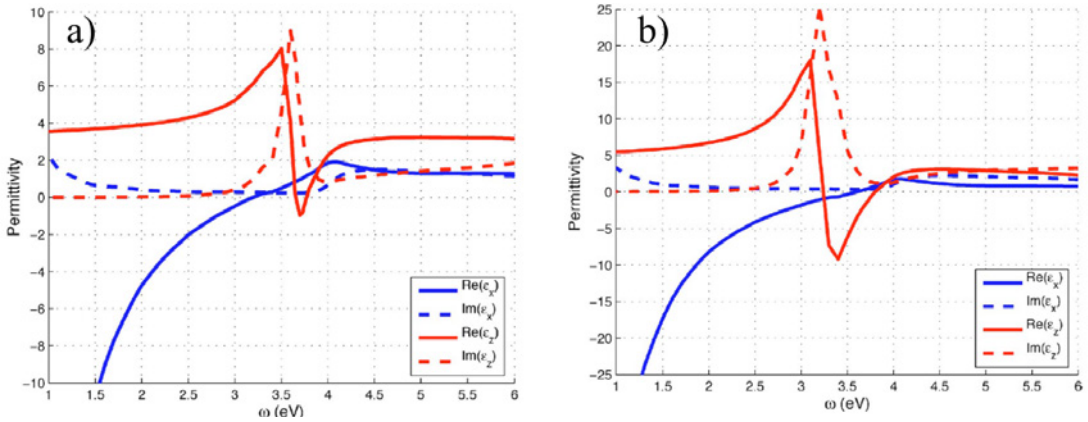

Figure 1.4: Real and imaginary permittivities of Ag/SiO_2 multilayer stacks with Ag filling ratio: a) p_{Ag}=0.4 and b) p_{Ag}=0.6. Reproduced from [10]. ($\varepsilon_x = \varepsilon_\square$ and $\varepsilon_z = \varepsilon_{zz}$)

1.3.2 Periodic Array of Metallic Nanowires

Determination of effective permittivity parameters for the nanowire media depicted in Figure 1.3 b is not as straightforward as for metal-dielectric multilayers. The permittivity tensor for a wire medium is reported to be [7],[22],[23]:

$$\varepsilon_{xx} = \varepsilon_{yy} = \varepsilon_\square = \frac{[(1+p)\varepsilon_m + (1-p)\varepsilon_d]\varepsilon_d}{(1-p)\varepsilon_m + (1+p)\varepsilon_d} \tag{1.28}$$

$$\varepsilon_{zz} = p\varepsilon_m + (1-p)\varepsilon_d \tag{1.29}$$

Where p is the percentage area occupied by nanowires in the {xy} plane. As for the multilayer HMM, the dispersion response of nanowires can be tuned to different regimes by varying ω and p.

1.4 Applications and Technological Challenges

Near-field light matter interactions in HMMs results in various applications, such as sub-wavelength imaging and light manipulation [11], enhancement in spontaneous emission rate [11], realizing a large Purcell factor [24], applications in heat transport [25], acoustics [26] and even cosmology modeling [27]. A full list of possible HMMs applications is still in progress, due to the novelty of such materials and remaining fabrication limitations.

1.4.1 Hyperlensing

One of the major applications of optical metamaterials has been in the area of subwavelength imaging [28]. The spacial resolution of conventional optics is known to be limited by diffraction which is caused by the loss of evanescent waves in the far field. The diffraction limit causes the resolution to be limited to distances $R > (0.61\lambda)/NA$, where NA is a numerical aperture of the optical system. Indeed, the isotropic medium (keeping equation 1.17 in mind with all positive permittivities) contains a limited wavevector, and momenta larger in magnitude correspond to evanescent waves. The recovery of evanescent waves is essential to resolve sub-diffraction images [28]-[30]. The resulting concept of hyperlenses based on metal-dielectric multilayers presented in Figure 1.5 a), has been intensively studied [28]-[36]. The unique properties of HMMs such as negative refraction and partial focusing of radiation can make a huge impact in this field.

1.4.2 Nanolithography

The diffraction limit poses a constraint not only on object details detectable with far field equipment, but also on the resolution of patterns written by photolithography. To improve the resolution, one straitforward approach is to reduce the wavelength of the illuminated light into the deep-ultraviolet (UV) regime or even implement e-beam or x-ray lithography for patterning structures smaller than 200 nm [38]. The main disadvantages of these approaches are tremendous price of operation and equipment complexity. Using a designed slab of metal-dielectric metamaterial (see Figure 1.5 b) it should be possible to realize the deep subwavelength photolithography [37], [39]. This approach is still based on a conventional optical lithography procedure, but waves that propagate through the HMM enables the ratios between the transferred image and the object smaller than 1:1.

1.4.3 Technological Challenges

The above-mentioned hyperlens structures is far from being fully developed and implemented. One of the main difficulties is imperfections in fabrication. With an increase in the number of layers, the hyperlenses start to loose their concentricity which causes optical losses and image distortion. This question can be addressed not only to hyperlenses, but also to a simpel form of hyperbolic medium: a metal-dielectric stack. Typical multilayer structures produced by physical vapor deposition (PVD) are either based on electron beam or sputter techniques. Fabrication poses a limit to the number of periods that can be stacked while preserving an actual structure; a total of eight layers was estimated to be the threshold to observe the predictions of the effective medium theory [40], although as little as

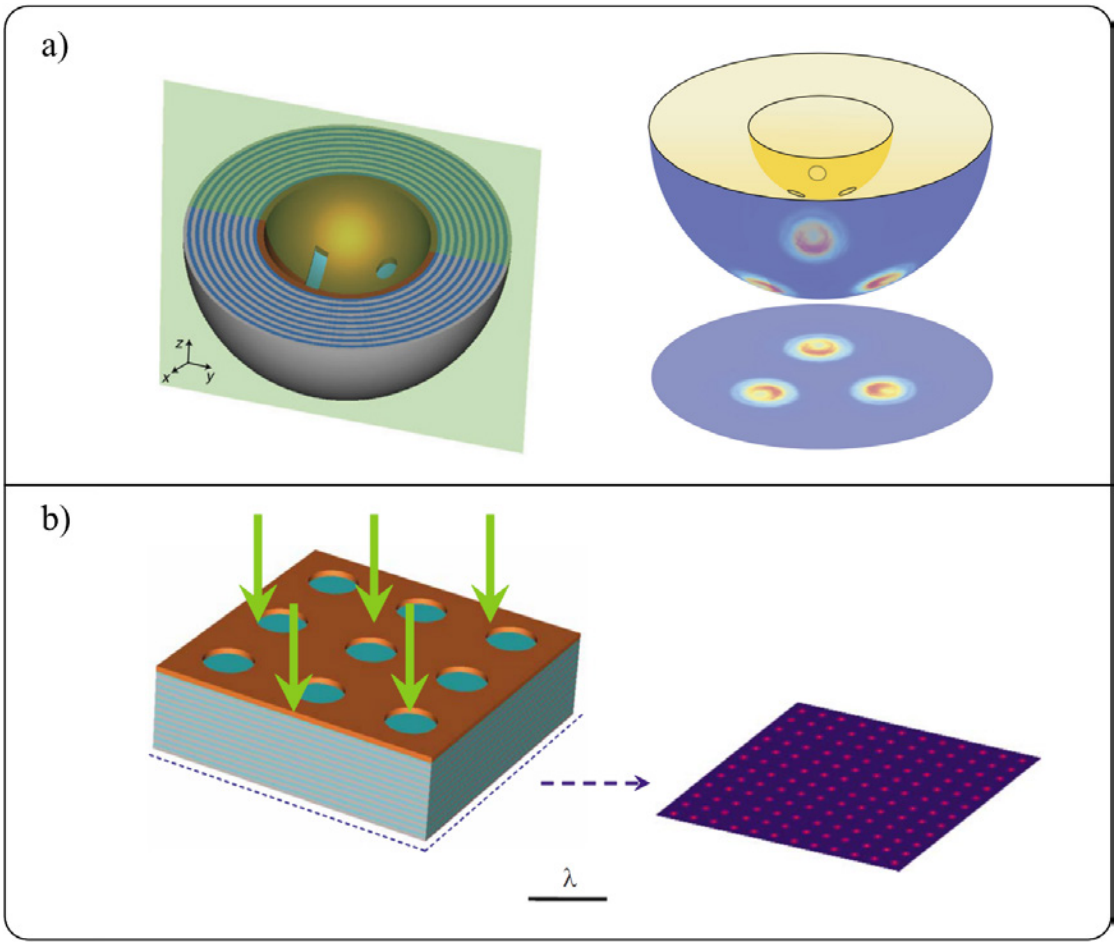

Figure 1.5: a) Schematic of a spherical hyperlens comprised of nine pairs of Ag and TiO2 layers. The right side shows a magnified image of sub-diffraction-limited objects. Source [36] b) Schematic of deep-subwavelength photolithography using metal-dielectric multilayer. Reproduced from [37].

six layers were shown to achieve an effective hyperbolic behavior [41],[42]. In order to minimize losses, ultra-thin continuous layers with negligible roughness are heavily demanded. Recently, ultra-smooth 6 nm thin layers of Au sputtered on Si and SiO_2 have been reported [43]. In this case amino- and mercaptosilanes wer predeposited in order to enhance the adhesion of Au on Si wafers.

Nanowire HMMs are usually made by electrochemical deposition of Ag or Au inside self-assembled porous alumina (Al_2O_3) template [22] due to the extreme high aspect ratio of such structures. A multistep control in electrodeposition is essential in order to secure that the metal filling is consistent across the sample [44]. Additionally, a significant issue of metal overfilling or discontinuity within

the alumina pores has to be considered. Furthermore, due to structure complexity, the number of papers describing the actually produced plasmonic high aspect ratio nanowires is very limited.

According to A. Poddubny *et. al* [9] the successful application of HMMs requires the following four improvements. First, it is important to realize hyperbolic iso-frequency surfaces that cover wide spectral ranges. For actual metamaterials, the inverse of the size of structural elements represents an upper limit for the magnitude of wave vectors. Second, losses need to be addressed. Third, it is necessary to overcome the limited performance of hyperbolic metamaterials as imaging and hyperlensing devices for particular orientations and polarizations. Fourth, nanophotonic applications may require tailoring the surface of a metamaterial to mediate coupling between waves propagating in air and the high-k states inside the metamaterial.

A big part of research on metamaterials is still on a theoretical level, and it would be desirably to get more focused attention on nanofabrication and technology development. The challenges are fabrication of smooth, homogenous, structures with precise thickness control and reproducibility. High expectations are placed on the atomic layer deposition (ALD) technique. Although this technique has been around for two decades [45], nowadays it sees a major revolution in process development. ALD is undoubtedly the technique that will bring the metamaterial fabrication technology to a new level. Even though it has been known for decades, it is still overlooked by scientists in the metamaterial community. With the new development of Au and Ag ALD processes [46], the situation is expected to change. Not only gold is important, but other alternative plasmonic materials can be implemented, such as TiN, TiC, doped semiconductors such as $Al\text{-}ZnO$ (AZO) and many other [21].

CHAPTER 2

ATOMIC LAYER DEPOSITION

As it was described in a previous chapter, the realization of hyperbolic metamaterials (HMMs) requires manufacturing of thin films that can be grown conformally, homogenously, and that would be able to cover structures with high aspect ratios. The other important factor is the choice of the available material. Ideally, it should be possible to select either dielectric or metallic films or in general, the materials with the desired physical properties. Additionally, the typical dimensions of metamaterials building blocks are in the subwavelength order, which would demand a strict deposition thickness control on nanometer scale. Here comes the atomic layer deposition (ALD) to to to play an essential role as it is exactly the technique that can meet the requirements.

2.1 Basic Principles

ALD is a vapor-phase deposition technique in which ultra thin films are synthesized on atomic scale by repeating two subsequently executed half-cycles. Since the beginning of the 2000's this technique has developed into a well established method [45]. It evolved originally from chemical vapor deposition (CVD), where a film is deposited on a surface due to a chemical reaction in semi-vacuum conditions. ALD is not new anymore, since the first research was conducted in the 1960-1970's [47], in former USSR and Finland, and the method was patented by Suntola *et al.* [48]. The extensive history of ALD development has been described in details by R. L. Puurunen [49]. Before the beginning of the 2000's the method was mainly called Atomic Layer Epitaxy and later changed to ALD due to the huge interest for this technique from the semiconductor industry that has become a key driver for it [50], [51]. The coating of flat, two-dimensional surfaces is not a big problem

in modern technology. Several deposition techniques have existed for decades for such purposes which includes physical vapor deposition (PVD) and CVD.

Issues start when control of thickness on atomic scale and excellent uniformity on samples with complex surface structures are required. The fabrication of metamaterials is only one of many applications where such deposition conditions are needed. No other technique can approach the conformality achieved by ALD on such matters.

Most ALD processes are based on binary reaction sequences, where two self limiting surface reactions occur and deposit a binary compound film. The method is displayed in Figure 2.1. The surface at the beginning should be reactive towards the first precursor, otherwise the growth will not start. In other words, there should be "anchors" or sites, where the reaction will be initiated.

The first half-cycle starts after the introduction of the first precursor. Chemical interactions proceed until all sites available on the surface are occupied, and when it happens the reaction stops. At this moment the surface has reacted and reached saturation, now the remaining unreacted precursor together with byproducts need to be purged away by an inert gas (normally N_2).

During the second half-cycle, the second percussor is introduced. It reacts with the first precursor anchored to the surface. This reactions leads to the desired deposition product. The second precursor - surface interaction is also self-limiting, and after the completion, a second purge needs to be performed. Precursors are introduced separately, and the purge steps secures that they never meet in the gas phase. In practice however, this condition is difficult to fulfill completely, and some traces of the previous precursor will remain. It leads to undesired CVD characteristics especially if the purge time is too short.

The thickness of the deposited ALD layer is controlled by the number of cycles, as a consequence of the self-limiting chemistry. Each reaction cycle adds a given amount of material to the surface, refereed to as the *growth per cycle* (GPC) This is a major difference from the CVD technique, where the deposition thickness is controlled by the time, since reaction is continuous.

There exist two types of ALD. The one that has been described above and illustrated by Figure 2.1 refers to thermal ALD, where chemical reactions are thermally driven. Another type is plasma-assisted ALD or Plasma-Enhanced ALD (PEALD). In this method, the surface is exposed to the species generated by plasma during the reaction step [52]. Typical plasmas used in PEALD are those generated in O_2, N_2 or H_2 reactant gasses. Plasma can replace ligand-exchange reactions typically of H_2O, O_3 or NH_3. PEALD offers some advantages over thermal processes. First, except for a limited number of processes which includes Pt, Ru and W [51], single element films of metals and semiconductors are very difficult to deposit using only temperature driven ALD. Plasma sources can overcome this

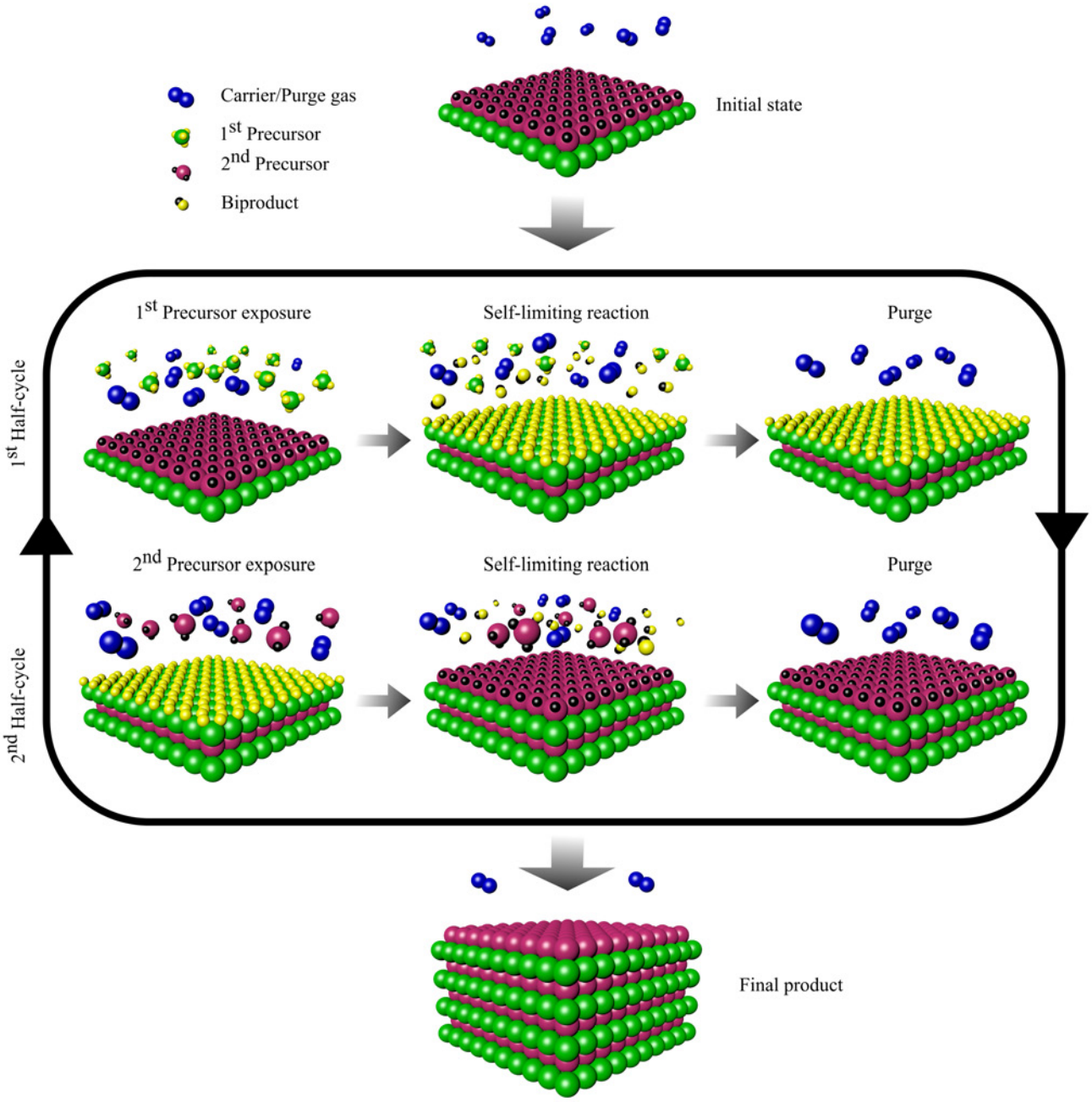

Figure 2.1: Schematic representation of the ALD technique. The image in the center illustrates one ALD reaction cycle, with binary reaction sequence and self-limiting surface chemistry. Since the two surface reactions are self-limiting, thet may proceed in a sequential fashion in order to deposit a thin film with atomic level thickness control.

problem by generating hydrogen radicals that reduce the metal or semiconductor precursors.

Another important advantage is that PEALD can be used to deposit films at much lower temperatures. For example, using PEALD it is possible to deposit Al_2O_3 using TMA and O_2 plasma at room temperature.

The plasma processes also have some disadvantages and one of them is the poor coverage of high aspect ratio structures compared to thermal processes. This is due to the difficulties for the plasma species to penetrate the sample and interact with the surface.

Since all the work in this project is done using a thermal ALD tool, only thermal processes will be considered from now on.

The used equipment was a commercial thermal hot-wall ALD chamber from Picosun^{TM}[53]. A photography of the tool is shown in Figure 2.2. The working pressure was below 20 hPa, and the deposition temperature could go up to 350 $°C$. Before starting a deposition, it was possible to implement an optional "flush" function, which would ventilate the chamber by N_2 flow. This option would allow to reduce environmental contamination of the chamber, because air is introduced in the chamber during sample loading. Several processes have been implemented: Al_2O_3, TiO_2, ZnO and Al-doped ZnO. Moreover, deposition of Cu was tested with varied results. The mounted precursors were trimethylaluminum (TMA), titanium tetrachloride ($TiCl_4$), diethylzinc (DEZ), copper dimethylamino-2-propoxide (Cu(dmap)2), water and ozone. Organometallic precursors were supplied by either Sigma-Aldrich or Strem Chemicals. Nitrogen was used as a carrier and purge gas. The next sessions will be dedicated to the main processes and achieved results.

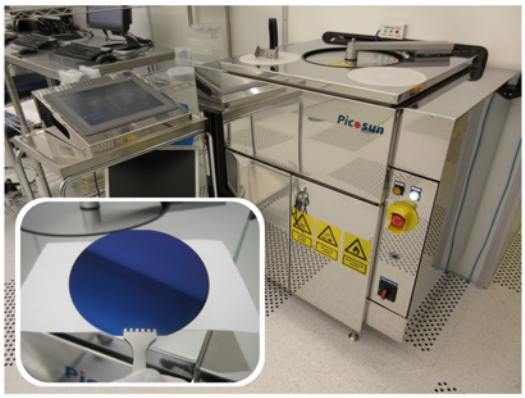

Figure 2.2: Picosun R200 thermal tool. The inset shows a 100 nm thick Al_2O_3 film grown on a Si wafer.

2.2 ALD of Al_2O_3

Aluminium oxide (Al_2O_3) film growth based on TMA and water is nowadays considered to be a model system for the ALD technique. It was first reported in 1989 by Higashi and Fleming [54]. This process has now become the most successful ALD process. A detailed description of the reaction mechanism is explained in several famous ALD review papers such as R. L. Puurunen in 2005 [49]. The mechanism basics is quite easy to understand. Since ALD is a sequential technique, during the first precursor exposure the reaction is:

$$\underset{\text{Surface}}{\text{AlOH}^*} + \underset{\text{TMA}}{\text{Al(CH}_3)_3} \longrightarrow \underset{\text{Surface}}{\text{AlOAl(CH}_3)_2} + \underset{\text{Methane}}{\text{CH}_4\uparrow}$$

When the first half cycle is done, the surface is passivated by reactive CH_3 groups. After the purge step which removes the excess of TMA and methane, the next reaction takes place:

$$\underset{\text{Surface}}{\text{Al(CH}_3)_2^*} + \underset{\text{Water}}{\text{H}_2\text{O}} \longrightarrow \underset{\text{Surface}}{\text{AlOH}^*} + \underset{\text{Methane}}{\text{CH}_4\uparrow}$$

Here H_2O reacts with CH_3 groups, methane leaves and a monolayer of Al_2O_3 is created. The whole sequence is repeated until a film with a desired thickness is grown.
The overall reaction is the following:

$$\underset{\text{TMA}}{2\,\text{Al(CH}_3)_3} + \underset{\text{Water}}{3\,\text{H}_2\text{O}} \longrightarrow \underset{\text{Solid film}}{\text{Al}_2\text{O}_3} + \underset{\text{Methane}}{3\,\text{CH}_4\uparrow}$$

In this project the Al_2O_3 thin film was grown on Si (100) 4" substrates with native oxide. The deposition temperature was in a range of $100 - 350\ ^\circ C$. The number of deposited cycles was between 100 and 1000. A conventional spectroscopic ellipsometry (SE)[1] was implemented to measure the thickness distribution as well as optical constants such as refractive index and extinction coefficient. Figure 2.3 shows ellipsometry results for the thickness uniformity of deposited 500 TMA/water cycles. The recipe for one Al_2O_3 cycle is shown in Table 2.1.

[1] Ellipsometer VASE from J.A. Woolam Co.

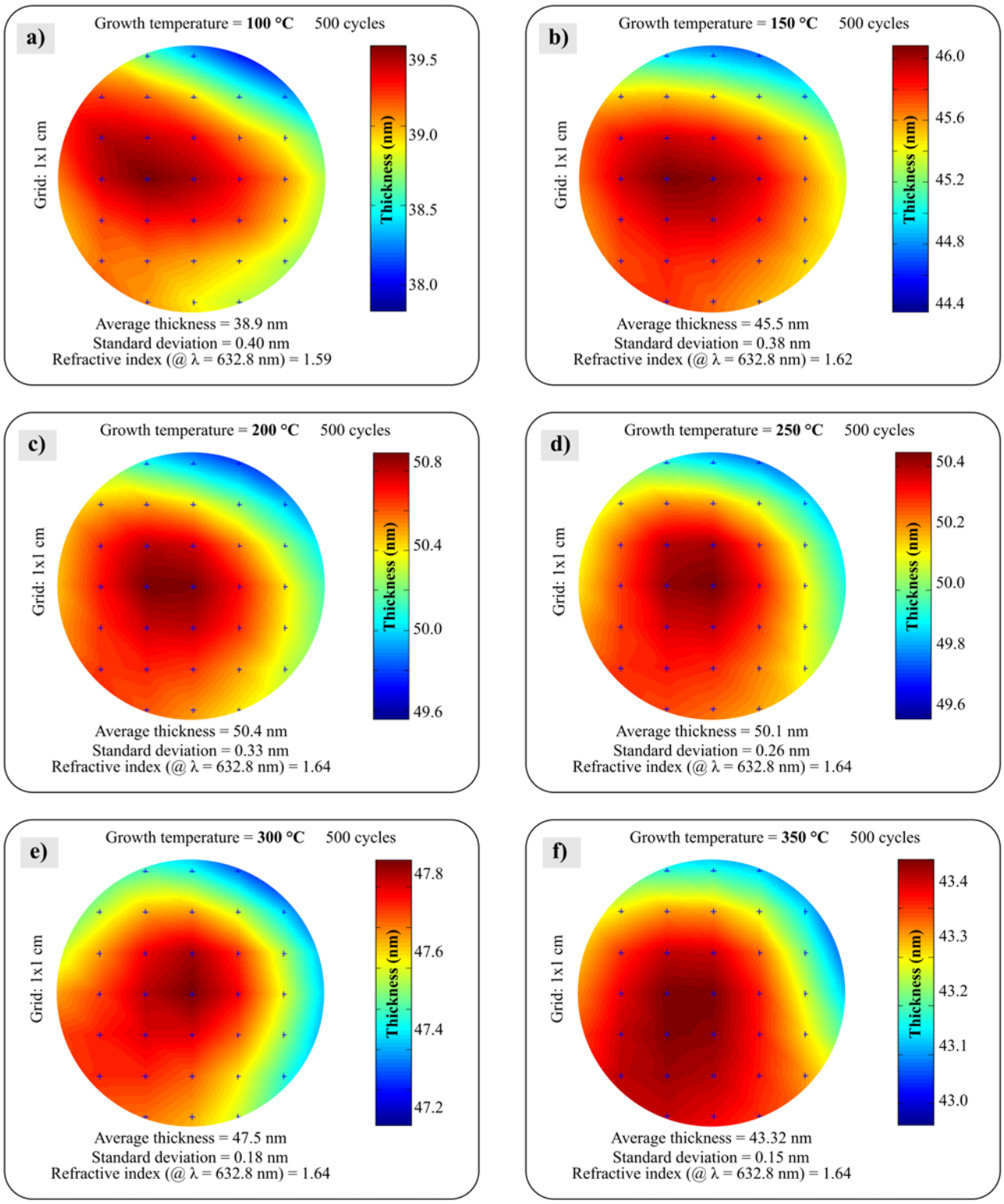

Figure 2.3: Thickness distribution of deposited Al_2O_3 thin films. a)-f) show ellipsometry results for each temperature between 100 $°C$ and 350 $°C$ in intervals of 50 $°C$.

Precursor	Pulse time (s)	N_2 flow (sccm)	N_2 purge time (s)
TMA	0.1	150	3
H_2O	0.1	200	4

Table 2.1: One cycle of the TMA/water process. The recipe especially suitable for flat layer depositions.

Precursor	Pulse time (s)	N_2 flow (sccm)	N_2 purge time (s)
TMA	0.1	150	0.5
TMA	0.1	150	20
H_2O	0.1	200	0.5
H_2O	0.1	200	20

Table 2.2: One cycle of the TMA/water process. The recipe especially suitable for passivation of high aspect ratio structures and growth at low temperatures (150°C and below).

During the deposition of Al_2O_3 with different number of cycles for each temperature it was possible to confirm linear growth for each temperature, as shown in Figure 2.4 a), what verifies a linear growth in the 300 °C temperature deposition regime. Figure 2.4 b) shows the deposition rate (GPC) as a function of the temperature. The result here is quite remarkable, since it contradicts with the scheme presented in Figure 2.1. Historically, it is assumed that the growth does not depend on temperature as long as the deposition lies within the so-called ALD window, where the thermal energy is high enough to allow the reaction to take place. However, it seems here that the GPC increases from 100 °C to 200 °C, then remains constant up to 250 °C, and then gradually decreases.

The reason why the GPC is increasing with temperatures up to 200 °C is the insufficient exposure of the precursors. The saturation is not reached before the purge steps starts. The consequential decrease at higher temperatures has different origin and is caused by surface recombination. The CH_3 groups at the end of the first half-cycle and the OH groups at the end of the second half-cycle become unstable at elevated temperatures and might leave the surface, which will decrease the growth rate. This hypothesis is described by R. L. Puurunen [49], but it still remains not fully understood. At temperatures above 327 °C, TMA starts to decompose (as it is the case for most organometallic aluminum precursors above 300 °C), and the ALD process is no longer ideal, which also leads to a decrease in the GPC rate.

Chemical compositions of the deposited Al_2O_3 films were carefully investigated

using the X-ray photoelectron spectroscopy (XPS) technique[2]. No impurities have been detected in the range between 150 $°C$ and 350 $°C$. The survey scan shown in Figure 2.6 a) reveals no contaminations. Samples were measured in-depth mode, meaning that the investigated area of the sample was consistently bombarded in-situ by Ar^+ ions. These partially remove the surface, allowing the bulk investigations. Here it must be emphasized that XPS is a surface sensitive technique which only senses a few nm in depth, this is why the Ar^+ ion gun come into play.

In the films grown at 100 $°C$ some amount of carbon has been found. Normally, airborne hydrocarbon impurities are always present on virtually any surfaces, and a characteristic carbon signal around 287 eV binding energy is an indication of that the XPS measurements proceed as expected (see strong C 1s peak in Figure 2.5a) and 2.5 b). Ar^+ ions remove these contaminations, however for the film grown at 100 $°C$ a week C 1s peak is still present (Figure 2.5a). This is the evidence of remaining unreacted CH_3 groups. At temperatures of 150 $°C$ and above no unreacted methyl groups were observed. (Figure 2.5 b).

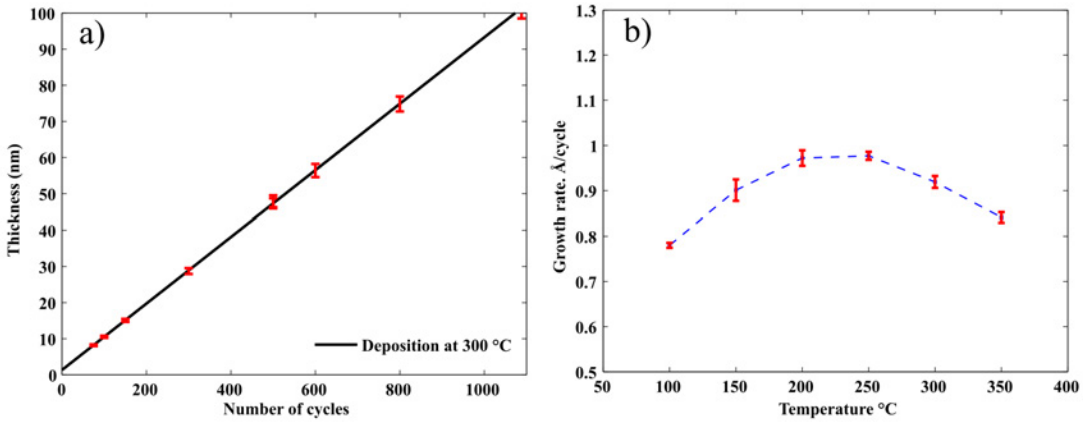

Figure 2.4: Growth condition of Al_2O_3. a) Linear growth at 300 $°C$ b) Measured GPC as a function of deposition temperature.

In order to solve the unsaturation condition for low temperature growth, a more advanced recipe has to be introduced. This is shown in Table 2.2. It is based on prolonged exposure and purge times, securing the sufficient saturation. The recipe is also very useful for depositions on surfaces with advanced topographies, Scanning electron microscopy image (SEM)[3] is shown in Figure 2.6 b). Here 100 nm Al_2O_3 is deposited on Si trenches with a hight of 4 μm and a pitch of 400 nm, giving an overall high aspect ratio of 1:20. The manufacturing of such trench structures

[2]XPS system from Thermo Scientific equipped with a monochromatic Al Kα X-rays
[3]SEM Zeiss Supra 60VP [55]

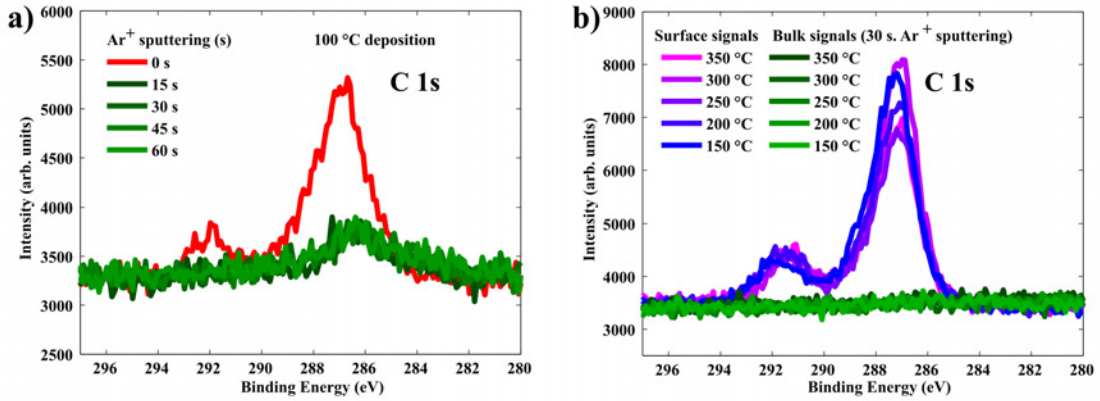

Figure 2.5: High resolution XPS measurements of carbon C 1s. a) The film grown at 100 $°C$ contains small amount (approx. At 1%) of carbon due to an incomplete reaction. b) Films grown at higher temperatures show no carbon after their surfaces have been cleaned by Ar^+ ions.

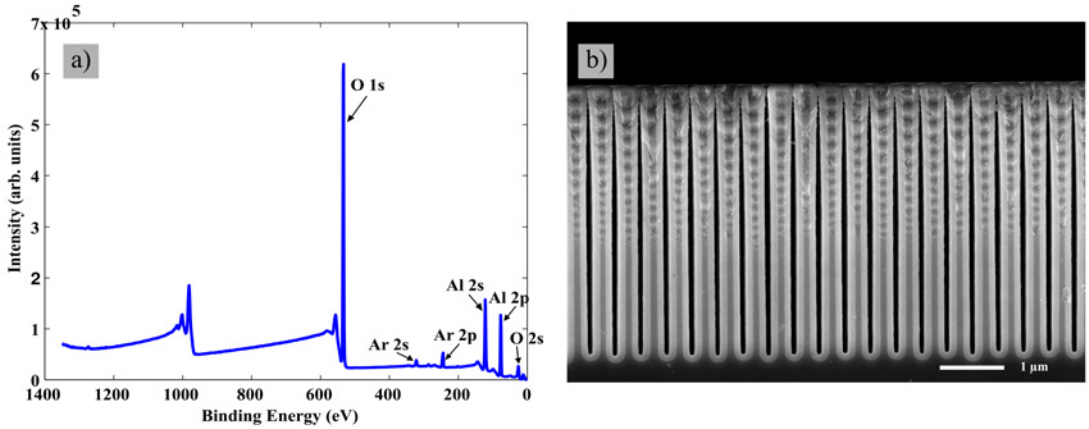

Figure 2.6: XPS and SEM characterization. a) Survey XPS spectrum of Al_2O_3 and b) Al_2O_3 deposited on silicon trenches with high aspect ratio.

plays an essential role in metamaterials manufacturing and will be described in the following chapters. The result of the passivation looks very satisfying.

Another issue has to be mentioned. Al_2O_3 based on a TMA/water ALD process can passivate many surfaces. However, the above-mentioned chemical reaction are based on existing initial OH groups. If one uses for instance a pure silicon surface, the native oxide has to be etched away using for example hydrofluoric acid (HF) treatment, as the initial surface will be strictly $-H$ terminated. Here the reaction would not start immediately due to the absence of initial $-OH$ groups, and up to 10-15 cycles would be required to obtain a linear growth per cycle. Other examples

Precursor	Pulse time (s)	N_2 flow (sccm)	N_2 purge time (s)
$TiCl_4$	0.1	150	4
H_2O	0.1	200	5

Table 2.3: One cycle of the $TiCl_4$/water process. The recipe is especially suitable for flat layer depositions

includes deposition on Au or other metals, so one need to be careful claiming a deposition of few nm film on arbitrary material due to possible nucleation issues. It should never be forgotten that ALD is in fact a chemical reaction!

2.3 ALD of TiO_2

Titanium oxide (TiO_2) is probably the oldest ALD process with roots going back to experiments performed in the 1960s [47]. It is a nontoxic, low cost, wide band semiconducting material with high refractive index and strong chemical stability. The material has been used in a variety of applications including solar cells, sensors, photocatalysts, and photonic crystals [51]. The deposition characteristics is widely described in many publications [56]-[60]. Just like in the previous case of Al_2O_3, the TiO_2 ALD process is accomplished by dividing the binary reaction into two separate half-reactions:

$$\underset{\text{Surface}}{\text{TiOH}^*} + \underset{\text{Titaniumtetrachloride}}{\text{TiCl}_4} \longrightarrow \underset{\text{Surface}}{\text{TiOTi(Cl)}_3} + \underset{\text{Hydrochloric acid}}{\text{HCl}\uparrow} \quad \text{A)}$$

When the first half cycle is done, the surface is passivated by reactive $TiCl_4$ groups. After the purge step, which removes the excess of $TiCl_4$ and hydrogen chloride (byproduct), the next reaction takes place:

$$\underset{\text{Surface}}{\text{TiCl}^*} + \underset{\text{Water}}{\text{H}_2\text{O}} \longrightarrow \underset{\text{Surface}}{\text{TiOH}^*} + \underset{\text{Hydrochloric acid}}{\text{HCl}\uparrow} \quad \text{B)}$$

Here H_2O reacts with $TiCl$ groups, hydrogen chloride leaves and a monolayer of TiO_2 is created. The whole sequence is repeated until a film with a desired thickness is grown. The overall reaction is:

$$\underset{\text{Titanium tetrachloride}}{\text{TiCl}_4} + 2\,\underset{\text{Water}}{\text{H}_2\text{O}} \longrightarrow \underset{\text{Solid film}}{\text{TiO}_2} + \underset{\text{Hydrochloric acid}}{4\,\text{HCl}\uparrow}$$

Precursor	Pulse time (s)	N_2 flow (sccm)	N_2 purge time (s)
$TiCl_4$	0.1	150	0.5
$TiCl_4$	0.1	150	20
H_2O	0.1	200	0.5
H_2O	0.1	200	20

Table 2.4: One cycle of the $TiCl_4$/water process. The recipe is especially suitable for passivation of high aspect ratio structures.

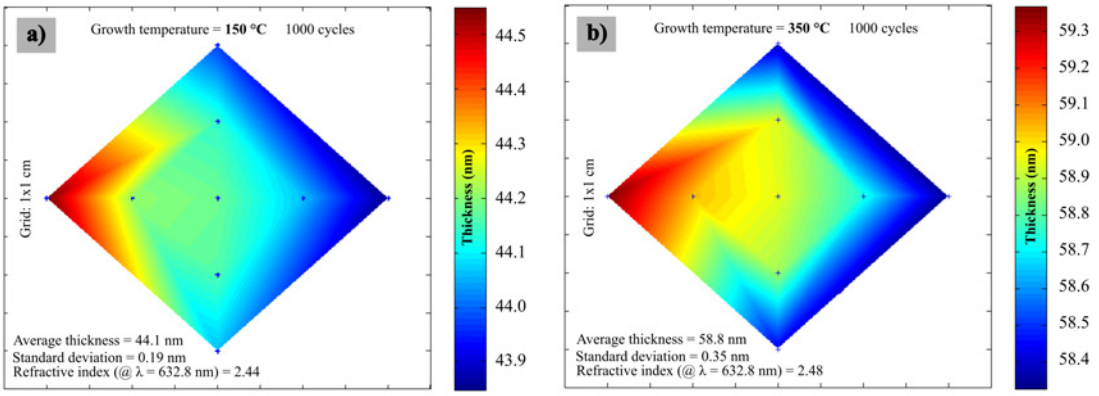

Figure 2.7: Spectroscopic ellipsometry measurements of deposited 1000 cycles of $TiCl_4$/water. a) Film deposited at 150 $°C$ and b) 350 $°C$.

Each surface reaction is observed to be self-limiting. Thin TiO_2 films have been deposited on Si (100) substrates with and without native oxide in the temperature range between $150-350$ $°C$. The uniformity and refractive indexes are displayed in Figure 2.7. Chlorides tolerate much higher temperatures, so the highest temperature (350 $°C$) is limited by equipment restrictions. The deposition recipe is shown in Table 2.3. It is known that TiO_2 ALD films can grow either as amorphous or anatase polycrystalline films [61]. Amorphous growth dominates at lower temperatures up to 150 $°C$, and at higher temperature the anatase phase transition starts to appear. At a temperature above 300 $°C$ mainly anatase TiO_2 is grown. Figure 2.7 a) and 2.7 b) show ellipsometry results for amorphous and anatase surfaces respectively. A linear growth rate has been observed at both temperatures and is measured to be 0.04 and 0.06 nm/cycle for 150 $°C$ and 350 $°C$ respectively. (see Figure 2.8). At temperatures around 250 $°C$ the growth rate was non-linear, and the deposition was observed to be non-uniform. The possible explanation could be the extensive phase transition at a given temperature. It also suggests that two possible temperature regimes have to be considered, one at low temperatures up

to 150 °C for amorphous deposition and one at the higher temperature regime for polycrystalline anatase above 300 °C deposition.

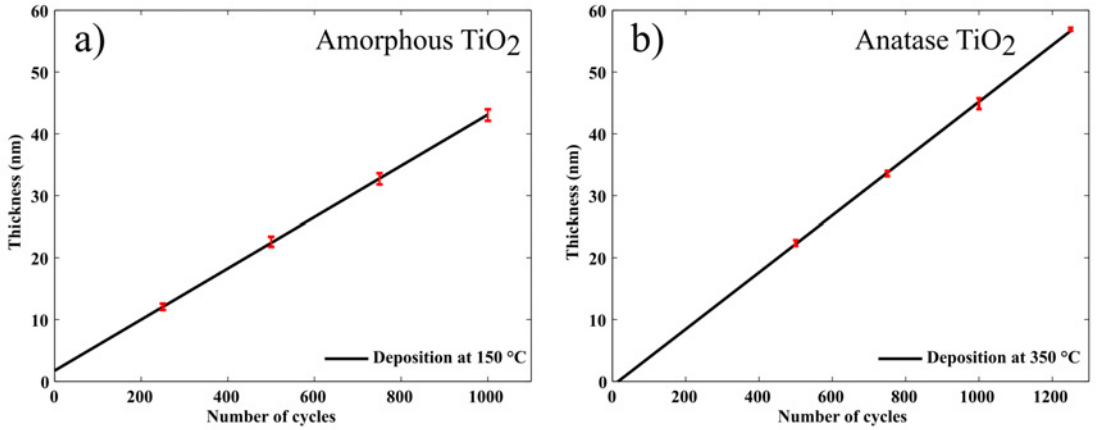

Figure 2.8: Linear growth for a) amorphous (150 °C) and b) anatase 350 °C TiO_2. GPC is measured to be 0.04 and 0.06 nm/cycle respectively.

The surface morphology was investigated using SEM imaging (Figure 2.9 a-c). Here 1200 cycles were deposited at a) 350 °C and at b)-c) 150 °C. At 350°C the anatase crystals are grown on Si surfaces without native oxide. It was noticed that the crystallinity was pronounced differently on different surfaces. The anatase growth was more pronounced on pure HF treated silicon surfaces. Figure 2.9 b) and c) compare TiO_2 surfaces grown at 150 °C on Si with and without native oxide respectively. Anatase crystallites were clearly more promoted on pure, $-H$ terminated Si surfaces. TiO_2 grown on Al_2O_3 pre-deposited layers remained mainly amorphous even at 300 °C (not shown here).

The ability to passivate high aspect ratio structures was tested on Si trenches, with the same dimensions as in the case of Al_2O_3. A uniform, homogeneous deposition was observed (Figure 2.9 d). The TiO_2 passivation was done at 150 °C by depositing 2000 cycles and implementing the recipe suitable for such deposition (see Table 2.4).

XPS elemental analysis have been performed on samples with TiO_2 layers deposited at 120 °C - 300 °C. Chlorine impurities were found for a broad range of temperatures. The biggest amount was found at the lowest investigated temperature (120 °C), corresponding to 1-3 at.% in the deposited film. Starting from 300°C the amount of chlorine was below the detection level. Figure 2.10 displays XPS results for 120 °C and 300 °C. No other impurities except Cl were found. Minor amounts of Ar results from sputtering for surface preparation in the XPS.

TiO_2 plays an essential role in this work. It has a high refractive index which can be an advantage in many optical applications where refractive index contrast

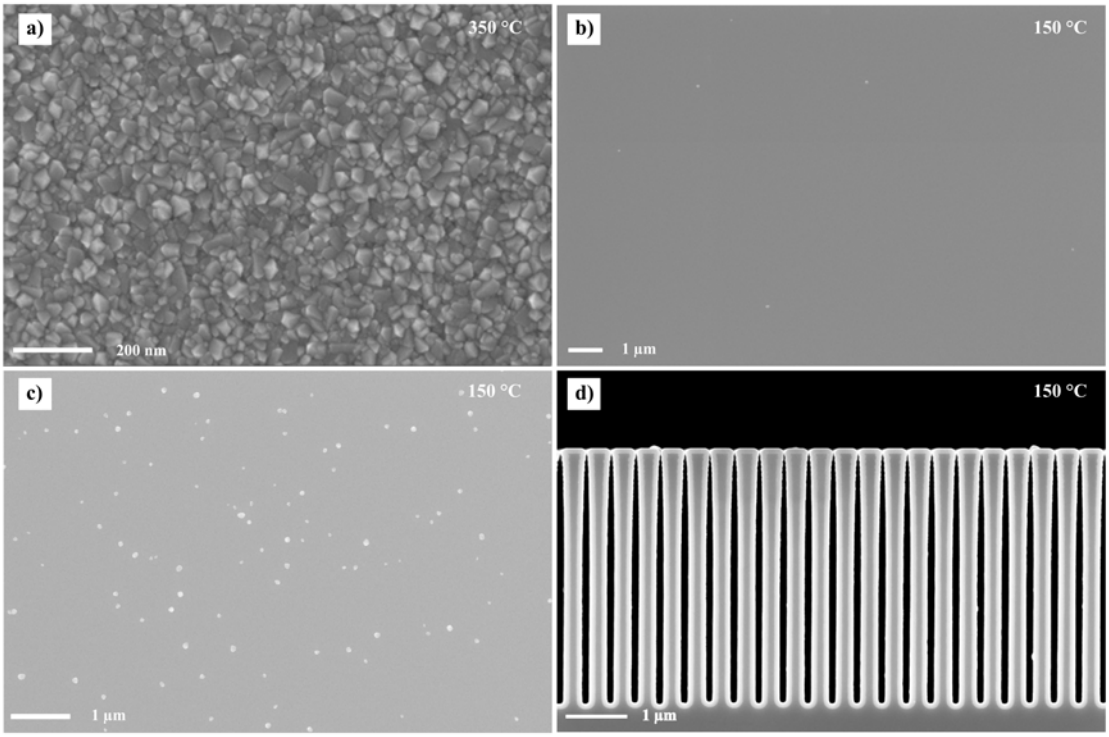

Figure 2.9: Morphology of deposited TiO_2 thin films. a) Anatase deposition of 1200 cycles done at 350 °C. b) Deposition of 1200 cycles done at 150 °C on silicon with native oxide and c) on pure, HF treated silicon. d) Morphology of TiO_2 deposition on Si trenches (2000 cycles, 150 °C).

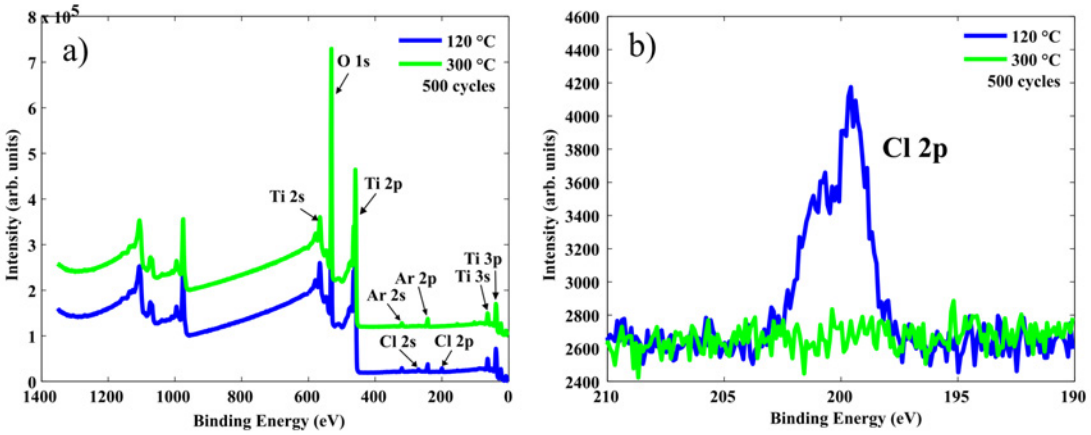

Figure 2.10: XPS elemental analysis. a) Survey scans and b) Cl 2p high resolution scans.

is important. Additionally, the structures made of TiO_2 can be nitrided [62]. The resulting TiN can be implemented in metamaterial applications, due to its plasmonic properties. Such synthesis can be considered in case it cannot be grown by ALD directly [63].

2.4 ALD of ZnO

Deposition of zinc oxide (ZnO) is one of the oldest ALD processes. During the last two decades it has been very intensively studied [64]-[70]. The most studied precursor combination for ZnO ALD is DEZ and water.

The two self-terminating reactions for ZnO growth from DEZ and water occur as follows: [64]

$$\underset{\text{Surface}}{\mathrm{ZnOH^*}} + \underset{\text{Diethylzinc}}{\mathrm{Zn(CH_2CH_3)_2}} \longrightarrow \underset{\text{Surface}}{\mathrm{ZnOZnCH_2CH_3}} + \underset{\text{Ethane}}{\mathrm{CH_3CH_3}\uparrow} \quad \text{A)}$$

When the first half cycle is done, the surface is passivated by reactive $ZnOCH_2CH_3$ groups. After the purge step which removes the excess DEZ and ethane, the next reaction takes place:

$$\underset{\text{Surface}}{\mathrm{ZnCH_2CH_3^*}} + \underset{\text{Water}}{\mathrm{H_2O}} \longrightarrow \underset{\text{Surface}}{\mathrm{ZnOH^*}} + \underset{\text{Ethane}}{\mathrm{CH_3CH_3}\uparrow} \quad \text{B)}$$

Here H_2O reacts with $Zn(CH_2CH_3)_2$ groups, the producing ethane byproduct leaves and a monolayer of ZnO is created. The detailed mechanism of the DEZ-water interactions were studied by J. Ren [69] and C. Thiandoume *et. al.* [70]. The whole sequence is repeated until a film with desired thickness is deposited. In summary the whole reaction is:

$$\underset{\text{DEZ}}{\mathrm{Zn(CH_2CH_3)_2}} + 2\,\underset{\text{Water}}{\mathrm{H_2O}} \longrightarrow \underset{\text{Solid film}}{\mathrm{ZnO}} + 2\,\underset{\text{Ethane}}{\mathrm{C_2H_6}\uparrow}$$

The optimal deposition temperature for the DEZ/water process is less explored compared to ALD of Al_2O_3. Some reports suggest an ALD window of 100-170°C [66]. Moreover *Hou Q. et.al* claims that ZnO cannot be deposited uniformly at temperatures above 200 °C due to thermal decomposition of the DEZ precursor [71]. However, numerous publications report ZnO growth at 250 °C and even at 350 °C [72].

Precursor	Pulse time (s)	N_2 flow (sccm)	N_2 purge time (s)
DEZ	0.1	150	0.5
DEZ	0.1	150	20
H_2O	0.1	200	0.5
H_2O	0.1	200	20

Table 2.5: One cycle of the DEZ/water process.

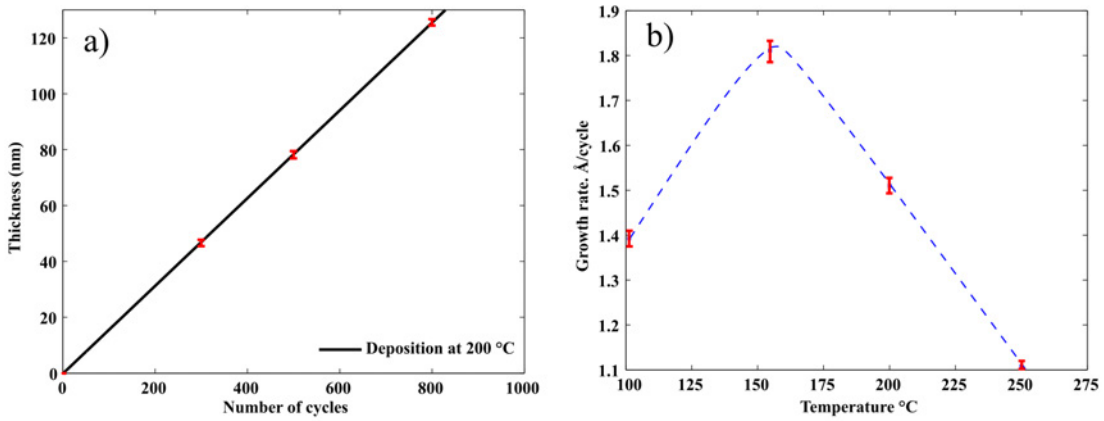

Figure 2.11: ZnO deposition characteristics. a) Linear growth at 200 $°C$ b) GPC as a function of temperature.

ZnO was grown on natively oxidized 4" Si (100) substrates. The deposition of ZnO has been tested in a temperature range of $100 - 250$ $°C$. The main part of the results are covered in a Chapter 5 as this is entirely dedicated to Al-doped ZnO growth and characterization. Here a summary of undoped ZnO is presented.

A self-limiting growth has been observed at all temperatures. The recipe that was used is presented in Table 2.5. Linear growth at 200 $°C$ and measured GPC as a function of temperature are displayed in Figure 2.11 a) and b). Spectroscopic ellipsometry was used to measure thicknesses, uniformities and optical constants (see Figure 2.12 a) for uniformity distribution). Figure 2.12 b) displays a photography of Si wafer with the deposited 125 nm ZnO film).

The ZnO thin films produced by ALD are all polycrystalline with hexagonal Wurtzite structures. Deposited on silicon, ZnO films are typically orientated towards the (100) or (002) directions. The orientation depends on the deposition temperature. At low temperature, the (100) orientation is favored, whereas at higher temperatures along c-axis orientation (002) dominates.

XPS results presented in Figure 2.13 shows a clean film with no traces of any contaminations for any deposition temperature. The ZnO process plays a

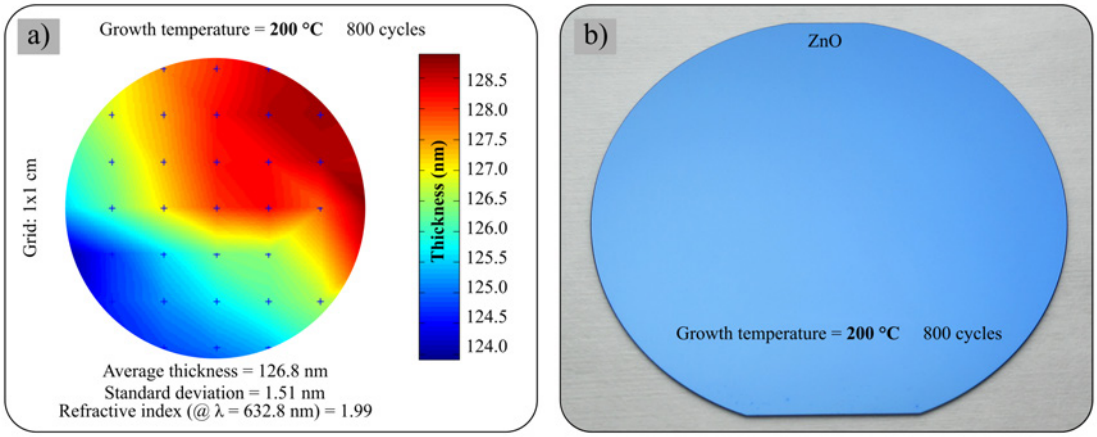

Figure 2.12: Uniformity measurements. a) Spectroscopic ellipsometry data based on 49 points across a 4" *Si* wafer b) Photography of the measured wafer.

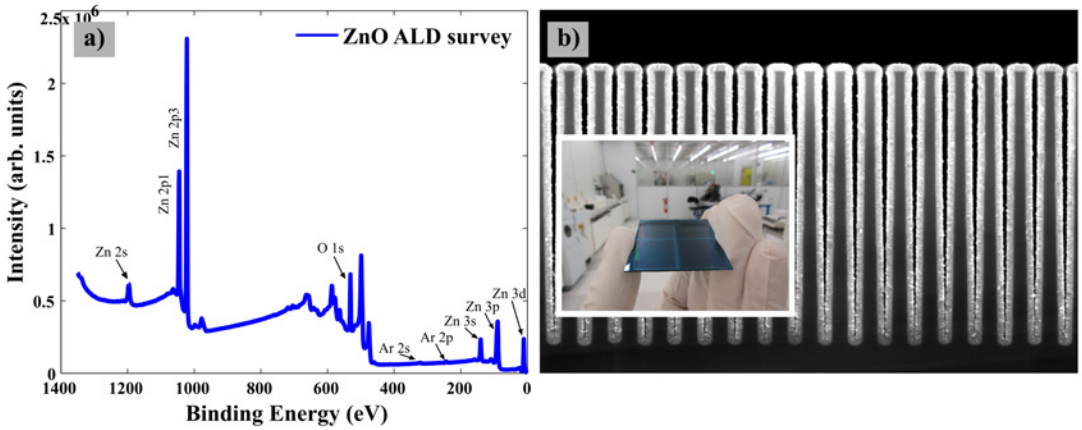

Figure 2.13: Deposition characteristics. a) Typical XPS survey scan of *ZnO* and b) cross-sectional SEM image of *ZnO* coating deposited on *Si* trenches. The inset shows a photography of a sample containing *ZnO* coated *Si* trenches.

central part of this project. It will be shown that once doped with Al, it becomes plasmonic in the near-/mid-infrared optical range, possessing low optical loss and high conductivity. The recipe (Table 2.5) was tuned, so it could passivate high aspect ratio structures (See Figure 2.13 b) which is important for realization of metamaterial plasmonic components.

2.5 ALD of Cu

Copper (Cu) is an alternative plasmonic material with possibility to replace gold and silver. Gold, due to its cost and patterning problems caused by limiting chemistry, and silver, due to oxidation issues [21]. Typically, copper film have been prepared by PVD, CVD and electroplating. In semiconductor industry [44], where the individual devices (transistors, capacitors, resistors, etc.) get interconnected with wirings on a sample, the metallization layer is required. Here, the second portion of Integrated circuit (IC) fabrication are called *The Back End of Line* (BEOL). Copper is a good choice for BEOL processing in contrast to aluminium, because is has better conductivity, superior resistance to electromigration, as well as good thermal stability. At a sub-20 nm technology regime, ALD is expected to play an important role in BEOL process for logic devices. While the ALD deposition of high-k dielectric oxides such as HfO_2, ZrO_2 and even rare earth oxides has been already implemented or at least heavily studied as gate and capacitor dielectrics, there are still no standard BEOL metallization process based on ALD[50].

There have been many reports on ALD deposition of copper metal thin films [73]- [81], however all of these reports lacked self terminating behavior, purity, conformality, reproducibility and selectivity. One of the most successful copper depositions was done by T. J. Kinsley *et. al.* [82]. Here a rather unusual three precursors steps ALD process was utilized. ALD chemistry kinetics is described by G. Dey and S. D. Elliott [83]. Unfortunately, one of the precursors are hydrazine N_2H_4 which is extremely toxic and hard to implement safely in a normal cleanroom environment. Previously, yet another copper process based on ligand exchange reactions of coper dimethylamino-2-propoxide Cu(dmap2) with DEZ was reported by B. H. Lee *et. al.* [84]. The process reaction is the following:

$$\underset{\text{Copper dimethylamino-2-propoxide}}{\mathrm{Cu(dmap)_2}} + \underset{\text{DEZ}}{\mathrm{Zn(CH_2CH_3)_2}} \longrightarrow \underset{\text{Solid film}}{\mathrm{Cu^0}} + \underset{\text{Butane}}{\mathrm{C_4H_{10}\uparrow}} + \underset{\text{Zinc dimethylamino-2-propoxide}}{\mathrm{Zn(dmap)_2\uparrow}}$$

Later, this process was investigated in details by G. Dey and S. D. Elliott [85] and it was stated that interchanges between Cu and Zn metalorganics leads to Zn incorporation in the deposited films, as Zn is close to Cu in the electrochemical series. The resulting $CuZn$ alloy might have sufficiently different properties than

Precursor	Pulse time (s)	N_2 flow (sccm)	N_2 purge time (s)
Cu(dmap)2	3	150	10
DEZ	0.2	150	10

Table 2.6: One cycle of the Cu process. Recipe for the most successful process.

pure copper. However it was decided to implement this process for plasmonic applications. Several recipes with different pulse times, flow rates and purge times were tested with the best results archived using the recipe presented in table 2.6. The deposition temperature was kept at 120 $°C$. The number of cycles was fixed to 1000.

Cu(dmap)2 is a powder at room temperature and needs to be heated to above 70 $°C$ before it sublimates and gives vapor pressure. The precursor bottle (source) was therefore constantly heated during the deposition. Since the initial Cu deposition is expected to be sensitive to surface chemistry, depositions on different surfaces have been tested. This includes natively oxidized Si, pure Si, samples with pre-deposited 50 nm Al_2O_3, ZnO, crystalline and amorphous TiO_2, and 30 nm CVD grown Si_3N_4. Additionally, Cu was deposited on Si trenches and black silicon.

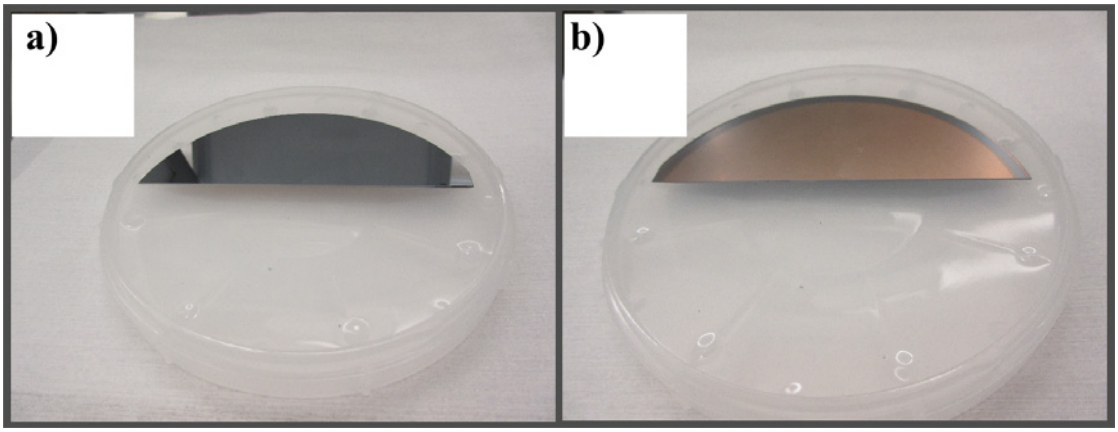

Figure 2.14: Photography of a Si sample a) before and b) after Cu deposition.

The result of the deposition is presented in Figure 2.14 where a Si substrate is shown before and after the ALD deposition. Here, the color change clearly indicates the deposition evidence. The best results for copper passivation of high aspect ratio structures are presented in Figures 2.15 and 2.16. A uniform passivation is achieved on black silicon and Si trenches. XPS results shown in Figure 2.16 a) show a clear presence of oxygen which does not go away after Ar^+ etching.

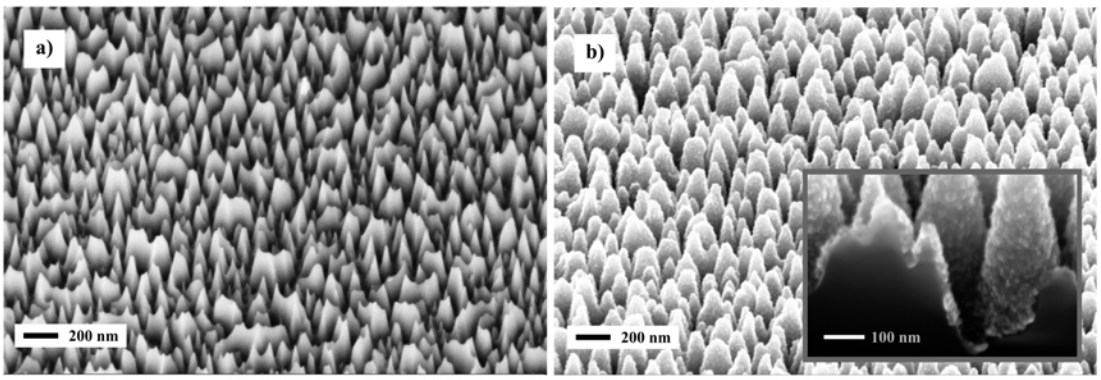

Figure 2.15: SEM image of black-silicon a) before and b) after Cu passivation.

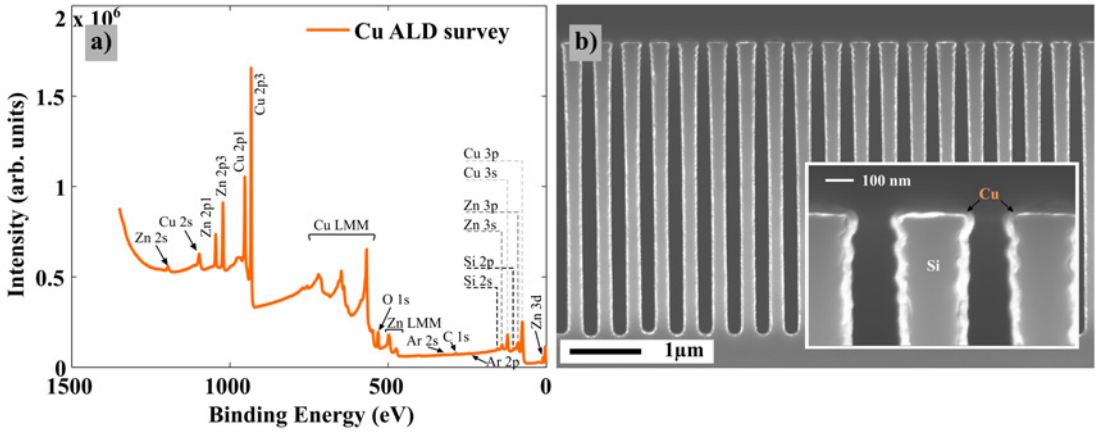

Figure 2.16: Cu deposition characteristics. a) Survey XPS scan of deposited Cu metal and b) Deposition of Cu on Si trenches.

The amount is approximately up to 10 at. %. The more noticeable problem is the presence of Zn. The amount was evaluated to be as high as 20 at. % in the film regardless the change of any recipe parameters presented in Table 2.6, indicating that the deposited coating is indeed a $CuZn$ alloy.

A Very interesting growth was observed on pure, -H terminated Si (100) and TiO_2 surfaces. $CuZn$ seems to form regular "Dodecahedron"-shape particles as shown in Figure 2.17a and 2.17 b). Even though a something remotely resembling was shown in case of Zn metal [67], the mechanism of such growth is absolutely unclear. The deposition on silicon with native oxide was very insufficient with small islands. Deposited coatings on Si_3N_4 contained smaller grains, with more continuous structure (Presented in figure 2.17 a) and 2.17 b) respectively).

The XPS elemental analysis for samples shown in Figure 2.17 were identical,

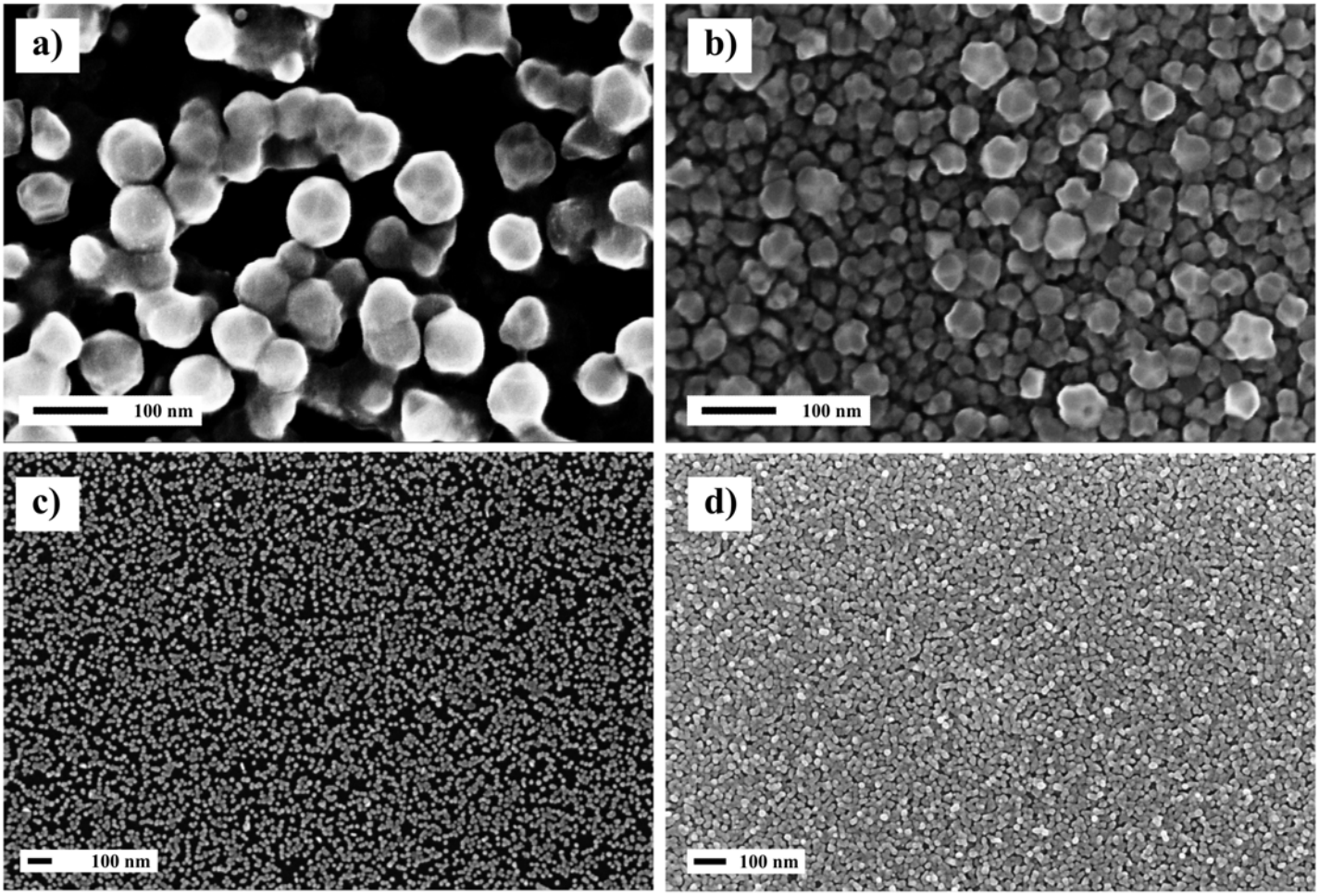

Figure 2.17: Results of Cu flat layer deposition on different samples. a) $-H$ terminated (100) Si b) Crystalline - anatase TiO_2 c) (100) Si surface with native oxide and d) LPCVD deposited 30 nm Si_3N_4 layer.

and the ratio of Cu to Zn was the same and approximately 4:1. The Cu particles deposited on pure Si displayed in Figure 2.17 a) have been SEM investigated half-a year after the deposition. The sharp edges of "polyhedral" particles disappeared and became rather spherical. The imaging suffered from charge effects, and XPS results showed that the amount of oxygen increased drastically, which all indicates that the sample become severely oxidized over time.

One of the most difficult challenges in Cu deposition was to measure and control the precursor vapor pressure. It has been decreasing during the deposition and hard to monitor and control. This instability together with the fact that the precursor bottle contained a very limited number of possible depositions were

the key factors to abandon this process for metamaterial fabrication. Another important limiting factor is the big amount of oxygen in the deposited film. The ALD chamber was mainly used for deposition of the previously mentioned oxides, which was the reason for the unavoidable oxygen contamination.

2.6 O_3 Processes

Ozone, O_3, can replace water as an oxygen source in ALD reactions. The ozone is a very reactive compound possessing strong oxidation properties, since it's weak oxygen bounds can easily be broken by light or heat. The advantage of ozone in ALD reactions compared to water is that it is a hydrogen free precursor, which results in lower hydrogen and hydroxyl residuals in the oxide films. It reduces problems such as film delamination during annealing. Comparative studies on Al_2O_3 films formed by ALD using ozone as opposed to ALD using water have shown that lower levels of leakage current are present in films formed using ozone [50]. It also has a higher volatility compared to water, especially at lower temperatures ($< 200\ ^\circ C$), giving it a significant advantage for improving process throughput in most ALD applications, since it is more easily purged away between deposition cycles than water. Since any residual oxidizer during a precursor pulse will lead to parasitic CVD behavior, ozone offers an advantage, especially in high aspect ratio structures.

The ozone is produced by the following scheme. Diatomic oxygen is broken down to monatomic oxygen atoms while passing through a system of two electrodes with applied high AC voltage. The ozone is generated by three body collision reactions. Nitrogen needs to be added as a catalyst to increase the rate of reaction and subsequently create a higher precursor concentration.

2.6.1 A Case of TMA/O_3

Ozone as an ALD oxidation agent typically involves transfers of oxygen atoms, for example TMA reacts with ozone to make Al_2O_3 by the overall reaction [50]:

$$\underset{\text{TMA}}{2\,Al(CH_3)_3} + \underset{\text{Ozone}}{4\,O_3} \longrightarrow \underset{\text{Solid film}}{Al_2O_3} + \underset{\text{Methane}}{3\,CH_4\uparrow} + \underset{\text{Water}}{3\,H_2O\uparrow} + \underset{\text{Carbon dioxide}}{3\,CO_2\uparrow}$$

The installed ALD setup has a build-in ozone generator, but the O_2 source line deliver pure oxygen only, without a N_2 catalyst, which results in a insufficient O_3 generation. The above mentioned Al_2O_3 process was tested with the best results archived in the temperature range $300 - 350\ ^\circ C$, where TMA is actually at the edge of decomposition ($327\ ^\circ C$). Figure 2.18 a) and b) show the uniformity of

Al_2O_3 deposited by 1000 cycles of TMA+O_3 for 300 °C and 350 °C, receptively. After depositing Al_2O_3 with different numbers of cycles for both temperatures, a linear growth was verified (Figure 2.19 a) and b).

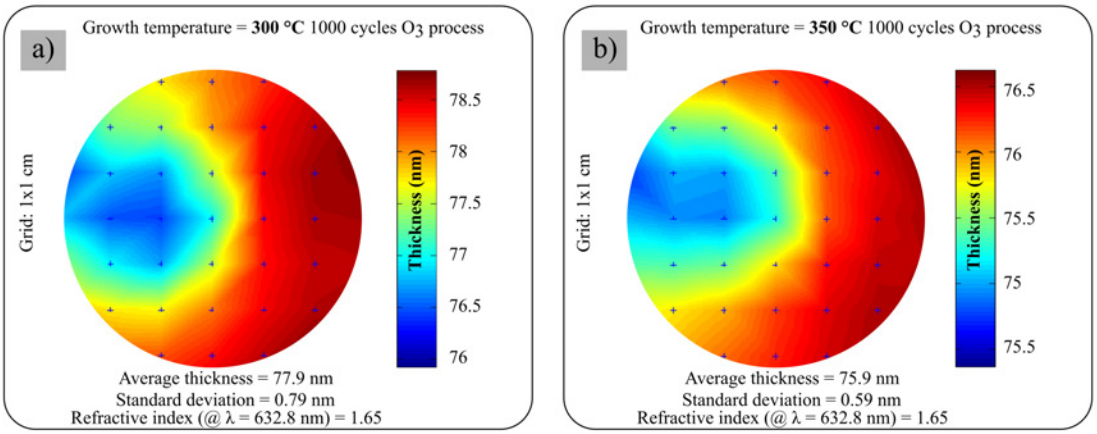

Figure 2.18: Ellipsometry measurements of thickness, uniformity and refractive index of Al_2O_3 deposited using O_3 as oxidation agent at a temperature of a) 300 °C and b) 350 °C.

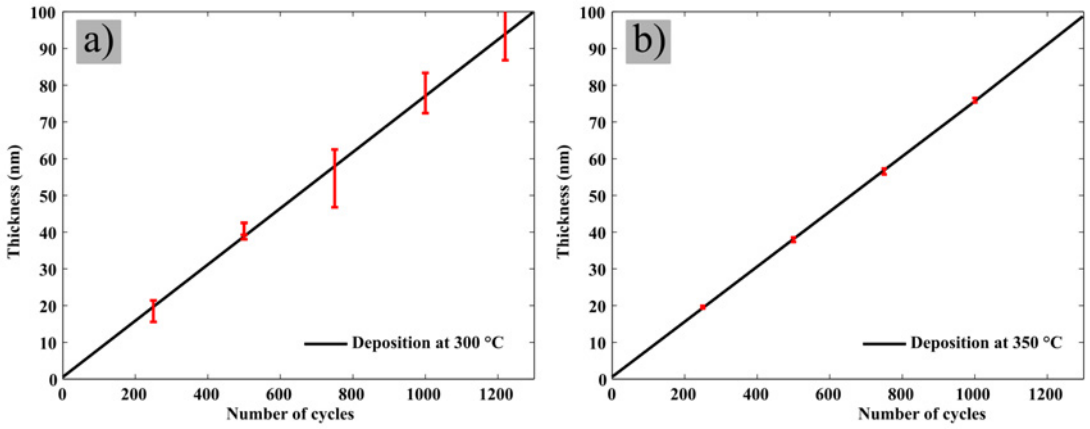

Figure 2.19: Linear growth rate verification for the TMA/O_3 process. a) A Growth rate of 0.077 nm/cycle at 300 °C and b) 0.075 nm/cycle at 350 °C was observed.

The best growth characteristics was observed at 350 °C. Unfortunately, as it was mentioned earlier, the TMA-based processes is then no longer an ideal ALD process due to decomposition of TMA at such a high temperature. The deposition uniformity results below 300 °C were not satisfying and not shown here. Additionally, it is observed from Figure 2.19 a), that the non-uniformity at 300 °C is much higher compared to water process.

2.6.2 Other Cases

Another important O_3 process is the deposition of ZnO using DEZ and O_3. The deposition mechanism proceeds according to the following reaction [86]:

$$\underset{\text{DEZ}}{Zn(CH_2CH_3)_2} + \underset{\text{Ozone}}{2\,O_3} \longrightarrow \underset{\text{Solid film}}{ZnO} + \underset{\text{Ethane}}{CH_3CH_3\uparrow} + \underset{\text{Oxygen}}{2\,O_2\uparrow} + \underset{\text{acetaldehyde}}{CH_3CHO\uparrow}$$

A research paper by S. Keun Kim *et. al.* from 2005 [87] reports that the resistivity of the ZnO thin films deposited using O_3 as oxidant is 10-1000 times higher than that of films deposited using water. The resistivity of ZnO is in fact sensitive to stoichiometry. Oxide films prepared in vacuum are normally oxygen deficient and therefore rather conducting. Ozone can improve the stoichiometry and thereby increase the resistivity. This was also tested by depositing of Al-doped ZnO [88].

Since ZnO is normally deposited at temperatures below 250 $°C$, it was not possible to verify these results. A few tests have been performed with decent uniformity, but with very insufficient, low deposition rate (Results not included).

Limited reports exist on TiO_2 thin film growth based on $TiCl_4$ and O_3 [89]. Authors however, do not provide a reaction mechanism for the process. Tests performed at 350 $°C$ did not confirmed ALD growth.

Yet another interesting process has been implemented in the development of Cu(II) oxide using Cu(dmap)2 and ozone [90] The process was not tested due to time constraints, precursor cost and the lack of implementations for HMMs production.

2.7 Concluding Remarks

The amount of possible materials produced by ALD is quite remarkable. They include metal oxides, nitrides, carbides, metals and semiconductors [72]. The list of possible materials grows constantly. During this project several new important ALD processes have been developed and published. For instance, the thermal deposition of titanium [91] and even gold [46]. New chemistries for copper is also under intense investigation [92].

The Cu ALD process based on Cu(dmap)2 and DEZ was slightly unsuccessful, in terms of reproducibility and uniformity. It was decided to switch the focus from implementation of alternative plasmonic materials for HMMs fabrication towards Al-doped ZnO. The sacrifice is that Al-doped ZnO is plasmonic in the near and mid infrared range, whereas Cu becomes plasmonic in the visible optical range. However, both TMA/water and DEZ/water processes seem to be implemented

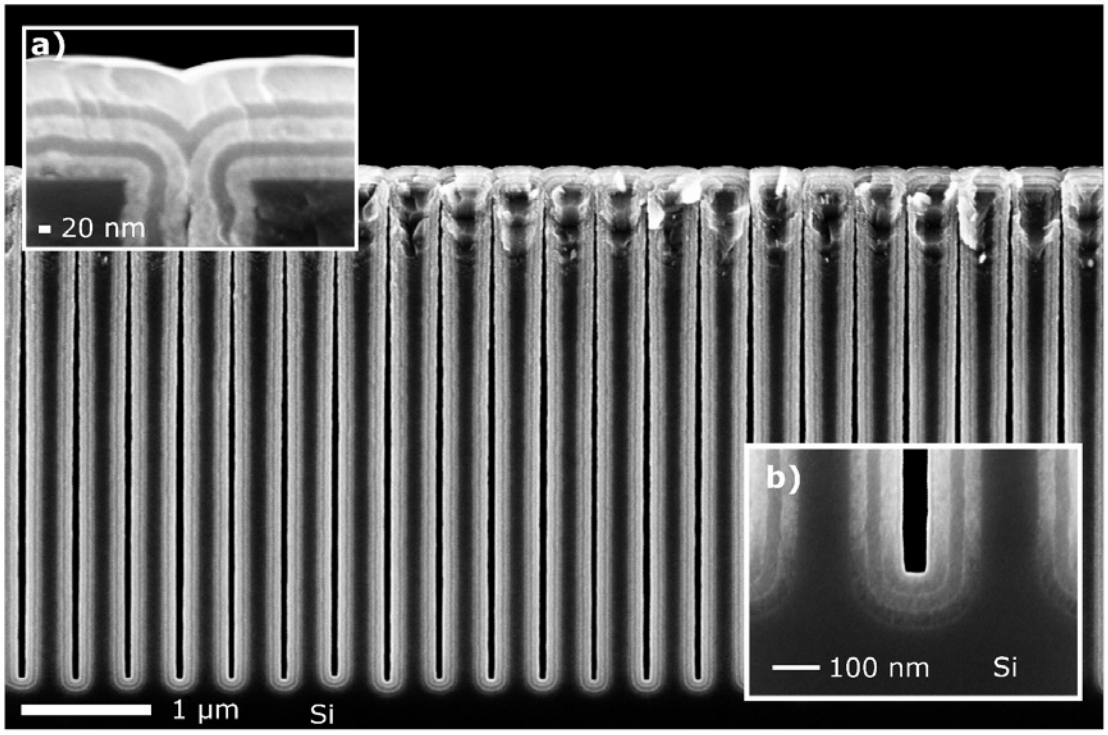

Figure 2.20: SEM cross-sectional image shows passivation of Si trenches by Al_2O_3/TiO_2 multilayers. Insets display magnifications of a) the top part and b) the bottom part of the trenches.

without any significant difficulties which will give a good advantage for working with plasmonic, doped ZnO, and realization of HMMs would be more straightforward. Nevertheless, the $CuZn$ alloy process will not be fully forgotten as some interesting, realized structures will be presented in the outlook of this thesis.

The next two chapters will be fully dedicated to Al_2O_3 and TiO_2 dielectric structures. It was shown previously that those two oldest ALD processes gives a highly conformal coatings that can passivate surfaces with advanced topography such as displayed in Figure 2.20. The next chapter will deal with Al_2O_3/TiO_2 multilayers deposited on flat surfaces with consistent optical characteristics, and the chapter after it will cover the subject of patterning dielectric structures such as one and two dimensional freestanding lattices.

CHAPTER 3

SUBWAVELENGTH ALL-DIELECTRIC PHOTONIC MULTILAYERS

As described in Chapter 2, atomic layer deposition (ALD) allows the realization of ultra thin continuous coatings on different substrates with different geometries. This ability indeed allows the fabrication of many kinds of materials, where topography and uniformity is a crustal issue.
Before going into study of vertically arranged one and two dimensional structures, the more simple case has to be considered - the flat dielectric multilayers with precise thicknesses and fixed order. The above mentioned Al_2O_3 and TiO_2 amorphous dielectrics is a perfect choice of such materials, because they are very easy to reproduce and at the same time most studied ALD grown materials. TiO_2 /Al_2O_3 ALD multilayers has been proposed for variety of practical applications included bandpass filters [93] corrosion resistance [94], polymer protectors [95] and capacitor dielectrics [96]. Despite very intensive study of these structures in the last decade, there are still rooms for discoveries of unexplored and peculiar properties of these materials.

3.1 Effective Medium Approximation Breakdown

At the visionary level, the multilayer geometry is the simplest case of inhomogeneous media. In terms of complexity, only one direction separates this structure from the continuous medium. On practical level, multilayers can be fabricated in reliable and cost effective manner by implementing a variety of common planar deposition methods such as physical vapor deposition (PVD) or chemical vapor deposition (CVD) techniques. From mathematical point of view the photonic mul-

tilayers are one of the most studied systems in optics [97]. One may mention antireflection coatings, omni-directional reflectors and Bragg mirrors [98],[99]. Optical effects of such structures arise from interference effects underlying the photonic band gap phenomena [99], and therefor traditionally associated with multilayers, where thickness of each layer d is comparable to the wavelength of light λ. On the other hand, dielectric structures with subwavelength thicknesses ($d \ll \lambda$) did not received close attention, due to the fact that field variation inside such thin layers is so small that it leads to negligible interference effects. Therefore one used to assume, that a light wave interacts with the structure as a whole, rather than with its individual layers. Such structure can be treated as homogeneous medium with some effective material parameters, regardless of their atomic, molecular or any other intrinsic construction, just as ordinary materials are treated. The applicability of this homogenization approach known as Effective Medium Approximation (EMA) to all-dielectric multilayers with deeply subwavelength thicknesses has hardly ever being questioned.

However recent theoretical publication by Sheinfux *et. al.* [100] suggests that EMA assumption may fail in certain circumstances. In particular, when the angle of incidence is close to the angle of total internal reflection (TIR), the multilayer stack and its effective medium model exhibit significantly different transmission. Moreover, the optical spectra become sensitive to variations of layer thicknesses hundred times smaller than λ, as well as the layer ordering. This sensitivity is totaly incompatible with EMA predictions, which are independent of individual layer features. Physically, the EMA breaks down close to TIR because the waves becomes evanescent in low-index layers but remains propagating in high index layers. Since the layers are deeply subwavelength, the light wave may still propagate through the multilayer via tunneling, whereas the EMA does not capture this physics and prohibits the propagation. In other words, according to Sheinfux *et. al.* [100], the wave propagating through the multilayer accumulates its phase via repeated Fresnel reflection at layer interfaces, rather then propagation effects.

Such "anomalous" effect is practically promising for sensing application and new, better spectroscopic ellipsometry models that treats multilayer systems. However, in order to observe the breakdown effect, the large number of layers (few hundred) requires with less than 1 nm thickness tolerance. This is practically challenging to realize. Nevertheless, a recent paper by Andyieuski *et. al.* [101] suggests the alternative design that enhances the effect of EMA breakdown by introduction of photonic resonator below the dielectric multilayer which only contain a few tens of layers. Such multilayer can be relatively easily fabricated using ALD technique, which is known for its precise thickness control on sub-nanometer scale, excellent step coverage and conformal deposition. The photonic resonator has to be a material with the refraction index somewhere in between the refractive

indices of two multilayer components.

Four samples with different configuration of multilayers have been proposed as depicted in Figure 3.1 a). Two of them comprise 10 bilayers of TiO_2 and Al_2O_3 with the thickness of 10 nm for each single layer, and denoted in Figure 3.1 a) as TIO10 or ALU10, depending on the surface of topmost layer (TiO_2 or Al_2O_3). The other two samples comprise 10 layers (or 5 bilayers) of alternating TiO_2 and Al_2O_3 layers with thickness of 20 nm with the same type of notation (TIO20 and ALU20). This strategy allows the realization of two thicknesses and two multilayer orders (one reverse to another). The overall thickness of each of the four structures is fixed to 200 nm. Silicon nitride (Si_3N_4) with thickness of 1 μm was selected as photonic resonator with refractive index match: $n_{Si_3N_4} \simeq \sqrt{(n^2_{TiO_2} + n^2_{Al_2O_3})/2}$. In order to perform the optical experiments the light must enter the samples from the high refractive index medium because angles above TIR require for effect verification. This condition can be satisfied by using $ZnSe$ ($n = 2.64$) semi-cylindrical prism.

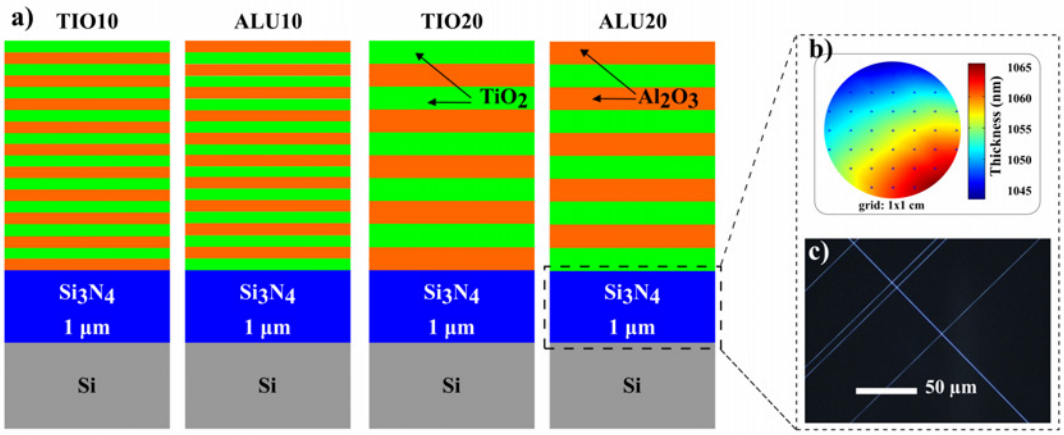

Figure 3.1: Schematic illustration. a) Thicknesses and order of ALU10, TIO10, ALU20 and TIO20 proposed samples. b) Ellipsometry thickness estimation of Si_3N_4 LPCVD deposited layer. c) Dark field optical microscopy image of silicon nitride bottom layer.

3.2 Fabrication and Characterization

All samples were prepared and assembled in a class 100 clean room (ISO class 4). The central part of fabrication was ALD of multilayers on top of the Si_3N_4 resonator. The intermediate steps and outputs of the fabrication process was monitored by several different characterization techniques including conventional

Optical and scanning electron microscopy (SEM)[1], spectroscopic ellipsometry[2], and X-ray photoelectron spectroscopy XPS[3]. Samples have also received serials of cleaning session (using N_2/O_2 plasma) in order to get rid of any possible organic contaminations.

3.2.1 Fabrication Flow

The substrates for the samples were fabricated by depositing 1 μm of Si_3N_4 (the resonator layer) on 100 mm Si (100) wafers using low pressure chemical vapor deposition (LPCVD)[4]. The process was carried out at 780 $°C$ with ammonia (NH_3) and dichlorosilane (SiH_2Cl_2) as reactive gases. Thickness and refractive index of the deposited silicon nitride was measured and confirmed using ellipsometry. (Figure 3.1 b). The deposited Si_3N_4 film was carefully analyzed for existence of cracks, particles and other defects using dark field optical microscopy (See Figure 3.1 c). The best-quality wafer with Si_3N_4 was selected and cleaved in pieces, which were used as substrates for the deposition of Al_2O_3/TiO_2 multilayers.

The fabrication of the multilayers was performed in a commercial hot-wall ALD system[5]. The precursors used for Al_2O_3 and TiO_2 deposition were trimethylaluminum $Al(CH_3)_3$ and titanium tetrachloride ($TiCl_4$), respectively. An oxidant source in both processes was deionized water. The deposition temperature was at 120 $°C$ in order to prevent the crystal anatase phase transition of TiO_2 known to occur at temperatures above 150$°C$ [5]. Such transition would increase the films roughness. To establish the deposition rate, Al_2O_3 and TiO_2 films with thickness ranging between 10 and 50 nm were deposited on Si substrates with subsequent ellipsometric characterization of the films thicknesses and refractive indices. It was determined that TiO_2 and Al_2O_3 have constant growth rates of 0.047 and 0.089 nm/cycle, respectively. Deposition recipes for Al_2O_3 and TiO_2 are summarized in Tables 3.1 and 3.2.

Before inserting each substrate into the ALD reactor, it was placed on a Si carrier wafer. Therefore the Al_2O_3/TiO_2 multilayers were grown not only on the Si_3N_4 layer but also on the dummy carrier wafer. After the ALD process was completed, the dummy was cleaved and its cross-section was characterized using SEM. These images (Figure 3.2 a-d) reveal high-quality homogeneous, thin coatings. Such method of characterization turned out to be more feasible than the direct SEM inspection of multilayers on Si_3N_4, since the later suffers from issues related to charge accumulation on the dielectric silicon nitride.

[1]SEM Zeiss Supra 60VP [55]
[2]Ellipsometer VASE from J.A. Woolam Co.
[3]XPS system from Thermo Scientific equipped with a monochromatic Al Kα X-rays
[4]Furnace from Tempress [102]
[5]Picosun R200 Thermal tool [53]

Precursor	Pulse time (s)	Flow (sccm)	Purge time (s)
TMA	0.1	150	5
H_2O	0.2	200	10

Table 3.1: One cycle of optimized Al_2O_3 process at low temperature (120 $°C$).

Precursor	Pulse time (s)	Flow (sccm)	Purge time (s)
$TiCl_4$	0.2	150	10
H_2O	0.2	200	15

Table 3.2: One cycle of optimized TiO_2 process at low temperature (120 $°C$).

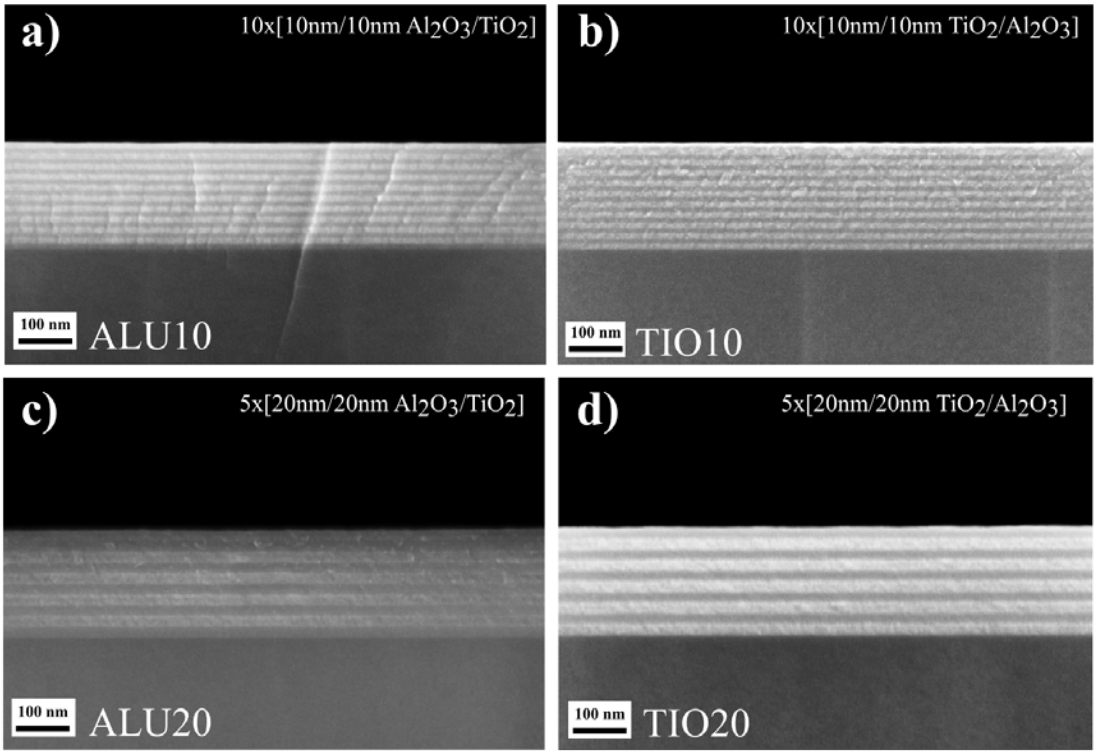

Figure 3.2: SEM cross-section images of prepared Al_2O_3 and TiO_2 multilayers a) ALU10 b) TIO10, c) ALU20 and d) TIO20.

3.2.2 XPS Depth Profiles

The chemical composition, as well as chemistry distribution in the multilayers was investigated using XPS depth profile technique. The procedure contains repetition of Ar^+ ion sputtering and surface elemental analysis. Each sputtering session proceeds for 20 sec on a spot size of 400 μm. Flood gun was used for charge compensation. The acquired data was analyzed and illustrated in Figures 3.3, 3.4 and 3.5. Survey data depicted in Figure 3.3 shows high quality chemical materials without any observable contaminations except for minor predictable impurity of chlorine in TiO_2 layers. Characteristic multilayer elements (Al, Ti, O and Si for substrate identification) was acquired using high resolution scans. Results are presented in Figures 3.4 and 3.5 comparing chemical response from different order of multilayers (TIO10 vs. ALU10 and TIO20 vs. ALU20). It is clear from these figures that layers are well separated and show the same signal consistency and clear borders. O1s signals are present in all samples, but have a remarkable feature with a certain energy shift depending on the element which is bounded to. It is clear that the O1s has a higher energy shift in Al_2O_3($\approx$533 eV) rather than in TiO_2($\approx$531 eV). These difference result in wavy profile as illustrated in Figures 3.4 a) and b) and 3.5 a) and b). Si 2p profile signal is shown in order to verify that the Ar^+ sputtering succeeded through the whole structure and all chemical data was acquired.

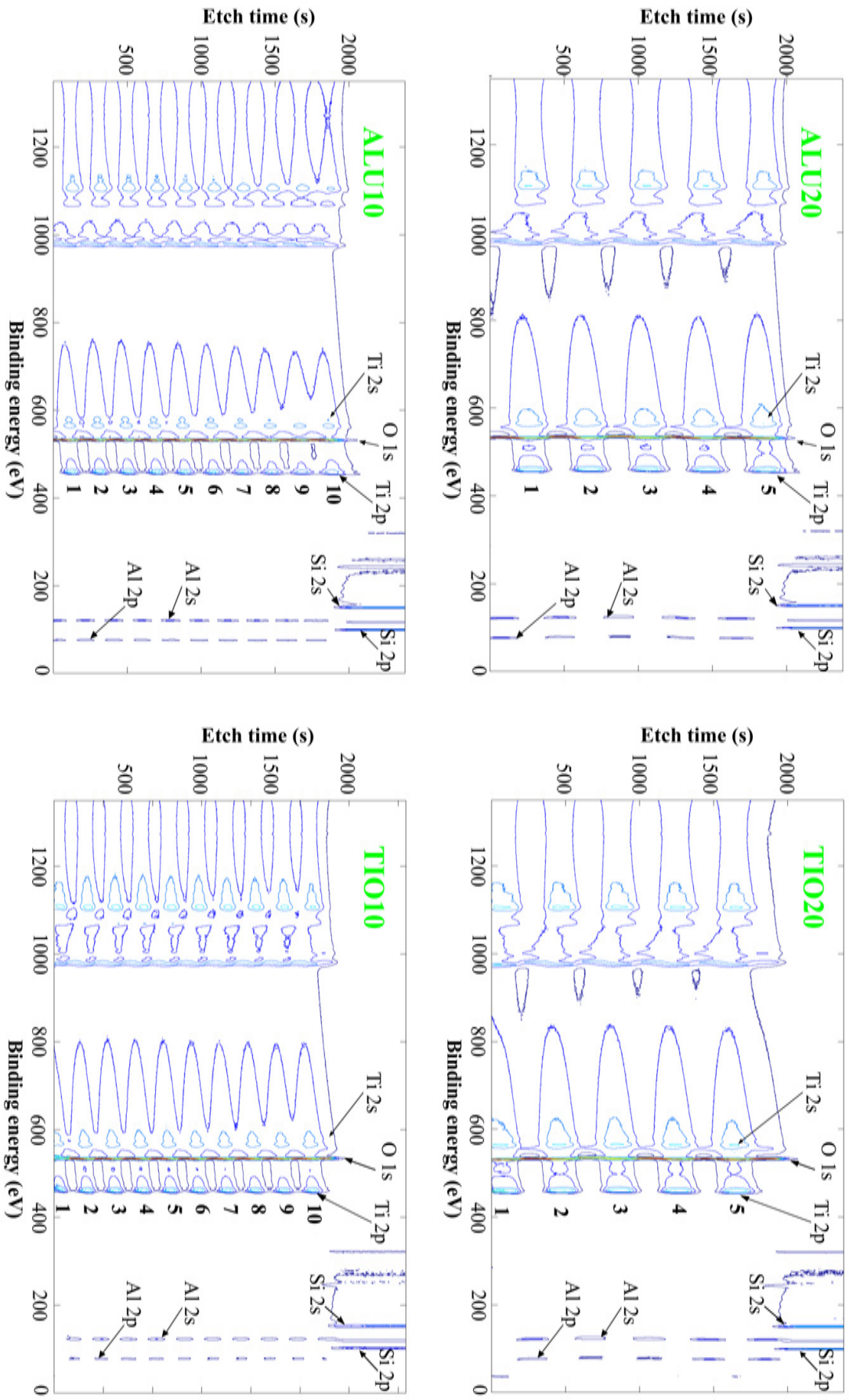

Figure 3.3: Contour plots of XPS depth-p files for all prepared samples. Signals from present characteristic elements are depicted by arrows and layers of specific Ti and Al elements are marked by numbers.

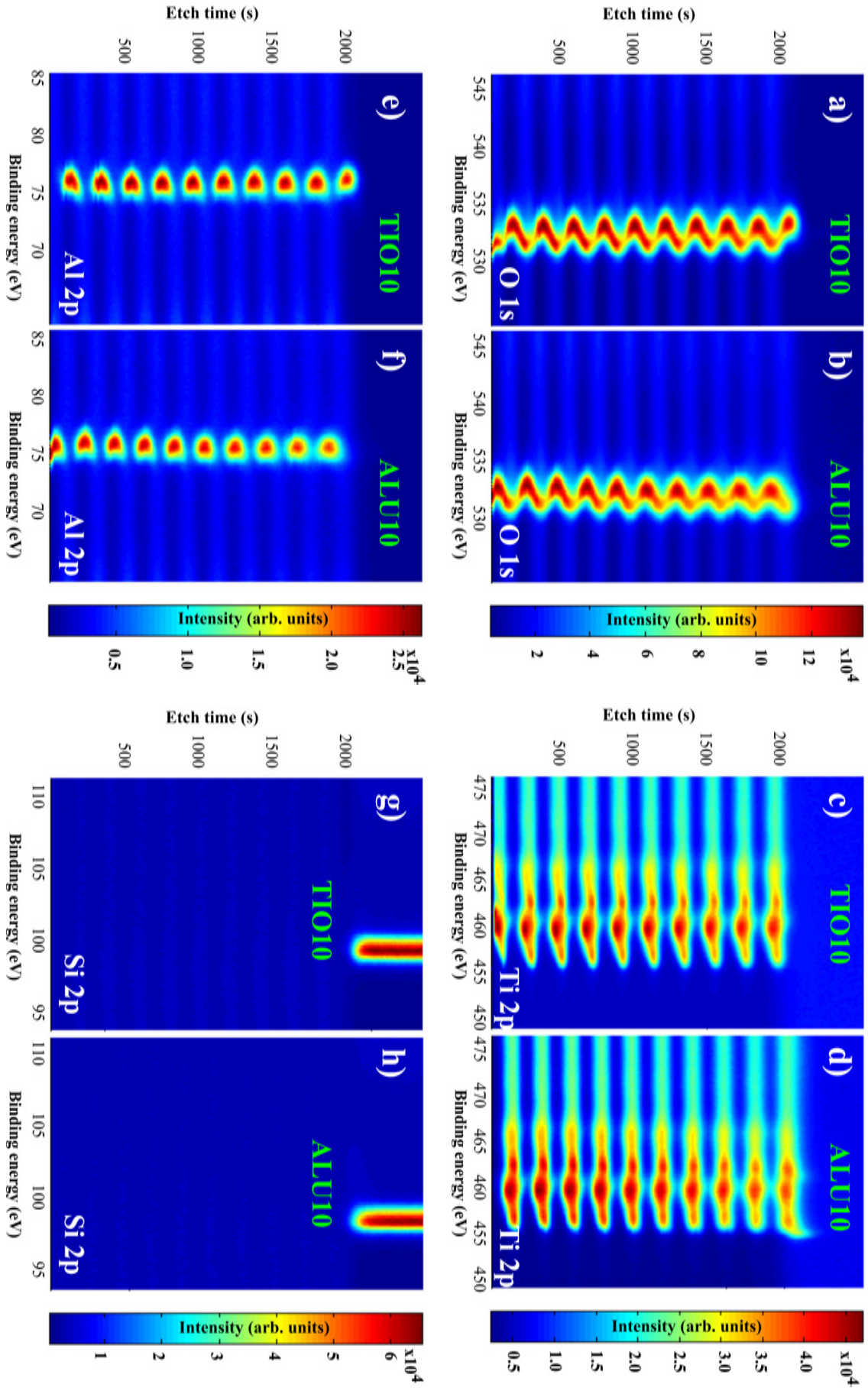

Figure 3.4: High resolution depth profile XPS signals for ALU10 and TiO10. a) - b) O 1s; c) - d) Ti 2p; e) - f) Al 2p; and g) - h) Si 2p signals for TiO10 and ALU10 respectively.

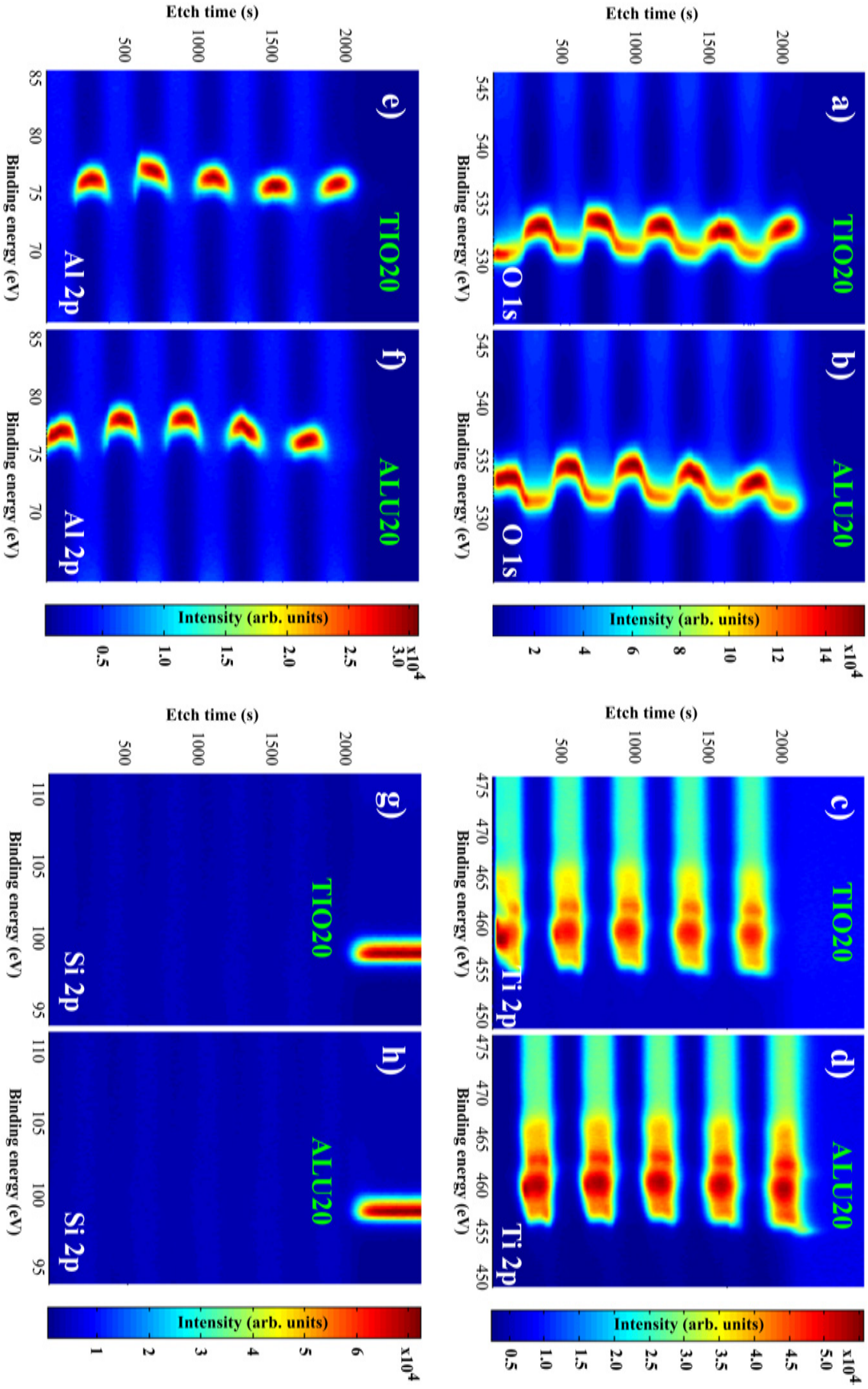

Figure 3.5: High resolution depth profile XPS signals for ALU20 and TiO20. a) - b) O 1s; c) - d) Ti 2p; e) - f) Al 2p; and g) - h) Si ap signals for TiO20 and ALU20 respectively.

3.3 Optical Experiment

To observe the EMA breakdown effect experimentally, a modified Otto-Kretchmann configuration has been employed as illustrated in Figure 3.6 a) and b). A multilayer sample is placed in close proximity to a semi-cylindrical $ZnSe$ prism, which has a sufficient high-index to achieve TIR around 50°. The light source was a supercontinuum broadband laser[6] at $\lambda = 600$ - 2500 nm). Its collimated output beam was polarized by a double Glan-Thompson polarizer and focused at the $ZnSe$ - sample interface, using a set of parabolic mirrors. The reflected beam was collected to a multimode fiber using another parabolic mirror and led into an optical spectrum analyzer[7] with the measurement range of 350 - 1750 nm. The setup illustrated in Figure 3.6 a).

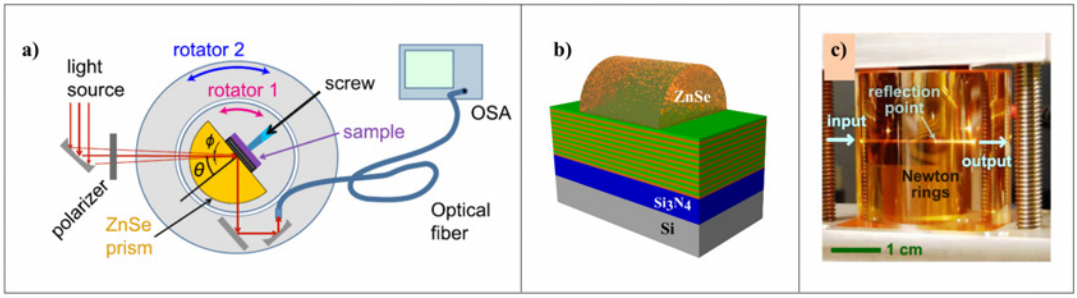

Figure 3.6: Optical characterization. a) Sketch image of the experiment setup. b) Illustration of $ZnSe$ semicylinder attached to the multilayer. c) The photography of actual semicylinder with that the attached sample. Newton's rings in the middle are clearly observed.

The sample was attached to the prism with a custom-made steel-holder tightened by small-diameter elastic screw. To minimize the air gap, which would have a dramatic influence on reflection measurements, the sample assembly was performed inside the clean room, in order to avoid the risk of dust trapping between the prism and the sample. Figure 3.6 b) illustrates the assembly of the sample to the prism. The quality of the attachment was monitored visually by controlling the appearance of the Newton rings around the location of the screw on the holder as the screw was tightened (see Figure 3.6 c). These rings originate from the interference between the back surface of the prism and the surface of the sample as

[6]SuperK, NKT Photonics A/S
[7]OSA, Yokogawa Electric Corp.

the later was pressed to the prism at the screw location, resulting in a variable air gap between the sample and the prism.

3.4 Results and Discussion

The homogenization concept of of EMA theory would require the description of permittivity of all four samples using the following tensor components:

$$\varepsilon_{\square} = \frac{1}{D}\sum_{j=1}^{N} dn_j^2, \qquad \frac{1}{\varepsilon_{zz}} = \frac{1}{D}\sum_{j=1}^{N} dn_j^{-2}, \tag{3.1}$$

Here the permittivity is given in the direction parallel and perpendicular to the multilayer with thickness $D = 200$ nm, N is the number of individual layers and n_j is the refractive index of j^{th} layer. The EMA predict the identical reflection spectra, and in order to observe the difference, following quantities needs to be introduced:

$$\begin{aligned} \Delta R_1 &= R_{ALU10} - R_{ALU20} \\ \Delta R_2 &= R_{TIO10} - R_{TIO20} \\ \Delta R_3 &= R_{ALU20} - R_{TIO20} \\ \Delta R_4 &= R_{ALU10} - R_{TIO10} \end{aligned} \tag{3.2}$$

The first two expressions describe the reflection difference for the same multilayer order but different thicknesses, and the last two treat different order. According to calculations performed by the standard transfer matrix approach done by Andyieuski *et. al.* [101], the breakdown effect is more sensitive to the ordering of the layers rather then layers thicknesses, and is more clear in TE polarization. In addition, calculations show that ΔR_3 has most pronounced (up to 25%) deviations in the reflectance spectrum. These results are illustrated in Figure 3.7 a) and b). Both experimental and theoretical results for ΔR_3 in a variety of incident angles θ are shown in Figure 3.7 c) and d) for TE and TM polarizations, respectively. It seems that the measured reflection difference behave very close to the theoretical predictions. In TE case, ΔR_3 has a minor perturbations in the lower range of incident angles θ, just in line with expectations. As the angle of incidence approaches TIR, the EMA breakdown becomes stronger, and oscillations become more clear. Finally, after TIR, both ALU20 and TIO20 samples undergo TIR with resulting in no reflection difference since no light enters the structures.

In summary, it has been demonstrated that all-dielectric subwavelength photonic multilayers can exhibit peculiar optical properties such as deviation from well established EMA theory. The results have been published [103], revealing that one

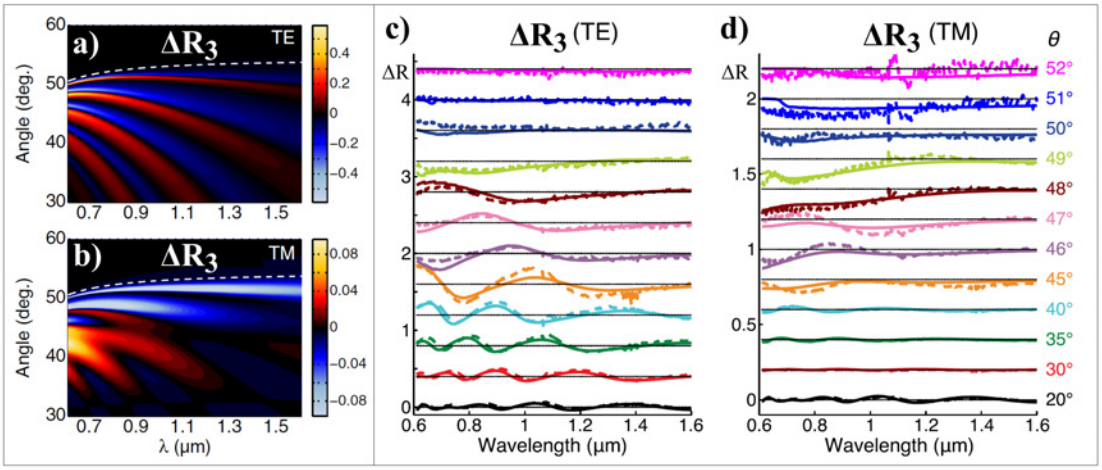

Figure 3.7: Reflectance difference results. a) and b) Calculated reflectance difference for TE (a) and TM (b) polarized incident light. c) and d) experimental results for each polarization. Solid lines represents theoretical calculations, while dashed lines experimentally measured ones.

should be careful in applying the concept of homogenization to the ellipsometry models treating multilayers system at extreme conditions such as the angle of incidence close to that of TIR. Furthermore, since the EMA breakdown happens at a very narrow incident angle range (close to TIR) the phenomena can be exploited in a variety of sensing and switching applications. This project also confirmed the possibility of growing thin, conformal, reproducible multilayer systems based on TiO_2 and Al_2O_3 materials. Next chapter discusses the concept of multilayer complexity slightly higher, namely the realization of vertically arranged and 2D multilayers of transparent dielectrics. This brings the effort one step closer to the realization of hyperbolic metamaterials.

CHAPTER 4

HIGH ASPECT RATIO Al_2O_3 AND TiO_2 FREESTANDING NANOSTRUCTURES

This chapter will cover the topic of fabrication of Al_2O_3 and TiO_2 nanostructures by using atomic layer deposition (ALD) in combination with several dry etch techniques. Three different types of structures have been investigated: nanostructured gratings, circular arrangements of cylinders and pillars.

The gratings and other structures were made by the combination of ALD and dry etch techniques. The workflow included fabrication of a Si template using deep reactive ion etching (DRIE) followed by ALD deposition of the TiO_2 or Al_2O_3. Then the template was etched away using SF_6 in an inductively coupled plasma (ICP) tool or conventional reactive ion etching (RIE) equipment, which resulted in the formation of isolated ALD coatings thereby achieving high aspect ratio structures. SF_6 plasma removes silicon selectively without any observable influence on TiO_2 or Al_2O_3 layers, thus revealing high selectivity throughout the etching. Scanning electron microscopy (SEM) was used to analyze every fabrication step. Due to non-released stress in the ALD coatings the top parts of the gratings were observed to bend inwards as the Si template was removed thus resulting in a gradual change in the pitch value of the structures. The pitch on top of the gratings is 400 nm, and it gradually reduces to 200 nm at the bottom. The form of the bending can be reshaped by Ar^+ ion beam etching. The chemical purity of the ALD grown materials was analyzed by X-ray photoelectron spectroscopy (XPS). The approach presented opens the possibility to fabricate high quality optical metamaterials and functional nanostructures.

4.1 Vertically Arranged Al_2O_3 and TiO_2 Nanogratings

This section presents the fabrication of periodic nanostructured gratings of TiO_2 and Al_2O_3 with an aspect ratio up to 50 and it demonstrates controllable highly selective etching of Si during the TiO_2 and Al_2O_3 grating formation. The procedure combines dry etch and ALD techniques. ALD is the only technique that allows the deposition of extremely conformal coatings on complex three-dimensional nanostructures [45]. Deposition of TiO_2 and Al_2O_3 has been intensively studied and heavily implemented in a variety of applications in physics [104]-[112].

4.1.1 Introduction

In recent years, the theoretical advances in nanophotonics impose a great demand on developing fabrication techniques that allow patterning of high quality optical materials at nanoscale [17]. High aspect ratio trench structures can serve as one-dimensional photonic crystals (1D PhCs) as an alternative to conventional thin-film multilayers in a vertical strata arrangement. A photonic crystal consisting of a periodic arrangement of high and low refractive index media possesses a photonic bandgap, where light within a certain wavelength range is prohibited to propagate [99]. 1D PhCs by definition have no complete bandgaps opened in all directions inside the structure. Nevertheless, in the reduced space of the wavevectors inside the structure, a PhC may exhibit a unique property of the omnidirectional reflection of the external radiation [99],[98]. Such a structure serves, for example, as a bandpass filter [113]. Previously, high aspect ratio vertical 1D PhCs have been realized as Si trench structures and studied for telecommunication wavelengths of around 1.5 μm where Si is transparent [114],[115]. However, Si is not transparent in the visible wavelength region. Therefore 1D PhCs made of TiO_2 and Al_2O_3 are desirable candidates for applications in the visible and near-infrared regimes. Moreover, the capability to deposit thin films in a conformal way on trench structures can effectively tune a stopband. Such tuning of a photonic bandgap by a third layer (SiO_2) has been performed by oxidizing the surface of Si [116]. Fabrication of photonic crystals by ALD can also be applied towards realization of two dimensional PhCs [117] as well as other kinds of structured functional materials such as epsilon-near-zero metamaterials [118]. In addition to the advanced deposition of dielectric layers, the deposition capability of metals (e.g. Cu [84]) and conductive oxides, (e.g. aluminum-doped ZnO [119]) also provides fabrication flexibility for demands of metamaterials with metal or metallic-like components. Apart from the telecommunication applications, high aspect-ratio vertical 1D PhCs can find various applications ranging from color filters [120] to

optofluidic sensors for biosensing [121],[122]. In the latter case liquid flows through trenches, and the refractive index of the liquid is analyzed by a shift of a photonic bandgap [123].

In contrast to vertical silicon trenches, high aspect ratio structures in oxides such as TiO_2 and Al_2O_3 cannot be patterned in the same way by conventional methods such as RIE. A recent paper by Huang *et. al.* [117] proposed a new method to pattern TiO_2. In this approach ALD plays a key role, since patterning formation is based on deposition rather than etching the desired material. The main idea of this method is based on three steps: 1) Fabrication of a Si template which is coated by an ALD-deposited film. 2) The ALD film is partially removed by plasma etching techniques, which provide an open access to the original Si template core. 3) The template is etched away leaving the ALD coated structure with an advance topology. Such a procedure requires high selectivity during the back etching of the template.

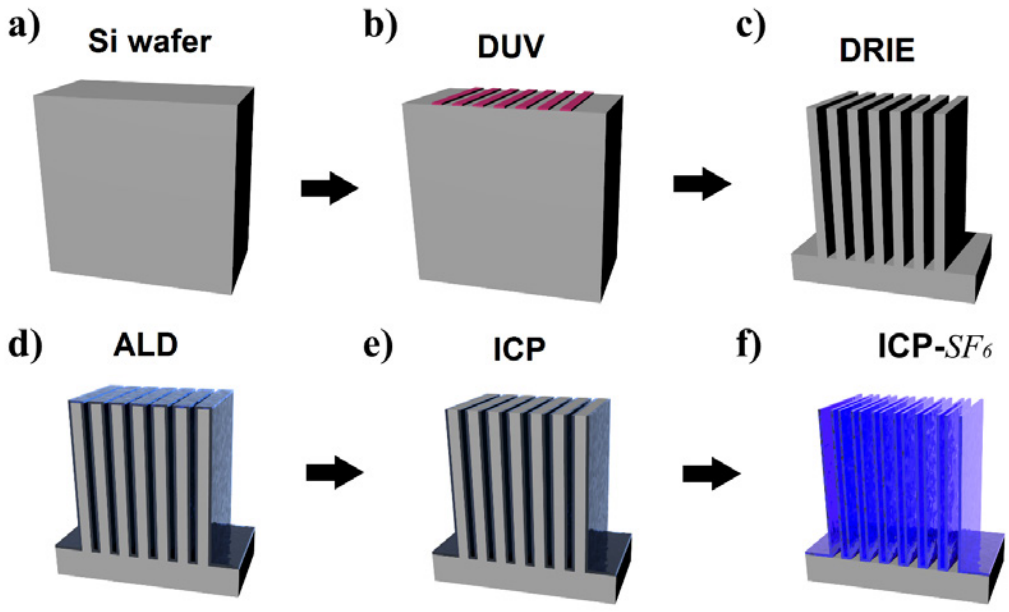

Figure 4.1: The scheme of fabrication flow. a) Si substrate. b) Deep-UV lithography. c) Fabrication of trenches in silicon using DRIE. d) Atomic layer deposited TiO_2 or Al_2O_3 coatings. e) Selective removal of the top part. f) Isolation of the coatings by silicon etching.

4.1.2 Fabrication Flow

All samples were prepared and characterized in a class 100 cleanroom. 150 mm Si (100) wafers were used as a substrate. The main steps in the gratings fabrication are shown in Figure 4.1. First, silicon trenches were realized by DRIE (see Figure 4.1 a)-c). Then the trenches were ALD coated, (Figure 4.1 b). After the selective removal of the top parts, as depicted in 4.1 c), the silicon core between the ALD coatings was etched away during the last step. Figure 4.1 d) represents the final structure, which is the highly anisotropic vertical grating. Each fabrication step was carefully evaluated using cross-sectional SEM imaging[1].

Template Fabrication

Conventional deep-ultraviolet (UV) lithography[2] was implemented for defining the grating pattern. The normal procedure includes bottom anti-reflective coating (BARC) and photo resist coating followed by spray development. To promote adhesion and minimize interference effects the substrate surface was coated with a 65 nm thick BARC coating (DUV42S-6, Brewer Science USA) followed by a bake-out at 175 $°C$ for 60 s. A positive photoresist (KRF M230Y, JSR Micro NV) was spin-coated to a thickness of 360 nm and baked at 130 $°C$ for 90 s. A pitch of 400 nm was chosen for the gratings. The resist was exposed on field sizes of 2x2 cm^2. In the next step silicon trenches were prepared using the advanced DRIE technique [124]. Three main steps were used in the Si trench fabrication: Etching of the BARC layer, selective silicon etching and resist removal. The BARC etching step proceeded for 1 min. using 40 sccm of oxygen plasma with coil and platen powers of 400 W and 20 W, respectively. In the DRIE[3] silicon etch a Bosch process [124] was implemented where the etching was done by repetitive steps of surface passivation and etching for 2.5 s and 5 s, respectively, with process pressure of 10 mTorr. The processing substrate temperature was kept at 20 $°C$. Table 4.1 summarizes the process parameters. The depth of the trenches was controlled by adjusting the number of cycles. In this work this depth was kept at 4.5 μm, which with the present etching conditions corresponded to 70 cycles.

The last step in the Si trench fabrication was the removal of the photoresist mask using oxygen plasma for 2 min. with a flow of 100 sccm and coil and platen powers of 800 W and 20 W respectively. The depth, pitch and general shape of the silicon trenches were confirmed by cross-section SEM investigation (Illustrated on Figure 4.2 a).

[1] SEM Zeiss Supra 60VP [55]
[2] Canon FPA-3000 EX4 DUV stepper
[3] DRIE Pegasus from SPTS [125]

		Passivation (5.0 s.)	Etching (2.5 s.)
Process gas flow (sccm)	C_4F_8	50	20
	SF_6		60
	O_2		5
Powers (W)	Coil	600	400
	Platen		40

Table 4.1: DRIE parameters for Si trench fabrication. The process temperature is 20 $°C$ and pressure of 10 mTorr for all processes.

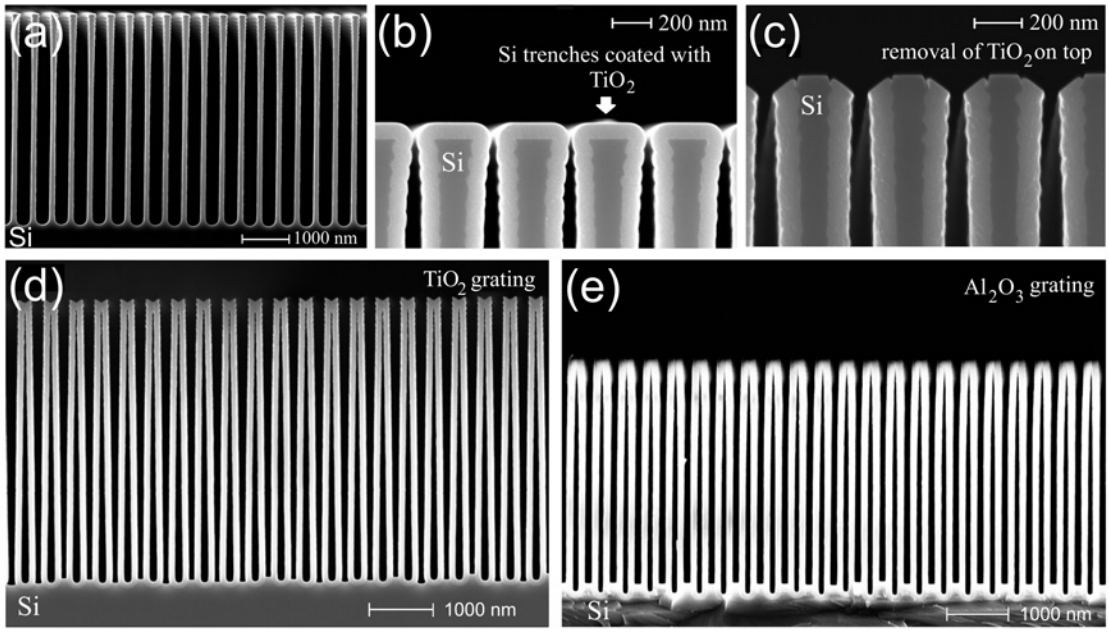

Figure 4.2: a) Fabricated silicon trenches. b) TiO_2 ALD coating of trenches c) Selective opening of the top parts of the gratings. d) Fabricated TiO_2 and e) Al_2O_3 gratings.

Atomic Layer Deposition

The TiO_2 and Al_2O_3 ALD film deposition are described in details in Chapters 2 and 3. In the case of TiO_2 deposition, a temperature of 150 $°C$ was chosen in order to minimize the TiO_2 surface roughness caused by crystalline anatase transitions known to occur at high temperatures [61]. The growth rates of the TiO_2 and Al_2O_3 coatings were found to be 0.045 and 0.089 nm/cycle, respectively (in agreement with previously reported data [126]) using varying-cycles deposition with ellipsometric characterization of the film thicknesses and refractive indices. No

significant variations of deposition rates were observed. ALD deposition[4] recipes for TiO_2 and Al_2O_3 on high aspect ratio structures are represented in Tables 2.2 and 2.4. The same precursor was introduced into the chamber twice in order to ensure successful diffusion to the bottom of the trenches. In order to grow 90 nm coatings 2000 and 1000 cycles were used for TiO_2 and Al_2O_3, respectively. Figure 4.2 shows a cross-section SEM image which reveals the high quality conformal coatings.

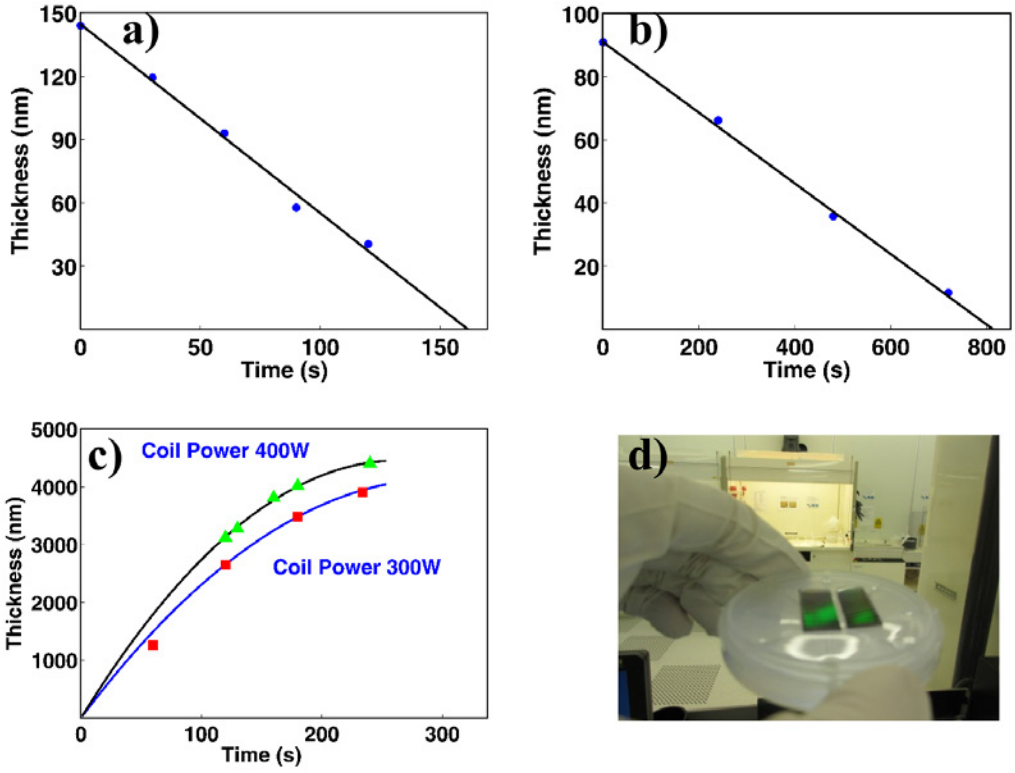

Figure 4.3: Etch rate measurements of ALD layers on planar Si substrates for a) TiO_2 using Cl_2 based etching and b) Al_2O_3 using Cl_2/BCl_3 based etching, respectively. c) Depth of silicon vs. etching time during Si template removal in the ICP using SF_6. d) Photography of the sample.

[4]Picosun R200 Thermal tool [53]

Removal of the Top Part and Template Back Etching

The top TiO_2 and Al_2O_3 layers were removed by inductive coupled plasma (ICP)[5]. Etching of TiO_2 and Al_2O_3 in ICP systems were previously reported [127],[128], especially etching of Al_2O_3 has received attention due to its beneficial use as a hard mask and a gate dielectric [128]. In case of TiO_2, a Cl_2 flow was used. The removal of Al_2O_3 involved BCl_3 and Cl_2 gases. First, the removal of TiO_2 etching and Al_2O_3 was investigated on planar Si substrates. 145 nm of Al_2O_3 and 90 nm of TiO_2 were deposited on silicon and etched using the recipes described in Table 4.2. The remaining thickness of the deposited layers was measured using spectroscopic ellipsometry[6] for different process times. The results are summarized in Figure 4.3 a) and b). The etch rates of TiO_2 and Al_2O_3 following these recipes are 0.11 nm/s and 0.89 nm/s, respectively. It is important to strictly control the etching of the top part of TiO_2 and Al_2O_3 since an overetch can damage the silicon core beneath the ALD coatings. Figure 4.4 a) presents the extreme case of such an event, and the control of the grating fabrication can be lost, due to the fact that the depth of the Si core will become unknown. The TiO_2 grating after removal of the top part, but still with the Si template can be seen in Figure 4.2 c).

The subsequent selective silicon etching (template removal) proceeded using a continuous isotropic silicon etch in the ICP etch system based on SF_6 at a substrate temperature of 20 $°C$. This process exhibits an extreme selectivity with respect to oxides, and the selectivity of Si to Al_2O_3 was previously reported to be 66000:1 for SF_6 ICP plasma [129]. Table 4.2 summarizes the process. Figure 4.3 c) shows the etch depth as a function of time. Controlling the time is essential, since overetching will lead to a collapse of the gratings as one depicted in Figure 4.4 b). The coil power can be reduced in order to slow down the silicon etching. However, reducing it to below 300 W results in non-uniform etching across the sample. Figure 4.2 d) and 4.2 e) show SEM cross-sections of the fabricated nanostructured TiO_2 and Al_2O_3 gratings. Photography of the cleaved sample with the diffracted light is presented in Figure 4.3 d).

4.1.3 Results and Discussion

The TiO_2 and Al_2O_3 nanostructured gratings were successfully grown and isolated on the Si substrates. The SEM cross-section investigation as shown in Figure 4.2 a) - e), reveals high selectivity and precise control in all steps throughout the fabrication. With a thickness of the Al_2O_3/TiO_2 coatings of 90 nm and a grating height of 4500 nm, the aspect ratio of the fabricated nanostructures is 1:50. During DRIE etching the substrate suffers from the scallops formed during

[5]Multiplex ICP Etcher from SPTS[125]
[6]Ellipsometer VASE from J.A. Woolam Co.

Process parameters	TiO_2 etch	Al_2O_3 etch	Si etch
Cl_2 (sccm)	30	1.2	-
BCl_3 (sccm)	-	6.8	-
SF_6 (sccm)	-	-	90
Pressure (mTorr)	3	4	10
Coil Power (W)	900	1200	400
Platen Power (W)	50	200	3

Table 4.2: Recipes for Al_2O_3, TiO_2 and Si etching in the ICP etch system. The process temperature is 20 °C for all processes.

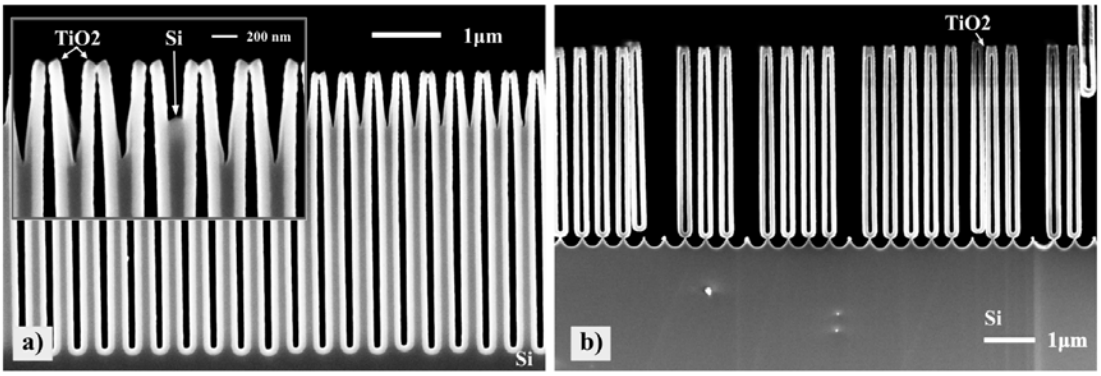

Figure 4.4: Imperfections caused by too long etching time. a) An extreme case of TiO_2 overetch. The silicon core between ALD coatings is clearly damaged. The inset shows a magnified SEM image. b) Overetch of Si leads to a partial collapse of the fabricated structures. The reader can see successful results in Figure 4.2 c) and d) for comparison.

the first 5-10 etching cycles. These scallops are typical for the Bosch etch process [124] and cause the undesired roughness of the subsequent ALD coatings. After these first DRIE cycles the etching proceeds smoothly with only a very small variation of the Si trench width. The thickness of the fabricated Si walls at the bottom is 100 nm, and 150 nm at the very top. The variation of the wall thickness mainly occurs during DRIE etching of the first micrometer depth. ALD deposition of 90 nm Al_2O_3 and TiO_2 revealed very high quality layers with no noticeable variation in thickness, despite the very high aspect ratio of DRIE etched Si trenches. For evaluating the chemical composition, ALD depositions of TiO_2 and Al_2O_3 were made on planar Si substrates. The planar structures were analyzed by XPS[7] in order to detect possible impurities in the ALD layers. The reader is referred to Chapter 2 for details on Al_2O_3 and TiO_2 ALD deposition and XPS

[7]XPS system from Thermo Scientific equipped with a monochromatic Al Kα X-rays

characterization. Al_2O_3 samples revealed chemically high quality films with no observable contaminations (Figure 2.6), whereas the TiO_2 film contained around 2-3 at. % of chlorine residuals, which originate from the unreacted $TiCl_4$ precursor (Figure 2.10). The presence of chlorine can be reduced to below the detection level (around 1 at. %) of the XPS for ALD growth temperatures around 300 $°C$ as it was concluded in Chapter 2. However, such high growth temperatures lead to the crystalline anatase phase transition, which will heavily increase coating roughness [60]. Chlorine free precursors such as Titaniumtetraisopropoxide (TTIP) [130] must be considered as an alternative for ALD deposition of TiO_2 at 150 $°C$ and below.

The removal of the top part has to be done with care since the silicon beneath the TiO_2 and Al_2O_3 coatings immediately will start to be etched by the Cl_2 or Cl_2/BCl_3 based plasma. The back etch of the original silicon template using the isotropic dry etching recipe based on a continuous SF_6 process shows no significant height differences of the fabricated gratings across the sample. This process, however, is nonlinear and very sensitive to the coil power of the ICP tool (Figure 4.3c). A coil power of 400 W was the most optimum, since decreasing to below 300 W, leads to larger deviations in the height of the remaining Si core, and increasing it to above 400 W results in a higher etching speed and less control of the etching conditions. The nonlinearity during the Si core removal represented in Figure 4.3 c) puts a demand on controlling the condition during the previous TiO_2/Al_2O_3 top opening step. During the silicon etching between the ALD coating steps no influence on the TiO_2/Al_2O_3 thin film morphology has been observed as a result of the very selective Si etch. This is a rather significant result since it opens the opportunity to fabricate similar structures using other materials by using the right chemical selectivity and the possibility of ALD growth. The fabricated Al_2O_3 and TiO_2 gratings have a shape similar to the surface of the original Si template. Due to the highly conformal nature of the ALD growth, the shape of the scallops from the silicon template is transferred to the ALD grown gratings. This initial roughness together with the fact that the ALD films are grown at elevated temperatures, while the silicon template removal between ALD coatings occurs at room temperature, leading to an outward bending of the top grating parts. This bending is caused by the built-in stress and was observed for both TiO_2 and Al_2O_3 gratings. This is the main drawback of the above described fabrication method. The reason for the bending is that the ALD deposition is a thermally activated process and in this case the deposition was carried out at 150 $°C$, while the Si back etching in the ICP etcher was done at 20 $°C$. The accumulated stress is released during the silicon removal. Indeed, Al_2O_3 and TiO_2 have thermal expansion coefficients of $8.2 \cdot 10^{-6}$ $°C^{-1}$ and $9 \cdot 10^{-6}$ $°C^{-1}$ respectively, while for Si this parameter is much less ($2.6 \cdot 10^{-6}$ $°C^{-1}$). The difference in thermal expansion between oxides

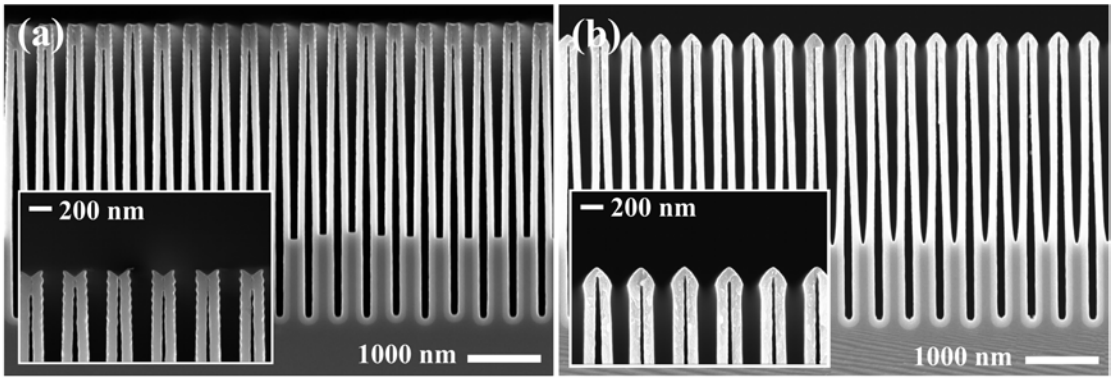

Figure 4.5: Shaping the top part of fabricated gratings by the "fence" profile. a) Fabricated TiO_2 grating. b) Shaping the top part of TiO_2 grating profile using Ar^+ IBE etching. The insets show magnified pictures.

and silicon is the reason why the oxide coatings tend to bend outwards and get attached to their neighbors during Si template removal. Nevertheless, the bending features are perfectly periodic, which allows for improvements of the top part. One way of improvement is ion beam etching (IBE) using Ar^+ ions. This will allow to shape the fabricated gratings with the "fence" profile as shown in Figure 4.5 a) and b), for a grating that has now a pitch of the original one 400 nm with small gap between coatings.

4.1.4 Highlights

To summarize, vertically nanostructured TiO_2 andAl_2O_3 gratings were fabricated and later published [131]. The present work demonstrates the powerful combination of conformal ALD growth of dielectric layers on a high aspect ratio Si template and subsequent highly selective etching of the Si template. Silicon etching is an isotropic process which makes it extremely flexible to realization of different types of 3D ALD structures such as trenches, pillars, pores etc. By combining DRIE and ALD it is possible to create vertical oxide nanogratings with a high aspect ratio, that is not possible to obtain by any other techniques. Additionally, it is also possible to create high ratio ternary compounds such as $Al_xTi_yO_z$, with different constituent concentrations by varying the number of TMA and $TiCl_4$ cycles in the ALD recipes [132]. This will allow tailoring of the effective refractive index of the gratings. Periodic structures of other materials, which are known for their difficulties in patterning such as ZnO, and more important for this project Al-doped ZnO, will be tested for realization. Realized structures can be further improved by Ar^+ ion beam etching which allows tuning the top part of the gratings, minimizing their roughness and changing the top shape. The well-defined high aspect ratio

trench structures made of Al_2O_3 and TiO_2 are good candidates for 1D PhCs in the visible and near infrared regions. Furthermore, combined with other materials that can be deposited by ALD such as ZnO and Cu, the trench structures can serve as a generic platform for different types of metamaterials possessing extraordinary optical properties.

4.2 Circular Arranged TiO_2 Concentric Rings

The next tested geometry was TiO_2 gratings with a polycylindrical shape. The difference here is not only the implementation of new, circular topology, but also an attempt to fabricate an entirely transparent device by growing transparent TiO_2 periodic structures on fused silica. These high aspect ratio *glass-on-glass* structures are quite novel in terms of technology development, since the limited chemistry of TiO_2 provides patterning constrains. The procedure is similar to the grating preparation, but this attempt would require an entirely different substrate preparation since TiO_2 nanostructures have to be placed on SiO_2 and not on a common silicon wafer. Such circular structures can act as a so-called Q-plates [133].

4.2.1 Q-Plates

Q-plates are well known devices that couple spatial and polarization degrees of freedom for optical beams [134]. Due to this coupling, it is possible to exchange electromagnetic angular momentum between circular polarization modes (spin angular momentum) and helical wavefront modes (orbital angular momentum) [135],[136]. The orbital angular momentum (OAM) eigenstates [137], such as the Laguerre-Gauss (LG modes) transverse modes [138], are characterized in the cylindrical coordinate system by the azimuthal phase factor $e^{il\phi}$, where l is an integer, and ϕ is the azimuthal angle. These modes have many applications including fiber mode selection [139], optical tweezers and micromanipulation [140]. In the domain of quantum optics, LG beams carry an OAM of $l\hbar$ per photon [141] and define an infinite basis in the Hilbert space that can be represented, along with the spin angular momentum states, in a higher-order Poincaró sphere [142]. In order to generate an helical phase front, which carries OAM, one must introduce a convenient polarization and position dependent phase shift $\delta(\sigma, \boldsymbol{r})$ on the beam cross section. Usually, this task is realized in a q-plate by a thin layer of liquid crystal whose molecules have their axes oriented along a certain pattern engraved on a glass surface [143]. For example, when a circularly polarized Gaussian beam passes through a q-plate with $\delta = \pi(\delta = 0)$ for linear polarization along the radial (azimuthal) direction, its polarization handedness is flipped and this acquires an OAM

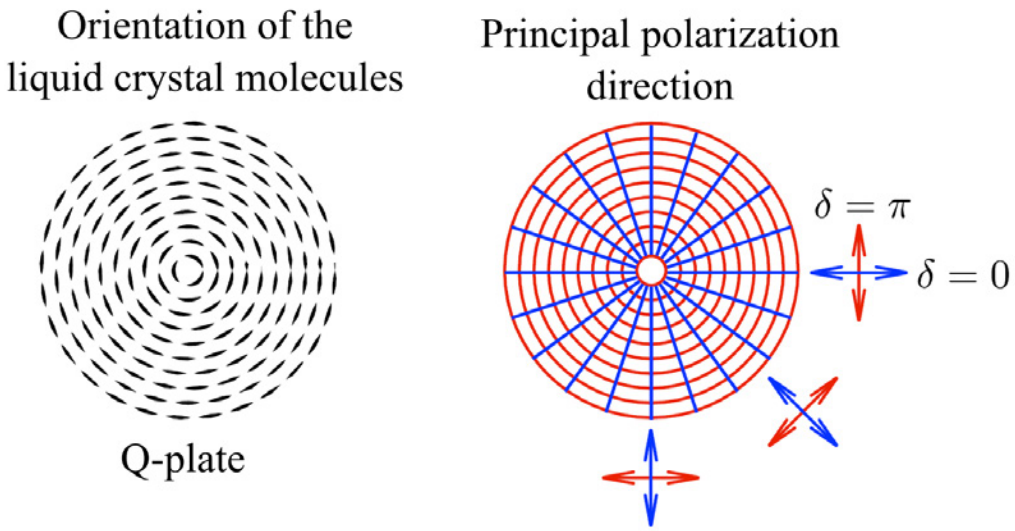

Figure 4.6: Example of a liquid crystal q-plate whose molecules are azimuthally oriented. The phase shifts are $\delta = 0$ for linear polarization along the radial direction and $\delta = \pi$ for linear polarization along the azimuthal direction.

of ± 2. This situation is illustrated in Figure 4.6. The right value of δ is achieved by tuning the q-plate either thermally [144] or electrically [145],[146]. Although the use of a liquid-crystal allows for relatively simple fabrication techniques [147], its absorption spectrum may set limits to the wavelength and power ranges that can be handled by the q-plate. These possible limitations can be circumvented by exploiting the phenomenon of form birefringence to fabricated q-plates with subwavelength surface relief gratings [148]. Due to technical difficulties in fabrication, subwavelength surface relief q-plates are in general limited to wavelengths in the order of 10 μm. Here the fabrication of q-plates without liquid crystals is presented, using processes of e-beam lithography, atomic layer deposition and dry etch techniques.

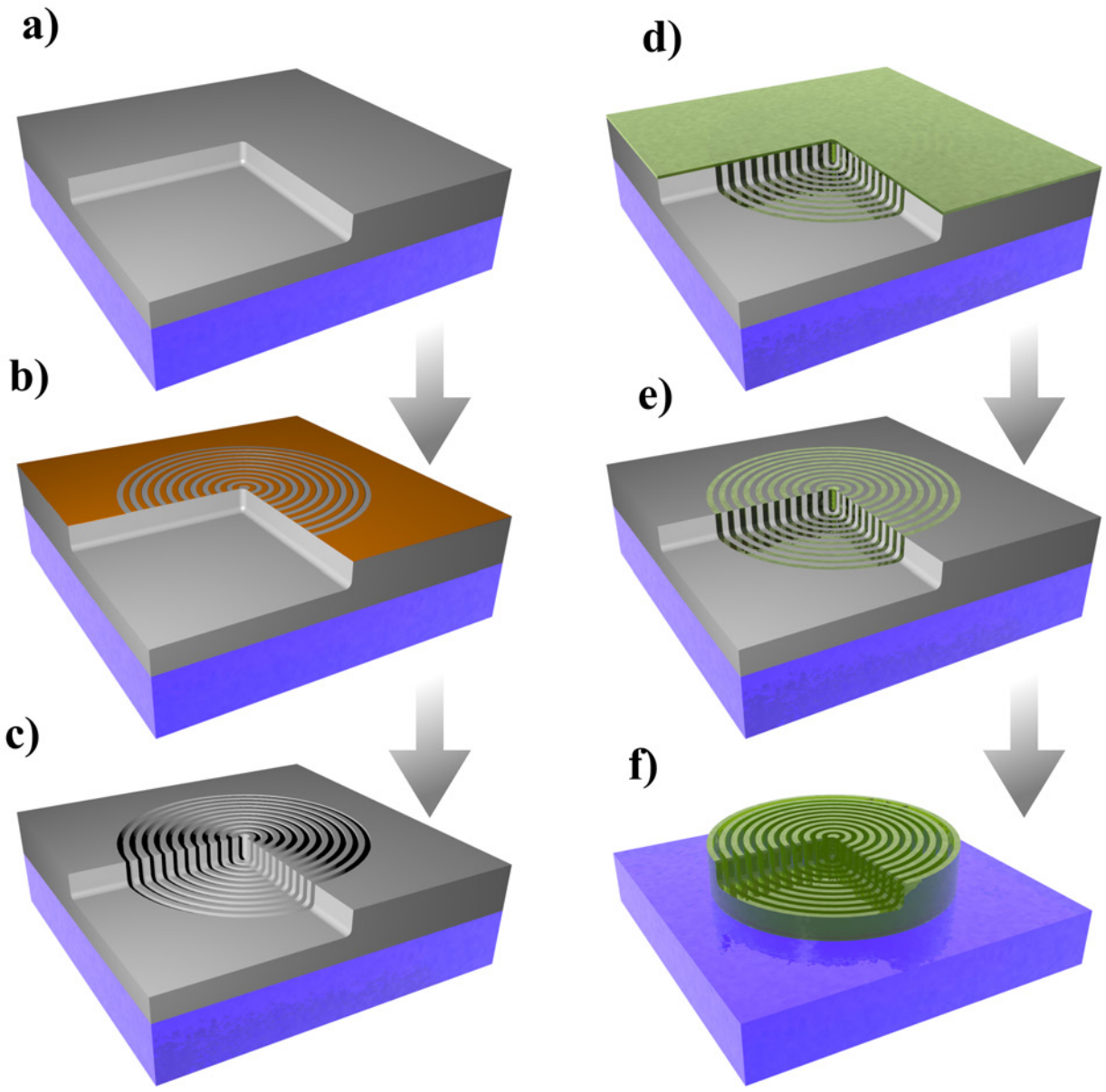

Figure 4.7: Scheme of the fabrication flow for ALD Q-plates. a) Si deposited on SiO_2 by a LPCVD process (only the top part is considered, sub sequential removal of the backside is not included). b) E-beam lithography. c) Advance silicon etching (ASE). d) ALD deposition of amorphous TiO_2. e) Removal of TiO_2 by IBE (only the top part is considered). f) Isotropic SF_6 based RIE etching and final structure.

4.2.2 Fabrication of ALD Q-Plates

A fused silica wafer (SiO_2) goes through RCA clean. This is a standard set of wafer cleaning steps which need to be performed before high-temperature processing steps (oxidation, diffusion, CVD) of silicon wafers in semiconductor manufacturing. Next, a layer of 680 nm amorphous silicon (Figure 4.7 a) was deposited by using low pressure chemical vapor deposition (LPCVD[8] based on SiH_4 (silane) at $560°C$. The back side of deposited amorphous silicon was removed using SF_6 (not shown here). In order to remove residues from the etching process an oxygen plasma cleaning was performed. A deposition of 150 nm of the resist CSAR was done followed by an exposure to electron beam lithography (EBL)[9] (Figure 4.7 b) generating a template of resist with concentric ring patterns. The Q-plates will a diameter of 0.5 mm with a grating period of 320 nm (each patterned line has a width of 160 nm). After development, the wafer was subjected to advanced silicon etch (ASE)[10] (Figure 4.7 c). EBL and ASE steps was performed by DTU Fotonik collaborators. To form the trenches of the structures, a thin film of TiO_2 was deposited using the recipe presented in table 2.4, with 2000 cycles at 150 $°C$ (Figure 4.7 d) [131], meaning that the thole ALD step was exactly the same as in the previous TiO_2 nanograting case. To remove the excess of the deposited TiO_2 coating, Ar^+ ion beam etching (IBE)[11] on both sides of the wafer was implemented (Figure 4.7 e) instead of chemical Cl_2 ICP etch. In principal both plasma and Ar^+ sputtering can be used in this removal case, however the exact thermal behavior of the glass (SiO_2) substrate is unknown in ICP systems. Due to this unpredictable response is was decided to use Ar^+ etch instead. Finally, a reactive ion etch of silicon based on continuous SF_6 flow has been performed[12], leaving only the TiO_2 structures on the wafer. The final system comprehends a base of SiO_2 with nanostructures of TiO_2 on it (Figure 4.7 f). Figure 4.8 depicts a SEM image the final structures of TiO_2. The insets a) and b) of the same figure illustrate samples as a) an optical microscopy image and b) a SEM image of the entire sample.

[8] Furnace from Tempress [102]
[9] JEOL JBX-9500 Electronbeam [149]
[10] Manufactured by STS
[11] Ionfab 300 plus from Oxford Instruments [150]
[12] RIE, from SPTS

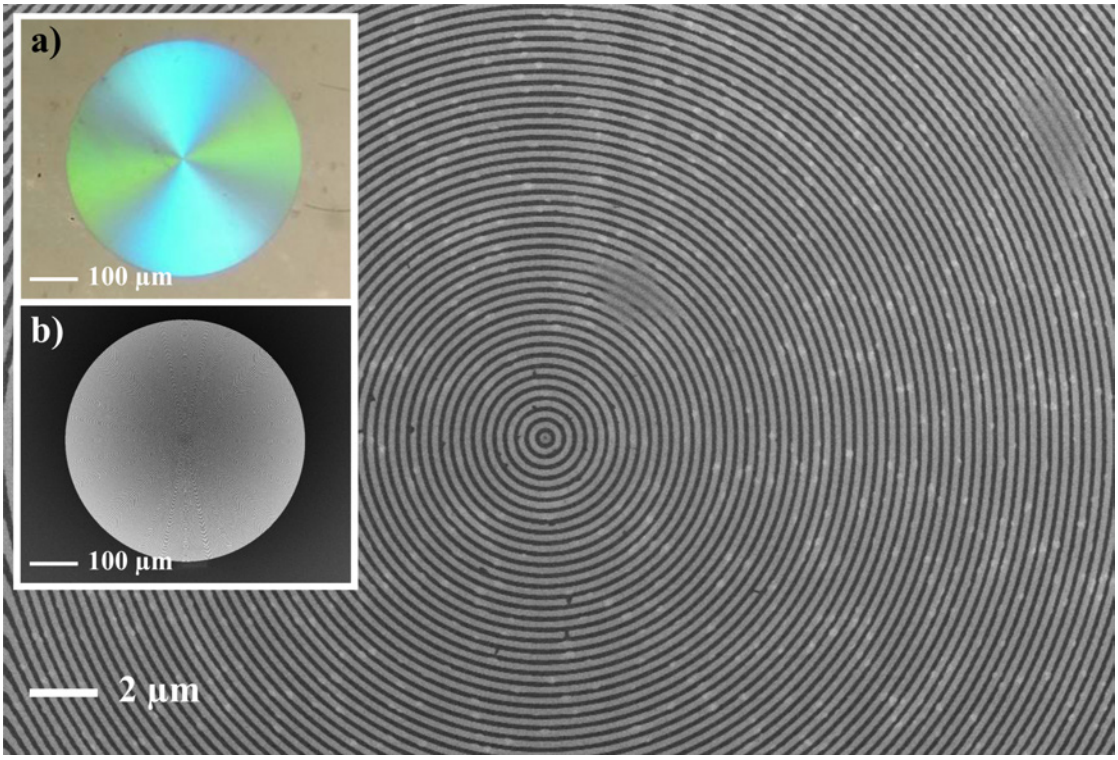

Figure 4.8: Fabricated polycylindrical TiO_2 structures. The insets show the entire structures a) Optical microscopy image of TiO_2 . b) SEM image of TiO_2 structure.

4.3 Al_2O_3 and TiO_2 Freestanding Nanopillars

the last implemented structure were TiO_2 and Al_2O_3 nanopillars. As it was mentioned earlier in this chapter the TiO_2 pillars fabrication have been reported previously by Y. Huang *et. al.* [117]. Such structures can act as 2-dimensional PCs which has been shown [117], but with the right dimensions and choice of material they can also become hyperbolic metamaterials (HMMs) [151]. The fabrication steps are presented in Figure 4.9, and the final result is shown in Figure 4.10.

4.3.1 Fabrication Flow

The fabrication starts with preparation of *silicon-on-insulator* (SOI) wafers. The main idea here is to include a stop etch barrier, a thin layer of SiO_2 inside a silicon

		Passivation (1.50 s.)	Etching (2.75 s.)
Process gas flow (sccm)	C_4F_8	50	20
	SF_6		60
	O_2		5
Powers (W)	Coil	600	400
	Platen		40

Table 4.3: DRIE parameters for Si holes array fabrication. The process temperature is 0 $°C$ and pressure 10 mTorr for all processes.

host. First, standard Si (100) wafers were oxidized in a conventional quartz tube[13] using a dry oxidation process based on O_2 at 1100 $°C$, resulting in a 200 nm SiO_2 layer on Si. Next, a 2 μm amorphous Si layer was grown on the SiO_2 surface using a conventional LPCVD process (just like in the circular TiO_2 structures case) based on SiH_4 at 560 $°C$. The surface roughness is below 1 nm, thus of sufficient quality to be used as base material for the Si template (Figure 4.9 a).

The produced home-made SOI wafers were patterned using Deep-UV stepper lithography just like in the nanogratings case, the difference was only in a new mask design, which now contains dots instead of lines, and an adjusted exposure dose. The diameter of the dots was 200 nm with square lattice pattern. The lattice constant (the pitch) was either 400 nm or 500 nm. The optimal exposure dose was found to be 840 - 860 J/m^2 for the 400 nm pitch and 1100 J/m^2 for the 500 nm pitch. The sizes of the dots and lattices were chosen so that they were at the very limit of resolution for Deep-UV lithography and at the same time could be able to fabricate a big number of samples in a relatively quick and cheap way compared with for example EBL. Additionally, the area of the final pillar samples (1x1 cm) and the amount of these samples on one 6" Si wafer (69 pieces) as well as the number of wafers that can be managed by the Deep-UV lithography stepper (25 wafers handled simultaneously) outperform the speed and cost of EBL, which is important for future commercial product release.

The preparation of the hole template was done by DRIE etching using the recipe shown in Table 4.3. A BARC etch was done for 45 sec. Process pressure was 10 $mTorr$, the temperature was kept at 0 $°C$. 80 cycles was enough to etch down to the SiO_2 layer, and by reaching this insulating layer the etching stopped.

The remaining steps including ALD, ICP top part removal and Si back-etch were the same as in grating case with the same ALD and ICP recipes (Figure 4.3 c)-f). One needs not to worry about possible collapse of the produced structures as in the grating case illustrated in Figure 4.4 b), because the back-etch stops

[13]Furnace from Tempress [102]

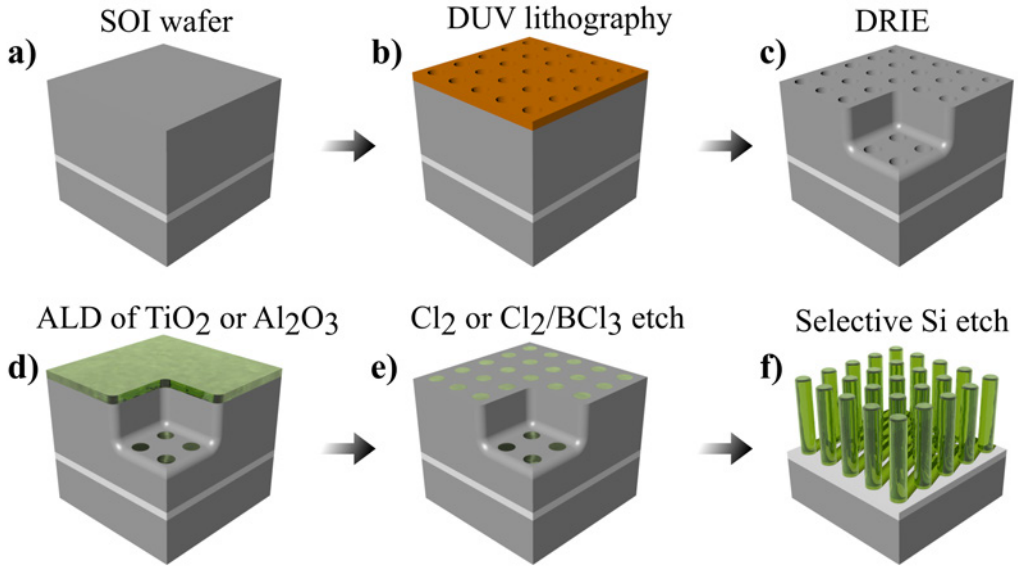

Figure 4.9: Fabrication flow for TiO_2 and Al_2O_3 pillars. a) "Home-made" SOI wafer. b) Deep-UV resist patterning. c) Si template preparation using DRIE etching. d)ALD deposition of TiO_2 or Al_2O_3. e) ICP etching of the ALD deposited top layer. f) Selective Si etch.

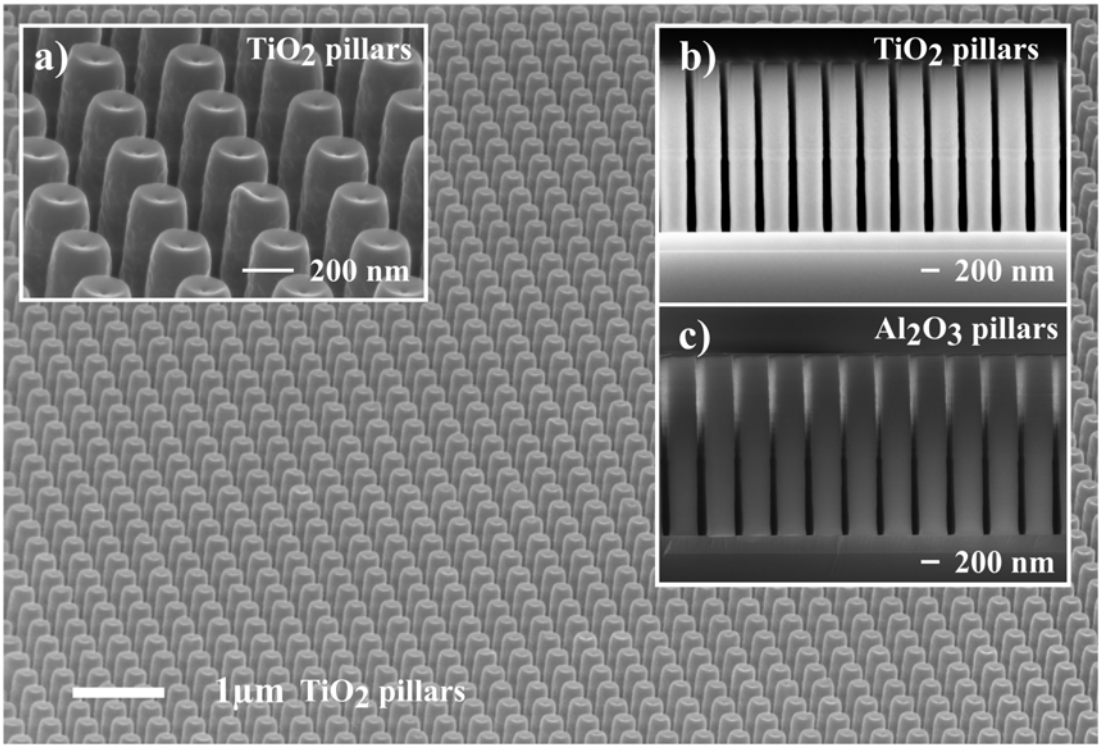

Figure 4.10: Fabrication result. SEM image of TiO_2 nanopillars. a) Magnified SEM image. b) TiO_2 and c) Al_2O_3 pillars shown from the side.

4.4 Closing Remarks

The presented fabrication technique of novel 3D nanostructures made by a combination of ALD and dry etch techniques allows to fabricate independent free-standing TiO_2 and Al_2O_3 components from sacrificial "Si mold". The fabrication output has an excellent quality and reproducibility. The technology platform can finally be tested on plasmonic structures such as Al-doped ZnO (AZO), which will directly gain the desired materials with hyperbolic dispersion. However, prior to these structures are fabricated, the fundamental physical and optical properties of AZO thin films needs to be analyzed.

CHAPTER 5

FABRICATION AND CHARACTERIZATION OF ALD GROWN AZO THIN FILMS

The successful deposition of common dielectric materials such as Al_2O_3 and TiO_2 using atomic layer deposition (ALD) and their patterning using dry etch techniques described in Chapters 2-4 is a necessary step for the realization of hyperbolic metamaterials (HMMs). The final step is the switch from dielectric to plasmonic structures. It was shown in Chapter 2 that Cu ALD growth was unsuccessful in terms of control and reproducibility. However, it is possible to implement other alternative plasmonic materials such as transparent conductive oxides (TCOs). One of the most studied TCOs is Al-doped ZnO (AZO) which is known to be plasmonic in the near- and mid- infrared region [21]. This chapter describes the fundamental properties of ALD grown AZO thin films.

5.1 Introduction

TCOs are important materials within optical physics and engineering [152]-[154]. Indium tin oxide is the most investigated and implemented compound [155]. However, it has disadvantages including toxicity and the cost of indium. Recent development on alterative TCOs revealed that AZO could become a promising replacement for Indium tin oxide [156]-[160]. A variety of deposition methods exists for the preparation of AZO. These include RF magnetron sputtering [160], chemical vapor deposition [161], chemical spray pyrolysis [162], pulse laser deposition [163]-[165] and ALD [45],[156]-[159]. Specifically, ALD technology is important since it is the only technique allowing a conformal and uniform deposition on surfaces with advanced topology such as pores, trenches, holes, etc. ALD also has advantages as

low temperature deposition, precise thickness and composition control. For these reasons, ALD grown AZO films have been extensively studied in the last decade because of their physical and optical properties. Additionally, AZO has both important and peculiar optical properties such as plasmonic response in the near- and mid- infrared region [166],[167]. This makes AZO an important and promising alternative plasmonic material having a wide range of tunable optical and electrical properties. AZO can be used as a plasmonic component in optical metamaterials where it can exhibit near-epsilon-zero regime and hyperbolic dispersion.

ALD growth conditions and physical properties of AZO thin films with a thickness of 100 nm and different Al concentrations have been investigated on flat silicon (100) substrates. For transparency measurements, optical absorption and bandgap evaluation as well as electrical resistivity measurements, the AZO films were deposit on double side polished glass wafers (fused silica). All work has been carried out in a class 100 cleanroom. The physical, optical and electrical properties have been investigated. The applied characterization techniques include four-point probe resistivity measurements, atomic force microscopy (AFM), scanning electron microscopy (SEM), X-ray photoelectron spectroscopy (XPS), X-ray diffraction (XRD), and spectroscopic ellipsometry.

5.2 ALD Growth Characterization

Three temperatures regimes were selected (150 $°C$, 200 $°C$ and 250 $°C$) for investigation in order to cover most of the ZnO ALD temperature window [45],[71]. AZO with various Al:ZnO ratios, has been deposited in a thermal, hot-wall ALD system[1] on flat silicon (100) and fused silica (glass) substrates. Precursors were bought from Stream Chemicals. ZnO was deposited using diethylzinc ($Zn(C_2H_5)_2$, DEZ) and deionized water (H_2O), whereas Al doping has been introduced by a single cycle of trimethylaluminium ($Al(CH_3)_3$, TMA) and H_2O into a ZnO matrix made by "n" cycles of "DEZ+H_2O". This notation defines an AZO macrocycle used in this work: "n" cycles of "DEZ+H_2O" and 1 cycle of "TMA+ H_2O". In this case, for example "D10" corresponds to 9 cycles of (DEZ+H_2O) and one cycle (TMA+H_2O). AZO films were grown with "n" between 4 and 34 with 5 cycles of intermediate steps. Table 5.1 summarizes the parameters of one ALD AZO macrocycle. Each precursor was introduced in the reactor chamber twice, with a very short purge time of 0.5 sec in-between the pulses. After this two precursor exposures with a very long purge time of 20 sec follows. Such an approach is suitable for passivation of very high aspect ratio structures, where it is necessary to make sure that the precursor molecules diffuse and react with a complicated surface topology such as deep holes, trenches or pillars. Prolonged purge times secure

[1] Picosun R200 Thermal tool [53]

Precursor	Number of repetitions	N_2 Carrier gas flow (sccm)	Pulse time (s)	N_2 Purge time (s)
DEZ		150	0.1	0.5
DEZ		150	0.1	20
H_2O	4-34 (D5-D35)	200	0.1	0.5
H_2O		200	0.1	20
TMA		150	0.1	0.5
TMA		150	0.1	20
H_2O	1	200	0.1	0.5
H_2O		200	0.1	20

Table 5.1: Recipe for one AZO macrocycle.

that the extent of the precursor as well as the reaction product can escape from the sample. For ALD deposition characteristics of Al_2O_3 and ZnO, the interested reader should refer to Chapter 2.

The overall numbers of deposited macrocycles were chosen for certain temperatures so that the overall thickness of the deposited AZO layers is as close to 100 nm as possible. The thickness was measured by spectroscopic ellipsometry. A summary of the deposition conditions and the scheme of the ALD AZO layers is shown in Figure 5.1.

The deposition rate of undoped ZnO was measured to be 0.18 nm/cycle, 0.15 nm/cycle and 0.11 nm/cycle for temperatures of 150 $°C$, 200 $°C$ and 250 $°C$ respectively. The corresponding deposition rate of Al_2O_3 is 0.09 nm/cycle with neglect deviations in temperature (see Figure 5.1 a). These values are in agreement with the previous reported [71]. The thickness of the AZO film can be calculated using the following expression: $T = N \cdot (n \cdot GPC_{ZnO} + GPC_{Al_2O_3})$. Here, T is the thickness, N is the total number of macrocycles, n is the number of (DEZ+H_2O) repetitions, GPC_{ZnO} and $GPC_{Al_2O_3}$ are growth-per-cycle (GPC) of ZnO and Al_2O_3 respectively.

In many practical cases however, the deposition rate of Al_2O_3 can be assumed to be identical with deposition rate of ZnO, in such a scenario the film thickness becomes $T = N \cdot D \cdot GPC_{AZO}$, here $D = n + 1$ according to the concept presented in Figure 5.1 b). This assumption is valid in the temperature region $200 - 250$ $°C$, but in the case of 150 $°C$ the difference in growth rate between ZnO and Al_2O_3 becomes too significant, and the GPC ratio of these oxides should be treated separately.

The more important discrepancy in deposition rate occurs where the thickness of the ZnO host layer becomes small, it is in the case for the D05 recipe for

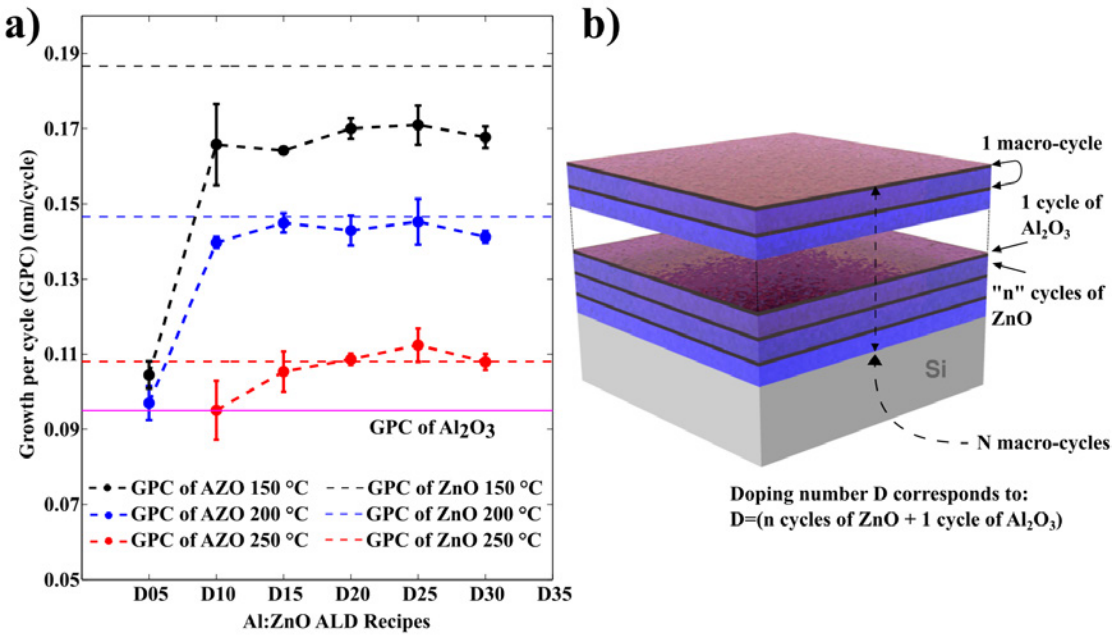

Figure 5.1: ALD deposition conditions. a) Growth per cycle of Al_2O_3 ZnO and AZO for each temperature regime: 150 °C, 200 °C and 250 °C. b) Schematic drawing of deposited AZO layers and concept illustration of doping "D" number.

depositions of 150 °C and 200 °C and D10 for 250 °C (Figure 5.1 a). The difference here is so pronounced that it cannot be explained by a slower deposition rate of Al_2O_3. Several explanations have been proposed for the reason of this behavior. It could be related to hindering of the ZnO phase after (TMA/H_2O) pulses [157] or an etching of ZnO by TMA [156]. The next sessions reveals that these highly Al doped AZO films indeed contain more amorphous, dielectric Al_2O_3 than ZnO.

5.3 Elemental Analysis

XPS elemental analysis[2] revealed a high quality chemical film with no observable impurities. Figure 5.2 a) shows a typical scan of a ZnO/AZO sample. Prior to XPS measurements the film surface was sputtered in-situ with Ar^+ ions in order to get rid of native airborne hydrocarbons. Thermo Avantage v5.948 software was used in order to calculate the Al concentration in the AZO films. Figure 5.2 b) shows the high resolution Al 2p area for ZnO/AZO deposited at 250 °C. The obtained aluminum concentrations is plotted vs. the ALD recipes in Figure 5.2 c). Remarkably, the actual concentration of Al is significantly higher than

[2]XPS system from Thermo Scientific equipped with a monochromatic Al Kα X-rays

predicted by simple estimation. From ideal ALD behavior the Al concentration can be calculated using this simple expression:

$$Al(\%) = 100\% \cdot \frac{GPC_{Al_2O_3}}{GPC_{Al_2O_3} + n \cdot GPC_{ZnO}}$$

The straight dashed blue line in Figure 5.2 d) shows the ideal case, while XPS measured Al concentrations are higher. These observations are confirmed by other experimental techniques such as energy dispersive x-ray spectroscopy (EDX) [159] and X-ray fluorescence (XRF) [157]. The proposed explanation is the inhibition of ZnO growth after the (TMA+H_2O) cycle. An alternative explanation suggests that TMA exposure etches the underlying ZnO causing the mass loss [156].

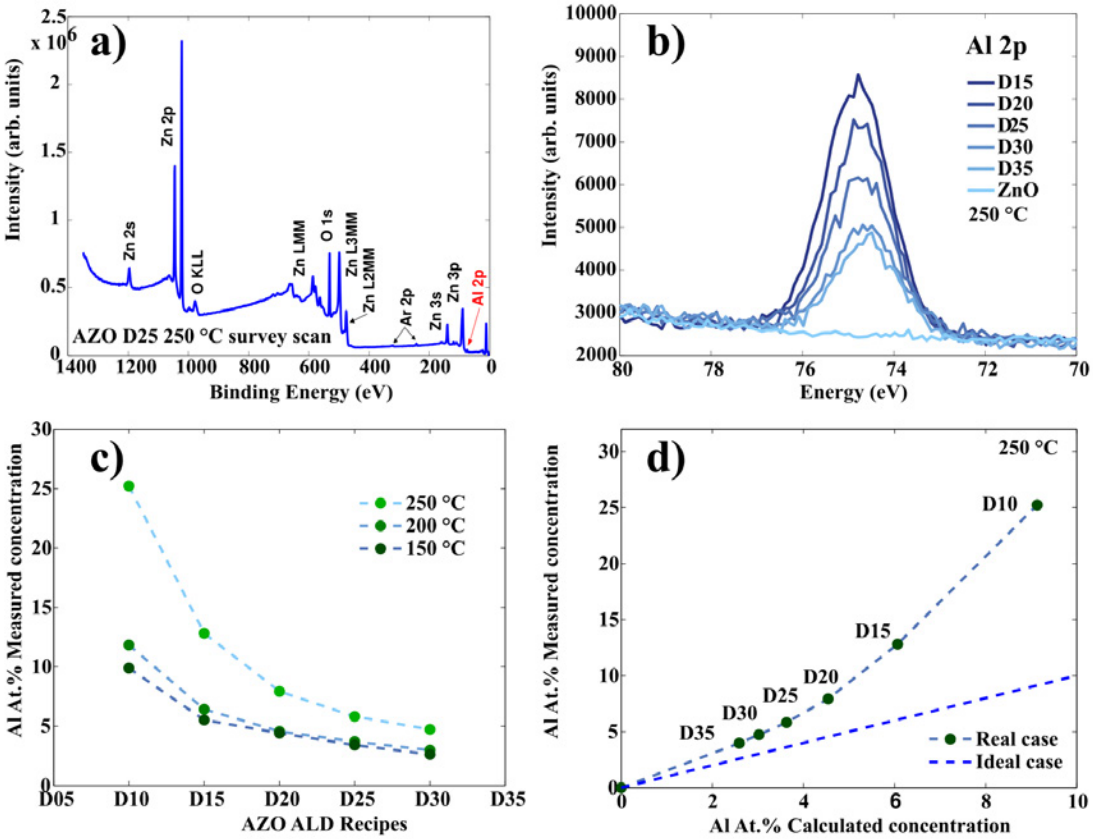

Figure 5.2: XPS investigation of AZO layers. a) Typical survey scan of AZO/ZnO. b) High resolution scan of the Al 2p region for AZO/ZnO samples prepared at 250°C. c) Measured Al concentration in AZO films prepared at three temperatures: 150°C, 200°C and 250°C. d) Deviation of the measured Al at.% concentration from the theoretical estimation in case of 250°C deposition temperature.

5.4 Morphology of Deposited Layers

The surface morphology of deposited 100 nm ZnO/AZO thin films has been analyzed by scanning electron microscopy[3] and atomic force microscopy[4]. SEM images (Figure 5.3) reveals a polycrystalline nature of deposited thin films. AFM inspections (Figure 5.4) of deposited ZnO/AZO films D10-D35 at 250 $°C$ reveals a surface roughness of approx. 2 nm RMS, which slightly decreases with increasing Al content in the films. In case of D10, the Al_2O_3 phase dominates and it result in a roughness below the acceptable detection value. The AZO films deposited at 250 $°C$ tend to obtain a cylindrical morphology, which can be related to preferred (002) ZnO crystal orientation growth, which will be discussed in the next section.

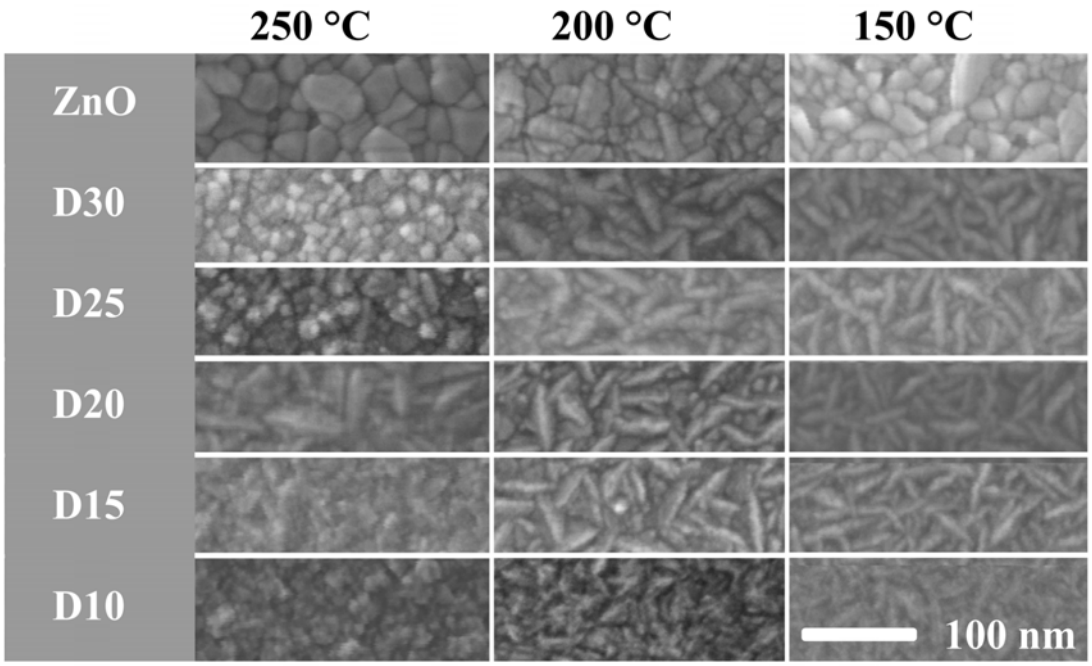

Figure 5.3: SEM investigation of surfaces morphology for samples with different doping levels and growth temperature.

[3]SEM Zeiss Supra 60VP [55]
[4]AFM, Icon PT from Bruker [168]

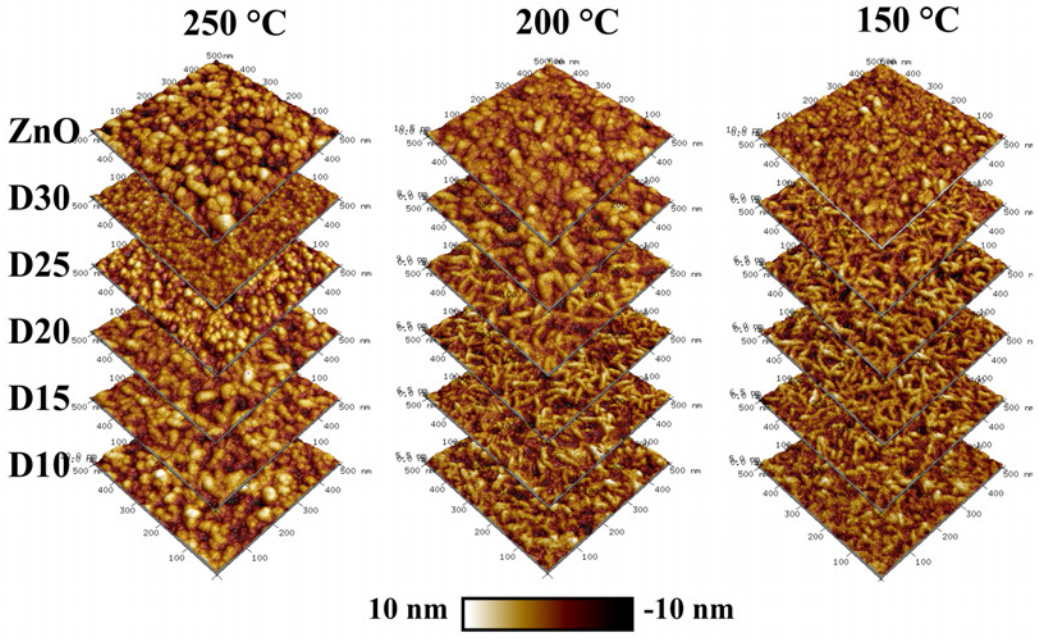

Figure 5.4: AFM investigation of surfaces morphology for samples with different doping levels and growth temperatures.

5.5 XRD Measurements

The crystal orientations have been studied by analyzing X-ray diffraction (XRD)[5] patters. θ-2θ scans were acquired in a Bragg-Brentano geometry with a Cu Kα X-ray source. The instrumental broadening was taken into account by performing a LaB_6 powder standard scan. The obtained scans were additionally checked for the alignment by controlling the corresponding position of the $Si(400)$ Kα_1 and Kβ peaks coming from the substrates.

XRD results are summarized in Figure 5.5. It is revealed that AZO films deposited at 250 $°C$ are polycrystalline films with preferential (002) orientation. Two main peaks have been found: (002) and weak (101), all other orientations were not observed in the range 2θ between 20 and 72. Figure 5.5 e) shows ZnO/AZO XRD obtained patterns at 250 $°C$.

A (100) peak is observed in the 150 $°C$ deposited films, where this orientation is preferential. In 150 $°C$ AZO films both (100) and (002) peaks are present. XRD results obtained at 150 $°C$ and 200 $°C$ are shown in Figure 5.5 a) and c). Finally the (100) orientation vanished at 250 $°C$ and is not observed in Figure 5.5 e). The

[5]Bruker D8 diffractometer [168], equipped with Göbbel mirror

noisy part from quasi-forbidden Si (200) reflections [169] has been removed from the scans.

The central positions of the orientation peaks move to higher 2θ values with increasing of Al concentrations in the films. When the concentration becomes too high (like in the case of D15 and D10 recipes processed at 250 $°C$), the films become amorphous (Figure 5.5 a). Characterization of the crystal structure is conducted by fitting the Lorentzian functions through the (002) and (101) peaks (Figure 5.6 a). According to the Bragg law:

$$n\lambda = 2d \sin\theta \tag{5.1}$$

The d-spacing of a ZnO Wurtzite crystal structure is related to the lattice parameters a and c by:

$$\frac{1}{d^2} = \frac{4}{3}\left(\frac{h^2 + hk + k^2}{a^2}\right) + \frac{l^2}{c^2} \tag{5.2}$$

Here, d is the interplanar distance, h, k and l are Miller indices. The lattice constants of hexagonal Wurtzite unit cell are given by a and c. In this case the (002) and (101) peaks were used to calculate lattice parameters. Figure 5.5 b), d) and f) show that the a parameter does not undergo any significant changes, while the constant c reduces from 5.20 Å (undoped ZnO) to 5.12 Å (D20) in an almost linear trend. The compression of the lattice constant c is due to the replacement of larger Zn^{2+} ions by smaller Al^{3+} ions (ionic radii 72 and 53 pm respectively). The Lorentzian fit through the measured peaks allows the estimation of corresponding grain sizes. The method mostly used is based on the Scherrer equation using either FWHM or integral breadth (area below the peak normalized by its height):

$$D = \frac{K\lambda}{\beta_{INT}\cos\theta}, \text{ where:} \tag{5.3}$$

$$\beta_{INT} = \beta_{observedINT} - \beta_{instrumentalINT} \tag{5.4}$$

Here, K is the Scherrer factor, λ is the wavelength of Cu Kα_1 radiation, θ is a Bragg angle and β_{INT} is the instrument corrected integral breadth, where $\beta_{observedINT}$ and $\beta_{instrumentalINT}$ are the corresponding integral breadth of an observed peak and instrumental correction respectively. The use of integral breadth leads to a more accurate estimation of grain sizes compared to the FWHM approach since it takes the Lorentzian tails of diffraction peaks into account [170]. However, additional factors responsible for peak broadening, such as microstrains, requires more rigorous deconvolution analysis with implementation of Pseudo-Voigt functions, which is a weighted superposition of Gaussian and Lorentzian

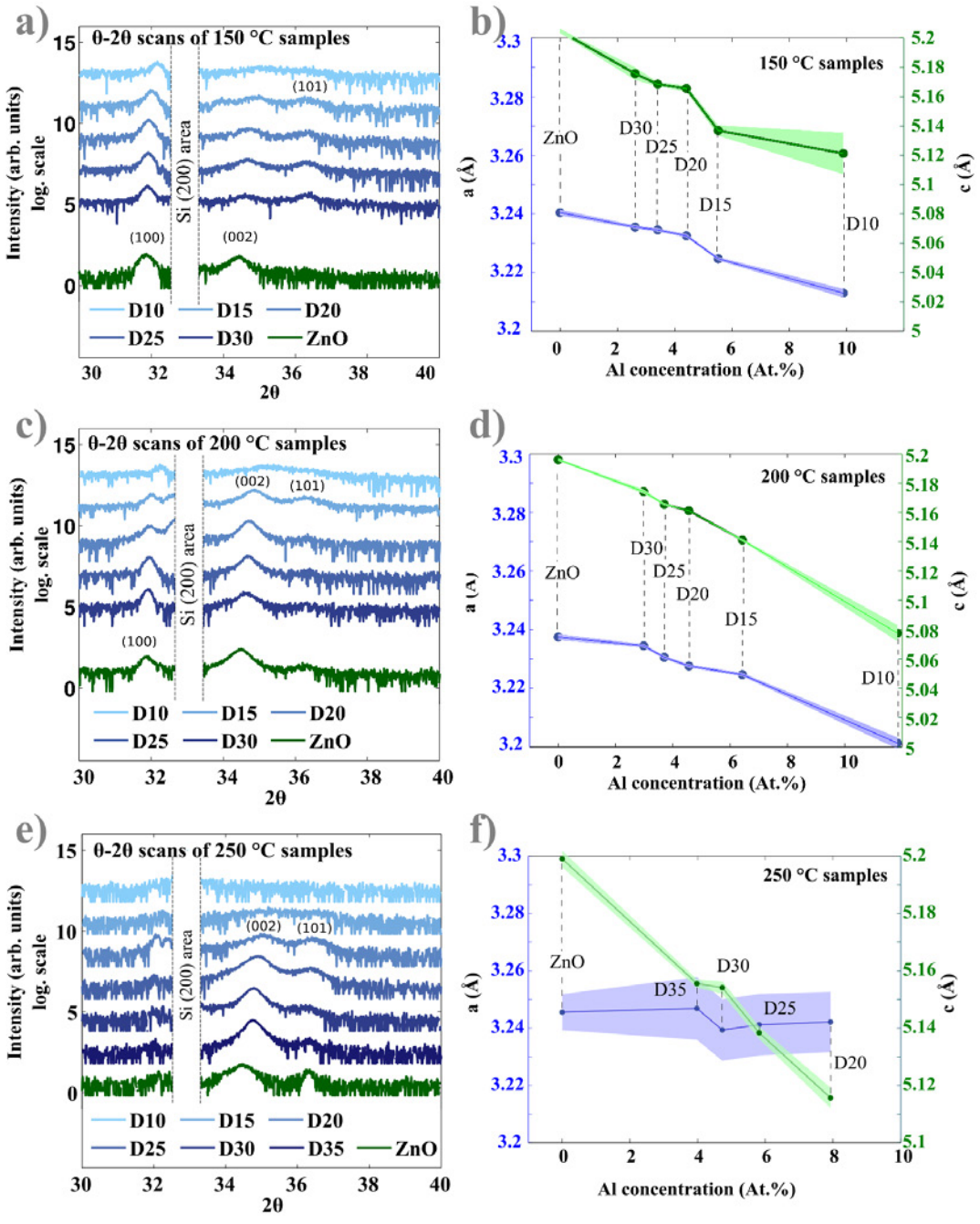

Figure 5.5: XRD analysis. a), b) and c) Diffraction patterns of all ZnO/AZO samples prepared at 150 °C, 200 °C and 250 °C respectively. b), d) and f) ZnO lattice dimensions constants a and c as a function of Al at. % concentration (150 °C, 200 °C and 250 °C, respectively).

contributions [170]. This goes above the scope of this research, since it will require a more intense X-ray source and better accrued statistics. Estimated grain sizes are presented in Figure 5.6 b) for all investigated temperatures. Grains with (002) orientations are 2-3 times smaller than corresponding (100) oriented grains. It seems that for AZO films the (002) grains becomes larger with increasing Al concentration, until 4 at.% of Al, then the grain size decreases. (101) oriented crystallites sizes were not calculated due to bigger uncertainties.

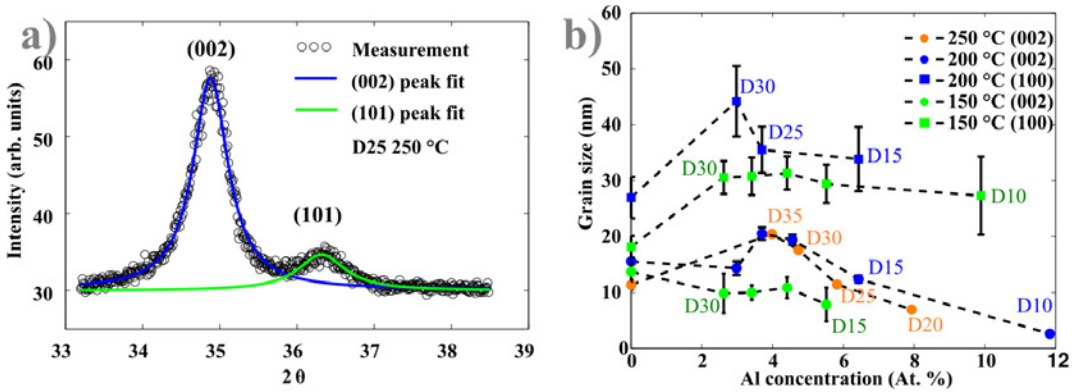

Figure 5.6: a) Typical area around (002) and (101) ZnO crystal orientations with applied Lorentzian fit function. b) Estimated grain sizes as a function of Al concentration in the samples (samples corresponding to all three deposition temperatures 150 $°C$, 200 $°C$ and 250 $°C$).

5.6 Electrical Properties

A conventional four-point probe[6] was used for resistivity measurements. A strong correlation between resistivity, Al concentration, and grain size has been found (see Figure 5.7). Undoped ZnO 100 nm films has a resistivity of 8 $m\Omega \cdot cm$, except ZnO grown at 250 $°C$. The high resistivity of this particular film is believed to be caused by an existence of small pores in the film. The existence of small pores around bigger ZnO clusters is visible in the SEM image in Figure 5.3.

For 100 nm thick AZO films the lowest resistivity of 1.3-1.4 $m\Omega \cdot cm$ is achieved at the Al doing level around 4 at.%. In general, the resistance of 150$°C$ prepared films are higher compared to 200 $°C$ and 250 $°C$ prepared films (Figure 5.7 a).

Figure 5.7 b) shows the dependencies between (002) and (100) grains sizes and resistivity. The general trend is that the larger the grains the lower the resistivity, which is observed for both orientations, regardless of growth temperature. Several

[6]Veeco FPP-5000

reports [156]-[159] suggest that the resistivity of AZO films strongly correlates with the degree of pronunciation of the (002) orientation. This work does not provide a direct prove of this concept. Indeed the AZO films grown at 250 $°C$ and without (100) orientation, has a strong tendency of reduced resistivity with increase of (002) grains (Figure 5.7 b). However, this tendency abbeys all grown films with both orientations. The larger the grains, the lower the resistivity.

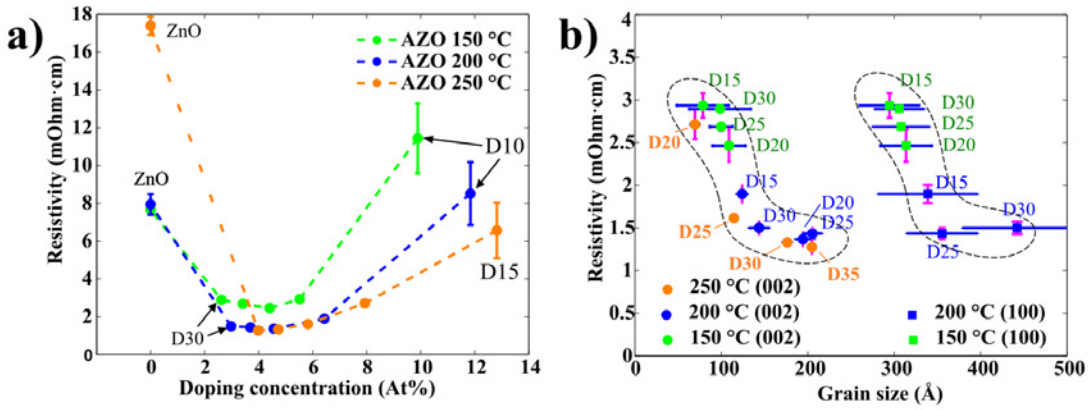

Figure 5.7: Resistivity of all prepared AZO/ZnO samples as a) function of Al at% concentration and b) Resistivity vs. grain sizes for AZO samples.

5.7 Optical Properties

The optical characterization of AZO films has been done using spectroscopic ellipsomtry[7]. Figure 5.8 illustrates the results for 100 nm AZO films grown at 250 $°C$ (results for 200 $°C$ and 150 $°C$ presented in Figures 5.9 and 5.10, respectively. In spectroscopic ellipsometry the parameters of amplitude component Ψ and phase difference Δ are measured over a certain wavelength range (in this case 210 - 1690 nm), where Ψ and Δ are defined by:

$$\frac{r_p}{r_s} = \tan(\Psi) \cdot e^{i\Delta} \tag{5.5}$$

where r_p and r_s are the reflection coefficients of p- and s- polarized light. The experimentally obtained values of Ψ and Δ were fitted using the Kramers-Kronig relation to get permittivity values. Figure 5.8 a) illustrates the real and imaginary part of the permittivity for ZnO and AZO films. It shows that the permittivity of AZO decreases rapidly with increasing wavelength, while the permittivity of

[7]Ellipsometer VASE from J.A. Woolam Co.

ZnO remains rather stable. Such results were very recently discussed [171],[172] in context to implementation of AZO films in plasmonic applications, where the permittivity crosses zero and becomes negative. The corresponding wavelength of this zero-crossing corresponds to plasma frequency ω_p. An observation of the plasmonic behavior of AZO films is above the equipment wavelength range, but the extrapolation of the Kramers-Kronig function can give a prediction of ω_p values, with the highest value of 166.44 THz (1800 nm) corresponding to a D25 250 $^{\circ}C$ and 147.8 THz (2020 nm) corresponding to a D20 200 $^{\circ}C$ AZO films. The coatings deposited at 150 $^{\circ}C$ temperature have sufficiently lower ω_p (Figure 5.10).

Figure 5.8 b) displays the transmission spectra for 100 nm AZO films grown at 250 $^{\circ}C$ on fused silica (quartz). In this experiment the ellipsometer was used in transmission mode, where the moving arms of the source and detector were placed at 90° to the surface normal. In the visible wavelength range, all of the films exhibit an average optical transmittance greater than 90%. The spectrum shows a sharp adsorption edge in the ultraviolet range, which shifts to the shorter wavelengths (blue shift), as the concentration of Al in the AZO samples increases. The adsorption edge can be used to estimate an optical bandgap of AZO thin films. Since ZnO is a direct bandgap semiconductor material, it can reasonably be assumed that the absorption coefficient α and the Tauc relationship [173] are given by:

$$\alpha \propto -ln(T) \tag{5.6}$$

$$(\alpha h\nu)^2 \propto (h\nu - E_g) \tag{5.7}$$

These relations are plotted in Figure 5.8 c) and d). The energy bandgap (E_g) can be obtained by plotting $(\alpha h\nu)^2$ vs $h\nu$ and linearly extrapolating the fit of the linear region to $\alpha = 0$ as shown in Figure 5.8 e. As it displayed in Figure 5.8 e), the higher the Al concentration in the film, the higher the optical bandgap. It can be explained by the increase of the carrier concentration which is caused by Al-doping. This widening of the optical bandgaps is generally attributed to the Burstein-Moss shift effect [174],[175].

5.8 Concluding Remarks

It has been shown that good control of AZO deposition can be achieved using ALD. The physical and optical material properties such as resistivity, permittivity and crystallinity can be strictly controlled by varying Al doping and deposition temperature. Precursors used for AZO ALD deposition is very common, chemically stable and widely available. The recipe presented in Table 5.1 allows deposition

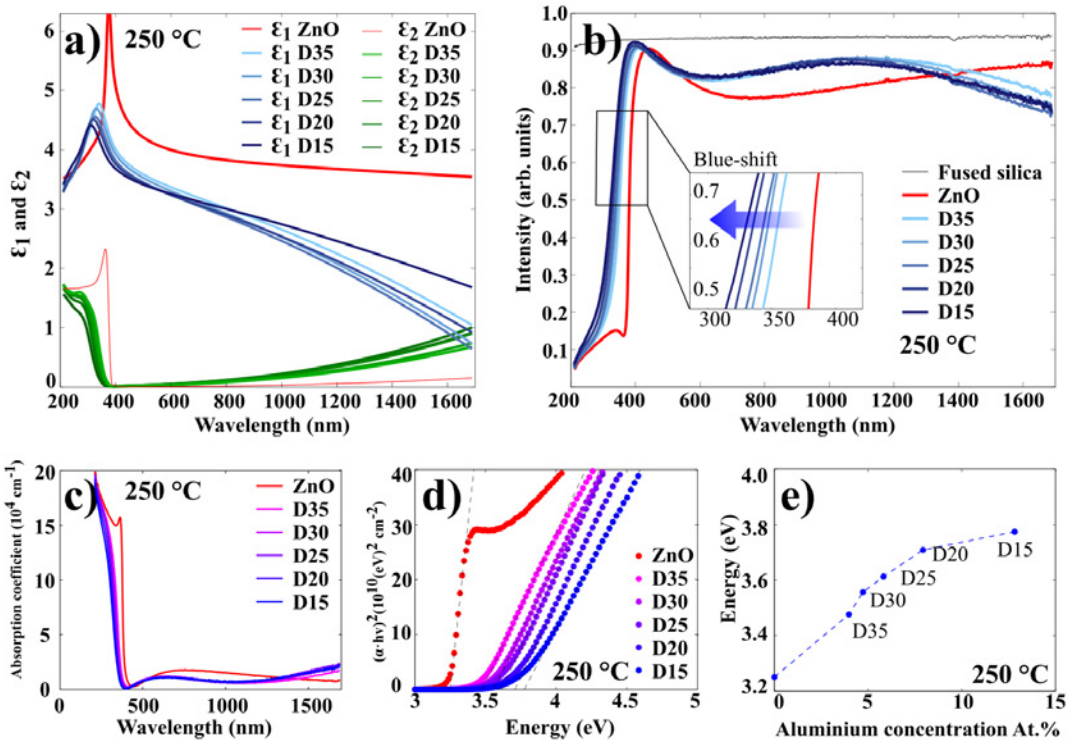

Figure 5.8: Optical properties of AZO/ZnO thin films deposited at 250 °C. a) Real ε_1 and imaginary ε_2 parts of the permittivity. b) Transmission spectra with a small absorption edge shift (shown in inset). c) Absorption coefficient. d) Plot of $(\alpha h\nu)^2$ versus photon energy (Tauc plot). e) Optical bandgap as a function of Al concentration.

on high aspect ratio structures. The most important feature here is the metallic behavior at the higher wavelength range. The extrapolation of fitted permittivities presented in Figures 5.8-5.10 results in a omega cross-over ω_p at 1800-2000 nm for D25 250 °C and D20 200 °C AZO films. The plasmonic nature of AZO at the mid-infrared range, together with the ability to pattern structures as one and two dimensional lattices using several dry etch techniques, can be directly implemented to fabrication of HMMs.

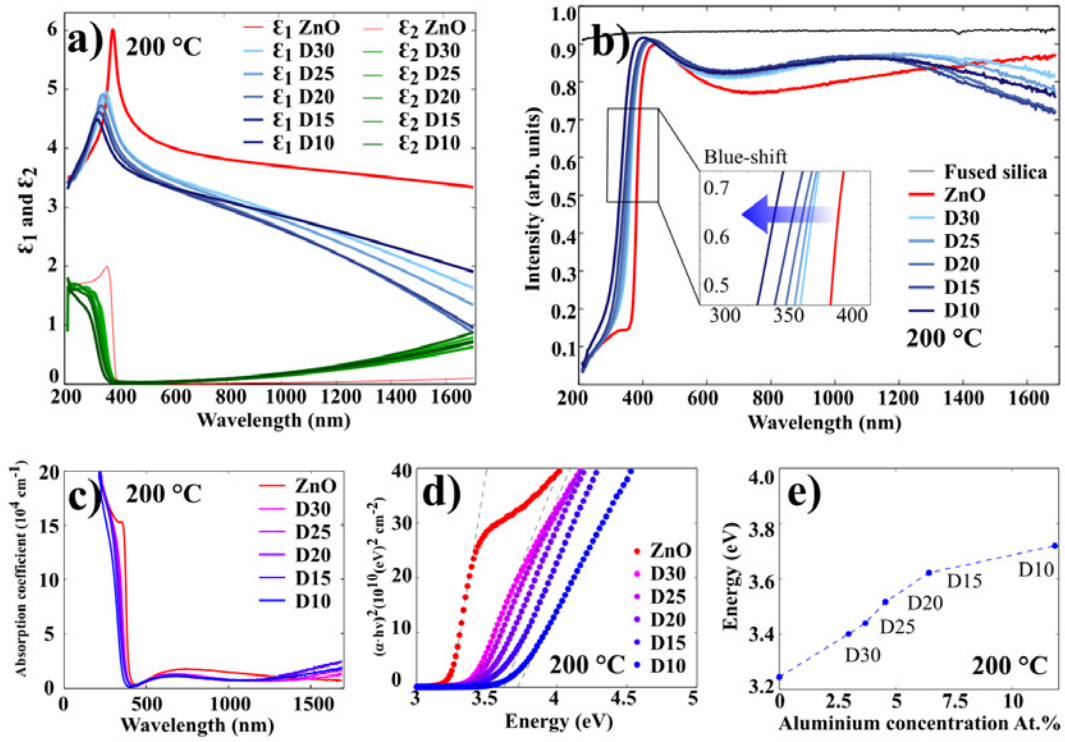

Figure 5.9: Optical properties of AZO/ZnO thin films deposited at 200 °C.

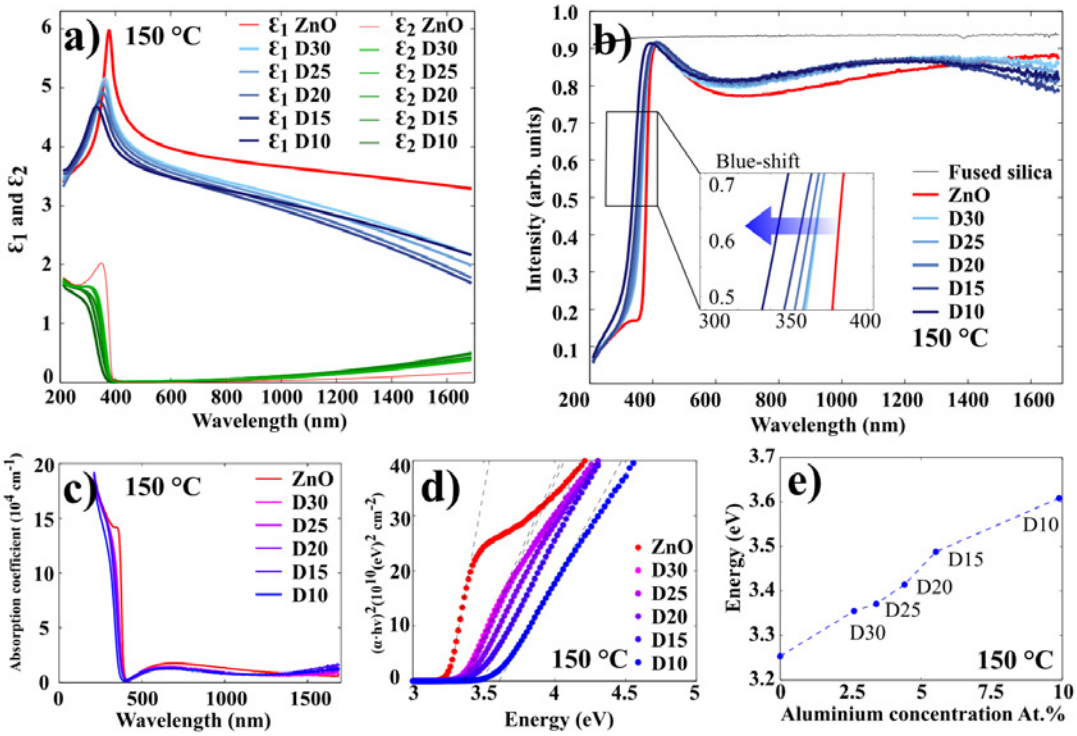

Figure 5.10: Optical properties of AZO/ZnO thin films deposited at 150 °C.

CHAPTER 6

FABRICATION OF HYPERBOLIC METAMATERIALS BASED ON *Al*-DOPED *ZnO* PLASMONIC STRUCTURES

Nanoscale realization of one- and two- dimensional high aspect ratio structures based on Al_2O3 and TiO_2 with precisely controlled shape and profile depth have been successfully tested. The successful deposition of AZO thin films with stable growth rate, predicted chemical composition, and controlled film morphology provides realization of coatings with plasmonic properties.

The last step is applying the high aspect ratio fabrication scheme on the AZO material platform to form hyperbolic metamaterials (HMMs) with different geometry. Since the plasma frequency ω_p, of ALD deposited AZO films corresponds to a wavelength of approximately 2 μm, the realized HMMs will be operational in the mid-infrared range. This regime do not receive as much attention, as the visible light but, still has its own advantages.

The chapter describes the fabrication procedure and optical performance of two types of HMM geometries: vertically arranged multilayer stack and array of pillars. The entire optical characterization of fabricated HMMs and data analysis has been performed by the other research members of DTU Fotonik Metamaterial group.

6.1 Plasmonics in Mid-Infrared Region

Plasmonics in the mid-infrared regime offer various unique applications such as thermal imaging and bio chemo-sensing applications [176]-[177]. Especially, mid-infrared spectroscopy in the wavelength range of 2.5-25 μm (4,000 cm^{-1} to 400 cm^{-1}) provides specific chemical and compositional molecular information in the gas, liquid and solid phases owing to molecules' vibrational and rotational absorption bands, thus enabling a wide variety of sensing applications in industrial production monitoring, materials science, biotechnology, detection of toxic gas and liquid, environmental analysis, medicine, and medical diagnostics [178]. Traditionally noble metals are used as plasmonic materials due to their abundant free electrons in the conduction band. However, their large real and imaginary parts of the permittivity, especially in the infrared range, result in high loss and weak confinement to the surface. Therefore the exploration for alternative plasmonic materials suitable for a certain wavelength range in the vast mid-infrared region has been the focus of research in last several years for mid-infrared plasmonics. Consequently, various types of alternative plasmonic materials have been investigated: transparent conductive oxides [21],[179], heavily doped III-V semiconductors [180],[181] polar materials [182], 2D materials (graphene, hBN, etc.) [183],[12], and CdO [184] have been studied because of their plasmonic properties. Each group of alternatives has its own preferential operating wavelength regime due to the available free carrier concentrations and mobilities. Doped semiconductors, such as Ge [180],[185], GaAs [180], Si [186],[187], InAs [188], InGaAsBi [189] and InP [181] have been investigated for their plasmonic properties and their tunability by controlling the doping level. AZO also benefits from its tunability of plasmonic properties that can be achieved by adjusting the doping level as it was shown in Chapter 5. The realization of AZO-based HMMs would require the deep reactive ion etching (DRIE) patterning procedure (see Chapter 4) realized in case of Al_2O_3 and TiO_2 nanostructures.

6.2 HMMs Based on AZO Trenches

The first HMM structure is based on AZO/dielectric structures with multiple high aspect ratio multilayers. The 1D HMM multilayer model is depicted in Figure 1.3 a) of Chapter 1. The dielectric component in the HMMs is chosen to be either Si or ambient air. The main difference will be a slightly different geometry, it will not be based on a simple repeated stack of flat layers, but rather a vertical arrangement of those. It can be considered as a flat 1D multilayer turned 90°, it will however by no means affect the permittivity tensor of the material. The fabrication of these structures starts with the preparation of a Si template.

		Passivation (1.5 s.)	Etching (2.5 s.)
Process gas flow (sccm)	C_4F_8	50	20
	SF_6		60
	O_2		5
Powers (W)	Coil	600	400
	Platen		40

Table 6.1: DRIE parameters for Si trench fabrication. Slightly overetch process result a positive slope with $\alpha = 0.5°$. Process temperature is 0 $°C$ and pressure 10 mTorr

6.2.1 DRIE Challenges

The realized Si grating template described in Chapter 4 and presented in Figure 4.2 a) possess several disadvantages. The top part of the produced TiO_2 and Al_2O_3 grating lamina suffers from an outward bending due to the built-in stress, initial surface roughness and defects in DRIE prepared template. One of the most distinct features of DRIE is the scalloping of the sidewalls of the etched features (visible in Figure 4.2 a). It results from the cyclic nature of the Bosch process.

The etching profile can be improved by adjusting the process recipe. The DRIE etching process is based on a switched Bosch process [124] consisting of cyclic steps of etching and passivation. Typically, a mixture of two gases is used. One of the gases forms a uniform protecting layer all over the sample including the sidewalls of already etched cavities, which inhibits spontaneous chemical etching. The other gas supplies the radical species. An applied wafer bias results in a continuous ion bombardment normal to the wafer surface causing directional sputtering, leaving vertical sidewalls essentially unaffected. Thus, the protecting layer is locally removed, thereby enabling chemical etching by the radical etching species. Since the sidewalls remain protected the etching pursues normal to the wafer surface. A typical gas used for etching silicon is SF_6 and the protecting gas may be O_2 or a fluorocarbon such as C_4F_8 or combination of both. In a switched process the deposition of the protecting layer, the local sputtering of this layer and the etching are separated in time.

Many parameters control the Bosh process including coil and platen powers, gases flow rates, chamber pressure, temperature, cycle time etc. It is clear that optimizing the Bosch processes can be done in many ways. Reducing the cycle time is a very convenient way of reducing scallops. The faster the process switches between the etch and passivation, the smaller the scallops will be. However, at

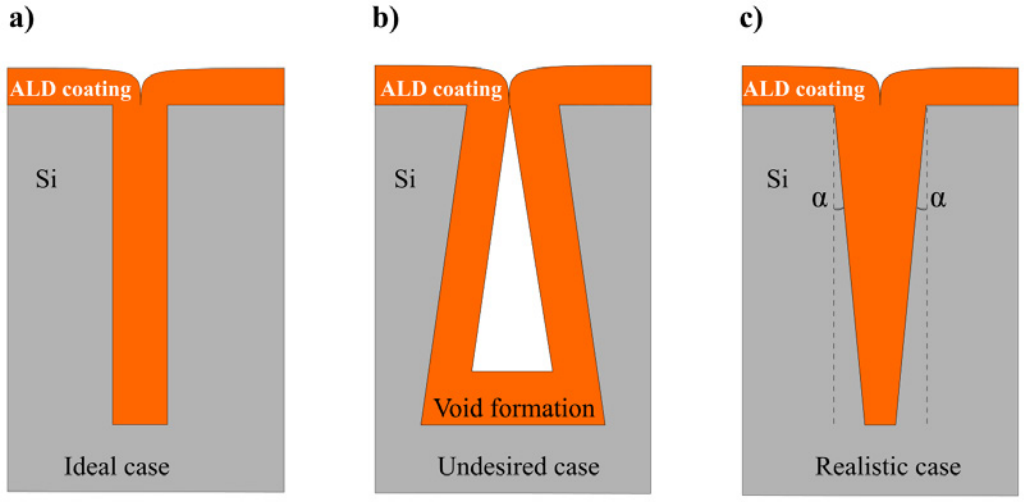

Figure 6.1: Trench profiling. a) Ideal case with straight walls, which is hard to realize in reality. b) The trench gets wider, normally due to overetching also known as negative or retrograde profile. c) Optimal case caused by a slightly overpassivated DRIE etching process, known as a positive or sloped profile.

some point the hardware cannot keep up with the demand, and the process will then be continuous causing the Bosch process to break down. Figure 6.1 illustrates three typical output profiles. If the recipe is perfectly tuned, one would approach the profile illustrated in Figure 6.1 a). Such a profile is hard to realize in reality, and during ALD deposition, the coating would unlikely fill the entire template due to unavoidable initial imperfections.

If process has a prolonged etch time the profile becomes negative (Figure 6.1 b), meaning that the width of the trench starts to get broader (scanning electron microscopy (SEM)[1] image shown in Figure 6.2 a). Such profile is highly undesirable, since the ALD coating closes on top and forms a void inside the trench.

In case of passivation cycle getting too long, the profile becomes positive (sloped) as it shown on Figure 6.1 c) (SEM image presented on Figure 6.2 c). Such profile is suitable for ALD filling and structure manufacturing if the tilted angle α is as low as possible.

Three parameters were adjusted in order to optimize the produced Si template: process temperature, cycle time for passivation and etching. The optimized results are summarized in Table 6.1 and Full SEM image depicted in Figure 6.2. The process pressure was 10 mTorr. No scallops are observed at the top part of the

[1]SEM Zeiss Supra 60VP [55]

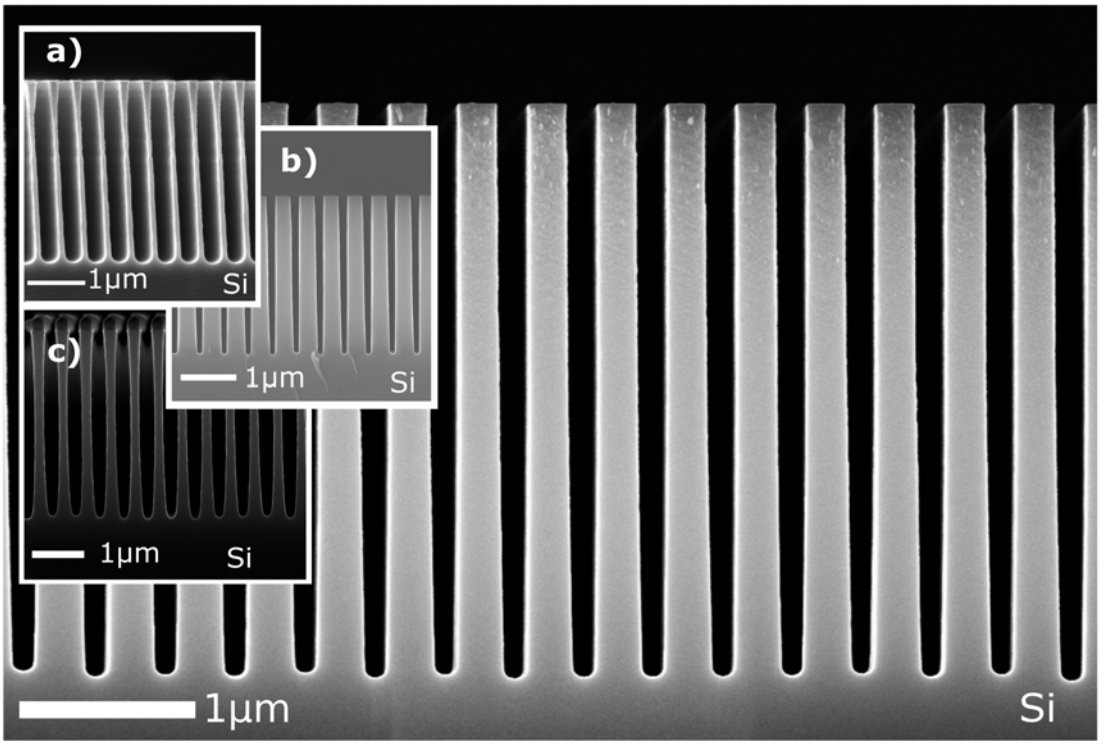

Figure 6.2: SEM image of *Si* template optimized for HMM trench production. The insets show badly designed templates: a) overetched b) overpassivated and c) both etch and passivation parameters are wrongly chosen.

produced *Si* template. Any change of the parameters would lead to a deviation from the presented result. However, a caution needs to be taken before generalizing this recipe. In the three years of thesis work, several incidents caused major process drifts. For example a showerhead, which sits on the top of the plasma source and intended to distribute the process gases uniformly in the DRIE chamber, so that a uniform etch process is achieved, has been changed which leading to various necessary adjustments of recipes.

6.2.2 Fabrication Flow

In the case of 1D multitrench HMM structure, it was found that the scheme described in Chapter 4 Figure 4.1 works very well for the AZO deposition with minor modifications.

DUV and DRIE

First, standard double side polished $Si(100)$ wafers were selected and RCA cleaned. A convential Deep-UV lithography (DUV)[2]) was used for defining the grating patterns (lines 200 nm wide and 400 nm pitch) on 2x2 cm scale chips. To promote photoresist adhesion and to minimize interference effects, the substrate surface was coated with a 65 nm thick bottom anti-reflective coating (BARC) coating (DUV42S-6, Brewer Science, USA) followed by a bake-out at 175 $°C$ for 60 s. The positive photoresist (KRF M230Y, JSR Micro, NV) was spin-coated to a thickness of 360 nm and baked at 130 $°C$ for 90 s. Thereafter, deep reactive ion etching (DRIE)[3] was used to etch trenches in the silicon substrate with a depth of 3 μm. The recipe is presented in Table 6.1. The last step of Si template fabrication is removal of the remaining resist. This was done by use of O_2 plasma for 2 min with a gas flow of 100 sccm. The coil and platen powers were 800 and 20 W, respectively. The scheme of the template and SEM images of the resulting Si template are shown in Figure 6.3 a).

ALD of AZO

The AZO coatings were made in a thermal, hot-wall ALD system[4]. Precursors were obtained from Strem Chemicals. ZnO was deposited using diethylzinc ($Zn(C_2H_5)_2$, DEZ) and deionized water (H_2O), whereas Al doping of the ZnO has been introduced by a single cycle of trimethylaluminium ($Al(CH_3)_3$, TMA) and H_2O into a ZnO matrix made by 20 cycles of "DEZ +H_2O". This defines an AZO macrocycle: 19 cycles of "DEZ+H_2O" and one cycle of "TMA+H_2O". The deposition temperature was kept constant at 200 $°C$. ALD recipe for deposition of one AZO macrocycle on the Si trench template structures is presented in Chapter 5, Table 5.1. Hence, the used recipe is D20, 200 $°C$. The deposition results are visualized in Figure 6.3 b). Approximately 55 AZO macrocycles needs to be deposited in order to fill the Si trench template entirely. For more details of the peculiar properties of AZO thin films the reader is referred to Chapter 5.

[2]Canon FPA-3000 EX4 DUV stepper
[3]DRIE Pegasus from SPTS [125]
[4]Picosun R200 Thermal tool [53]

Top Layer Removal and Selective Si Etching

In order to remove the deposited top layer of AZO and to gain access to the Si template core, a pure physical etching with Ar^+ ions[5] was done. Here, the process was tuned to an etch rate of 20 nm/min which provided a well-controlled top layer breakthrough (see Figure 6.3 c). Following this, the subsequent selective silicon etching (template removal) was done using a continuous isotropic etch in a reactive ion etching tool[6] based on SF_6 at a substrate temperature of 20 $°C$. The SF_6 gas flow was kept constant at 35 sccm and the process pressure was 80 mTorr. The coil power was 30 W. This etching process proceeds with an extreme selectivity to the deposited AZO without any observable harm on the prepared AZO grating structure.

Controlling the time is the most essential issue, since a prolongation of the etching will results in the collapse of the AZO gratings. 18 min of etching was required to fabricate free-standing, separated AZO gratings with a minimal amount of the Si core between the AZO lamellas, which is eventually needed to support the grating skeleton (SEM image in Figure 6.3 d). Moreover, since the etch rate is approximately 165 nm/min one can, in principle, decide the etching depth with an accuracy of 5-10 nm, equivalent to 2-4 seconds error in the etching time.

The fabricated AZO/Si and AZO/Air trench structures comprise the AZO lamellas with thickness of 200 nm and height of 3μm. Each lamella was separated from the neighbor by 200 nm Si or Air depending of the output HMM structure. The whole sample had a dimensions of 2x2 cm. The produced samples have been delivered to the group collaborators for optical investigations, in order to prove the existence of hyperbolic behavior.

[5]Ionfab 300 plus from Oxford Instruments [150]
[6]RIE, from SPTS

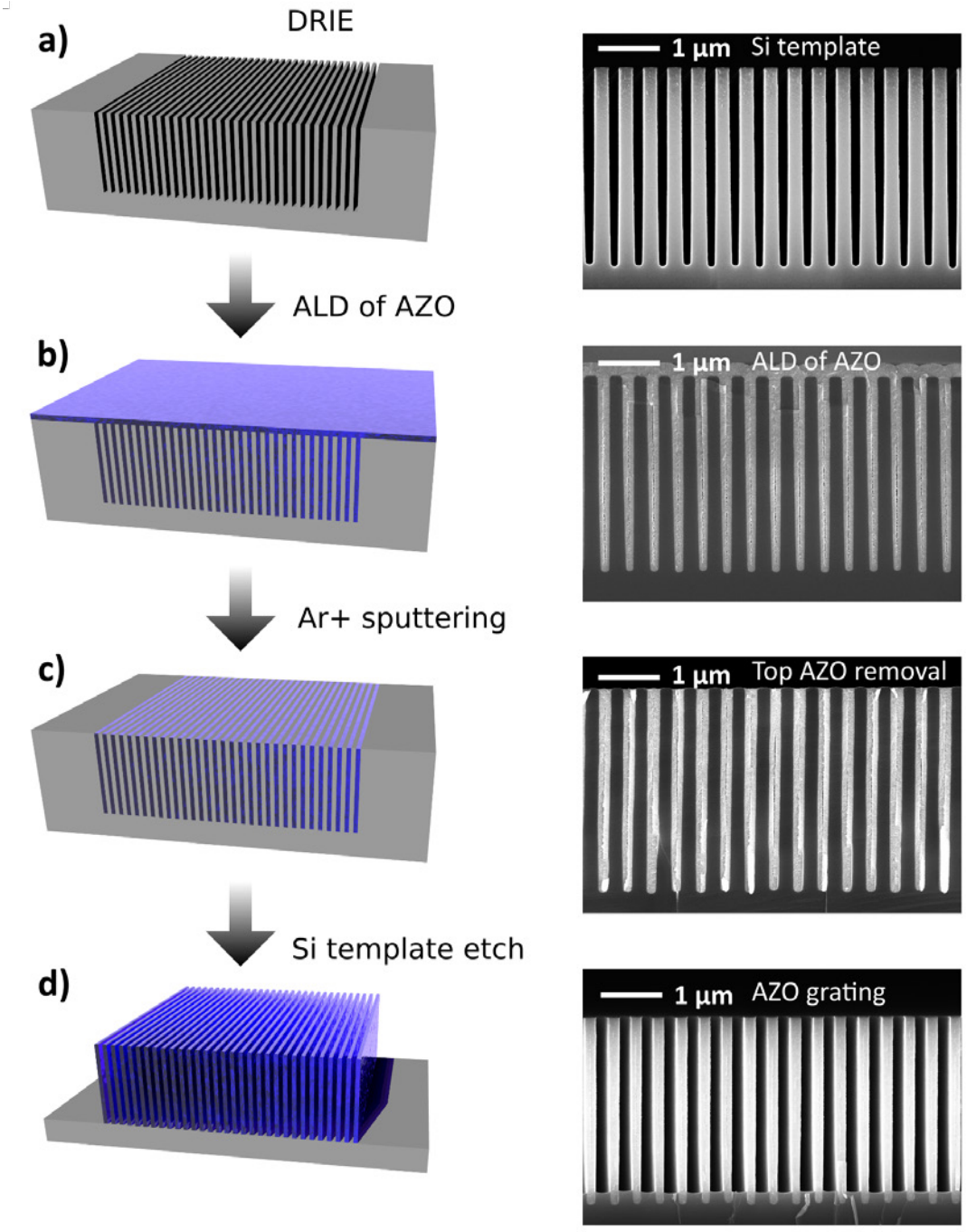

Figure 6.3: Fabrication flow for AZO structures with high aspect ratio nanotrenches. Schematics with corresponding SEM images. a) Initial Si template after DRIE etching. b) ALD of AZO D20 200 $°C$. c) Ar^+ sputtering (top AZO removal), and d) Si template removal.

6.2.3 Optical Characterization of AZO Trench Hyperbolic Metamaterials

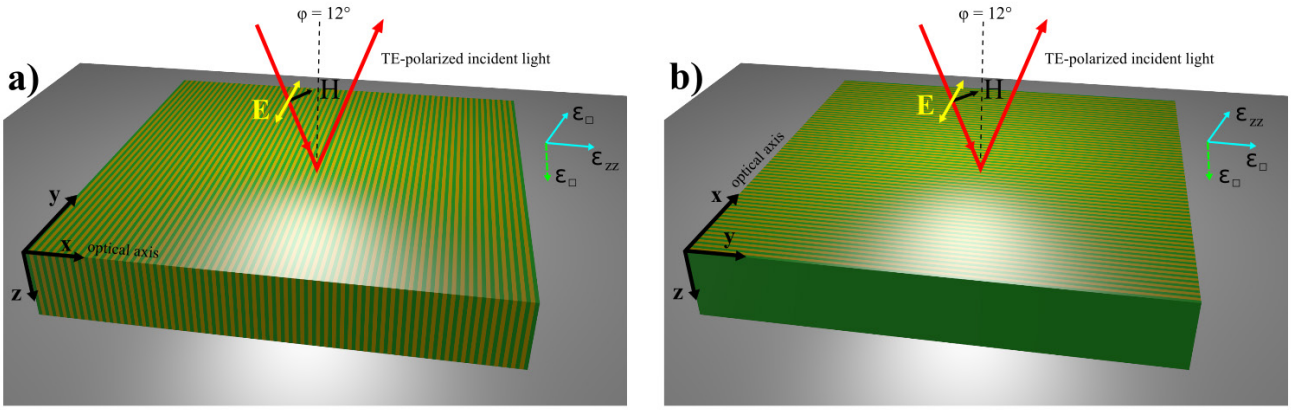

Figure 6.4: Configuration of AZO trench HMM. a) The sample is aligned so the **E** field of incident TE-polarized light, is parallel to the trenches. Configuration is suitable for recovery of ordinary permittivity ε_o. b) The sample is 90° rotated with respect to the previous case. Now, the **E** field of incident light is perpendicular to trenches, allows the measurement of extraordinary dielectric function ε_e.

The permittivity equations of flat multilayer system are valid in vertically arranged multilayer structures, if the switch of the $\{x, y, z\}$ axis is taken into account. The AZO trench HMM geometry is presented in Figure 6.4. The effective uniaxial permittivity tensor is defined by $\varepsilon_{y,z} = \varepsilon_\square = \varepsilon_o$ and $\varepsilon_x = \varepsilon_{zz} = \varepsilon_e$, where ε_o and ε_e are the effective ordinary and extraordinary permittivities, respectively. Lets represent here the previously derived equations 1.23 and 1.26 from Chapter 1 once more. According to the Effective Medium Theory (EMT) the ordinary and extraordinary permittivities in trench case, are given by:

$$\varepsilon_o = \varepsilon_\square = p_m \varepsilon_m + p_d \varepsilon_d$$

$$\varepsilon_e = \frac{\varepsilon_m \varepsilon_d}{p_d \varepsilon_m + p_m \varepsilon_d}$$

Finding these dielectric functions will require a knowledge about frequency dependent permittivity values of dielectric and metallic components.

Permittivities of the 100 nm AZO thin films and *Si* (acts as a dielectric in HMMs) can be found experimentally. The procedure is based on collection and

j	1	2	3	4	5
S_j	0.000389	0.000618	$9.81 \cdot 10^{-5}$	0.000136	$2.72 \cdot 10^{-5}$
Γ_j (THz)	3.07	1.468	1.37	2.97	0.72
$\omega_{f,j}$ (THz)	15.24	18.32	22.396	26.69	33.18

Table 6.2: Retrieved dielectric function parameters for Si.

	γ (THz)	ω_p (THz)	ε_∞
DEZ D20 200 $°C$	35.00	147.8	3.45
DEZ D25 250 $°C$	40.73	166.4	3.45

Table 6.3: Retrieved dielectric function parameters for AZO D20 200 $°C$ (used as plasmonic component in AZO trench HMMs) and AZO D25 250 $°C$ (used as plasmonic component in AZO pillar HMMs).

analyzing of the reflection spectrum using the fourier transform infrared spectroscopy (FTIR) technique. The measurements was conducted for a wavelength range of $\lambda = 1.428 - 25.0\ \mu m$. The obtained reflectance spectrum[7] was fitted using the Drude-Lorentz model in order to retrieve the parameters of the dielectric functions. According to this model the permittivity function is:

$$\varepsilon(\omega) = \varepsilon_\infty \left(1 - \frac{\omega_p^2}{\omega^2 + i\omega\gamma}\right) + \sum_j \frac{S_j \omega_{f,j}^2}{\omega_{f,j}^2 - \omega^2 - i\omega\Gamma_j} \tag{6.1}$$

where ε_∞, ω_p, and γ are the high-frequency dielectric constant, plasma frequency and electrons plasma damping, respectively. S_j, $\omega_{f,j}$, and Γ_j are the strength, resonance frequency and damping for the j^{th} Lorentzian oscillator, respectively. The measurement was conducted on five different points on each sample so that an efficient statistics was achieved and the error bars were considered in the curve fitting algorithm which is based on the Levenberg-Marquardt method [190].

100 nm AZO Film, and Si Material Permittivity in the Mid-Infrared Range

In case of the plain AZO film, only the Drude part of equation 6.1, and in the case of Si substrate, only the Lorentzian terms of the dielectric function were used.

[7] by using a VERTEX 70 FTIR spectrometer from Bruker [168]

	S_1	S_2	Γ_1 (THz)	Γ_2 (THz)	$\omega_{f,1}$ (THz)	$\omega_{f,2}$ (THz)	γ (THz)	ω_p (THz)	ε_∞ (THz)
AZO in Si ε_o	0.2300	50.2000	4.44	2.87	32.43	7.24	66.02	67.81	8.88
AZO in Si ε_e	16.7400	5.7400	76.79	15.84	69.93	31.43	-	-	4.63
AZO in Air ε_o	7.1800	-	103.51	-	47.20	-	16.06	84.24	1.60
AZO in Air ε_e	0.2830	0.0136	40.00	9.05	134.63	43.17	-	-	1.24

Table 6.4: Retrieved ordinary ε_o and extraordinary ε_e dielectric function parameters of AZO trench HMMs.

In order to find the optical properties of the AZO D20 200 $°C$ (used in trench geometry) and AZO D25 250 $°C$ (used in pillar geometry) films, the 500 μm thick double side polished (100) Si substrate, on top of which the films were deposited, needs to be characterized. Si is transparent in the mid-infrafed range, so the spectrometer sample holder's mirror and the airgap below the samples had to be considered in the fitting. Five Lorentzian terms together with ε_∞ were used as the dielectric function of silicon substrate. Figure 6.5 a) shows the measured reflectance spectrum together with the fitted function and Table 6.6 summarizes the fitted parameters for Si. The dips in reflection curves at around 11 and 16.5 μm originate from the absorption in silicon, and dips at 9 and 13.5 μm comes from the native SiO_2 that grows on the Si surface [191]. The fitted value for ε_∞ was 12.04. Figure 6.5 b) shows the real and imaginary parts of the Si permittivity. Although, the dispersion of Si is very limited in this wavelength range, it have to be taken into account. The thickness of the airgap below the sample was also fitted and found to be around 8 μm.

Using the retrieved permittivity for the substrate, the curve fitting procedure was done for the 100 nm thick AZO D20 200 $°C$ and AZO D25 250 $°C$ films, considering Drude dielectric function for AZO. Figure 6.5 c) and e) shows the measured reflectance spectrum together with the fitted curve for the AZO films and Figure 6.5 d) and f) represents corresponding dielectric permittivities. Table 6.3 shows the retrieved parameters of the Drude model.

Ordinary and Extraordinary Permittivity of AZO/Si and AZO/Air Trench Structures

The very important factor is that the ordinary and extraordinary permittivities (ε_o and ε_e) for the HMMs trench structures in air and in Si can also be determined directly by FTIR and compared with EMT results.

In this approach, intensity transfer matrix method was used to calculate the normal incidence reflectance spectra of the metamaterial/substrate system. Using this method the Fabry-Perot interference fringes from the metamaterial structure or the AZO film will be retained, whereas the fringes from the substrate will cancel [192].

In order to find ε_o and ε_e, reflectance spectra from the samples were measured at 12 ° angle of incidence using a TE-polarized light with the sample placed such that the electric field **E** was parallel or perpendicular to the trench layers respectively. After finishing the measurement of reflection for the ordinary case, the sample was simply rotated 90 ° and the next measurement with TE-incident light would acquire the information for the extraordinary configuration. Both cases are shown on Figure 6.4. Following parameters have been used in order to retrieve ε_o and ε_e permittivities:

- Drude-Lorentz dielectric function with two Lorentzian terms was used to model the ordinary permittivity of the AZO trench structure in Si (AZO/Si). Figure 6.6 a) shows the measured and fitted reflectance spectrum for this case. Figure 6.6 b) shows the real and imaginary parts of ε_o for AZO/Si structure as solid lines.

- Two Lorentzian terms together with ε_∞ were implemented for the extraordinary permittivity of the AZO/Si trench structure. Measured reflectance spectrum together with the fitted curve are presented in Figure 6.6 c). Retrieved permittivity is depicted on Figure 6.6 d).

- Drude-Lorentz dielectric function with one Lorentzian term was used to retrieve the ordinary permittivity of the AZO trench structure in air (AZO/Air) trench structure. Figure 6.6 e) shows the measured and fitted reflectance spectrum for this case. Corresponding permittivities presented in Figure 6.6 f).

- Two Lorentzians together with ε_∞ were implemented to describe the extraordinary permittivity of the AZO/Air trench structure. The measured and the fitted reflectance spectra for this case are illustrated in Figure 6.6 g). The absorption dips originating from the Si substrate are observed at around 9, 11, 13.5 and 16.5 μm and the features below 3 μm are attributed

to Fabry-Perot oscillations. The corresponding permittivities are given by Figure 6.6 h).

EMT theory allows to estimate ordinary ε_o and extraordinary ε_e permittivities for both AZO/Si and AZO/Air cases using equations 1.23 and 1.26 where dielectric function ε_d for Si and dielectric function of metal component ε_m (AZO) are given by Drude-Lorentz model with parameters presented in Tables 6.6 and 6.3. Permittivity of air assumed to be equal 1 with zero loss. The ε_o and extraordinary ε_e results of EMT is plotted (dashed lines) together with FTIR delivered permittivities (solid lines) in Figure 6.6 b), d), f) and h). Generally, there are good agrement between those two approaches.

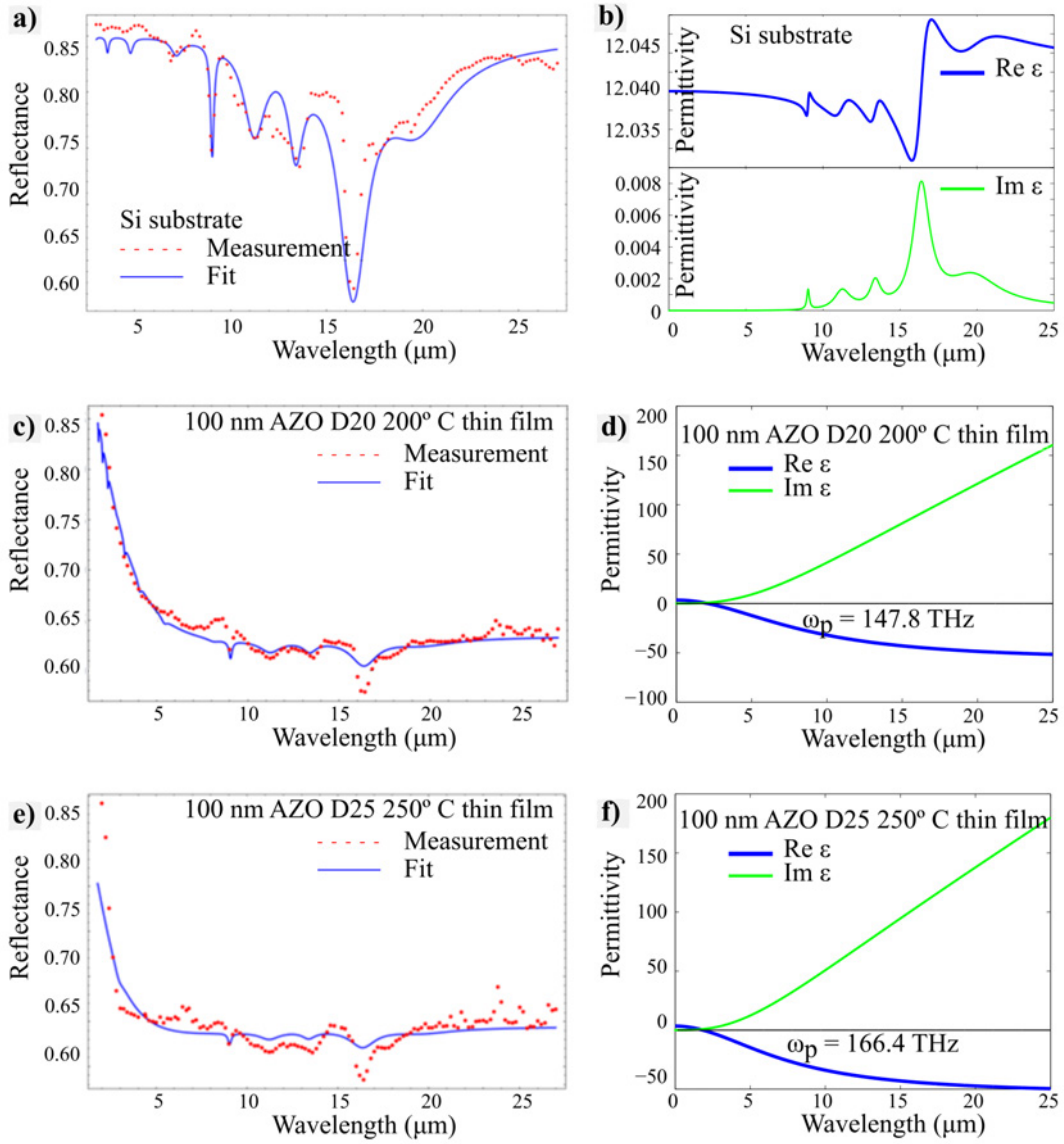

Figure 6.5: Material permittivities. a) Measured and fitted reflectance spectra for the *Si* substrate. b) Calculated permittivities based on Lorentziasn functions of the Drude-Lorentz model. c) Measured and fitted reflectance from AZO D20 200 °*C* thin film. d) Calculated permittivities using the Drude model. e) and f) Reflectance and permittivity for the AZO D25 250 °*C* thin film.

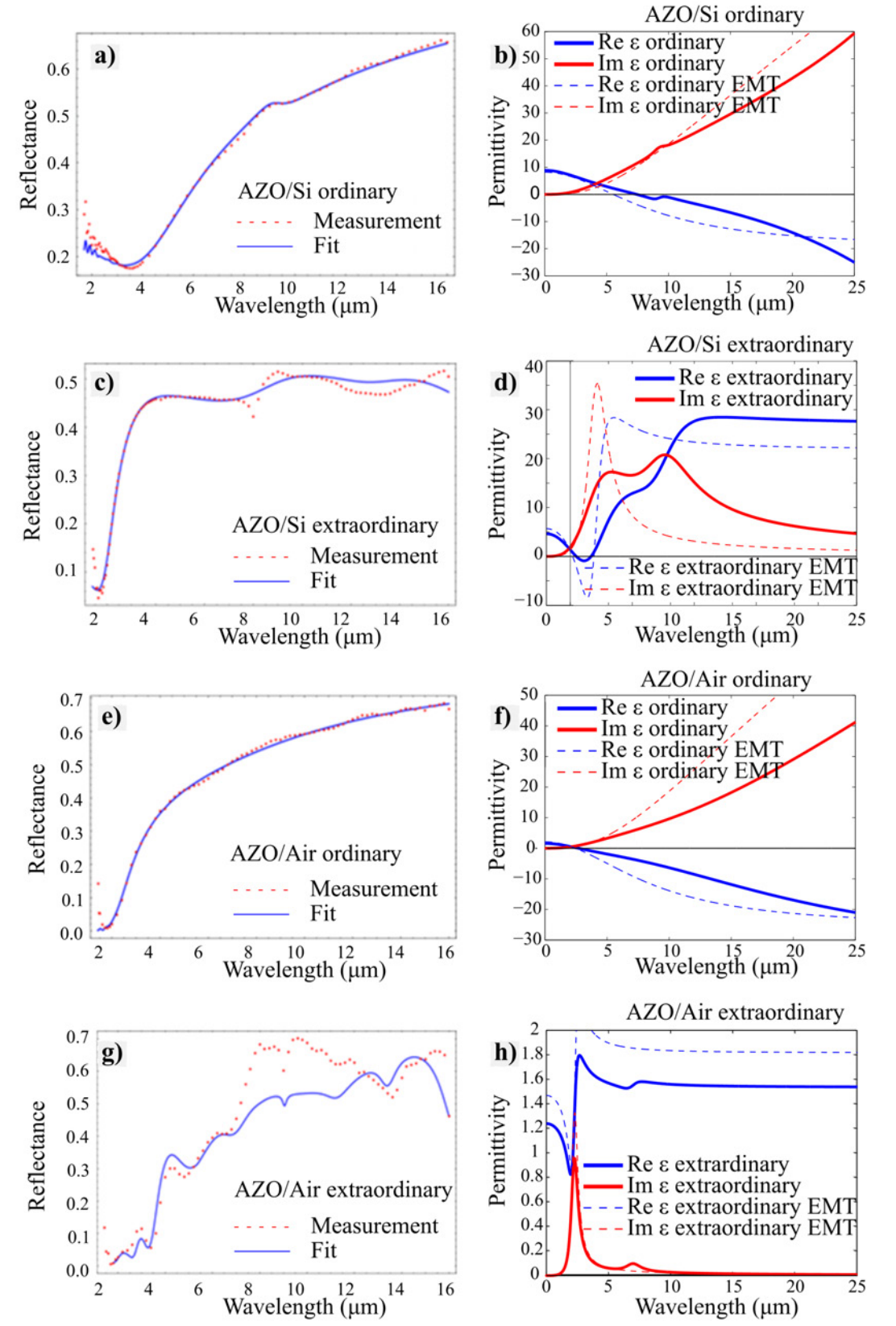

Figure 6.6: FTIR measured and fitted reflection spectra and corresponding retrieved permittivities, together with EMT derived dielectric functions. a) and b) AZO/Si ordinary. c) and d) AZO/Si extraordinary. e) and f) AZO/Air ordinary. g) and h) AZO/Air extraordinary.

6.3 General Remarks

Two types of AZO trench HMMs have been fabricated: AZO/Si trench and AZO/Air trench structures. In the case of AZO/Si, the ordinary permittivity ε_o becomes negative at a wavelength of $\lambda > 7.45$ μm, while the extraordinary permittivity ε_e remains positive, which means that the system moves into the hyperbolic regime of Type II as presented in Figure 6.7 a). Additionally, an interesting regime exists in the wavelength range between $\lambda = 2.4$ μm and $\lambda = 3.6$ μm, here the opposite situation occurs. The ordinary permittivity is positive, while the extraordinary becomes negative. It can be interpreted as the existence of Type I hyperbolic regime. However, the extraordinary dielectric function never becomes very negative, and taken losses into account, it will possibly diminish any hyperbolic performance. Nevertheless, the region is excellent for epsilon-near-zero (ENZ) applications [18],[193]. A cross-sectional SEM image of HMM sample is shown on Figure 6.7 b).

AZO/Air HMMs originate from the previous sample. The Si matrix of the structure needs to be removed using continuous dry etch process, based on SF_6 plasma chemistry as it illustrated in Figure 6.3 d). The fabricated metamaterial becomes Type II hyperbolic at a wavelength of $\lambda > 2.71$ μm. SEM image of the sample cross-section is shown in Figure 6.8. Si etching was very uniform across the sample, which has dimensions of 2x2 cm.

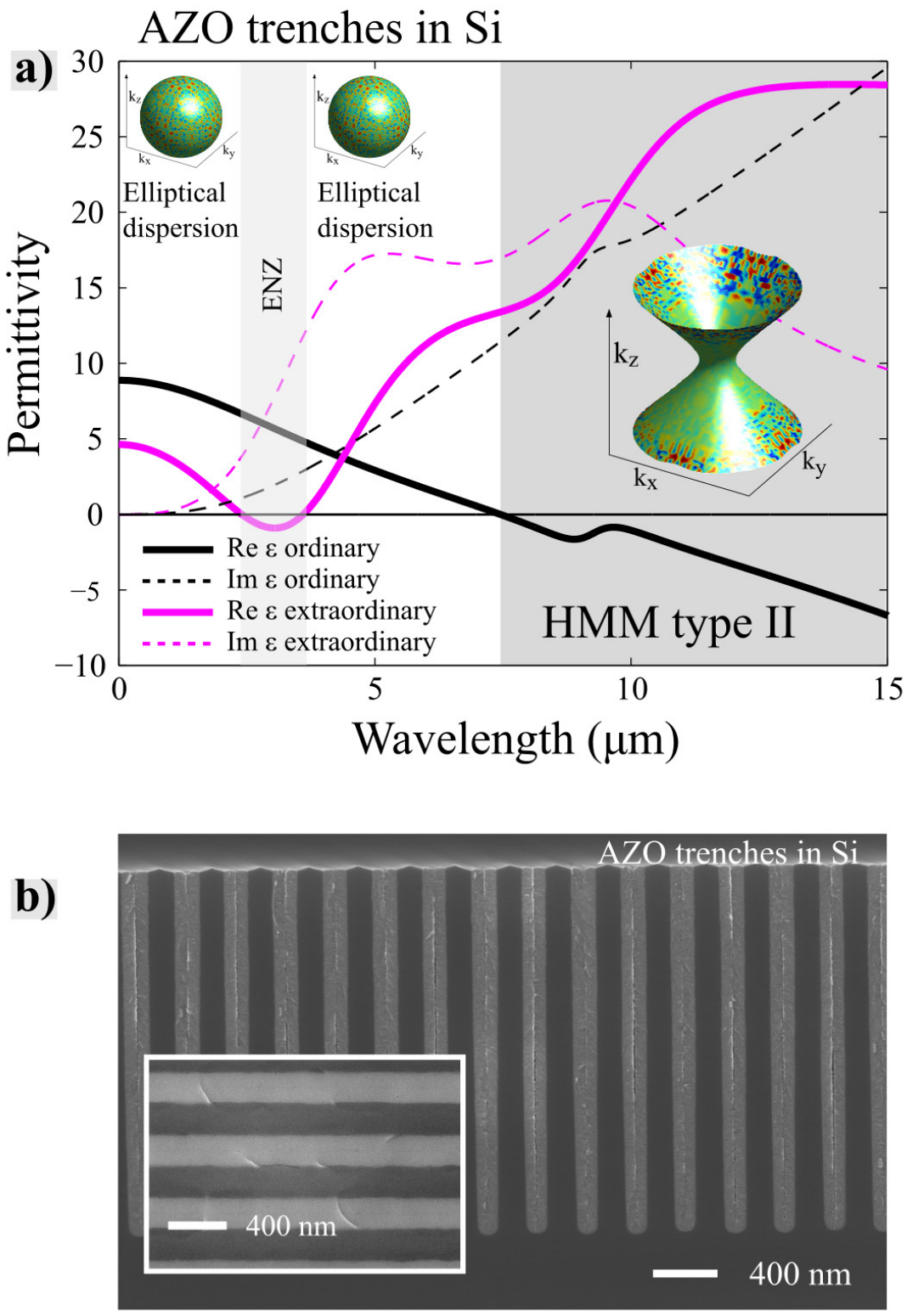

Figure 6.7: AZO/Si trench HMM. a) Permittivity determined by FTIR. At a wavelength higher than $\lambda = 7.45\mu m$ the structure is moving into the Type II hyperbolic regime. b) SEM image of sample cross-section. The insets shows the trenches from the top.

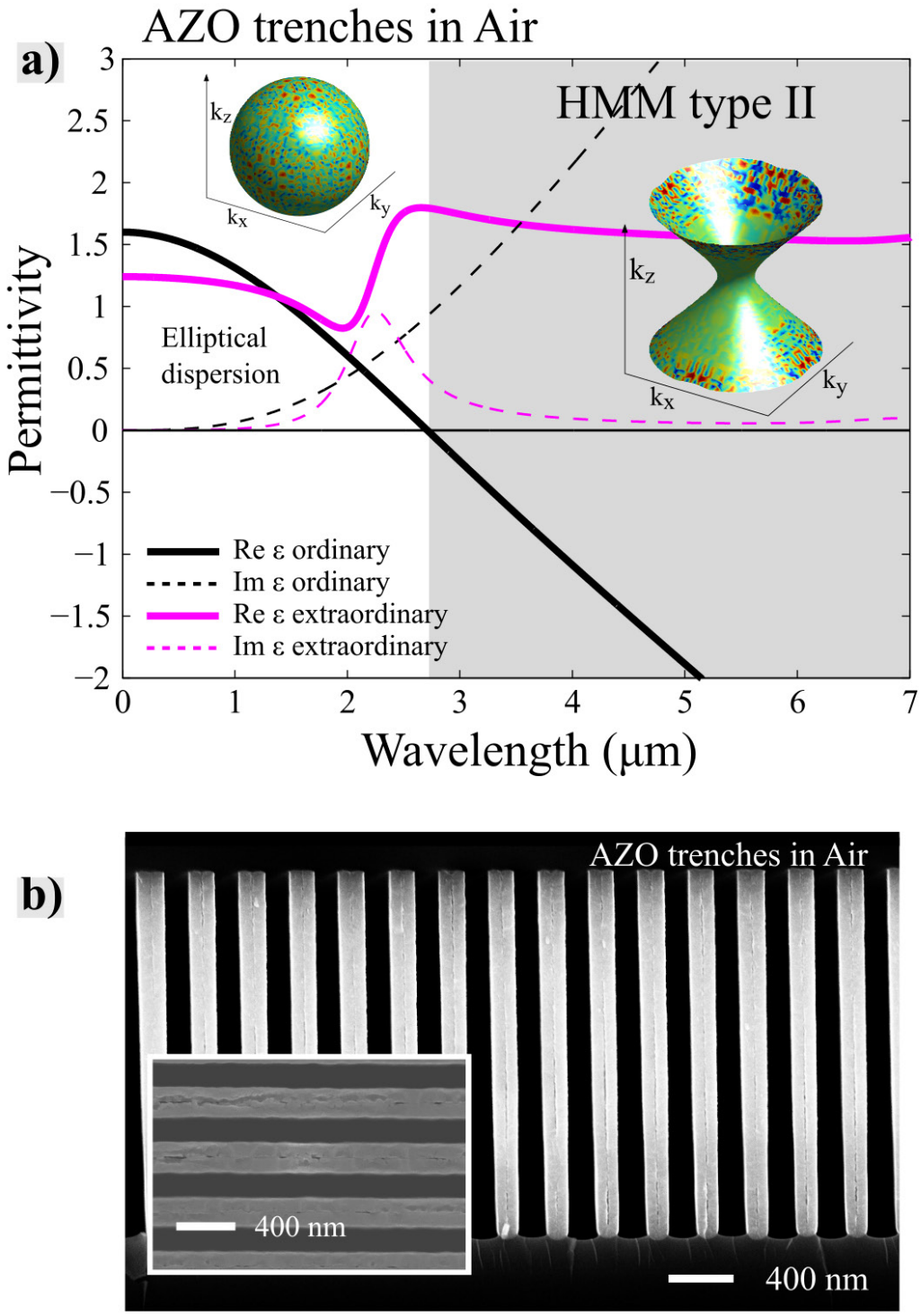

Figure 6.8: AZO/Air trench HMM. a) Permittivity determined by FTIR. At a wavelength higher than $\lambda = 2.71\mu m$ the structure is moving into the Type II hyperbolic regime. b) SEM image of sample cross-section. The insets shows the trenches from the top.

6.4 HMMs Based on AZO Pillars

The second HMM platform is based on AZO/dielectric structures with multiple high aspect ratio plasmonic pillars. The two-dimensional HMM pillar model is depicted in Figure 1.3 b) of Chapter 1. The dielectric component in HMM is chosen to be either Si or ambient air. The successful realization of TiO_2 high aspect ratio pillars (see Figure 4.10) was the starting point. The fabrication of these structures begins with the preparation of Si template.

6.4.1 Fabrication Flow

It was decided to fabricate two types of pillars - one is the complete filled pillars with the diameter of approximately 280 nm and the other is the AZO tubes with the wall thickness of only 20 nm. The full pillars should act as AZO pillar HMM, while tubes should be used for technology demonstration.

The main steps in the fabrication procedure for pillars are shown in Figure 6.9. Initially, the silicon holes with diameter of 280 nm were realized in *(silicon-in-insulator)* SOI wafers by Deep-UV lithography and DRIE (Figure 6.9 a). The holes were arranged in a square lattice with the pitch of 400 nm. The template were then filled with an ALD D25 AZO coating (Figure 6.9 b) at 250 $°C$. The thickness of the deposited AZO was depending on the desired output. An entire filling would result in a formation of pillars, while a partial deposition leads to fabrication of hollow tubes. After the removal of the top parts by Ar^+ ion etching (Figure 6.9 c), the silicon core between the ALD coated holes was etched away during the last step. Figure 6.9 d) shows the final structures. Each process step was carefully analyzed using cross-sectional SEM imaging (see Figures 6.10 and 6.11 for SEM cross-sectional evaluations of the steps presented in Figure 6.9 for fabrication of both AZO pillars and tubes).

In order to produce AZO pillars, 150 mm (100) Si wafers have been selected for device fabrication. These have been RCA cleaned, and a 200 nm SiO_2 layer was grown by thermal oxidizing process in a conventional quartz tube[8]. This step is optional, but it eases the fabrication process, because it provides a stop barrier during the last step of fabrication (the etching), because it prevents an eventual collapse due to overetching. On the other hand, it increases the complexity the final structure, and the existence of the SiO_2 barrier should be taken into account when fitting the reflection signal. On top of the SiO_2 layer amorphous silicon

[8]Furnace from Tempress [102]

with a thickness of 2 μm was deposited using low pressure chemical vapor deposition (LPCVD)footnoteFurnace from Tempress [102]. This procedure enables the preparation of home-made (SOI) substrates. The entire fabrication procedure of the Si-holes template is described in Chapter 4, in the section dedicated to fabrication of TiO_2 pillars. The next session will describe it briefly.

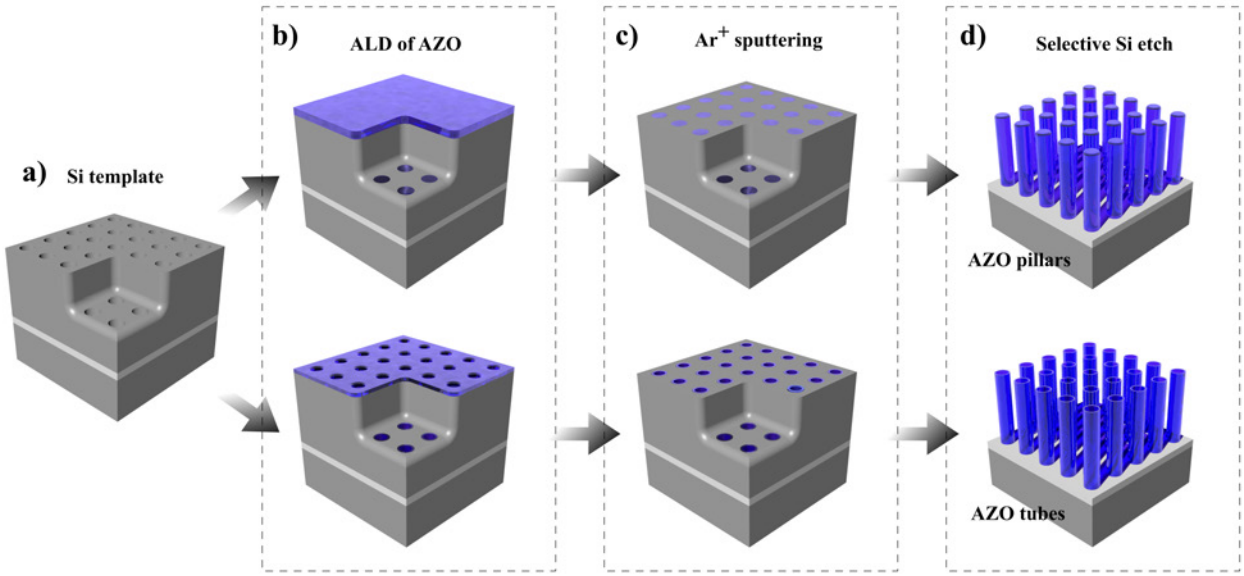

Figure 6.9: Schematic drawing of the pillars and tubes fabrication: a) SOI template with DRIE etched holes, b) ALD deposition of AZO D25 250 $°C$. Complete filling for HMM pillars or partial for tubes. c) The top layer removal. d) Selective Si etch using conventional RIE process.

6.4.2 Deep-UV and DRIE

Parameters for Deep-UV lithography is described in Chapter 4 dedicated to fabrication of vertically arranged nanostructures. The applied DRIE recipe was not changed. The processing temperature was kept at 0 $°C$ and the process pressure at 10 mTorr. Three main steps were used for the Si template fabrication: etching of the BARC layer, high anisotropic silicon etching (Table 4.3 summarizes the Bosch process parameters) and resist removal. The BARC etch proceeds for 45 s. using 40 sccm O_2 plasma with coil and platen powers of 400 and 20 W, respectively. The depth of holes was controlled by adjusting the number of cycles (85 cycles correspond to $2\mu m$ deep holes). The strict control of the etching depth is required on bare Si substrates, though it is less important for SOI substrates with

a SiO_2 stop layer. The last step in the Si hole fabrication is the removal of the remaining resist. It was done using O_2 plasma for 2 min with an O_2 flow of 100 sccm. The coil and platen powers were 800 and 20 W respectively. The shape of the produced Si-template hole structures was carefully investigated by SEM in cross-sectional mode by sacrificing some of the prepared structures shown in Figure 6.10 a) and 6.11 a). The achieved diameter of the holes is slightly larger than 200 nm due to imperfections in the etching process especially in middle part of the cylinders. Prior to the next step (ALD deposition), the prepared template structure received additional O_2/N_2 plasma treatment in order to remove any possible organic residuals from resist coatings and surroundings.

ALD Deposition

The 100 nm AZO thin film analysis reveals that AZO deposited at 200-250°C has lowest resistivity, highly preferential growth along the c axis with (002) crystal orientation and most pronounced decrease in permittivity with increase of the wavelength compared with lower deposition temperatures. It makes those films excellent candidates for plasmonic components in optical metamaterial structures. Among them, D25 250 °C AZO has the highest ω_p. This is selected for the fabrication of AZO HMMs, based on freestanding pillars.

An AZO film has been deposited with the D25 250 °C recipe film has been deposited on a DRIE prepared Si template with holes at a temperature of 250°C. Two ALD depositions with two thicknesses have been made. The first one which allows the full pillars manufacturing required deposition of approximately 140 nm D25 250 °C AZO film in order to fill Si holes entirely. The second run was a deposition of an only 20 nm AZO D25 250 °C thin film in order to test and verify the technology. This allows the fabrication of thin free standing AZO cylinders. SEM cross-sectional inspections reveal homogeneous conformal coatings (see Figures 6.10 b) and 6.11 b)). Due to minor imperfections in the Si etching process the small empty gap (approx. 30 nm) in the middle of the structures is created after ALD filling in the case of full pillars.

Ar^+ Ion Etching of Deposited AZO and Selective Removal of the Si Host

Pure physical Ar^+ Ion sputtering (Ionfab 300 Plus from Oxford Instruments) has been implemented for removal of the deposited AZO top layer in order to get an access to the silicon core as illustrated in Figures 6.10 c) in case of full pillars and 6.11 c) in case of tubes. Here the process was tuned to an etch rate of 20 nm/min which provided a well-controlled top layer breakthrough. Even though only physical dry etch removal has been used in this work, several other techniques for etching of AZO have been reported. One of them is wet etching based on diluted

HCl [194]. Another is a dry etching based on methane and hydrogen plasma [195].

Removal of the silicon host is the last step in achieving the structures. Selective silicon etching (template removal) proceeded using a continuous isotropic etch in the conventional reactive ion etching tool (RIE) based on a continuous SF_6 process at a substrate temperature of 20 $°C$. The SF_6 gas flow was kept constant at 35 sccm and the process pressure was 80 mTorr. The Coil power was at 30 W. This process proceeds with an extreme selectivity to the deposited AZO layer without any observable harm to the prepared AZO pillar structure. The proof of the selectivity is demonstrated in the case of prepared 20 nm thin AZO tubes. No harm on the prepared tubes was observed even though the ratio of thickness to height was 1:100 (20 nm to $2\mu m$). Cross-sectional SEM images of the output structures is presented in Figures 6.10 d) in case of full pillars and 6.11 d) in case of tubes.

6.4.3 Structures Electron Microscopy Characterization

The fabricated AZO pillars structures comprise AZO wires with the diameter of 280 nm and height of $2\mu m$. Pillars was arranged in a square lattice with a pitch of 400 nm. The host between pillars was either Si or air depending on the output HMM structure. The whole sample had a dimensions of 1x1 cm. The produced samples have been delivered to the group of collaborators for optical investigations, in order to prove the existence of hyperbolic behavior, but before, they were carefully investigated using SEM and transmission electron microscopy (TEM) techniques. The prepared tubes are thin enough to be electron transparent. This allows us to estimate the dimensions of the crystal grains and compare them with the XRD measured values. It must be mentioned however, that the grains size are expected to be strongly dependent on the thickness of the deposited AZO layer. In this work only an AZO of thickness 100 nm was investigated. However, it is expected that physical and optical properties of AZO are strongly correlated with the layer thickness.

SEM characterization

Figure 6.12 shows the fabricated structures standing on a 200 nm thick SiO_2 layer (Figure 6.12 a) and b) for pillars and tubes respectively). The samples were tilted 30° inside the SEM chamber, and the corner of each sample was visualized using a variable pressure secondary electron (VPSE) detector at 15 kV with a bias voltage of +350 V and a pressure of 20 Pa. The high magnification inset images of Figure 6.12 were taking using in-lens detector at 10 kV. Here the individual pillars/tubes shape is clearly seen.

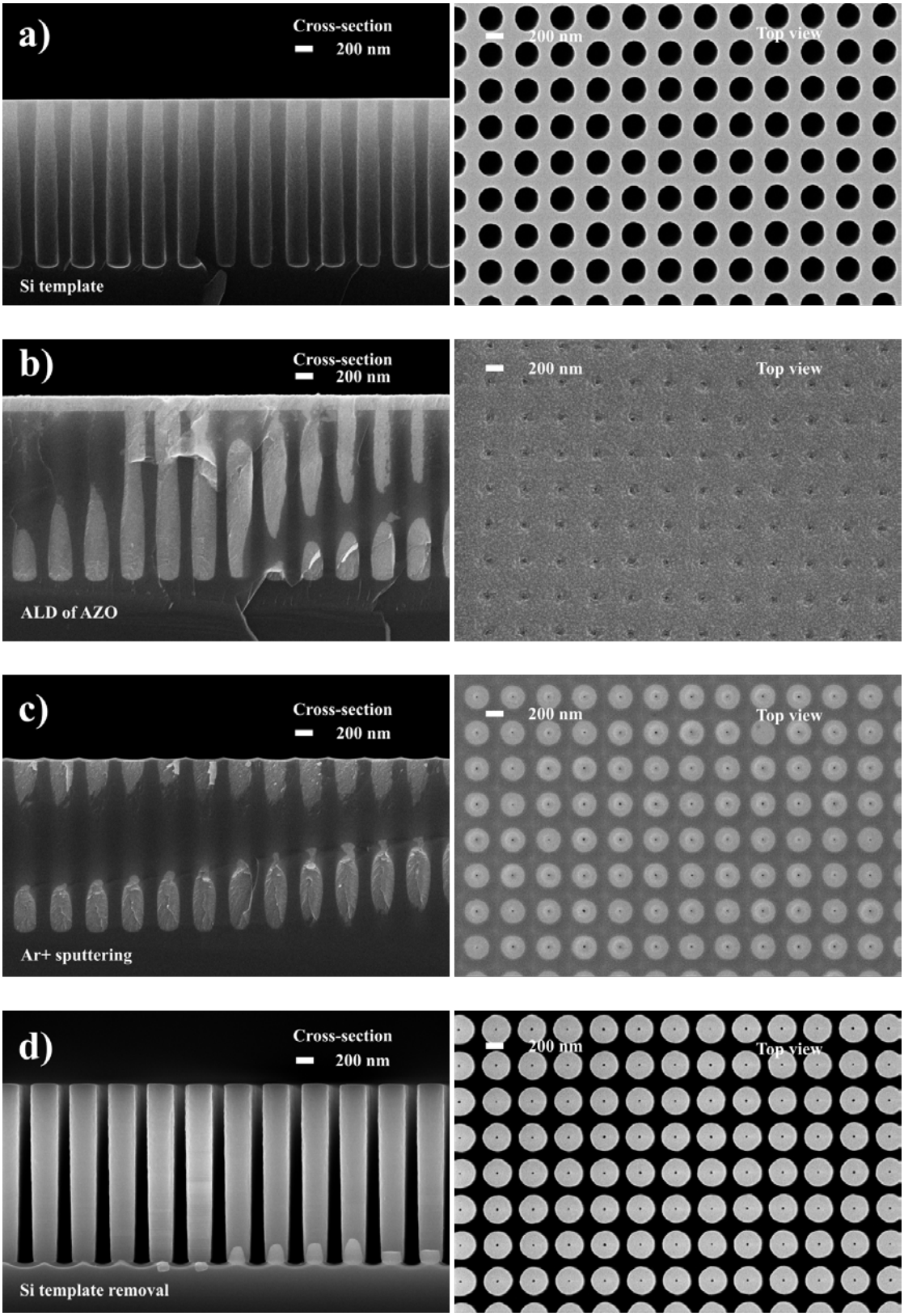

Figure 6.10: SEM verification for each fabrication step of pillars production. Left side shows cross-sectional images and right side of the Figure shows the top view of the structures. Each step a)-d) are in the same order as presented in Figure 6.9

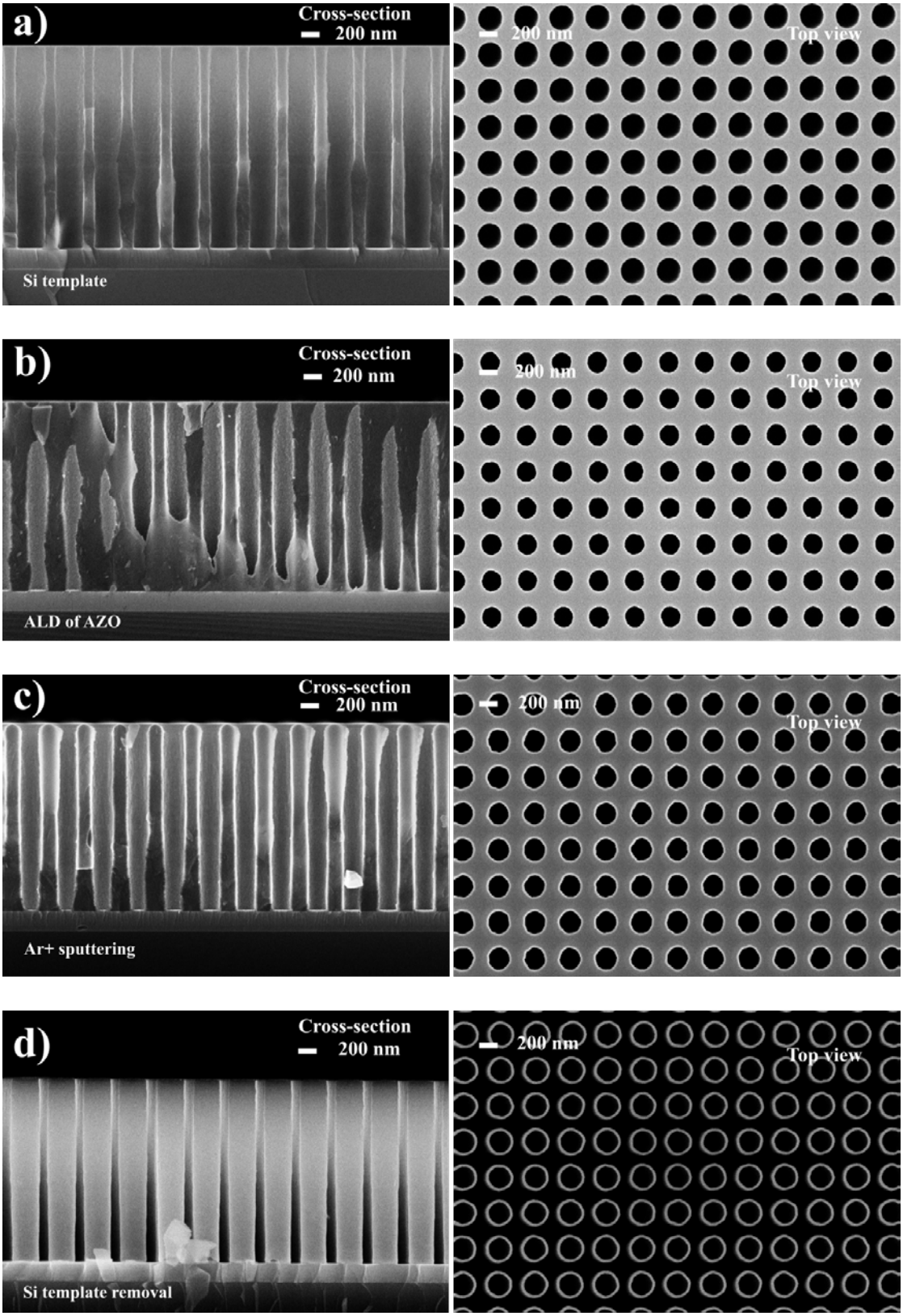

Figure 6.11: SEM verification for each fabrication step of tube production. Left side shows cross-sectional images and right side of the Figure shows the top view of the structures. Each step a)-d) are in the same order as presented in Figure 6.9

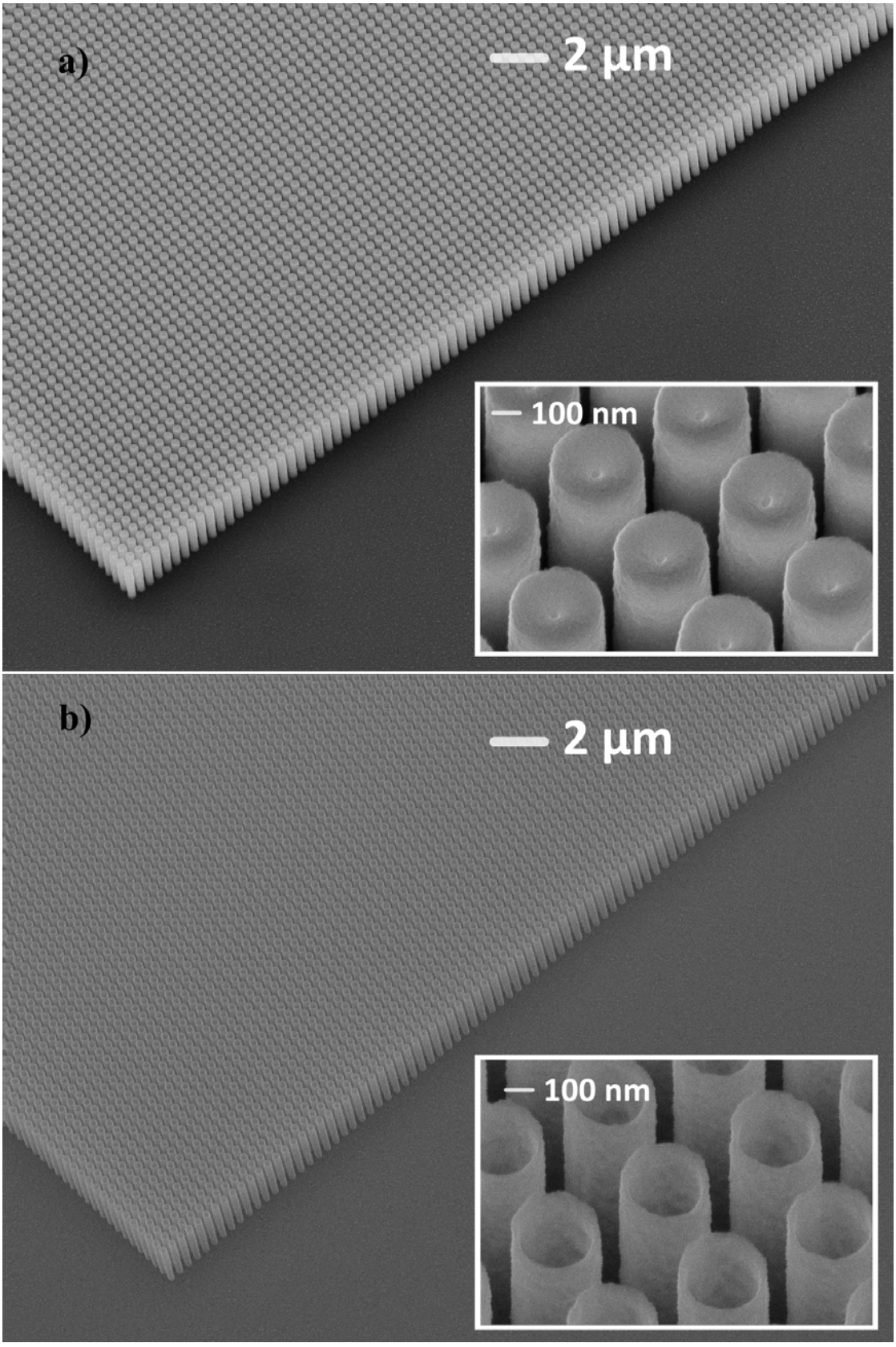

Figure 6.12: Side view 30 ° tilted SEM image showing the excellent ordered structure over a large area. a) Pillars b) Tubes. Insets show magnified images.

TEM Characterization

The crystallographic profile and microstructural analysis of D25 250 $°C$ AZO tubes were investigated using Transmission Electron Microscopy (TEM) by collaborators from DTU CEN. The experiment was conducted[9] at 300 kV with an Cs image corrector[10]. The elemental mapping using energy-dispersive X-ray spectroscopy (EDX) was performed[11] on selected AZO pillars.

Figure 6.13 shows TEM results obtained for pillars and tubes. The detailed explanation of the techniques is described elsewhere [196]. Figure 6.13 a) shows a magnified image of the pillar top part.

The selected area electron diffraction (SAED) performed inside the TEM reveals the same crystallographic information as was obtained using X-ray Diffraction (XRD). Figure 6.13 b) shows the diffraction pattern which tells, that the produced AZO film is polycrystalline with (002) (100) and (101) preferential orientations. Additionally, other minor ZnO orientations were observed. The (102), (110), (103), (112) etc. orientations were below the detection sensitivity of the XRD equipment described in Chapter 5, but commonly observed in ZnO species [197].

Dark field TEM images Figure 6.13 c) and d) of AZO tubes reveal the information of crystal grain sizes. The full AZO pillars are to thick for transparency images, while 20 nm thin tubes are sufficient for such purposes. The crystalline grains visible in Figure 6.13 c) and d) have dimensions of approximately 10 nm, which correlates well with the grain sizes obtained by XRD. (See Figure 5.7). However, one need to keep in mind that the AZO grains presented in Figure 5.7 come from the 100 nm thick films and cannot be directly compared with the crystalline structures for AZO tubes.

Figure 6.13 e) depicts a high angle annular dark-field (HAADF) imaging of AZO nanopillar and EDX elemental mapping which proves that ZnO was indeed doped homogeneously.

[9] A monochromatic FEI Titan TEM

[10] CETCOR unit from the CEOS Company

[11] probe-corrected FEI Titan 80-200 'ChemiSTEM' electron microscope equipped with four symmetric SDD detectors

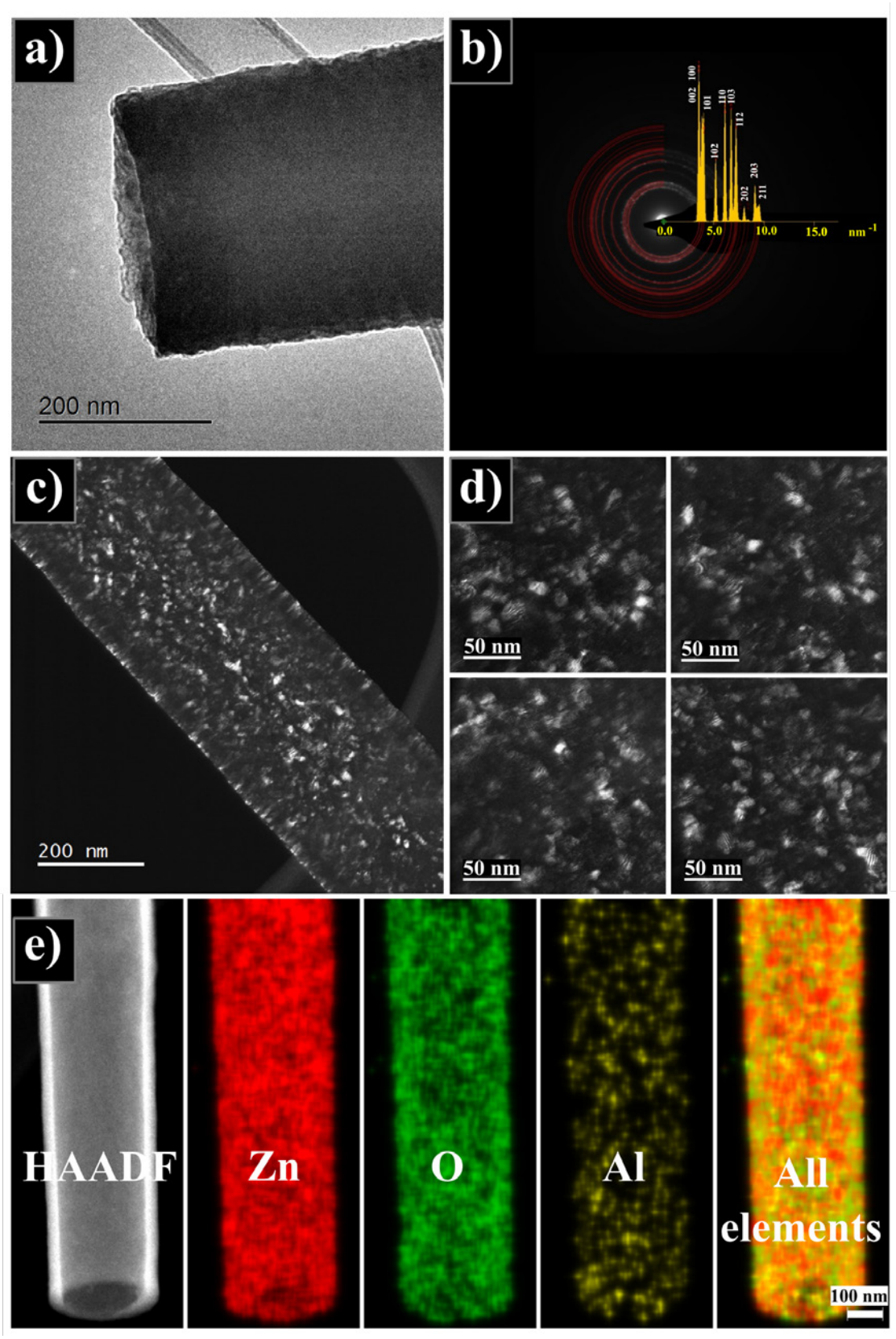

Figure 6.13: TEM investigation a) High resolution TEM image of the produced pillars. b) SAD pattern of AZO D25 pillar. c) and d) are dark field images: c) is the image at low magnification, d) are enlarged images of the same area with different positions of the object aperture. e) EDX elemental mapping and HAADF imaging of AZO nanopillar. The pixel size is 3 nm and the acquisition time is 10 μs per pixel.

j	1	2	3	4
S_j	9.35	0.1	1.43	3.87
Γ_j (THz)	56.37	3.48	8.32	11.02
$\omega_{f,j}$ (THz)	54.63	40.32	32.19	25.51

Table 6.5: Retrieved ε_o dielectric function parameters for AZO/Si pillars. High frequency ε_∞=6.16.

j	1	2
S_j	0.98	7.48
Γ_j (THz)	202.5	787.76
$\omega_{f,j}$ (THz)	193.65	17.97

Table 6.6: Retrieved ε_o dielectric function parameters for AZO/Air pillars. High frequency ε_∞=1.29.

6.4.4 Optical Characterization of Pillars Hyperbolic Metamaterial

The geometry of AZO pillars is presented in Figure 6.14. Here, the effective uniaxial permittivity tensor components are defined by $\varepsilon_{x,y} = \varepsilon_\square = \varepsilon_o$ and $\varepsilon_z = \varepsilon_{zz} = \varepsilon_e$, where ε_o and ε_e are the effective ordinary and extraordinary permittivities, respectively. Lets recall the EMT equations 1.28 and 1.29 from Chapter 1 that describe the permittivity tensor of nanowires.

$$\varepsilon_e = \varepsilon_{yy} = \varepsilon_\square = \frac{[(1+p)\varepsilon_m + (1-p)\varepsilon_d]\varepsilon_d}{(1-p)\varepsilon_m + (1+p)\varepsilon_d}$$

$$\varepsilon_o = p\varepsilon_m + (1-p)\varepsilon_d$$

Finding these values is easy, since the material permittivities of AZO D25 250°C and Si are already established using Drude Lorentz model (see equation 6.1). Parameters of these dielectric functions are summarized in Tables 6.3 and6.6. The air permittivity is assumed to be equal unity with no loss in any frequency.

The optical characterization of AZO pillars proceeds in a similar fashion as in the case of AZO trench structures. However, FTIR characterization of the produced AZO pillars showed up to be more complicated than in the case of AZO trenches. The ordinary permittivity ε_o of has been measured using the 12°

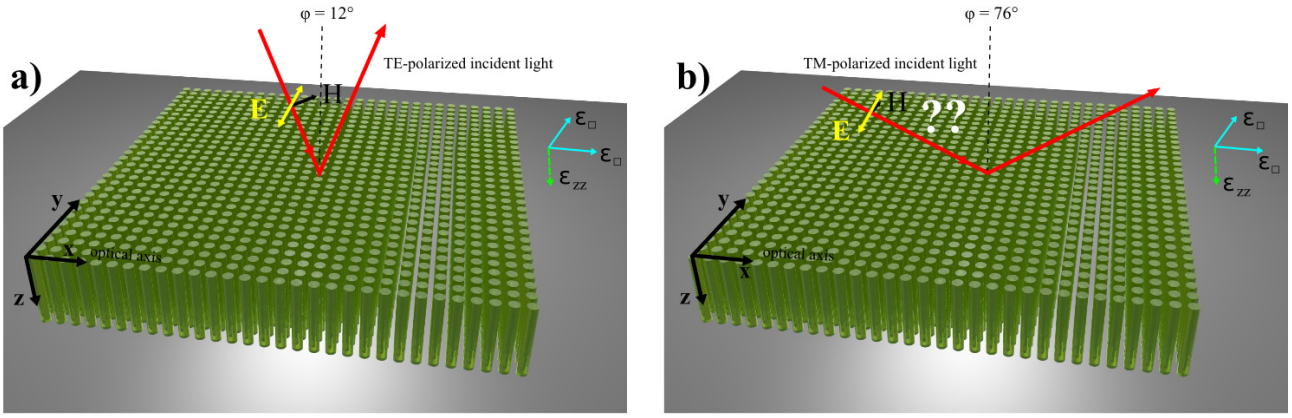

Figure 6.14: Configuration of AZO pillars HMM. a) **E** field of incident TE-polarized light, is parallel to the sample surface. Configuration is suitable for recovery of ordinary permittivity ε_o. b) In order to retrieve extraordinary dielectric function ε_e, **E** field of incident light must be aligned along the pillar direction. If TM-polarized light is incident on the sample with angle of 76°, there are still polarization mixture in the reflection signal, which prohibits the experimental evaluation of extraordinary component ε_e.

incident TE-polarized light with the electric field **E** parallel to the surface (the case is presented in Figure 6.14 a). The following parameters have been used to retrieve the ε_o dielectric function:

- Drude-Lorentz dielectric function with four Lorentzian terms together with ε_∞ was used to model the ordinary permittivity of the produced AZO pillar structures in Si (AZO/Si). Figure 6.15 a) shows the measured and fitted FTIR reflectance spectrum for this case. Figure 6.15 b) shows the real and imaginary parts of ε_o for AZO/Si structure as solid lines.

- Two Lorentzian terms together with ε_∞ were implemented for the ordinary permittivity of the AZO/Si pillar structure. The measured reflectance spectra together with the fitted curve are presented in Figure 6.15 c). The retrieved permittivities are plotted in Figure 6.15 d).

The FTIR measurements of the extraordinary permittivity ε_e case turn out to be far more complicated for both AZO/Si and AZO/Air pillar structures. In order to obtain the right reflection signal, the electric field **E** must be aligned along the pillar direction. The best way to do this is to use TM-polarized light and perform a measurement with as high an incident angle as possible (see Figure 6.14 b) An angle of 76 ° was tried due to equipment limitations, however it did not solve the problem. The mixture of polarizations due to electric field misalignment **E** did

not allow the measurement of the extraordinary permittivity. The gained results disagree with the prediction of EMT and are not shown here. Nevertheless, good agreement between EMT and FTIR measurements achieved in the ordinary case for both AZO/Si and AZO/Air pillars (Figure 6.15). The extraordinary dielectric function calculated from EMT equations are shown in Figure 6.15 e) and f).

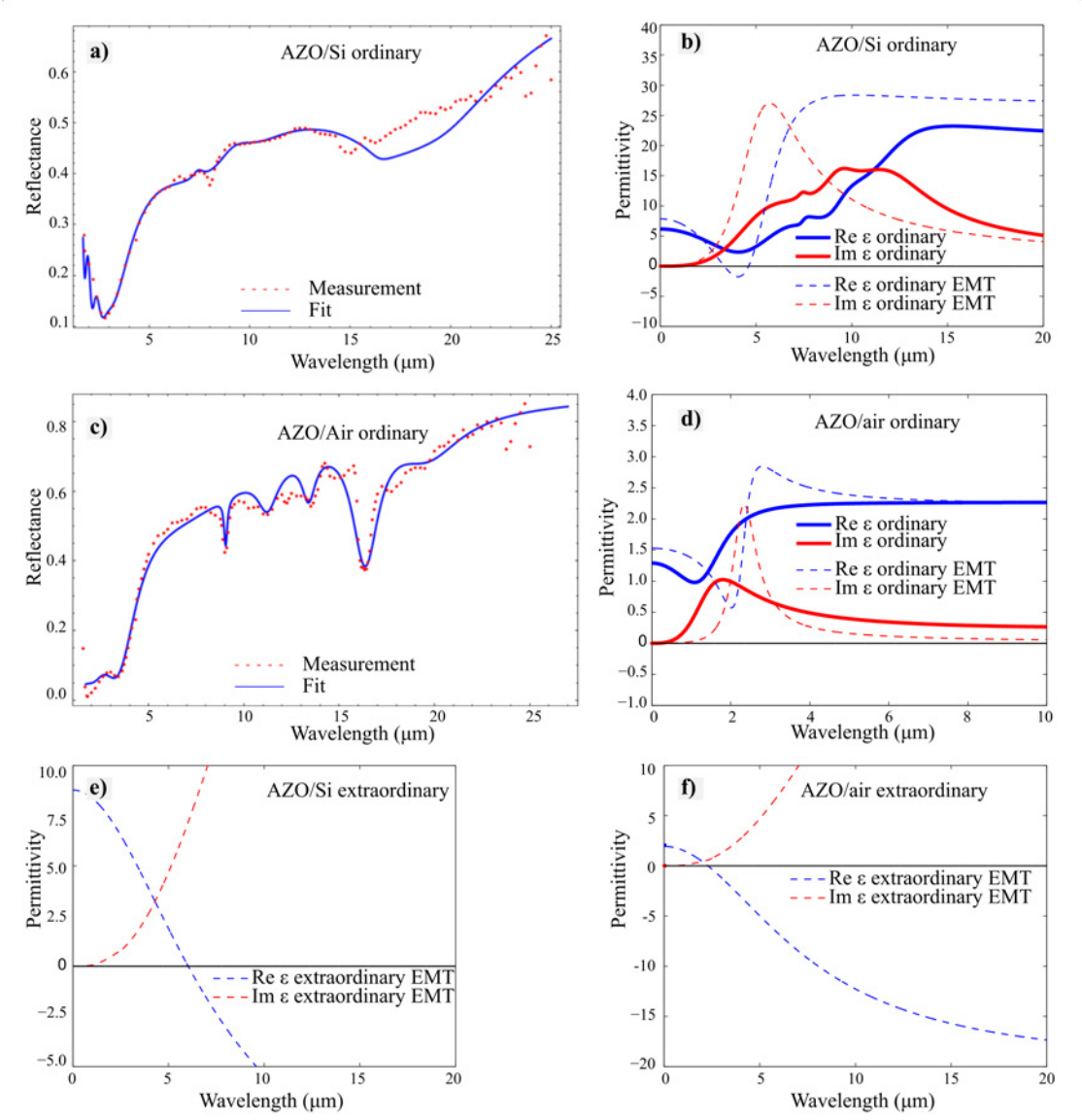

Figure 6.15: FTIR measured and fitted reflection spectra and corresponding retrieved ordinary permittivities together with EMT derived dielectric functions. a) and b) AZO/Si ordinary. c) and d) AZO/Air ordinary. e) and f) AZO/Si extraordinary and AZO/Air extraordinary ordinary retrieved from EMT, respectively.

6.4.5 General Remarks

Two types of AZO pillars HMM have been fabricated: AZO/Si pillars and AZO/Air pillar structures. In the case of AZO/Si HMM, the extraordinary permittivity ε_e becomes negative at a wavelength of $\lambda > 6.02\ \mu m$, while the ordinary permittivity ε_o remains positive, which means that the system moves into the hyperbolic regime of Type I as presented in Figure 6.16 a). Additionally, an interesting regime exists in the wavelength range between $\lambda = 3.34\ \mu m$ and $\lambda = 4.61\ \mu m$, here the opposite situation occurs. The extraordinary permittivity is positive, while the ordinary permittivity becomes negative. It can be interpreted as the existence of a Type I hyperbolic regime. However, the assumption is based on the EMT prediction, and the real ε_o measured by FTIR (see Figure 6.15 b) contradicts the ideal case and never becomes negative. Additionally, the ordinary dielectric function never becomes significantly negative even for EMT, and taken losses into account, it will possibly never become hyperbolic in this wavelength range. Nevertheless, the region is excellent for epsilon-near-zero (ENZ) applications [18],[198]. A cross-sectional SEM image of the HMM sample is shown in Figure 6.16 b).

AZO/Air HMM originates from the previous sample. The Si matrix of the structure needs to be removed using a continuous dry etch process, based on SF_6 plasma chemistry as illustrated in Figure 6.9 d). According to EMT, the fabricated metamaterial becomes Type I hyperbolic at a wavelength of $\lambda > 2.29\ \mu m$. SEM image of the sample cross-section is shown in Figure 6.17. Si etching was very uniform across the sample, which has dimensions of 1x1 cm.

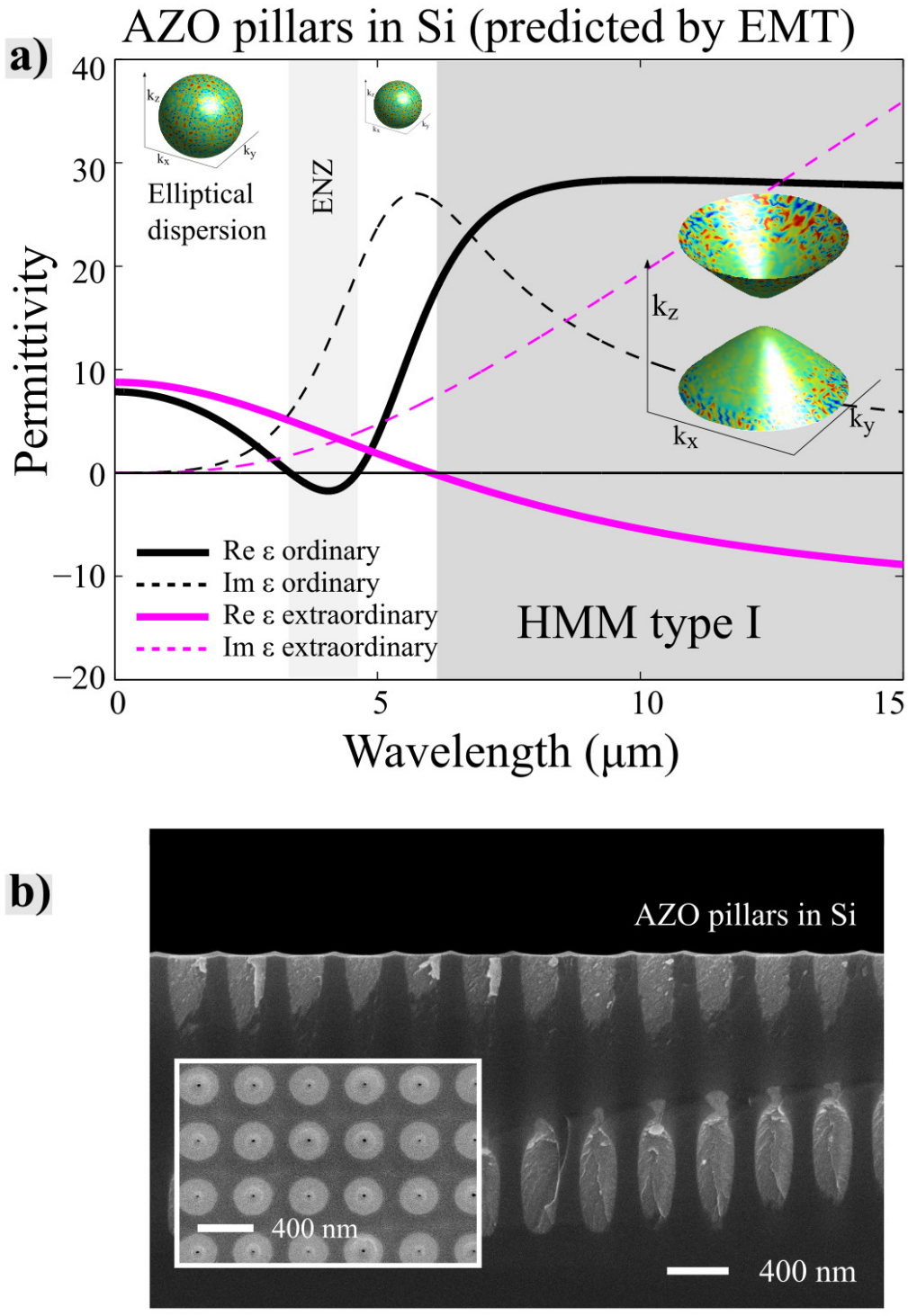

Figure 6.16: AZO/Si pillars HMM. a) Permittivity determined by EMT. At a wavelength higher than $\lambda = 6.02\mu m$ the structure becomes the Type I hyperbolic. b) SEM image of sample cross-section. The inset shows the pillars from the top.

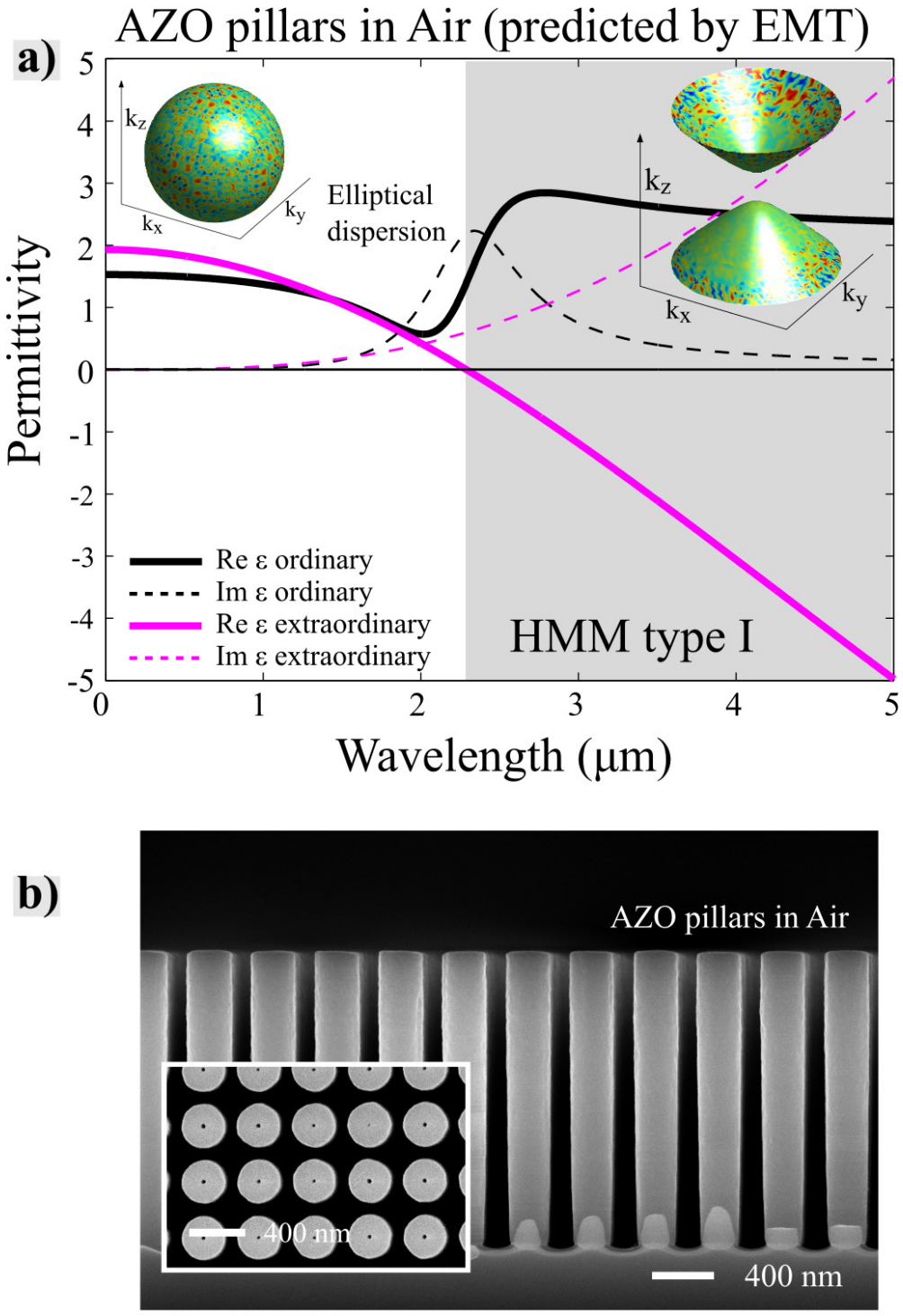

Figure 6.17: AZO/Air pillars HMM. a) Permittivity determined by EMTR. At a wavelength higher than $\lambda = 2.29\mu m$ the structure becomes the Type I hyperbolic. b) SEM image of sample cross-section. The inset shows the pillars from the top.

CHAPTER 7

HIGHLIGHTS AND OUTLOOK

7.1 Highlights

Atomic layer deposition (ALD) has proved be a reliable tool in nanofabrication of hyperbolic metamaterials (HMMs). The investigation of the ALD technique started with a performance test of the well established Al_2O_3, TiO_2 and ZnO processes. Next, four different Al_2O_3/TiO_2 multilayer stacks, with two different orders and an overall thickness of 200 nm and with individual layer thicknesses of either 20 nm or 10 nm have been fabricated and characterized using spectroscopic ellipsometry (SE), scanning electron microscopy (SEM) and X-ray photoelectron spectroscopy (XPS). After placing these stacks on top of a Si_3N_4 photonic resonator, reflection measurements have been performed in order to verify the effective medium approximation (EMA) theory close to the angle of total internal reflection (TIR)[103].

Fabrication of high quality, continuous Al_2O_3/TiO_2 ALD multilayers has pushed the fabrication of HMMs one step further: the realization of freestanding high aspect ratio nanostructured gratings and pillars. This was achieved by a combination of ALD and advanced dry etch techniques such as deep reactive ion etching (DRIE)[131].

Realization of HMMs would require an establishment of reliable ALD materials with plasmonic properties. The original idea of using Cu metal for the visible wavelength range was abandoned due to an uncontrolled growth of layer and subsequent oxidation of Cu. The switch to Al-doped ZnO (AZO) as another alternative plasmonic material resulted in a shift of the operational wavelength from visible

to mid-infrared. AZO has been grown on Si and SiO_2 substrates in a temperature range 150 $°C$ - 250 $°C$ with different Al-dopings. A variety of characterization techniques has been used for investigation of the properties of the deposited films. Besides the above-mentioned methods, they involved X-ray diffraction (XRD) and transmission electron microscopy (TEM). Two best AZO films with the highest plasma frequency (ω_p) have been selected as plasmonic components for fabrication of HMMs.

The last step to establish HMMs fabrication is to apply realization method for the high aspect ratio Al_2O_3 and TiO_2 nanogratings and pillars on the AZO material platform in order to form one- and two- dimensional structures. Four different types of HMMs have been fabricated: AZO/Si trenches, AZO/Air trenches, AZO/Si pillars and AZO/Air pillars. AZO pillars HMMs support Type I hyperbolic regime, while AZO trench structures become Type II (at a wavelength higher than $\lambda = 2.71\mu m$ for the AZO/Air case). The optical response was investigated using the fourier transform infrared spectroscopy (FTIR) technique. The performance can be widely tuned by adjusting several parameters such as Al doping or the amount of Si, acting as a dielectric host in HMMs.

The produced AZO trench and pillar structures illustrate the huge potential of the implemented fabrication technique as a highly versatile and generic scheme for a large variety of materials and structural elements. With the inherent accuracy and scalability of the lithography- and etching tools applied, it is possible to realize large coherent areas of nanostructural elements on a 150 mm Si wafer with feature sizes down to approximately 200 nm. Thus, the full potential of mass production of nanostructural elements in new material platforms opened up for advanced metamaterials fabrication.

7.2 Outlook

The realization of HMMs based on AZO trenches and AZO pillars have opened many perspective directions. Several projects have emerged and some of them already have established promising results. The following sections will describe some of them.

7.2.1 Surface Waves

It is believed that HMMs can support Dyakonov plasmons for the Type II hyperbolic regime. These are highly directional waves which travel along the planar interface of an isotropic material and a uniaxial dielectric [199]. The Dyakonov plasmons have been theoretically predicted [200]-[202], but so far only limited observations reported [32],[203]. The developed technological platform of AZO/Si and AZO/Air trench HMMs opens the possibility to observe these surfaces waves. Figure 7.1 illustrates the proposed set-up for such an observation. Notably, the AZO trench HMM optical performance can be widely tuned by adjustments of the remaining Si part between the AZO lamellas, since it is possible to control the etching depth with an accuracy of approximately 5-10 nm.

7.2.2 Surface Modification Using FIB

Another promising opportunity to excite surface waves is to create a small defect on top of the HMM which scatter light and some of scattered light can be coupled to surface waves. It could be a metallic particle, or a small hole, which can be made by focus ion beam (FIB), see Figure 7.2. This example shows fabrication results of a round hole in silicon grating using FIB[1]. Si trenches with a period of 400 nm and depth of 4.5 μm has been made. One of the samples has been cleaved for the investigation of the cross-section, see Figure 7.2 a). The fabricated samples has been cleaned for residual resist and transported to the FIB tool. Using default settings with a current of 6.5 nA a round hole in the silicon structure has been fabricated, see Figure 7.2 b). The sidewalls are relatively vertical although they are somewhat rounded at the top due to redeposition issues. The trenches are not separated any longer, and they get a "melted" shape at the edge of the hole. The surface modification on AZO-based HMM trench structures is yet to be explored.

[1]Helios NanoLab 400/400S/400 ML/600 System

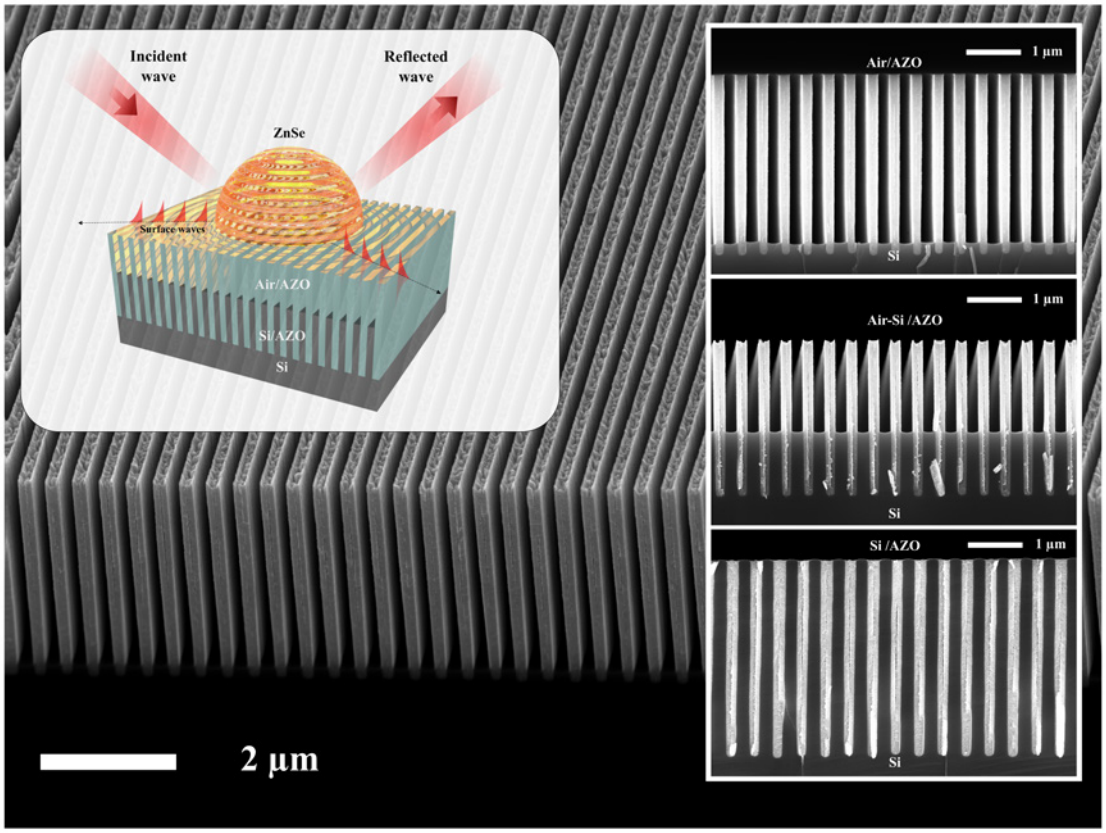

Figure 7.1: An AZO trench geometry with a variable Si level is a perfect choice for experimental observation of Dyakonov plasmons. Plasmons can be exited on the boundary between a HMM and an isotropic dielectric with a high refractive index such as$ZnSe$.

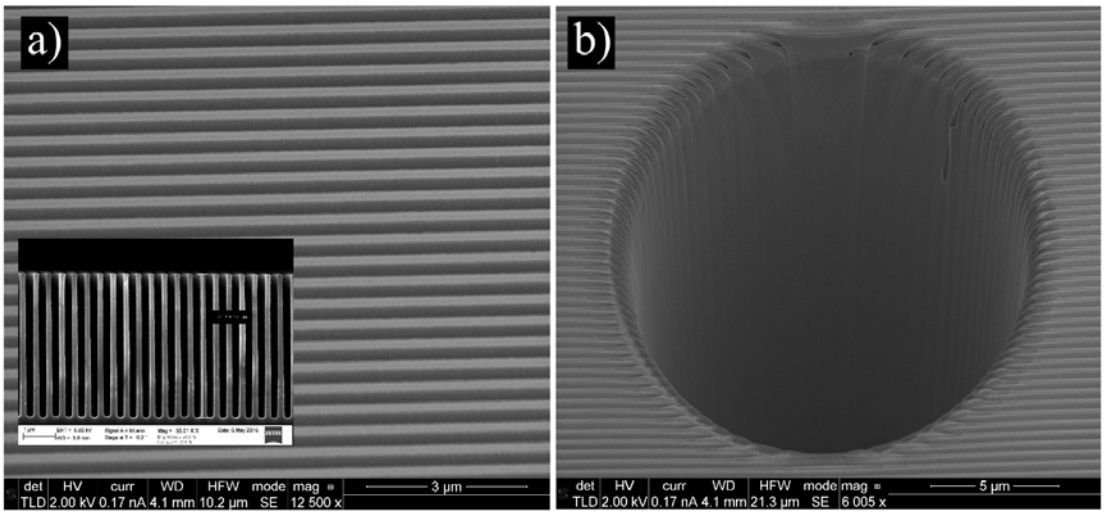

Figure 7.2: FIB surface modification. a) Silicon trenches, top view. The pitch is 400 nm and the depth 4.5 μm. The inset shows a cross-section of the trenches. b) A round hole in silicon trenches with diameter of 15μm and depth of 5 μm made by FIB. The sample is tilted at 52°.

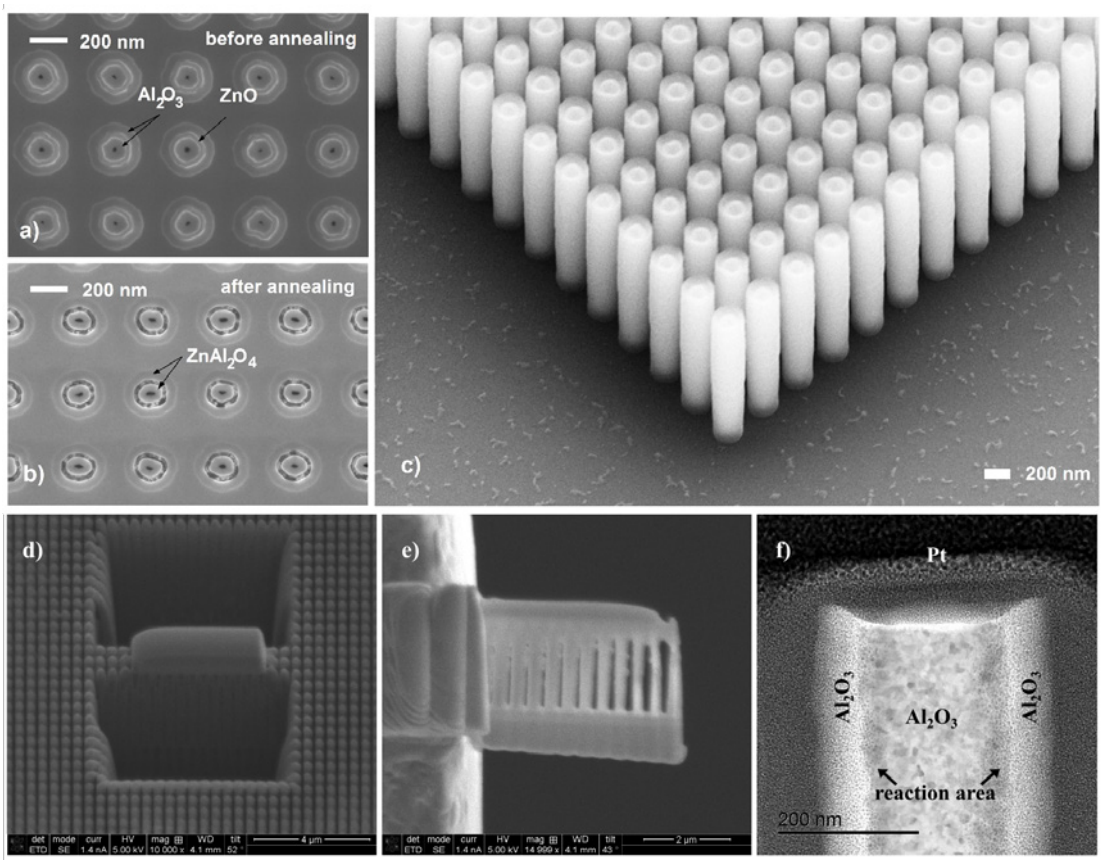

Figure 7.3: SEM images. a) ALD deposition of initial Al_2O_3 and ZnO coatings. b) Temperature induced Kirkendall effect and the formation of $ZnAl_2O_4$ hollow coaxial pillars. c) Final structure after selective silicon removal. d) Milling the sample using FIB in order to extract the lamella with pillars. e) Fabricated TEM sample, side view. f) High resolution TEM image of a single annealed pillar.

7.2.3 Kirkendall Effect in High Aspect Ratio Nanopillars

The topology of metamaterials typically consists of an array of nanopillars, trenches and flat multilayers. Realization of multi-coaxial cylindrical structures enables development of new promising materials with unusual and exiting responses to light. Exactly such structures are required in the field of cloaking and invisibility [204].

Latest reports brings a hope in achieving discrete multilayered structures by implementing the Kirkendall effect in Al_2O_3/ZnO nanolaminates [205],[206]. During the annealing at 800 $°C$ the diffusion of ZnO into Al_2O_3 leads to a creation of a crystalline $ZnAl_2O_4$ compound. This solid state reaction is highly sensitive to temperature, annealing time, layer thickness and other parameters.

$Al_2O_3/ZnO/Al_2O_3$ layers with thicknesses of 50 nm/25 nm/50 nm respectively, were deposited using ALD on a Si hole template as described in a Chapter 6. The prepared samples were annealed at 800 $°C$ for 12h in an N_2 environment at atmospheric pressure in order to induce the Kirkendall effect. SEM images on Figure 7.3 a) and b) reveals the surface morphology before and after the annealing. During the heat process ZnO migrated into Al_2O_3 areas resulting in a formation of large voids. Last fabrication step was silicon removal between the pillars. It was done by reactive ion etching with SF_6 process gas. Figure 7.3 c) shows an SEM image of the fabricated free-standing high aspect ratio $ZnAl_2O_4$ cylindrical nanopillars. Some additional work is required for improving the separation and minimizing the porosity between the coatings. This should be handled in combination with adjusting of multilayer thicknesses during ALD deposition and improving the annealing conditions. The TEM technique was involved in characterization of these pillars. Figure 7.3 d)-f) shows preparation of a lamella with pillars and a high resolution image of the pillar cross-section. Additional research is needed in order to understand the diffusion mechanism of ZnO.

7.2.4 Cu Platform

Metals such as Au and Ag are normally implemented in plasmonic structures in the visible wavelength range. Cu seems to be a good alternative [21]. Despite many trials it was not possible to establish a successful, reproducible Cu process. One of the interesting structure realized in this work was the $ZnO/Cu/ZnO$ sandwich stack. SEM image are shown in Figure 7.4, and XPS depth profile results are shown in Figure 7.5. Unfortunately, it was not possible to establish full operational multilayers and Cu HMM was never realized. Figure 7.6 shows the attempt to grow Cu/Al_2O_3 multilayers on a Si trench template. It is clear that the following Cu layer becomes discontinues. One of the major reasons is believed to be the unstable Cu precursor vapor during the deposition. The tuning of Cu process would probably require a way to properly monitor the partial pressure and temperature of the precursor. Additionally, an ALD chamber dedicated only to Cu deposition is desired, in order to eliminate any possible memory effects from other processes.

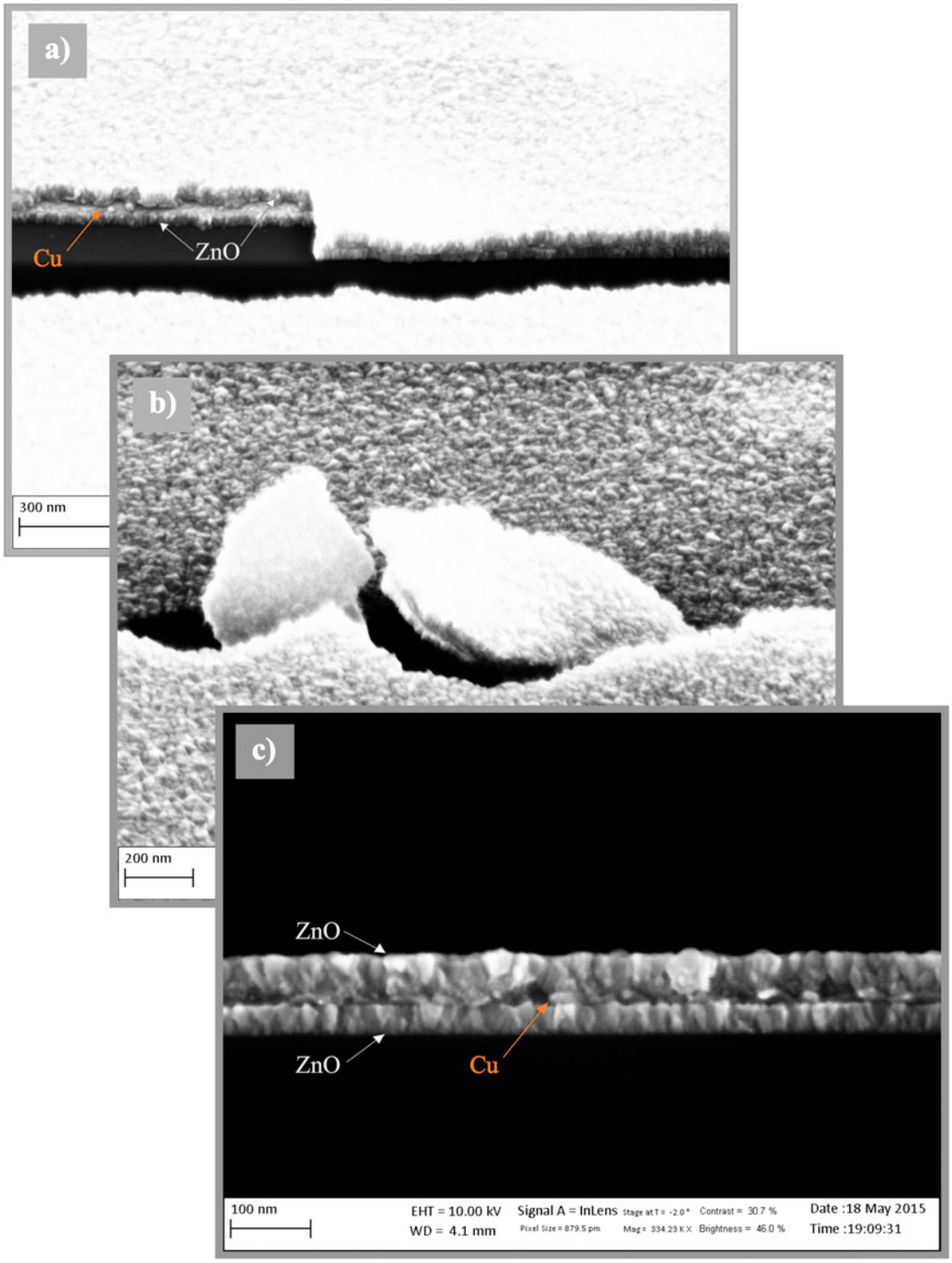

Figure 7.4: SEM images of a $ZnO/Cu/ZnO$ sandwich structure.

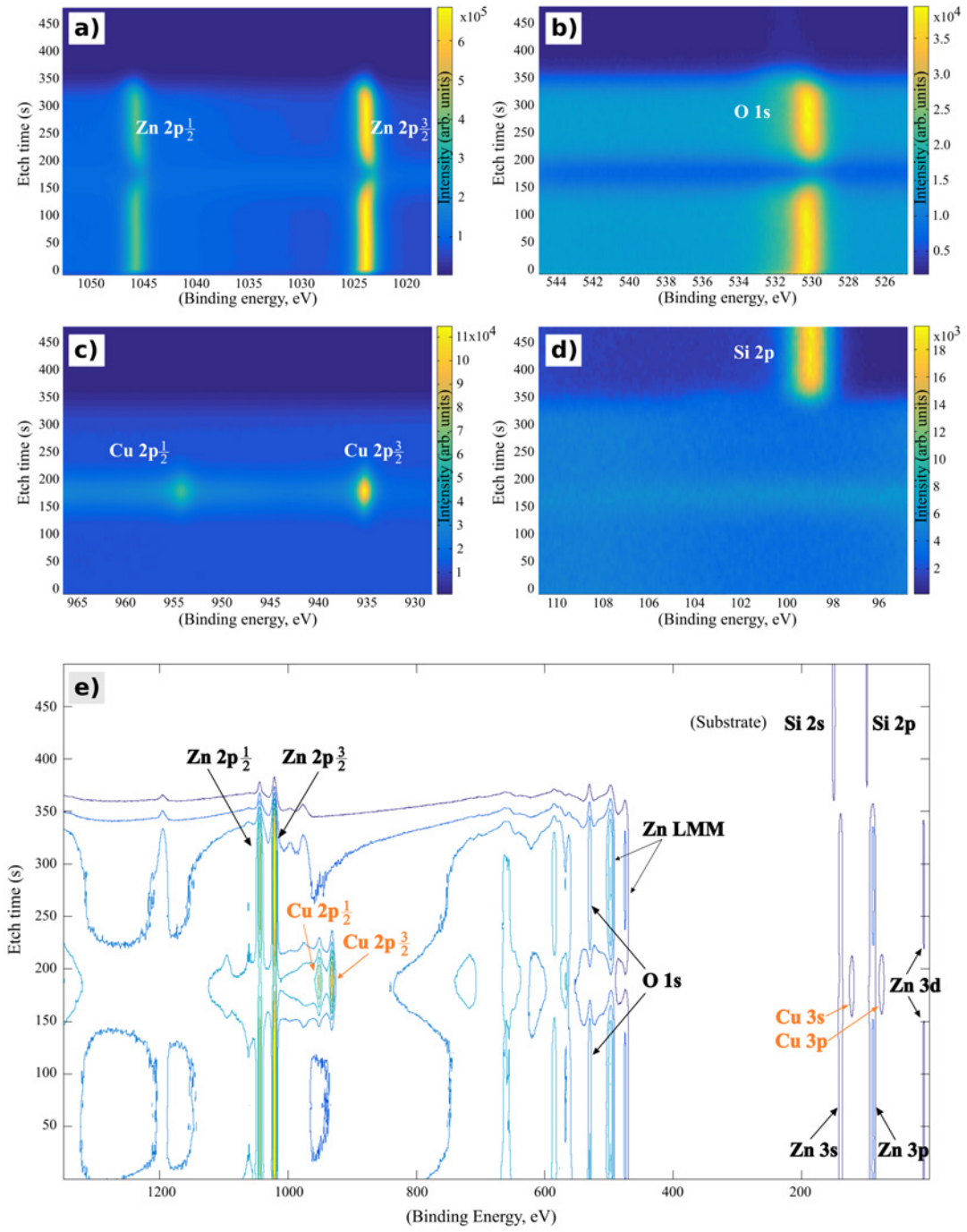

Figure 7.5: XPS investigation of a $ZnO/Cu/ZnO$ sandwich structure. a) - d)High resolution depth profile XPS signals of Zn 2p, O 1s, Cu 2p and Si 2p peaks, respectively. e) Contour plot of survey XPS depth-profile.

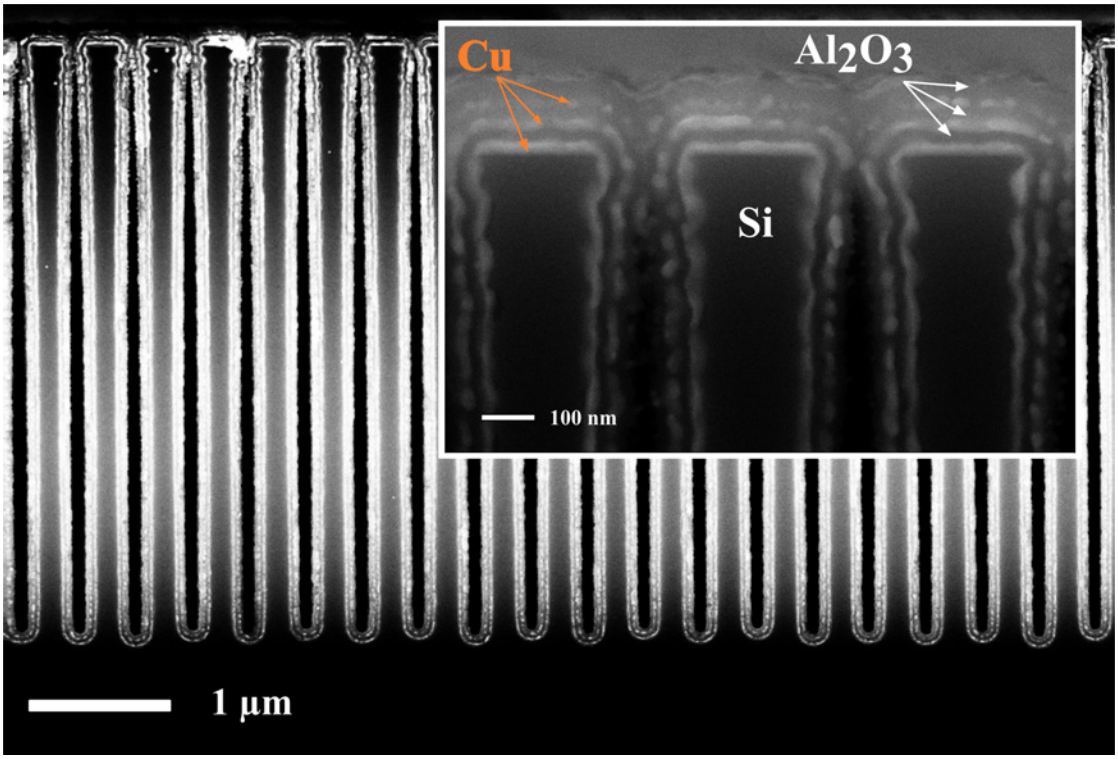

Figure 7.6: Al_2O_3/Cu multilayers deposited on a Si trench template.

7.2.5 TiN Platform

Along with Cu, structures made of TiN can be implemented in the visible wavelength range [151]. Some of plasmonic structures based on TiN have already been reported [63]. The current ALD equipment[2] did not support TiN deposition, although is is well explored and implemented process [51]. Collaborators from Birck Nanotechnology Center of Purdue University in US tried to nitrodize the TiO_2 pillars described in Chapter 4 using a conventional nitridation technique [62] in order to turn TiO_2 into TiN in nitrogen atmosphere. However, they only achieved partial transformation. Figure 7.7 a) and b) illustrates TiO_2 pillars before and after nitridation.

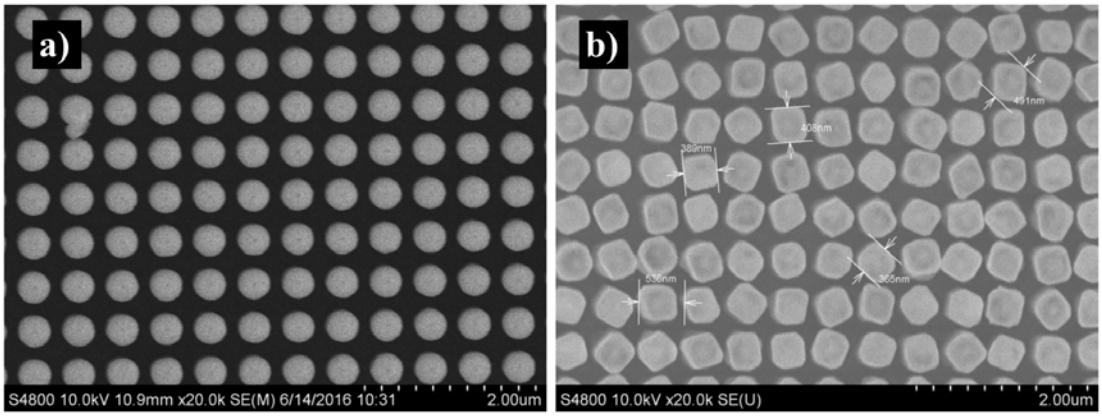

Figure 7.7: TiN pillars. a) Received TiO_2 pillars and b) Oxy-nitride pillars after the nitridation process.

7.2.6 TiC_x Deposition

The last ALD process which has been tested during these thesis is the TiC_x. Material is reported to be plasmonic in the visible-near infrared range, although having high losses compared to TiN [207]. The interesting part is the possibility to grow it by ALD using conventional TMA and $TiCl_4$ precursors. Several papers reported this possibility [208], [209]. The attempt to grow TiC_x is shown in Figure 7.8. XPS measurements showed that deposited coatings contain a big amount of impurities: 10% of Cl, 5-10% of O and traces of Al. The presence of Al can be explained by the fact that deposition temperature was 350 $^{\circ}C$ and it is above the acceptable level for the TMA precursor. Nevertheless, the coating can be used in other cases. A layer with a thickness of 40 nm, shown in Figure 7.8, was grown

[2]Picosun R200 Thermal tool [53]

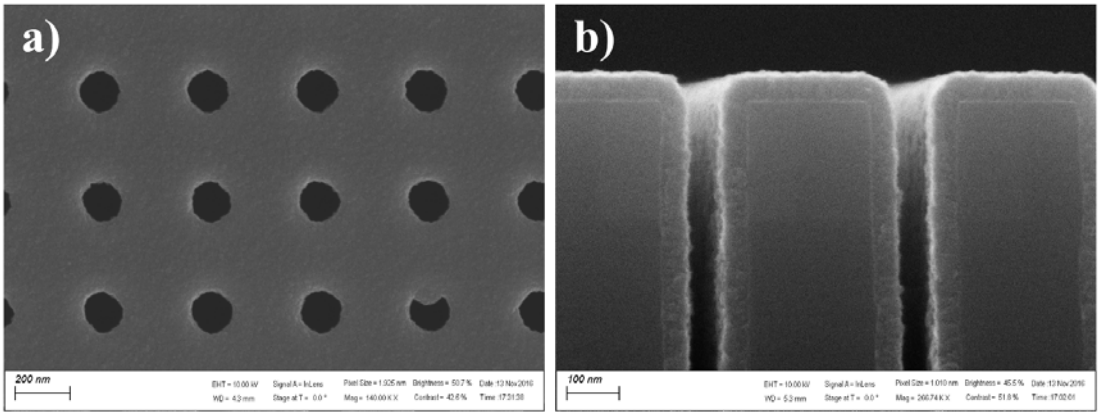

Figure 7.8: ALD Deposition of TiC_x. Conformal growth is observed. a) Deposition on a Si hole template (top view). b) Deposition on Si trenches (cross-sectional view).

on a glass substrate. Resistivity measurements showed a value of approximately 100 $\Omega/\square$. This is low compared to the best AZO films grown at 250 $°C$, despite being only 40 nm thick. Such a property can potentially be implemented in the nanofabrication of any metallic structures suitable for electroplating [44].

BIBLIOGRAPHY

[1] V. G. Veselago, "The electrodynamics of substances with simultaneously negative values of permittivity and permeability," *Soviet Physics Uspekhi*, vol. 10, pp. 509–514, apr 1968.

[2] M. A. Noginov, Y. A. Barnakov, G. Zhu, T. Tumkur, H. Li, and E. E. Narimanov, "Bulk photonic metamaterial with hyperbolic dispersion," *Applied Physics Letters*, vol. 94, no. 15, 2009.

[3] P. Shekhar, J. Atkinson, and Z. Jacob, "Hyperbolic metamaterials: fundamentals and applications," *Nano Convergence*, vol. 1, no. 1, p. 14, 2014.

[4] S. Jahani and Z. Jacob, "All-dielectric metamaterials," *Nature Nanotechnology*, vol. 11, no. 1, pp. 23–36, 2016.

[5] S. S. Kruk, Z. J. Wong, E. Pshenay-Severin, K. O'Brien, D. N. Neshev, Y. S. Kivshar, and X. Zhang, "Magnetic hyperbolic optical metamaterials," *Nature Communications*, vol. 7, p. 11329, 2016.

[6] Maier A. S., *Plasmonics: Fundamentals and Applications*, vol. 677. Boston, MA: Springer US, sep 2007.

[7] Y. Liu, G. Bartal, and X. Zhang, "All-angle negative refraction and imaging in a bulk medium made of metallic nanowires in the visible region," *Optics Express*, vol. 16, p. 15439, sep 2008.

[8] P. A. Belov, "Backward waves and negative refraction in uniaxial dielectrics with negative dielectric permittivity along the anisotropy axis," *Microwave and Optical Technology Letters*, vol. 37, no. 4, pp. 259–263, 2003.

[9] A. Poddubny, I. Iorsh, P. Belov, and Y. Kivshar, "Corrigendum: Hyperbolic metamaterials," *Nature Photonics*, vol. 8, no. 1, pp. 78–78, 2013.

[10] B. Wood, J. B. Pendry, and D. P. Tsai, "Directed subwavelength imaging using a layered metal-dielectric system," *Physical Review B*, vol. 74, p. 115116, sep 2006.

[11] L. Ferrari, C. Wu, D. Lepage, X. Zhang, and Z. Liu, "Hyperbolic metamaterials and their applications," *Progress in Quantum Electronics*, vol. 40, pp. 1–40, mar 2015.

[12] J. Sun, N. M. Litchinitser, and J. Zhou, "Indefinite by Nature: From Ultraviolet to Terahertz," *ACS Photonics*, vol. 1, no. 4, pp. 293–303, 2014.

[13] E. E. Narimanov and A. V. Kildishev, "Metamaterials: Naturally hyperbolic," *Nature Photonics*, vol. 9, pp. 214–216, mar 2015.

[14] M. Esslinger, R. Vogelgesang, N. Talebi, W. Khunsin, P. Gehring, S. de Zuani, B. Gompf, and K. Kern, "Tetradymites as Natural Hyperbolic Materials for the Near-Infrared to Visible," *ACS Photonics*, vol. 1, pp. 1285–1289, dec 2014.

[15] M. Shahzad, G. Medhi, R. E. Peale, W. R. Buchwald, J. W. Cleary, R. Soref, G. D. Boreman, and O. Edwards, "Infrared surface plasmons on heavily doped silicon," *Journal of Applied Physics*, vol. 110, no. 12, 2011.

[16] V. N. Guilengui, L. Cerutti, J. B. Rodriguez, E. Tournie, and T. Taliercio, "Localized surface plasmon resonances in highly doped semiconductors nanostructures," *Applied Physics Letters*, vol. 101, no. 161113, pp. 1–4, 2012.

[17] W. Cai and V. Shalaev, *Optical Metamaterials*. New York, NY: Springer New York, 2010.

[18] N. Engheta, "Pursuing Near-Zero Response," *Science*, vol. 340, pp. 286–287, apr 2013.

[19] S. Molesky, C. J. Dewalt, and Z. Jacob, "High temperature epsilon-near-zero and epsilon-near-pole metamaterial emitters for thermophotovoltaics.," *Optics express*, vol. 21 Suppl 1, no. January, pp. A96–110, 2013.

[20] H. N. S. Krishnamoorthy, Z. Jacob, E. Narimanov, I. Kretzschmar, and V. M. Menon, "Topological transitions in metamaterials.," *Science (New York, N.Y.)*, vol. 336, no. 6078, pp. 205–209, 2012.

[21] P. R. West, S. Ishii, G. V. Naik, N. K. Emani, V. M. Shalaev, and A. Boltasseva, "Searching for better plasmonic materials," *Laser and Photonics Reviews*, vol. 4, no. 6, pp. 795–808, 2010.

[22] J. Yao, Y.-l. Wang, K.-T. Tsai, Z. Liu, X. Yin, G. Bartal, A. M. Stacy, Y.-L. Wang, and X. Zhang, "Design, fabrication and characterization of indefinite metamaterials of nanowires," *Philosophical Transactions of the Royal Society A: Mathematical, Physical and Engineering Sciences*, vol. 369, pp. 3434–3446, sep 2011.

[23] J. Elser, R. Wangberg, V. A. Podolskiy, and E. E. Narimanov, "Nanowire metamaterials with extreme optical anisotropy," *Applied Physics Letters*, vol. 89, no. 26, p. 261102, 2006.

[24] Z. Jacob, I. I. Smolyaninov, and E. E. Narimanov, "Broadband Purcell effect: Radiative decay engineering with metamaterials," *Applied Physics Letters*, vol. 100, no. 18, 2012.

[25] S. A. Biehs, M. Tschikin, and P. Ben-Abdallah, "Hyperbolic metamaterials as an analog of a blackbody in the near field," *Physical Review Letters*, vol. 109, no. 10, pp. 1–5, 2012.

[26] J. Li, L. Fok, X. Yin, G. Bartal, and X. Zhang, "Experimental demonstration of an acoustic magnifying hyperlens.," *Nature Materials*, vol. 8, no. 12, pp. 931–934, 2009.

[27] I. I. Smolyaninov, Y. J. Hung, and E. Hwang, "Experimental modeling of cosmological inflation with metamaterials," *Physics Letters, Section A: General, Atomic and Solid State Physics*, vol. 376, no. 38-39, pp. 2575–2579, 2012.

[28] Z. Liu, H. Lee, Y. Xiong, C. Sun, and X. Zhang, "Far-Field Optical Hyperlens Magnifying Sub-Diffraction-Limited Objects," *Science*, vol. 315, pp. 1686–1686, mar 2007.

[29] S. A. Ramakrishna, J. B. Pendry, M. C. K. Wiltshire, and W. J. Stewart, "Imaging the near field," *Journal of Modern Optics*, vol. 50, pp. 1419–1430, jun 2003.

[30] I. I. Smolyaninov, "Optical microscopy beyond the diffraction limit," *HFSP Journal*, vol. 2, pp. 129–131, jun 2008.

[31] T. Repän, A. V. Lavrinenko, and S. V. Zhukovsky, "Dark-field hyperlens: Super-resolution imaging of weakly scattering objects," *Optics Express*, vol. 23, no. 19, p. 25350, 2015.

[32] A. A. High, R. C. Devlin, A. Dibos, M. Polking, D. S. Wild, J. Perczel, N. P. de Leon, M. D. Lukin, and H. Park, "Visible-frequency hyperbolic metasurface," *Nature*, vol. 522, pp. 192–196, jun 2015.

[33] X. Li, L. Jiao, H. Xu, Y. Lu, C. Zhu, J. Duan, X. Zhang, N. Dai, and W. Song, "Near-infrared subwavelength imaging using Al:ZnO-based near-field superlens," *Optical Materials Express*, vol. 6, no. 12, p. 3892, 2016.

[34] N. Yu and F. Capasso, "Flat optics with designer metasurfaces," *Nature Materials*, vol. 13, no. 2, pp. 139–150, 2014.

[35] D. Lu and Z. Liu, "Hyperlenses and metalenses for far-field super-resolution imaging.," *Nature communications*, vol. 3, p. 1205, 2012.

[36] J. Rho, Z. Ye, Y. Xiong, X. Yin, Z. Liu, H. Choi, G. Bartal, and X. Zhang, "Spherical hyperlens for two-dimensional sub-diffractional imaging at visible frequencies.," *Nature Communications*, vol. 1, no. 9, p. 143, 2010.

[37] Y. Xiong, Z. Liu, and X. Zhang, "Projecting deep-subwavelength patterns from diffraction-limited masks using metal-dielectric multilayers," *Applied Physics Letters*, vol. 93, no. 11, pp. 10–13, 2008.

[38] S. Franssila, "Introduction," in *Introduction to Microfabrication*, pp. 1–13, Chichester, UK: John Wiley & Sons, Ltd, nov 2010.

[39] Y. Xiong, Z. Liu, and X. Zhang, "A simple design of flat hyperlens for lithography and imaging with half-pitch resolution down to 20 nm," *Applied Physics Letters*, vol. 94, no. 20, pp. 10–13, 2009.

[40] C. L. Cortes, W. Newman, S. Molesky, and Z. Jacob, "Quantum nanophotonics using hyperbolic metamaterials," *Journal of Optics*, vol. 14, no. 6, p. 063001, 2012.

[41] S. Ishii, A. V. Kildishev, E. Narimanov, V. M. Shalaev, and V. P. Drachev, "Sub-wavelength interference pattern from volume plasmon polaritons in a hyperbolic medium," *Laser and Photonics Reviews*, vol. 7, no. 2, pp. 265–271, 2013.

[42] X. Yang, J. Yao, J. Rho, X. Yin, and X. Zhang, "Experimental realization of three-dimensional indefinite cavities at the nanoscale with anomalous scaling laws," *Nature Photonics*, vol. 6, pp. 450–454, jun 2012.

[43] L. Leandro, R. Malureanu, N. Rozlosnik, and A. Lavrinenko, "Ultrathin, Ultrasmooth Gold Layer on Dielectrics without the Use of Additional Metallic Adhesion Layers," *ACS Applied Materials and Interfaces*, vol. 7, no. 10, pp. 5797–5802, 2015.

[44] M. Schlesinger and M. Paunovic, "Modern Electroplating," in *Modern Electroplating*, pp. i–xviii, Hoboken, NJ, USA: John Wiley & Sons, Inc., feb 2011.

[45] S. M. George, "Atomic layer deposition: an overview," *Polymer*, vol. 1550, p. 125, 2010.

[46] M. B. E. Griffiths, P. J. Pallister, D. J. Mandia, and S. T. Barry, "Atomic Layer Deposition of Gold Metal," *Chemistry of Materials*, vol. 28, pp. 44–46, jan 2016.

[47] A. Shevjakov, G. Kusnetsowa, and W. Aleskovskii, "Interactions of the tetrachlorides of titanium and germanium with hydrated silicon oxide," in *Proceedings of the Second USSR Conference on High-Temperature Chemistry of Oxides*, (Leningrad), pp. 149–155, Nauka, Leningrad, USSR, 1965.

[48] T. Suntola and J. Antson, "Method for producing compound thin films.pdf," *Patent US 4058430*, 1977.

[49] R. L. Puurunen, "Surface chemistry of atomic layer deposition: A case study for the trimethylaluminum/water process," *Journal of Applied Physics*, vol. 97, no. 12, 2005.

[50] C. S. Hwang and C. Y. Yoo, *Atomic Layer Deposition for Semiconductors*. 2014.

[51] N. Pinna and M. Knez, *Atomic Layer Deposition of Nanostructured Materials*. Weinheim, Germany: Wiley-VCH Verlag GmbH & Co. KGaA, nov 2011.

[52] H. B. Profijt, S. E. Potts, M. C. M. van de Sanden, and W. M. M. Kessels, "Plasma-Assisted Atomic Layer Deposition: Basics, Opportunities, and Challenges," *Journal of Vacuum Science & Technology A: Vacuum, Surfaces, and Films*, vol. 29, no. 5, p. 050801, 2011.

[53] "http://www.picosun.com/en/home/."

[54] G. S. Higashi and C. G. Fleming, "Sequential surface chemical reaction limited growth of high quality Al2O3 dielectrics," *Applied Physics Letters*, vol. 55, no. 19, p. 1963, 1989.

[55] "https://www.zeiss.com/."

[56] J. Aarik, A. Aidla, T. Uustare, and V. Sammelselg, "Morphology and structure of TiO 2 thin films grown by atomic layer deposition," *Journal of crystal growth*, vol. 148, pp. 268–275, 1995.

[57] J. Aarik, A. Aidla, A.-A. Kiisler, T. Uustare, and V. Sammelselg, "Effect of crystal structure on optical properties of TiO2 films grown by atomic layer deposition," *Thin Solid Films*, vol. 305, pp. 270–273, aug 1997.

[58] J. Ferguson, A. Yoder, A. Weimer, and S. George, "TiO2 atomic layer deposition on ZrO2 particles using alternating exposures of TiCl4 and H2O," *Applied Surface Science*, vol. 226, pp. 393–404, mar 2004.

[59] R. L. Puurunen, T. Sajavaara, E. Santala, V. Miikkulainen, T. Saukkonen, M. Laitinen, and M. Leskelä, "Controlling the Crystallinity and Roughness of Atomic Layer Deposited Titanium Dioxide Films," *Journal of Nanoscience and Nanotechnology*, vol. 11, pp. 8101–8107, sep 2011.

[60] Y. Huang, G. Pandraud, and P. M. Sarro, "Characterization of low temperature deposited atomic layer deposition TiO2 for MEMS applications," *Journal of Vacuum Science & Technology A: Vacuum, Surfaces, and Films*, vol. 31, no. 1, p. 01A148, 2013.

[61] W.-J. J. Lee and M.-H. Hon, "Space-Limited Crystal Growth Mechanism of TiO2 Films by Atomic Layer Deposition," *The Journal of Physical Chemistry C*, vol. 114, pp. 6917–6921, apr 2010.

[62] C. Jiménez and M. Langlet, "Formation of TiN by nitridation of TiO2 films deposited by ultrasonically assisted sol-gel technique," *Surface and Coatings Technology*, vol. 68-69, pp. 249–252, dec 1994.

[63] L. Berthod, V. Gâté, M. Bichotte, M. Langlet, F. Vocanson, C. Jimenez, D. Jamon, I. Verrier, C. Veillas, O. Parriaux, and Y. Jourlin, "Direct fabrication of a metal-like TiN-based plasmonic grating using nitridation of a photo-patternable TiO_2 sol-gel film," *Optical Materials Express*, vol. 6, p. 2508, aug 2016.

[64] V. Lujala, J. Skarp, M. Tammenmaa, and T. Suntola, "Atomic layer epitaxy growth of doped zinc oxide thin films from organometals," *Applied Surface Science*, vol. 82-83, pp. 34–40, dec 1994.

[65] J. I. Skarp, P. J. Soininen, and P. T. Soininen, "ALE-reactor for large area depositions," *Applied Surface Science*, vol. 112, no. 0, pp. 251–254, 1997.

[66] E. Guziewicz, M. Godlewski, L. Wachnicki, T. a. Krajewski, G. Luka, S. Gieraltowska, R. Jakiela, a. Stonert, W. Lisowski, M. Krawczyk, J. W. Sobczak, and a. Jablonski, "ALD grown zinc oxide with controllable electrical properties," *Semiconductor Science and Technology*, vol. 27, no. 7, p. 074011, 2012.

[67] J. A. Libera, J. W. Elam, and M. J. Pellin, "Conformal ZnO coatings on high surface area silica gel using atomic layer deposition," *Thin Solid Films*, vol. 516, no. 18, pp. 6158–6166, 2008.

[68] Y.-S. Min, C. J. An, S. K. Kim, J. Song, and C. S. Hwang, "Growth and characterization of conducting ZnO thin films by atomic layer deposition," *Bull. Korean Chem. Soc.*, vol. 31, no. 9, pp. 2503–2508, 2010.

[69] J. Ren, "Initial growth mechanism of atomic layer deposition of ZnO on the hydroxylated Si(100)-2x1: A density functional theory study," *Applied Surface Science*, vol. 255, pp. 5742–5745, mar 2009.

[70] C. Thiandoume, V. Sallet, R. Triboulet, and O. Gorochov, "Decomposition kinetics of tertiarybutanol and diethylzinc used as precursor sources for the growth of ZnO," *Journal of Crystal Growth*, vol. 311, pp. 1411–1415, feb 2009.

[71] Q. Hou, F. Meng, and J. Sun, "Electrical and optical properties of Al-doped ZnO and ZnAl 2 O 4 films prepared by atomic layer deposition," pp. 1–8, 2013.

[72] V. Miikkulainen, M. Leskela, M. Ritala, and R. L. Puurunen, "Crystallinity of inorganic films grown by atomic layer deposition: Overview and general trends," *Journal of Applied Physics*, vol. 113, no. 2, p. 021301, 2013.

[73] L. Niinisto, "Studies of metallic thin film growth in an atomic layer epitaxy reactor using," *Applied Surface Science*, vol. 157, pp. 151–158, 2000.

[74] A. Mane and S. Shivashankar, "Growth of (1 1 1)-textured copper thin films by atomic layer deposition," *Journal of Crystal Growth*, vol. 275, no. 1-2, pp. e1253–e1257, 2005.

[75] M. Juppo, M. Vehkamaki, M. Ritala, and M. Leskela, "Deposition of molybdenum thin films by an alternate supply of MoCl5 and Zn," *Journal of Vacuum Science & Technology a-Vacuum Surfaces and Films*, vol. 16, no. 5, pp. 2845–2850, 1998.

[76] J. Huo, R. Solanki, and J. McAndrew, "Characteristics of copper films produced via atomic layer deposition," *Journal of Materials Research*, vol. 17, no. 9, pp. 2394–2398, 2002.

[77] B. P. Mbrtensson and J.-o. Carlsson, "Atomic Layer Epitaxy of Copper on Tantalum," *Chemical Vapor Deposition*, vol. 3, no. I, pp. 45–50, 1997.

[78] Z. Li, A. Rahtu, and R. G. Gordon, "Atomic Layer Deposition of Ultrathin Copper Metal Films from a Liquid Copper(I) Amidinate Precursor," *Journal of The Electrochemical Society*, vol. 153, no. 11, p. C787, 2006.

[79] B. Lim, A. Rahtu, and R. G. Gordon, "Atomic layer deposition of transition metals," *Nature Materials*, vol. 2, no. November, pp. 749–754, 2003.

[80] R. Solanki, "Atomic Layer Deposition of Copper Seed Layers," *Electrochemical and Solid-State Letters*, vol. 3, no. 10, p. 479, 1999.

[81] A. U. Mane and S. A. Shivashankar, "Atomic layer chemical vapour deposition of copper," *Materials Science in Semiconductor Processing*, vol. 7, no. 4-6 SPEC. ISS., pp. 343–347, 2004.

[82] T. J. Knisley, T. C. Ariyasena, T. Sajavaara, M. J. Saly, and C. H. Winter, "Low Temperature Growth of High Purity, Low Resistivity Copper Films by Atomic Layer Deposition," *Chemistry of Materials*, vol. 23, pp. 4417–4419, oct 2011.

[83] G. Dey and S. D. Elliott, "Copper reduction and atomic layer deposition by oxidative decomposition of formate by hydrazine," *RSC Advances*, vol. 4, p. 34448, jul 2014.

[84] B. H. Lee, J. K. Hwang, J. W. Nam, S. U. Lee, J. T. Kim, S. M. Koo, A. Baunemann, R. A. Fischer, and M. M. Sung, "Low-temperature atomic layer deposition of copper metal thin films: Self-limiting surface reaction of copper dimethylamino-2-propoxide with diethylzinc," *Angewandte Chemie - International Edition*, vol. 48, no. 25, pp. 4536–4539, 2009.

[85] G. Dey and S. D. Elliott, "Mechanism for the Atomic Layer Deposition of Copper Using Diethylzinc as the Reducing Agent: A Density Functional Theory Study Using Gas-Phase Molecules as a Model," *The Journal of Physical Chemistry A*, vol. 116, pp. 8893–8901, sep 2012.

[86] E. J. Warner, C. J. Cramer, and W. L. Gladfelter, "Atomic layer deposition of zinc oxide: Understanding the reactions of ozone with diethylzinc," *Journal of Vacuum Science & Technology A: Vacuum, Surfaces, and Films*, vol. 31, no. 4, p. 041504, 2013.

[87] S. Keun Kim, C. Seong Hwang, S.-H. Ko Park, and S. Jin Yun, "Comparison between ZnO films grown by atomic layer deposition using H2O or O3 as oxidant," *Thin Solid Films*, vol. 478, no. 1-2, pp. 103–108, 2005.

[88] H. Yuan, B. Luo, W. L. Gladfelter, and S. Campbell, "(Invited) Ozone Assisted ALD of Doped ZnO as a Transparent Metal," *ECS Transactions*, vol. 45, no. 3, pp. 389–400, 2012.

[89] L. Aarik, T. Arroval, R. Rammula, H. Mändar, V. Sammelselg, and J. Aarik, "Atomic layer deposition of TiO2 from TiCl4 and O3," *Thin Solid Films*, vol. 542, pp. 100–107, sep 2013.

[90] T. Iivonen, J. Hämäläinen, B. Marchand, K. Mizohata, M. Mattinen, G. Popov, J. Kim, R. A. Fischer, and M. Leskelä, "Low-temperature atomic layer deposition of copper(II) oxide thin films," *Journal of Vacuum Science & Technology A: Vacuum, Surfaces, and Films*, vol. 34, no. 1, p. 01A109, 2016.

[91] J. P. Klesko, C. M. Thrush, and C. H. Winter, "Thermal Atomic Layer Deposition of Titanium Films Using Titanium Tetrachloride and 2-Methyl-1,4-bis(trimethylsilyl)-2,5-cyclohexadiene or 1,4-Bis(trimethylsilyl)-1,4-dihydropyrazine," *Chemistry of Materials*, vol. 27, pp. 4918–4921, jul 2015.

[92] M. Joost, *Synthesis and Original Reactivity of Copper and Gold Complexes*. Springer Theses, Cham: Springer International Publishing, 2015.

[93] A. Szeghalmi, M. Helgert, R. Brunner, F. Heyroth, U. Gösele, and M. Knez, "Atomic layer deposition of Al2O3 and TiO2 multilayers for applications as bandpass filters and antireflection coatings," *Applied Optics*, vol. 48, no. 9, pp. 1727–1732, 2009.

[94] A. I. Abdulagatov, Y. Yan, J. R. Cooper, Y. Zhang, Z. M. Gibbs, A. S. Cavanagh, R. G. Yang, Y. C. Lee, and S. M. George, "Al2O3 and TiO2 Atomic Layer Deposition on Copper for Water Corrosion Resistance," *ACS Applied Materials & Interfaces*, vol. 3, no. 12, pp. 4593–4601, 2011.

[95] T. K. Minton, B. Wu, J. Zhang, N. F. Lindholm, A. I. Abdulagatov, J. O'Patchen, S. M. George, and M. D. Groner, "Protecting polymers in space with atomic layer deposition coatings," *ACS Applied Materials and Interfaces*, vol. 2, no. 9, pp. 2515–2520, 2010.

[96] K. Kukli, M. Ritala, M. Leskelä, J. Sundqvist, L. Oberbeck, J. Heitmann, U. Schröder, J. Aarik, and A. Aidla, "Influence of TiO2 incorporation in HfO2 and Al2O3 based capacitor dielectrics," *Thin Solid Films*, vol. 515, no. 16 SPEC. ISS., pp. 6447–6451, 2007.

[97] P. Yeh, *Optical Waves in Layered Media*. 1988.

[98] D. N. Chigrin, A. V. Lavrinenko, D. A. Yarotsky, and S. V. Gaponenko, "Observation of total omnidirectional reflection from a one-dimensional dielectric lattice," *Applied Physics A*, vol. 68, no. 1, p. 4, 1998.

[99] J. J. D. Joannopoulos, S. Johnson, J. N. J. Winn, and R. R. D. Meade, *Photonic crystals: molding the flow of light*. 2008.

[100] H. Herzig Sheinfux, I. Kaminer, Y. Plotnik, G. Bartal, and M. Segev, "Subwavelength multilayer dielectrics: Ultrasensitive transmission and breakdown of effective-medium theory," *Physical Review Letters*, vol. 113, no. 24, pp. 1–5, 2014.

[101] A. Andryieuski, A. V. Lavrinenko, and S. V. Zhukovsky, "Anomalous effective medium approximation breakdown in deeply subwavelength all- dielectric photonic multilayers," *Nanotechnology*, vol. 26, no. 18, p. 184001, 2015.

[102] "http://www.tempress.nl/."

[103] S. V. Zhukovsky, A. Andryieuski, O. Takayama, E. Shkondin, R. Malureanu, F. Jensen, and A. V. Lavrinenko, "Experimental Demonstration of Effective Medium Approximation Breakdown in Deeply Subwavelength All-Dielectric Multilayers," *Physical Review Letters*, vol. 115, no. 17, 2015.

[104] G. Dingemans and W. M. M. Kessels, "Status and prospects of Al2O3-based surface passivation schemes for silicon solar cells," *Journal of Vacuum Science & Technology A: Vacuum, Surfaces, and Films*, vol. 30, no. 4, p. 040802, 2012.

[105] K. Henkel, B. Seime, I. Paloumpa, K. Müller, and D. Schmeißer, "Buffer layer investigations on MFIS capacitors consisting of ferroelectric poly[vinylidene fluoride trifluoroethylene]," *IOP Conference Series: Materials Science and Engineering*, vol. 8, p. 012036, 2010.

[106] S. E. Potts, L. Schmalz, M. Fenker, B. Díaz, J. Światowska, V. Maurice, A. Seyeux, P. Marcus, G. Radnóczi, L. Tóth, and W. M. M. Kessels, "Ultra-Thin Aluminium Oxide Films Deposited by Plasma-Enhanced Atomic Layer Deposition for Corrosion Protection," *Journal of The Electrochemical Society*, vol. 158, no. 5, pp. C132–C138, 2011.

[107] M. Tallarida, M. Weisheit, K. Kolanek, M. Michling, H. J. Engelmann, and D. Schmeisser, "Atomic layer deposition of nanolaminate oxide films on Si," *Journal of Nanoparticle Research*, vol. 13, no. 11, pp. 5975–5983, 2011.

[108] C. Marichy, N. Donato, M. Latino, M. Georg Willinger, J.-P. Tessonnier, G. Neri, and N. Pinna, "Gas sensing properties and p-type response of ALD TiO ₂ coated carbon nanotubes," *Nanotechnology*, vol. 26, no. 2, p. 024004, 2015.

[109] I.-S. Yu, Y.-W. Wang, H.-E. Cheng, Z.-P. Yang, and C.-T. Lin, "Surface Passivation and Antireflection Behavior of ALD on n-Type Silicon for Solar Cells," *International Journal of Photoenergy*, vol. 2013, pp. 1–7, 2013.

[110] E. Jardinier, G. Pandraud, M. H. Pham, P. J. French, and P. M. Sarro, "Atomic layer deposition of TiO 2 photonic crystal waveguide biosensors," *Journal of Physics: Conference Series*, vol. 187, p. 012043, 2009.

[111] A. L. Linsebigler, A. L. Linsebigler, J. T. Yates Jr, G. Lu, G. Lu, and J. T. Yates, "Photocatalysis on TiO2 Surfaces: Principles, Mechanisms, and Selected Results," *Chemical Reviews*, vol. 95, no. 3, pp. 735–758, 1995.

[112] A. Rissanen and R. L. Puurunen, "Use of ALD thin film Bragg mirror stacks in tuneable visible light MEMS Fabry-Perot interferometers," *Advanced Fabrication Technologies for Micro/Nano Optics and Photonics V*, vol. 8249, pp. 1–9, 2012.

[113] V. A. Tolmachev, A. V. Baldycheva, S. A. Dyakov, K. Berwick, and T. S. Perova, "Optical contrast tuning in three-component one-dimensional photonic crystals," *Journal of Lightwave Technology*, vol. 28, no. 10, pp. 1521–1529, 2010.

[114] V. A. Tolmachev, E. V. Astrova, J. A. Pilyugina, T. S. Perova, R. A. Moore, and J. K. Vij, "1D photonic crystal fabricated by wet etching of silicon," *Optical Materials*, vol. 27, no. 5, pp. 831–835, 2005.

[115] G. Barillaro, L. Marsilio Strambini, V. Annovazzi-Lodi, and S. Merlo, "Optical characterization of high-order 1-D silicon photonic crystals," *IEEE Journal on Selected Topics in Quantum Electronics*, vol. 15, no. 5, pp. 1359–1367, 2009.

[116] A. Baldycheva, V. a. Tolmachev, T. S. Perova, Y. a. Zharova, E. V. Astrova, and K. Berwick, "Silicon photonic crystal filter with ultrawide passband characteristics.," *Optics letters*, vol. 36, no. 10, pp. 1854–1856, 2011.

[117] Y. Huang, G. Pandraud, and P. M. Sarro, "The atomic layer deposition array defined by etch-back technique: a new method to fabricate TiO2 nanopillars, nanotubes and nanochannel arrays.," *Nanotechnology*, vol. 23, no. 48, p. 485306, 2012.

[118] P. Moitra, Y. Yang, Z. Anderson, I. I. Kravchenko, D. P. Briggs, and J. Valentine, "Realization of an all-dielectric zero-index optical metamaterial," *Nature Photonics*, vol. 7, no. 10, pp. 791–795, 2013.

[119] T. Dhakal, D. Vanhart, R. Christian, A. Nandur, A. Sharma, and C. R. Westgate, "Growth morphology and electrical/optical properties of Al-doped ZnO thin films grown by atomic layer deposition," *Journal of Vacuum Science & Technology A: Vacuum, Surfaces, and Films*, vol. 30, no. 2, p. 021202, 2012.

[120] E.-H. Cho, H.-S. Kim, B.-H. Cheong, O. Prudnikov, W. Xianyua, J.-S. Sohn, D.-J. Ma, H.-Y. Choi, N.-C. Park, and Y.-P. Park, "Two-dimensional photonic crystal color filter development.," *Optics express*, vol. 17, no. 10, pp. 8621–8629, 2009.

[121] K. V. Sreekanth, Y. Alapan, M. ElKabbash, E. Ilker, M. Hinczewski, U. A. Gurkan, A. De Luca, and G. Strangi, "Extreme sensitivity biosensing platform based on hyperbolic metamaterials," *Nature Materials*, vol. 15, no. March, pp. 4–11, 2016.

[122] A. V. Kabashin, P. Evans, S. Pastkovsky, W. Hendren, G. a. Wurtz, R. Atkinson, R. Pollard, V. a. Podolskiy, and a. V. Zayats, "Plasmonic nanorod metamaterials for biosensing.," *Nature materials*, vol. 8, no. 11, pp. 867–71, 2009.

[123] S. Surdo, S. Merlo, F. Carpignano, L. M. Strambini, C. Trono, A. Giannetti, F. Baldini, and G. Barillaro, "Optofluidic microsystems with integrated vertical one-dimensional photonic crystals for chemical analysis," *Lab on a Chip*, vol. 12, no. 21, p. 4403, 2012.

[124] E. Rizzi, L. Mauri, M. Moraja, A. Conte, A. Bonucci, G. Longoni, and M. Amiotti, "Front-matter," in *Handbook of Silicon Based MEMS Materials and Technologies*, pp. i–iii, Elsevier, 2010.

[125] "http://www.spts.com."

[126] D. Mitchell, D. Attard, K. Finnie, G. Triani, C. Barbé, C. Depagne, and J. Bartlett, "TEM and ellipsometry studies of nanolaminate oxide films prepared using atomic layer deposition," *Applied Surface Science*, vol. 243, no. 1-4, pp. 265–277, 2005.

[127] J.-C. Woo, Y.-s. Chun, Y.-h. Joo, and C.-i. Kim, "The dry etching property of TiO2 thin films using metal-insulator-metal capacitor in inductively coupled plasma system," *Vacuum*, vol. 86, pp. 2152–2157, jul 2012.

[128] S. Tegen and P. Moll, "Etch Characteristics of Al2O3 in ICP and MERIE Plasma Etchers," *Journal of The Electrochemical Society*, vol. 152, no. 4, p. G271, 2005.

[129] L. Sainiemi and S. Franssila, "Mask material effects in cryogenic deep reactive ion etching," *Journal of Vacuum Science & Technology B: Microelectronics and Nanometer Structures*, vol. 25, no. 3, p. 801, 2007.

[130] K. Hudec, Boris, A. Tarre, J. H. Han, S. Han, A. Rosová, W. Lee, A. Kasikov, S. J. Song, J. Aarik, C. S. Hwang, and K. Fröhlich, "Electrical properties of TiO2-based MIM capacitors deposited by TiCl4 and TTIP based atomic layer deposition processes," *Microelectronic Engineering*, vol. 88, no. 7, pp. 1514–1516, 2011.

[131] E. Shkondin, O. Takayama, J. M. Lindhard, P. V. Larsen, M. D. Mar, F. Jensen, and A. V. Lavrinenko, "Fabrication of high aspect ratio TiO2 and Al2O3 nanogratings by atomic layer deposition," *Journal of Vacuum Science & Technology A: Vacuum, Surfaces, and Films*, vol. 34, p. 031605, may 2016.

[132] A. P. Alekhin, a. a. Chouprik, S. a. Gudkova, a. M. Markeev, Y. Y. Lebedinskii, Y. a. Matveyev, and a. V. Zenkevich, "Structural and electrical properties of TixAl(1-x)O(y) thin films grown by atomic layer deposition," *Journal of Vacuum Science & Technology B: Microelectronics and Nanometer Structures*, vol. 29, no. 1, p. 01A302, 2011.

[133] L. Vertchenko, E. Shkondin, R. Malureanu, and C. H. Monken, "Laguerre-Gauss beam generation in IR and UV by subwavelength surface-relief gratings," nov 2016.

[134] L. Marrucci, C. Manzo, and D. Paparo, "Optical spin-to-orbital angular momentum conversion in inhomogeneous anisotropic media," *Physical Review Letters*, vol. 96, pp. 1–4, dec 2007.

[135] M. Padgett and L. Allen, "Light with a twist in its tail," *Contemporary Physics*, vol. 41, pp. 275–285, sep 2000.

[136] L. Marrucci, S. Fisiche, N. Federico, and M. S. Angelo, "Rotating light with light : Generation of helical modes of light by spin-to-orbital angular momentum conversion in inhomogeneous liquid crystals," *Liquid Crystals*, vol. 6587, pp. 1–11, 2007.

[137] S. Van Enk and G. Nienhuis, "Commutation Rules and Eigenvalues of Spin and Orbital Angular Momentum of Radiation Fields," *Journal of Modern Optics*, vol. 41, pp. 963–977, may 1994.

[138] S. Bennett, "Lasers," *Optics and Lasers in Engineering*, vol. 8, p. 70, jan 1988.

[139] P. Gregg, M. Mirhosseini, A. Rubano, L. Marrucci, E. Karimi, R. W. Boyd, and S. Ramachandran, "Q-plates as higher order polarization controllers for orbital angular momentum modes of fiber," *Optics Letters*, vol. 40, p. 1729, apr 2015.

[140] A. M. Yao and M. J. Padgett, "Orbital angular momentum: origins, behavior and applications," *Advances in Optics and Photonics*, vol. 3, p. 161, jun 2011.

[141] M. Padgett, "Light's twist," *Proceedings of the Royal Society A: Mathematical, Physical and Engineering Sciences*, vol. 470, pp. 20140633–20140633, oct 2014.

[142] D. Naidoo, F. S. Roux, A. Dudley, I. Litvin, B. Piccirillo, L. Marrucci, and A. Forbes, "Controlled generation of higher-order Poincaré sphere beams from a laser," *Nature Photonics*, vol. 10, pp. 327–332, mar 2016.

[143] L. Marrucci, "Generation of Helical Modes of Light by Spin-to-Orbital Angular Momentum Conversion in Inhomogeneous Liquid Crystals," *Molecular Crystals and Liquid Crystals*, vol. 488, pp. 148–162, sep 2008.

[144] E. Karimi, B. Piccirillo, E. Nagali, L. Marrucci, and E. Santamato, "Efficient generation and sorting of orbital angular momentum eigenmodes of light by thermally tuned q-plates," *Applied Physics Letters*, vol. 94, no. 23, p. 231124, 2009.

[145] E. Brasselet and C. Loussert, "Electrically controlled topological defects in liquid crystals as tunable spin-orbit encoders for photons," *Optics Letters*, vol. 36, p. 719, mar 2011.

[146] B. Piccirillo, V. D'Ambrosio, S. Slussarenko, L. Marrucci, and E. Santamato, "Photon spin-to-orbital angular momentum conversion via an electrically tunable q-plate," *Applied Physics Letters*, vol. 97, no. 24, p. 241104, 2010.

[147] L. Marrucci, C. Manzo, and D. Paparo, "Pancharatnam-Berry phase optical elements for wave front shaping in the visible domain: Switchable helical mode generation," *Applied Physics Letters*, vol. 88, no. 22, p. 221102, 2006.

[148] A. Niv, G. Biener, V. Kleiner, and E. Hasman, "Spiral phase elements obtained by use of discrete space-variant subwavelength gratings," *Optics Communications*, vol. 251, pp. 306–314, jul 2005.

[149] "http://www.jeol.co.jp/en/."

[150] "https://www.oxford-instruments.com/."

[151] G. V. Naik, B. Saha, J. Liu, S. M. Saber, E. a. Stach, J. M. K. Irudayaraj, T. D. Sands, V. M. Shalaev, and A. Boltasseva, "Epitaxial superlattices with titanium nitride as a plasmonic component for optical hyperbolic metamaterials.," *Proceedings of the National Academy of Sciences of the United States of America*, vol. 111, no. 21, pp. 7546–7551, 2014.

[152] O. K. Varghese, M. Paulose, and C. a. Grimes, "Long vertically aligned titania nanotubes on transparent conducting oxide for highly efficient solar cells.," *Nature nanotechnology*, vol. 4, no. 9, pp. 592–597, 2009.

[153] K. Nomura, H. Ohta, A. Takagi, T. Kamiya, M. Hirano, and H. Hosono, "Room-temperature fabrication of transparent flexible thin-film transistors using amorphous oxide semiconductors.," *Nature*, vol. 432, no. 7016, pp. 488–492, 2004.

[154] D.-J. Lee, H.-M. Kim, J.-Y. Kwon, H. Choi, S.-H. Kim, and K.-B. Kim, "Structural and Electrical Properties of Atomic Layer Deposited Al-Doped ZnO Films," *Advanced Functional Materials*, vol. 21, no. 3, pp. n/a–n/a, 2010.

[155] H. Kim, C. M. Gilmore, A. Piqué, J. S. Horwitz, H. Mattoussi, H. Murata, Z. H. Kafafi, and D. B. Chrisey, "Electrical, optical, and structural properties of indium-tin-oxide thin films for organic light emitting devices," *Journal of Applied Physics*, vol. 86, no. 11, p. 6451, 1999.

[156] E. B. Pollock and R. J. Lad, "Influence of dosing sequence and film thickness on structure and resistivity of Al-ZnO films grown by atomic layer deposition," *J. Vac. Sci. Technol., A*, vol. 32, no. May, p. 041516, 2014.

[157] T. Tynell, H. Yamauchi, M. Karppinen, R. Okazaki, and I. Terasaki, "Atomic layer deposition of Al-doped ZnO thin films," *Journal of Vacuum Science & Technology A: Vacuum, Surfaces, and Films*, vol. 31, no. 2013, p. 01A109, 2013.

[158] Y. Geng, Z.-Y. Xie, S.-S. Xu, Q.-Q. Sun, S.-J. Ding, H.-L. Lu, and D. W. Zhang, "Effects of Rapid Thermal Annealing on Structural, Luminescent, and Electrical Properties of Al-Doped ZnO Films Grown by Atomic Layer Deposition," *ECS Journal of Solid State Science and Technology*, vol. 1, no. 3, pp. N45–N48, 2012.

[159] P. Banerjee, W.-J. Lee, K.-r. Bae, S. B. Lee, and G. W. Rubloff, "Structural, electrical, and optical properties of atomic layer deposition Al-doped ZnO films," *Journal of Applied Physics*, vol. 108, no. 4, p. 043504, 2010.

[160] A. Crovetto, T. S. Ottsen, E. Stamate, D. Kjær, J. Schou, and O. Hansen, "On performance limitations and property correlations of Al-doped ZnO deposited by radio-frequency sputtering," *Journal of Physics D: Applied Physics*, vol. 49, no. 29, p. 295101, 2016.

[161] M. Seung Yeop, S. J. Baik, C. H. Lee, W. Y. Cho, and K. S. Lim, "Extremely transparent and conductive ZnO:Al thin films prepared by photo-assisted metalorganic chemical vapor deposition (photo-MOCVD) using AlCl3(6H2O) as new doping material," *Japanese Journal of Applied Physics*, vol. 36, no. 8, pp. 1078–1081, 1997.

[162] P. P. Sahay and R. K. Nath, "Al-doped ZnO thin films as methanol sensors," *Sensors and Actuators, B: Chemical*, vol. 134, no. 2, pp. 654–659, 2008.

[163] S.-K. Kim and J.-Y. Son, "Epitaxial ZnO Thin Films for the Application of Ethanol Gas Sensor: Thickness and Al-Doping Effects," *Electrochemical and Solid-State Letters*, vol. 12, no. 2, pp. J17–J19, 2009.

[164] H. Kim, A. Piqué, J. Horwitz, H. Murata, Z. Kafafi, C. Gilmore, and D. Chrisey, "Effect of aluminum doping on zinc oxide thin films grown by pulsed laser deposition for organic light-emitting devices," *Thin Solid Films*, vol. 377-378, pp. 798–802, 2000.

[165] H. Tanaka, K. Ihara, T. Miyata, H. Sato, and T. Minami, "Low resistivity polycrystalline ZnO : Al thin films prepared by pulsed laser deposition," *Journal of Vacuum Science & Technology A*, vol. 22, no. 4, pp. 1757–1762, 2004.

[166] C. T. Riley, J. S. T. Smalley, K. W. Post, D. N. Basov, Y. Fainman, D. Wang, Z. Liu, and D. J. Sirbuly, "High-Quality, Ultraconformal Aluminum-Doped Zinc Oxide Nanoplasmonic and Hyperbolic Metamaterials," *Small*, vol. 12, pp. 892–901, feb 2016.

[167] a. K. Pradhan, R. M. Mundle, K. Santiago, J. R. Skuza, B. Xiao, K. D. Song, M. Bahoura, R. Cheaito, and P. E. Hopkins, "Extreme tunability in aluminum doped zinc oxide plasmonic materials for near-infrared applications.," *Scientific reports*, vol. 4, p. 6415, 2014.

[168] "https://www.bruker.com/."

[169] P. Zaumseil, "High-resolution characterization of the forbidden Si 200 and Si 222 reflections," *Journal of Applied Crystallography*, vol. 48, pp. 528–532, 2015.

[170] M. Birkholz, "A Practical Guide to X-Ray Crystallography of Biomacro- molecules Surface and Thin Film Analysis Electron Accelerators as X-Ray Sources Microscopic X-Ray Fluorescence Analysis X-Ray Spectrometry X-ray Characterization of Materials," *X-Ray Spectrometry*, 2006.

[171] M. Latzel, M. Gobelt, G. Bronstrup, C. Venzago, S. W. Schmitt, G. Sarau, and S. H. Christiansen, "Modeling the dielectric function of degenerately doped ZnO: Al thin films grown by ALD using physical parameters," *Optical Materials Express*, vol. 5, no. 9, pp. 1979–1990, 2015.

[172] P. R. K. Elly and M. I. L. Iu, "Designing optical metamaterial with hyperbolic dispersion based on an Al : ZnO / ZnO nano-layered structure using the atomic layer deposition technique," vol. 55, no. 11, 2016.

[173] J. Tauc, "Optical Properties and Electronic Structure of Amorphous Ge and Si," *Materials Research Bulletin*, vol. 3, pp. 37–46, 1968.

[174] E. Burstein, "Anomalous optical absorptiion limit in InSb," *Phys. Rev.*, vol. 93, no. 3, pp. 632–633, 1954.

[175] T. S. Moss, "The interpretation of the properties of indium antimonide," *Proceedings of the Physical Society, London*, vol. 67B, pp. 775–782, 1954.

[176] S. Law, V. Podolskiy, and D. Wasserman, "Towards nano-scale photonics with micro-scale photons: The opportunities and challenges of mid-infrared plasmonics," *Nanophotonics*, vol. 2, no. 2, pp. 103–130, 2013.

[177] Y. Zhong, D. Wasserman, Y. Zhong, S. D. Malagari, T. Hamilton, and D. Wasserman, "Review of mid-infrared plasmonic materials Review of mid-infrared plasmonic materials," *Journal of Nanophotonics*, vol. 9, p. 093791, 2015.

[178] J. Haas and B. Mizaikoff, "Advances in Mid-Infrared Spectroscopy for Chemical Analysis," *Annual Review of Analytical Chemistry*, vol. 9, no. 1, pp. 45–68, 2016.

[179] A. Boltasseva, "Empowering plasmonics and metamaterials technology with new material platforms," *MRS Bulletin*, vol. 39, no. 05, pp. 461–468, 2014.

[180] P. Biagioni, J. Frigerio, A. Samarelli, K. Gallacher, L. Baldassarre, E. Sakat, E. Calandrini, R. W. Millar, V. Giliberti, G. Isella, D. J. Paul, and M. Ortolani, "Group-IV midinfrared plasmonics," *Journal of Nanophotonics*, vol. 9, no. 1, p. 093789, 2015.

[181] M. Cada, D. Blazek, J. Pistora, K. Postava, and P. Siroky, "Theoretical and experimental study of plasmonic effects in heavily doped gallium arsenide and indium phosphide," *Optical Materials Express*, vol. 5, no. 2, p. 340, 2015.

[182] M. E. Aryaee Panah, "Highly Doped InP as a Low Loss Plasmonic Material for Mid-IR Region," *Manuscript in preparation.*

[183] A. N. Grigorenko, M. Polini, and K. S. Novoselov, "Graphene plasmonics - optics in flatland.," *arXiv.org, e-Print Archive, Condensed Matter*, pp. 1–25, arXiv:1301.4241v1 [cond–mat.mes–hall], 2013.

[184] J. D. Caldwell, I. Vurgaftman, J. G. Tischler, O. J. Glembocki, J. C. Owrutsky, and T. L. Reinecke, "Atomic-scale photonic hybrids for mid-infrared and terahertz nanophotonics," *Nature Nanotechnology*, vol. 11, no. 1, pp. 9–15, 2016.

[185] W. Streyer, S. Law, G. Rooney, T. Jacobs, and D. Wasserman, "Strong absorption and selective emission from engineered metals with dielectric coatings.," *Optics express*, vol. 21, no. 7, pp. 9113–22, 2013.

[186] K. Anglin, T. Ribaudo, D. C. Adams, X. Qian, W. D. Goodhue, S. Dooley, E. A. Shaner, and D. Wasserman, "Voltage-controlled active mid-infrared plasmonic devices," *Journal of Applied Physics*, vol. 109, no. 12, pp. 1–6, 2011.

[187] J. C. Ginn, R. L. Jarecki, E. A. Shaner, and P. S. Davids, "Infrared plasmons on heavily-doped silicon," *Journal of Applied Physics*, vol. 110, no. 4, 2011.

[188] S. Law, L. Yu, A. Rosenberg, and D. Wasserman, "All-semiconductor plasmonic nanoantennas for infrared sensing," *Nano Letters*, vol. 13, no. 9, pp. 4569–4574, 2013.

[189] Y. Zhong, P. B. Dongmo, L. Gong, S. Law, B. Chase, D. Wasserman, and J. M. O. Zide, "Degenerately doped InGaBiAs:Si as a highly conductive and transparent contact material in the infrared range," *Optical Materials Express*, vol. 3, no. 8, p. 1197, 2013.

[190] P. Frolkovič, "Numerical recipes: The art of scientific computing," *Acta Applicandae Mathematicae*, vol. 19, pp. 297–299, jun 1990.

[191] R. Kitamura, L. Pilon, and M. Jonasz, "Optical constants of silica glass from extreme ultraviolet to far infrared at near room temperature," *Applied Optics*, vol. 46, p. 8118, nov 2007.

[192] C. Gabriel and A. Nedoluha, "Transmittance and Reflectance of Systems of Thin and Thick Layers," *Optica Acta: International Journal of Optics*, vol. 18, pp. 415–423, jun 1971.

[193] R. Maas, J. Parsons, N. Engheta, and A. Polman, "Experimental realization of an epsilon-near-zero metamaterial at visible wavelengths," *Nature Photonics*, vol. 7, no. 11, pp. 907–912, 2013.

[194] W. Yen, Y. Lin, and J. Ke, "Surface textured ZnO:Al thin films by pulsed DC magnetron sputtering for thin film solar cells applications," *Applied Surface Science*, vol. 257, pp. 960–968, nov 2010.

[195] Q. Guo, N. Uesugi, T. Tanaka, M. Nishio, and H. Ogawa, "Reactive Ion Etching of Zinc Oxide Using Methane and Hydrogen," *Japanese Journal of Applied Physics*, vol. 45, pp. 8597–8599, 2006.

[196] D. B. Williams and C. B. Carter, *Transmission Electron Microscopy*. Boston, MA: Springer US, 2009.

[197] R. Raghavan, M. Bechelany, M. Parlinska, D. Frey, W. M. Mook, A. Beyer, J. Michler, and I. Utke, "Nanocrystalline-to-amorphous transition in nanolaminates grown by low temperature atomic layer deposition and related mechanical properties," *Applied Physics Letters*, vol. 100, no. 19, 2012.

[198] P. N. Dyachenko, S. Molesky, A. Y. Petrov, M. Störmer, T. Krekeler, S. Lang, M. Ritter, Z. Jacob, and M. Eich, "Controlling thermal emission with refractory epsilon-near-zero metamaterials via topological transitions," *Nature Communications*, vol. 7, no. May, p. 11809, 2016.

[199] J. Polo and A. Lakhtakia, "Surface electromagnetic waves: A review," *Laser & Photonics Reviews*, vol. 5, pp. 234–246, mar 2011.

[200] Y. Guo, W. Newman, C. L. Cortes, and Z. Jacob, "Applications of hyperbolic metamaterial substrates," *Advances in OptoElectronics*, vol. 2012, no. 1, pp. 1–10, 2012.

[201] Z. Jacob and E. E. Narimanov, "Optical hyperspace for plasmons: Dyakonov states in metamaterials," in *2009 IEEE LEOS Annual Meeting Conference Proceedings*, vol. 221109, pp. 563–564, IEEE, oct 2009.

[202] O. Takayama, D. Artigas, and L. Torner, "Practical dyakonons," *Optics Letters*, vol. 37, no. 20, p. 4311, 2012.

[203] N. Talebi, C. Ozsoy-Keskinbora, H. M. Benia, K. Kern, C. T. Koch, and P. A. van Aken, "Wedge Dyakonov Waves and Dyakonov Plasmons in Topological Insulator Bi 2 Se 3 Probed by Electron Beams," *ACS Nano*, vol. 10, pp. 6988–6994, jul 2016.

[204] K.-H. Kim, Y.-S. No, S. Chang, J.-H. Choi, and H.-G. Park, "Invisible Hyperbolic Metamaterial Nanotube at Visible Frequency.," *Scientific reports*, vol. 5, p. 16027, 2015.

[205] F. Güder, Y. Yang, S. Goetze, A. Berger, R. Scholz, D. Hiller, D. Hesse, and M. Zacharias, "Toward Discrete Multilayered Composite Structures: Do Hollow Networks Form in a Polycrystalline Infinite Nanoplane by the Kirkendall Effect?," *Chemistry of Materials*, vol. 23, pp. 4445–4451, oct 2011.

[206] A.-A. El Mel, R. Nakamura, and C. Bittencourt, "The Kirkendall effect and nanoscience: hollow nanospheres and nanotubes," *Beilstein Journal of Nanotechnology*, vol. 6, pp. 1348–1361, jun 2015.

[207] M. Kumar, N. Umezawa, S. Ishii, and T. Nagao, "Examining the performance of refractory conductive ceramics as plasmonic materials: a theoretical approach," pp. 1–9, oct 2015.

[208] J. Xiang, Y. Ding, L. Du, and J. Li, "Growth mechanism of atomic-layer-deposited TiAlC metal gate based on TiCl4 and TMA precursors," *Chinese Physics B*, vol. 25, no. 3, pp. 1–4, 2016.

[209] J. Xiang, Y. Ding, L. Du, C. Xu, T. Li, X. Wang, J. Li, and C. Zhao, "Investigation of N Type Metal TiAlC by Thermal Atomic Layer Deposition Using TiCl4 and TEA as Precursors," *ECS Journal of Solid State Science and Technology*, vol. 5, no. 5, pp. P299–P303, 2016.

List of publications

Parts of this thesis have been submitted and published in several peer-reviewed journals, conference proceedings and presented at international conferences:

- **Publications in peer-review journals**

  Realization of mid-infrared hyperbolic metamaterial based on high aspect ratio, highly ordered Al-doped ZnO nanopillars
  E. Shkondin, O. Takayama, M. E. A. Panah, P. Liu, P. V. Larsen, M. D. Mar, T. W. Hansen, F. Jensen, and A. V. Lavrinenko
  Optical Materials Express (in preparation) (2016)

  Directional infrared surface waves on aluminium doped ZnO-Si structures with multiple high aspect ratio nanotrenches
  O. Takayama, **E. Shkondin**, A. Bogdanov, M. E. A. Panah, K. Golenicki, P. Dmitriev, T. Repän, R. Malureanu, P. Belov, F. Jensen and A. V. Lavrineko
  Nature Nanotechnology (submitted) (2016)

  Laguerre-Gauss beam generation in IR and UV by subwavelength surface-relief graitings
  L. Vertchenko, **E. Shkondin**, R. Malureanu and C. H. Monken
  Optical Express (submitted) (2016)

  Fabrication of high aspect ratio TiO2 and Al2O3 nanogratings by atomic layer deposition
  E. Shkondin, O. Takayama, J. Lindhard, P. V. Larsen, M. D. Mar, F. Jensen, and A. V. Lavrinenko
  Journal of Vacuum Science and Technology A, 34, 031605 (2016)

  Experimental demonstration of effective medium approximation breakdown in deeply subwavelength all-dielectric multilayers
  S. Zhukovsky, A. Andryieuski, O. Takayama, **E. Shkondin**, R. Malureanu, F. Jensen, and A. V. Lavrinenko
  Physical Review Letters, 115(17), 177402 (2015)

- **Publications in proceedings**

  Effective medium approximation for deeply subwavelength all-dielectric multilayers: when does it break down?
  A. Lavrinenko, S. Zhukovsky, A. Andryieuski, O. Takayama, **E. Shkondin**, R. Malureanu and F. Jensen
  Proceedings of SPIE. Vol. 9883 SPIE - International Society for Optical Engineering, (2016)

  Fabrication of deep-profile Al-doped ZnO one- and two-dimensional lattices as plasmonic elements
  F. Jensen, **E. Shkondin**, O. Takayama, P. V. Larsen, M. D. Mar, R. Malureanu, A. V. Lavrinenko
  Proceedings of SPIE. Vol. 9921 SPIE - International Society for Optical Engineering, (2016)

  Hyperbolic metamaterials with complex geometry
  A. V. Lavrinenko, A. Andryieuski, S. Zhukovsky, O. Takayama, **E. Skhondin**, M. E. A. Panah, R. Malureanu, F. Jensen
  META'16, The 6th International Conference on Metamaterials, Photonic Crystals and Plasmonics, Malaga, Spain, 2A23, Proceedings, p.471-472 (2016)

  Surface waves on metal-dielectric metamaterials
  O. Takayama, **E. Shkondin**, M. E. A. Panah, T. Repän, R. Malureanu, F. Jensen, A. V. Lavrinenko
  Proceedings of 18th International Conference on Transparent Optical Networks. IEEE, (2016)

  Surface waves on metamaterials interfaces
  O. Takayama, **E. Shkondin**, M. E. A. Panah, T. Repän, R. Malureanu, F. Jensen, A. V. Lavrinenko
  Proceedings of 10th International Congress on Advanced Electromagnetic Materials in Microwaves and Optics. (2016)

  Ultra-thin metal and dielectric layers for nanophotonic applications
  E. Shkondin, L. Leandro, R. Malureanu, F. Jensen, N. Rozlosnik, A. V. Lavrinenko
  Proceedings of ICTON, IEEE, 7193380. (2015)

- **Conferences and workshops**

Conductive oxides trench structures as hyperbolic metamaterials in mid-infrared range
O. Takayama, **E. Shkondin**, M. E. A. Panah, T. Repän, R. Malureanu, F. Jensen, A. V. Lavrinenko
Abstract from 14th International Conference of Near-Field Optics, Nanophotonics and Related Techniques, Hamamatsu, Japan

Fabrication of hollow coaxial ZnAl2O4 high aspect ratio freestanding nanopillars based on the Kirkendall effect
E. Shkondin, F. Jensen, A. V. Lavrinenko
2016. Abstract from 42nd Micro and Nano Engineering 2016, Vienna, Austria.

Fabrication of Al-doped ZnO high aspect ratio nanowires and trenches as active components in mid-infrared plasmonics
E. Shkondin, O. Takayama, P. V. Larsen, M. D. Mar, F. Jensen, A. V. Lavrinenko
2016. Abstract from 16th Atomic Layer Deposition Conference, Dublin, Ireland.

TiO2 and Al2O3 ALD grown multilayers for subwavelength photonics
E. Shkondin, F. Jensen, A. V. Lavrinenko, M. D. Mar, P. V. Larsen, R. Malureanu, S. Zhukovsky, A. Andryieuski, O. Takayama
DTU's Sustain Conference 2015, Technical University of Denmark, Kgs. Lyngby, Denmark (2015)

Deep subwavelength photonic multilayers fabricated by atomic layer deposition
E. Shkondin, S. Zhukovsky, A. Andryieuski, O. Takayama, R. Malureanu, M. D. Mar, A. V. Lavrinenko, F. Jensen
2015. Paper presented at 41st International conference on Micro and Nano Engineering , The Hague, Netherlands.

Fabrication of TiO2 and Al2O3 High Aspect Ratio Nanostructured Gratings at Sub-Micrometer Scale
E. Shkondin, J. M. Lindhard, M. D. Mar, F. Jensen, A. V. Lavrinenko
2015. Paper presented at 15th International Conference on Atomic Layer Deposition, Portland, Oregon, United States

Depositing Materials on the Micro- and Nanoscale
M. D. Mar, B. Herstrøm, **E. Shkondin**, P. Pholprasit, F. Jensen
DTU's Sustain Conference 2014, Technical University of Denmark, Kgs. Lyngby, Denmark (2014)